NASA/TP-20260006857

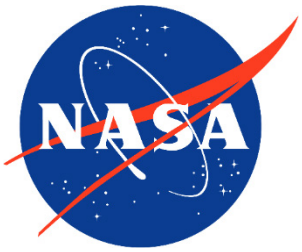

NASA Space Cancer Risk Model 2025: Multi-model Ensemble Quality Factor

Tony C. Slaba[1], *Charles M. Werneth*[1], *Floriane Poignant*[2], *Janice L. Huff*[1]

1. *NASA Langley Research Center, Hampton, Virginia*
2. *Analytical Mechanics Associates, Hampton, Virginia*

August 2026

NASA STI Program Report Series

Since its founding, NASA has been dedicated to the advancement of aeronautics and space science. The NASA scientific and technical information (STI) program plays a key part in helping NASA maintain this important role.

The NASA STI program operates under the auspices of the Agency Chief Information Officer. It collects, organizes, provides for archiving, and disseminates NASA's STI. The NASA STI program provides access to the NTRS Registered and its public interface, the NASA Technical Reports Server, thus providing one of the largest collections of aeronautical and space science STI in the world. Results are published in both non-NASA channels and by NASA in the NASA STI Report Series, which includes the following report types:

- TECHNICAL PUBLICATION. Reports of completed research or a major significant phase of research that present the results of NASA Programs and include extensive data or theoretical analysis. Includes compilations of significant scientific and technical data and information deemed to be of continuing reference value. NASA counterpart of peer-reviewed formal professional papers but has less stringent limitations on manuscript length and extent of graphic presentations.

- TECHNICAL MEMORANDUM. Scientific and technical findings that are preliminary or of specialized interest, e.g., quick release reports, working papers, and bibliographies that contain minimal annotation. Does not contain extensive analysis.

- CONTRACTOR REPORT. Scientific and technical findings by NASA-sponsored contractors and grantees.

- CONFERENCE PUBLICATION. Collected papers from scientific and technical conferences, symposia, seminars, or other meetings sponsored or co-sponsored by NASA.

- SPECIAL PUBLICATION. Scientific, technical, or historical information from NASA programs, projects, and missions, often concerned with subjects having substantial public interest.

- TECHNICAL TRANSLATION. English-language translations of foreign scientific and technical material pertinent to NASA's mission.

Specialized services also include organizing and publishing research results, distributing specialized research announcements and feeds, providing information desk and personal search support, and enabling data exchange services.

For more information about the NASA STI program, see the following:

- Access the NASA STI program home page at http://www.sti.nasa.gov

.

NASA/TP-20260006857

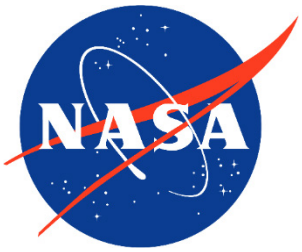

NASA Space Cancer Risk Model 2025: Multi-model Ensemble Quality Factor

Tony C. Slaba[1], Charles M. Werneth[1], Floriane Poignant[2], Janice L. Huff[1]

1. *NASA Langley Research Center, Hampton, Virginia*
2. *Analytical Mechanics Associates, Hampton, Virginia*

National Aeronautics and
Space Administration

Langley Research Center
Hampton, Virginia 23681-2199

August 2026

The use of trademarks or names of manufacturers in this report is for accurate reporting and does not constitute an official endorsement, either expressed or implied, of such products or manufacturers by the National Aeronautics and Space Administration.

Available from:

NASA STI Program / Mail Stop 050
NASA Langley Research Center
Hampton, VA 23681-2199

Contents

Figures

Tables

Abbreviations

1D	One Dimensional
3D	Three Dimensional
ACE	Advanced Composition Explorer
AI	Artificial Intelligence
AIC	Akaike Information Criterion
ALARA	As Low As Reasonably Achievable
AML	Acute Myeloid Leukemia
AMS	Alpha Magnetic Spectrometer
ARRT	Acute Radiation Risk Tool
ATIC	Advanced Thin Ionization Calorimeter
BEIR	Biological Effects of Ionizing Radiation
BESS	Balloon-borne Experiment with a Superconducting Spectrometer
BFO	Blood Forming Organs
BON	Badhwar-O'Neill
BPD	Biophysical Payload Detector
BRFSS	Behavioral Risk Factor Surveillance System
CAD	Computer-Aided Design
CAF	Computerized Anatomical Female
CAM	Computerized Anatomical Man
CAPRICE	Cosmic AntiParticle Ring Imaging Cherenkov Experiment
CDC	Centers for Disease Control and prevention
CHIP	Clonal Hematopoiesis of Indeterminate Potential
CI	Confidence Interval
CK	Cell-Killing
CNS	Central Nervous System
CRATER	Cosmic RAy Telescope for the Effects of Radiation
CREAM	Cosmic Ray Energetics And Mass
CRIS	Cosmic Ray Isotope Spectrometer
CSDA	Continuous Slowing Down Approximation
CT	Computed Tomography
CVD	CardioVascular Disease
DevCan	probability of DEVeloping or dying of CANcer
EAR	Excess Absolute Risk
ENDF	Evaluated Nuclear Data Files
ER	Excess Risk
ERR	Excess Relative Risk
DDFRG	Double Differential FRaGmentation
DDREF	Dose and Dose-Rate Effectiveness Factor
DNA	DeoxyriboNucleic Acid
DSB	Double Strand Break
FAX	Female Adult voXel
FISH	Fluorescence In Situ Hybridization
FLUKA	FLUctuierende KAskade
Geant	GEometry ANd Tracking
GCR	Galactic Cosmic Rays
GCRsim	GCR Simulator
GSI	Gesellschaft für Schwerionenforschung
HEAO	High Energy Astronomical Observatory
Hi-C	High-throughput Chromosome Conformation Capture
HPU	Hybrid electronic radiation assessor Processing Unit
HSU	Hybrid electronic radiation assessor Sensing Unit
HZETRN	High charge (Z) and Energy TRaNsport
ICRP	International Commission on Radiological Protection
IMAX	Isotope Matter-Antimatter eXperiment
INCLXX	Intra-Nuclear Cascade, Liege, version XX
ISS	International Space Station

LEO	Low Earth Orbit
LET	Linear Energy Transfer
LRO	Lunar Reconnaissance Orbiter
LSS	Life Span Study
MASS	Matter Antimatter Spectrometer System
MAX	Male Adult voXel
MCD	Mars Climate Database
MCM	Medical CounterMeasures
MCNP6	Monte Carlo N-Particle, version 6
MCNPX	Monte Carlo N-Particle eXtended
μD	Microdosimetry
ML	Machine Learning
mP	multilevel Probability
MPS	Million Person Study
MSLRAD	Mars Science Laboratory Radiation Assessment Detector
NASA	National Aeronautics and Space Administration
NASA STD	National Aeronautics and Space Administration STanDard
NASARTI	NASA Radiation Track Image
NASEM	National Academies of Sciences, Engineering, and Medicine
NCI	National Cancer Institute
NCRP	National Council on Radiation Protection and measurements
NCSH	National Center for Health Statistics
noNTE	no-Non Targeted Effect
NRC	National Research Council
NSCR	NASA Space Cancer Risk
NSRL	NASA Space Radiation Laboratory
NTE	Non-Targeted Effect
NUCFRG	NUClear FRaGmentation
NVSR	National Vital Statistics Reports
PAMELA	Payload for Antimatter Matter Exploration and Light-nuclei Astrophysics
PEL	Permissible Exposure Limit
PHITS	Particle and Heavy Ion Transport code System
QF	Quality Factor
QMD	Quantum Molecular Dynamics
RAADFRG	Relativistic Abrasion/Ablation/De-excitation FRaGmentation
RBE	Relative Biological Effectiveness
RBE_{max}	Maximum Relative Biological Effectiveness
REIC	Risk of Exposure-Induced Cancer
REID	Risk of Exposure-Induced Death
REM	Radiation Environment Monitor
RER	Relative Effects Ratio
RIF	Radiation-Induced Foci
RITCARD	Radiation-Induced Tracks, Chromosome Aberrations, Repair, and Damage
RITRACKS	Relativistic Ion Tracks
RMSE	Root Mean Square Error
SD	Sprague-Dawley
SPE	Solar Particle Events
SSE	Sum of Squares Error
SSN	SunSpot Number
TAD	Topological Associated Domains
TRACER	Transition Radiation Array for Cosmic Energetic Radiation
TE	Targeted Effects
UNSCEAR	United Nations Scientific Committee on the Effects of Atomic Radiation
US	United States
WONDER	Wide-ranging ONline Data for Epidemiologic Research

Executive Summary

Exposure to ionizing radiation in space is a significant hazard for crewmembers and is associated with health risks that may include acute radiation syndrome, degenerative tissue effects such as circulatory diseases and cataracts, central nervous system effects, and carcinogenesis. As the National Aeronautics and Space Administration (NASA) endeavors to expand exploration with sustained habitation of the lunar surface and extended missions to Mars, there is an increasing need to accurately quantify and effectively communicate information on space radiation health risks and uncertainties for individual crewmembers and to develop methods to evaluate the impact of proposed risk mitigation and surveillance strategies [NASEM 2021, Simonsen and Slaba 2021].

The NASA Space Cancer Risk (NSCR) model was developed to assess risk (incidence and mortality) for a wide range of solid cancers and leukemias attributable to mission radiation exposure. The NSCR model has been used operationally for astronaut risk assessment and mission planning since 2013, and in 2022 it was used to guide revisions to the career permissible exposure limit (PEL) [NASA 2022]. NSCR is based on epidemiological data and models derived from the Life Span Study (LSS) of Japanese atomic bomb survivors. Scaling factors are used to adjust for differences between the acute, predominantly low linear energy transfer (LET) exposure received by the LSS cohort and the unique space radiation environment, which is characterized by a chronic, low dose-rate exposure to a mixed field of energetic ions spanning a broad LET range. The radiation quality factor (QF) is the key component used to account for differences in biological effectiveness between the low LET exposures of the LSS cohort and the complex high LET exposures in space and represents the largest source of uncertainty in space radiation risk assessment.

This report introduces the 2025 version of the NSCR model (NSCR2025) and includes a detailed description of changes and updates to model subcomponents enabled by availability of new knowledge, data sources, and computational tools since the initial model release in 2012 (NSCR2012) [Cucinotta et al. 2013b]. Briefly, the NSCR2025 model incorporates significant improvements to the ambient space radiation environmental models, nuclear physics and radiation transport models; new anatomical human phantom models; updated baseline cancer incidence, mortality, and survival rates of the US population; a new space radiation QF, and an initial capability to evaluate medical countermeasures and individualized risk factors within space radiation risk projections. Importantly, the radiation QF was extensively reformulated within a rigorous multi-model ensemble framework with clear traceability to underlying data sources and robust assessment of associated uncertainties. Preliminary information obtained from the ground-based Galactic Cosmic Ray simulator (GCRsim) at the NASA Space Radiation Laboratory (NSRL) related to the use of simple additivity has been accounted for in the updated risk model. Highlights of the NSCR2025 model are summarized next in the order of appearance in the full document.

Ambient Space Radiation Environment, Nuclear Physics, Radiation Transport Models, and Validation

To evaluate the radiation exposure of crewmembers inside spacecraft or planetary habitats for a particular mission, the ambient space radiation environment impinging on mass shielding materials must first be characterized. Nuclear cross section models and databases describing the interaction of the space radiation environment with shielding materials are needed, and transport algorithms that accurately model the propagation of light and heavy particles (and any secondary particles produced from nuclear interactions) through spacecraft shielding materials and human tissue are required. Highlights of the updates included in NSCR2025 are as follows:

- Significant improvements in galactic cosmic ray (GCR) environment model accuracy have been achieved through updates to the BON2020 GCR model guided by precision measurements from the Alpha Magnetic Spectrometer (AMS-02) and the Payload for Antimatter Matter Exploration and Light-nuclei Astrophysics (PAMELA). This represents a key advancement for future long duration missions where exposure to GCR is the primary radiation hazard for crewmembers.
- Major advancements in nuclear physics models used in the High charge (Z) and Energy TRaNsport (HZETRN) radiation transport code include a relativistic heavy ion fragmentation model with nuclear structure effects; a thermal pion, nucleon, and light ion production model; a Serber intranuclear transport model for nucleon production. These advancements influence both the magnitude and qualitative features of the calculated radiation field behind moderate and thick shielding and are needed to enable more accurate lunar and Martian surface environment calculations.
- Substantial updates to radiation transport algorithms contained in HZETRN have occurred in recent years, including improved treatment of three-dimensional (3D) scattering and coupled pion-nucleon interactions. These physical processes are needed to accurately describe the propagation of light ions and neutrons through

moderate and thick shielding and more accurately estimate surface environments on the Moon and Mars. This capability is critical for sustaining human presence on the Moon as the GCR-induced albedo environment accounts for a significant proportion (10% - 30%) of crew exposure on the surface.

- The combined suite of environment, physics, and transport models used in NSCR2025 were successfully validated against spaceflight data simultaneously collected from the International Space Station (ISS), the Orion spacecraft, the BioSentinel CubeSat, and the Martian surface during the Artemis-I mission timeframe and showed excellent agreement with spaceflight data.

NASA Space Cancer Risk Model

Human phantom and tissue exposure assessment updates

NASA utilizes human phantom models to evaluate fluxes and dosimetric quantities in human surrogates. The Computerized Anatomical Man (CAM) and Computerized Anatomical Female (CAF) phantoms used in NSCR2012 have been replaced with the high-resolution Male Adult voXel (MAX) and Female Adult voXel (FAX) phantoms in NSCR2025. Tissue exposure uncertainties used in NSCR2012 have been updated as well based on more recent spaceflight validation studies and are now deemed applicable beyond LEO and on the lunar and Mars surfaces.

Baseline population updates

The baseline population databases for cancer incidence, cancer mortality, and survival probabilities have been updated for NSCR2025 using combined data from 2018, 2019, and 2021 with no significant changes to the data sources and analysis methods.

NASA radiation quality factor updates

The radiation QF model is an essential component of NSCR necessary for translation of epidemiological data from low LET exposed terrestrial cohorts to the space radiation environment. The QF model is constructed from the Maximum Relative Biological Effectiveness (RBE_{max}) — the ratio of the low dose linear induction coefficients for high-LET radiation compared to a low LET reference radiation for a given biological effect. RBE_{max} values are derived from radiobiology datasets of cancer surrogate endpoints from experimental studies with animal and cell model systems. Datasets with adequate coverage of high-LET components of the space environment and suitable statistics are scarce, leading to large uncertainties in this important component of NSCR. Recent advances in dose-response models and ensemble methodologies, along with the availability of new experimental data motivated the development of the new NASA QF model.

As depicted in Figure 16, dose-response models used to inform the NSCR2025 QF were calibrated to global experimental datasets encompassing observations collected in the same experimental system over a broad range of doses and particle types relevant to space radiation-induced carcinogenesis. Individual datasets that generally lack the requisite particle coverage to support global calibration, along with data from the simulation tool Radiation-Induced Tracks, Chromosome Aberrations, Repair, and Damage (RITCARD), serve as additional sources of Relative Biological Effectiveness (RBE) values that can influence specific QF components and uncertainty quantification. This approach provides clear traceability to underlying data sources and robust assessment of associated uncertainties. Furthermore, these updates are compliant with NASA STanDard (NASA STD) 7009 guidelines for the development and use of models and align with recommendations for improved space radiation risk communication provided by the National Academies of Sciences, Engineering, and Medicine (NASEM) in 2021.

Key features of the NSCR2025 QF

- Clear traceability to underlying experimental datasets and objective assignment of parameter values, uncertainties and correlations guided by experimental data.
- Utilization of ensemble global dose-response models capable of recapitulating experimental data and predicting responses where no data exist. This feature was made possible by new data and global dose-response models not previously available, which enable RBE_{max} calculations over the full range of particles comprising the space environment.
- Objective and robust QF uncertainty estimates that account for dose-response model errors, experimental data uncertainty, and variation across endpoints.
- Simplified dependence of the QF on ion LET, which facilitates integration within existing spaceflight dosimetry systems and improved linkage between spaceflight measurements and risk projections.

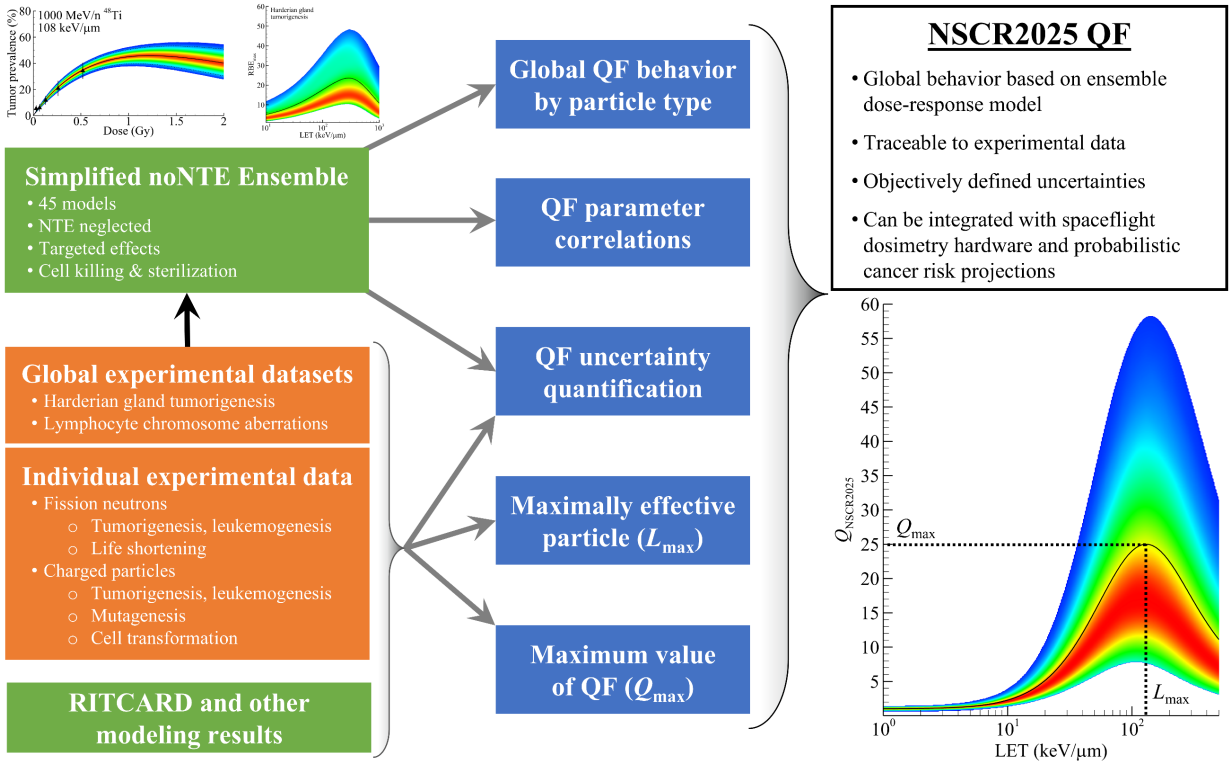

Figure 16. NSCR2025 QF development strategy flowchart. Global experimental datasets are used in conjunction with a simplified noNTE ensemble dose-response model to provide global RBE_{max} estimates (i.e., covering the range of particle types found in space). Global and individual experimental data are used to identify the maximally effective particle (L_{max}) and maximum QF (Q_{max}) and guide parameter correlations and uncertainty assignments.

Model components retained from NSCR2012

The excess risk models—Excess Relative Risk (ERR) and Excess Absolute Risk (EAR)—and uncertainties, population transfer weights and uncertainty distributions, cancer latency factors, and Dose and Dose-Rate Effectiveness Factor (DDREF) models implemented in NSCR2012 are retained in NSCR2025 without modification.

NSCR2025 Model Results

In Figure 41, the NASA and International Commission on Radiological Protection (ICRP) methods (QF and tissue weights) were used to evaluate the annual effective dose for 35 year old males and females as a function of aluminum shielding thickness with exposure from the 2009 solar minimum GCR environment. Also shown are comparisons with never smoker corrections to the average US population. Note that the NSCR2025 model shows appreciably lower effective doses compared to NSCR2020 [Simonsen and Slaba 2020, 2021] and is consistent with the ICRP models.

Further calculations were completed using the NSCR2025 model to determine the NASA effective dose corresponding to a 3% mean Risk of Exposure-Induced Death (REID) for a 35 year old female astronaut (never smoker). Assuming the 2009 GCR environment and 20 g/cm^2 aluminum shielding, it was found that a NASA effective dose of 661 mSv yields a 3% mean REID with an upper 95th percent confidence bound of 7.5%. The updated NSCR2025 QF and NASA effective dose tissue weights derived from NSCR2025 represent a collection of validated, evidence-based model advancements anchored by ground-based experimental data, epidemiological data, and spaceflight measurements which should be adopted for use at NASA as a replacement for the NSCR2012 quantities.

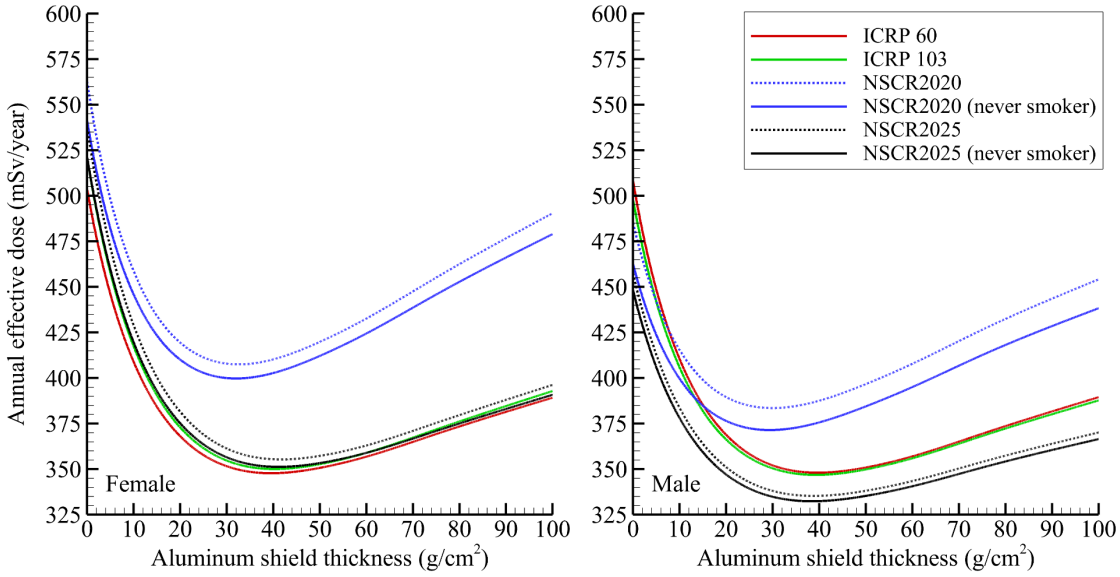

Figure 41. NASA and ICRP annual effective dose (mSv/year) versus aluminum shield thickness for males and females during the 2009 solar minimum GCR environment.

Medical Countermeasures and Individual Risk Assessment

NASA envisions an integrated approach to safeguard crewmembers from the health risks associated with space radiation exposure. The current strategy includes physical protection with optimized vehicle design, storm shelters, active dosimetry and mission planning to minimize crew exposures. However, for planned long duration lunar surface stays and future Mars exploration missions the current PEL will likely be exceeded, and additional protection strategies may be needed to reduce risks. NASA is investigating the use of medical countermeasures (MCM) (e.g., medications and supplements) to prevent or mitigate space radiation risks. Diet, exercise, and other modifiable lifestyle factors, along with understanding the role of individual susceptibility/sensitivity and clinical interventions such as increased post-mission surveillance, are also being considered. Protection of crew requires the ability to accurately quantify and effectively communicate information on space radiation health risks, possible mitigation approaches and associated uncertainties to crewmembers, mission planners, and other stakeholders. The NSCR2025 includes an initial capability to assess the impact of medical countermeasures on space radiation risk reduction and to assess individualized risks for crewmembers. A summary of the new capabilities is provided below:

- User-defined age- and sex-dependent scaling factors can be applied to cancer mortality rates, cancer incidence rates, and baseline US population survival curves.
- Uncertainty distributions for age- and sex-dependent scaling factors may be propagated with user-defined input.
- The ability to assess individual risks that can be expressed through differences in cancer hazard rates and survival curves as compared to a baseline reference population.

1. Introduction

The Artemis-II mission successfully carried humans farther from Earth than ever before. Future activities are expected to build upon this success with long duration mission architectures planned for deep space transit, lunar habitation, and Mars exploration. Commercial space activities in low Earth orbit are increasing as well which may include individuals with more heterogeneous health profiles and lifestyle factors as compared to typical crewmembers. Humans involved in either of these scenarios will be exposed to highly energetic and complex radiation fields unlike anything found on Earth.

Beyond the geomagnetic field, there is a continuous low dose-rate of GCR and the possibility of intense solar particle events (SPE) lasting hours to days [Benton and Benton 2001]. GCR include full ionized nuclei from H to Ni and beyond with energies ranging from MeV/n up to TeV/n. The GCR intensity is modulated by the heliospheric magnetic field below ~5 GeV/n over a time frame of approximately 11 years between solar minimum (maximal intensity) and solar maximum (minimal intensity), resulting in a dose-rate difference of roughly a factor of two. The complex mixed field of energetic primary GCR ions instigates nuclear collisions within spacecraft shielding, yielding secondary radiation including charged particles, mesons, leptons, photons, and neutrons. GCR shielding is thus a challenging endeavor that continues to be investigated, but at this time, no solution has been found that appreciably reduces exposure within practical launch constraints.

SPE include mainly moderate energy protons (<100 MeV) accelerated from the Sun during coronal mass ejections and solar flares with some storms producing GeV protons and heavier nuclei [Benton and Benton 2001]. It is known that storms are more likely to occur during solar maximum, but the duration, spectral characteristics, and overall intensity vary widely. SPE forecasting capabilities are highly uncertain as well. Shielding strategies have been developed to effectively reduce SPE crew exposures and acute biological risks. This includes both optimizing the distribution of available on-board mass and designing storm-shelters within the vehicle to ensure predicted exposures satisfy the As Low As Reasonably Achievable (ALARA) principle and remain below established limits.

On the surface of the Moon and Mars, primary GCR and SPE intensities are reduced by approximately a factor of two due to terrestrial/planetary shielding. However, there are upward directed albedo environments induced by nuclear interactions between downward directed GCR or SPE ions and the surface regolith (and atmosphere in the case of Mars). The albedo radiation fields include low energy charged particles and photons, but the primary concern arises from secondary neutrons emanating from the surface. These albedo neutrons contribute moderately to the total exposure and risk for crewmembers and cannot be ignored.

In Earth orbit, the GCR and SPE fields are attenuated due to planetary and geomagnetic shielding effects [Benton and Benton 2001] that vary with orbital/trajectory parameters. There are also intense belts of protons and electrons trapped by the geomagnetic field. The trapped electrons are generally low energy and incapable of penetrating human rated spacecraft. The trapped proton field, however, extends over a broad energy range up to hundreds of MeV and beyond and can penetrate through vehicle shielding and significantly enhance crew exposures. A majority of the dose received by humans in Earth orbit originates from trapped protons in the South Atlantic Anomaly and GCR in high latitude and polar regions.

NASA has identified exposure to space radiation as one of the five hazards of human spaceflight[1] based on an extensive body of evidence arising from terrestrial exposures and ground-based experimental data[2]. There are both in-flight and-long term health consequences that can arise from exposure to the various space radiation environments. In-flight health effects are mainly associated with SPE exposure which can initiate acute radiation responses (e.g., nausea, vomiting, hematopoietic effects) if adequate shielding is not provided. This risk is effectively controlled through pre-mission shielding design and optimization, exposure limits, and on-board real-time dosimetry. For long duration missions, there may also be a risk of in-flight cognitive decrements from prolonged GCR exposure; research is ongoing to establish an evidence base for this endpoint.

Long-term health consequences following exposure to space radiation can adversely affect quality of life and life expectancy for crewmembers. These include carcinogenesis, cardiovascular disease (CVD), and central nervous system (CNS) effects. The evidence base for CVD and CNS endpoints continues to be established through epidemiological studies of terrestrially exposed cohorts and ground-based experiments. A preliminary risk model for CVD was developed [Cucinotta et al. 2013a], but further research is needed to investigate possible thresholds and radiation quality effects [Huff et al. 2022].

The risk of space radiation-induced carcinogenesis has been studied extensively over the past several decades and continues to be an important area of research for NASA [Durante and Cucinotta 2008, Barcellos-Hoff et al. 2015,

[1] https://www.nasa.gov/hrp/hazards
[2] https://humanresearchroadmap.nasa.gov/Evidence

Patel et al. 2020] and other space agencies [Fogtman et al. 2023]. A key goal of these efforts is to arrive at accurate projections of carcinogenic risk attributable to spaceflight exposure received during one or more missions over a crewmember's career. The NSCR model was developed for this purpose; a high-level flowchart of the components contained in the NSCR model is shown in Figure 1.

As shown in Figure 1, the NSCR model is an integrated suite of computational models and data. Mission specific tissue fluence spectra are calculated by combining space radiation environment, physics, and transport models with complex shielding and anatomical human phantom models and available crew dosimetry. Cancer risks for the mission are estimated using the calculated tissue fluence spectra in conjunction with excess risk models derived from the LSS cohort extrapolated to account for differences in radiation quality, dose-rate, and population [Cucinotta et al. 2013b; Simonsen and Slaba 2020, 2021; Stegeman et al. 2025].

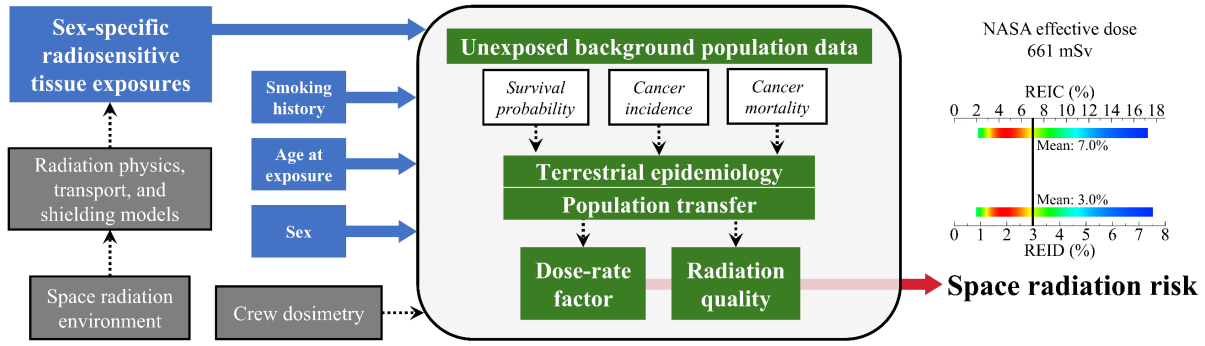

Figure 1. Overview of the NSCR computational framework. Example REID, REIC, and NASA effective dose values on the right were calculated with NSCR2025 for a 35 year old female astronaut (never smoker) on a 643 day mission (selected so the mean REID is 3%) behind 20 g/cm^2 aluminum exposed to the 2009 solar minimum GCR environment.

Cucinotta et al. [2013b] described the 2012 version of NSCR, denoted as NSCR2012, in a NASA technical report which is referred to throughout the rest of this document as the "NSCR2012 report". The NSCR2012 model was independently reviewed by the National Research Council (NRC) [NRC 2012] and subsequently approved for operational use at NASA. The overall structure of NSCR2012 is the same as indicated in Figure 1.

Major improvements in GCR environment models, nuclear physics models, radiation transport, and human phantom models were incorporated in the NSCR2020 model [Simonsen and Slaba 2020]. The computational framework was also substantially extended to allow ensemble analyses [Simonsen and Slaba 2021]. The ensemble framework incorporates multiple plausible models for major components of NSCR to provide a broader perspective of the risk and uncertainty landscape than what could be ascertained from a single model paradigm. Information from NSCR2020 and the ensemble framework were used by NASEM in their assessment of space radiation cancer risk communication strategies used at NASA [NASEM 2021].

In this paper, the 2025 version of the NSCR model (NSCR2025) is described. Significant updates have been incorporated into NSCR2025: a new space radiation QF; methods to evaluate medical countermeasures and individualized factors within space radiation risk projections; updated baseline cancer incidence, mortality, and survival rates; and updated environment, physics, and transport models.

The QF used in NSCR at NASA has not been updated or changed since the NSCR2012 report and represents one of the key terms determining the exposure-to-risk relationship and driving overall uncertainty in space radiation cancer risk projections. New experimental data have been collected since the NSCR2012 report, and advancements in dose-response models and ensemble methodologies have been completed as well. Ample motivation therefore exists to revisit the manner in which radiation quality effects and uncertainties are assessed in NSCR. Experimental data that were not available at the time of the NSCR2012 report (or not referenced) include:

- Chromosome aberration yields in irradiated normal human blood lymphocyte cells [Georget et al. 2013].
- Chromosome aberration yields in irradiated normal human skin fibroblast cells [Hada et al. 2014].
- Gastrointestinal and colon tumorigenesis in irradiated Apc$^{1638N/+}$ mice [Suman et al. 2016].
- Harderian gland tumorigenesis in irradiated CB6F1/Hsd mice [Chang et al. 2016].
- Lung tumorigenesis in irradiated CB6F1/Hsd mice [Chang et al. 2022].
- Cellular transformation data that were not referenced in the NSCR2012 report [Bettega et al. 2009].
- Cellular mutagenesis data that were not referenced in the NSCR2012 report [Stoll et al. 1995, 1996; Belli et al. 1998; Suzuki et al. 1996, 2003, 2006; Hei et al. 1988; Chen et al. 1984; Tsuruoka et al. 2009].

Experimental data noted in the NSCR2012 report are utilized in this update as well and are explicitly documented in Sections 5.7.2.1 and 5.7.3.1.

Dose-response models are a foundational aspect of QF development, as they provide the basis for quantifying biological effectiveness. Indeed, it was noted in the NSCR2012 report and by Chang et al. [2016] that global dose-response models capable of recapitulating limited experimental data and predicting responses for particle types where no data exist are particularly important given the breadth of particles found in space.

Guided in part by the additional experimental data identified in the bulleted list, new global dose-response models have been recently developed. Slaba et al. [2025a] presented a microdosimetry-based model and demonstrated its ability to accurately predict biological responses for a range of endpoints and experimental systems (Harderian gland tumorigenesis, lymphocyte chromosome aberrations, fibroblast chromosome aberrations). Xu et al. [2026] developed a multi-level probabilistic dose-response model accounting for both targeted and non-targeted effects with extensibility to mixed-fields and demonstrated its utility for predicting Harderian gland tumorigenesis.

Expanding upon these efforts and inspired by the work of Walsh and colleagues [Stabilini et al. 2023, Hafner and Walsh 2024], Slaba et al. [2026] developed a multi-model ensemble dose-response framework accounting for targeted effects, non-targeted effects, and cell-killing/sterilization. The framework included 378 dose-response models as ensemble members. It was shown that the ensemble dose-response framework can accurately reproduce limited data, predict responses for relevant particles lacking data, and serve as a robust foundation for calculating biological effectiveness with objectively defined uncertainties for QF development.

Related to these efforts is the simulation tool RITCARD [Plante et al. 2019a]. Dose-response models are typically empirical or biophysically motivated with adjustable parameters assumed to depend either on the experimental absorbed dose or fluence. In RITCARD, ion track structure is first explicitly simulated with the Monte Carlo tool Relativistic Ion Tracks (RITRACKS) [Plante and Cucinotta 2011]. The spatial distribution of microscopic scale energy deposition events clustered along the ion track are superimposed onto a detailed geometric representation of the DeoxyriboNucleic Acid (DNA) topology contained within a cell nucleus. Initial damage profiles are assessed from the energy deposition distribution. Repair is then simulated over timescales that can be adjusted to match experimental conditions, and various types of chromosomal aberrations are assessed. Improvements to the model continue to be made, but RITCARD is nevertheless positioned to inform certain aspects of QF development.

Combining the new experimental data with dose-response modeling advancements and multi-model ensemble analysis capability provides a new opportunity to characterize radiation quality effects for space radiation cancer risk projections. A new space radiation QF has therefore been developed for NSCR2025 with an emphasis on (1) maintaining clarity and traceability to underlying experimental datasets; (2) utilization of ensemble global dose-response models capable of recapitulating experimental data and predicting responses where no data exist; (3) providing objective and robust QF uncertainty estimates accounting for dose-response model errors, experimental data uncertainty, and variation across endpoints; (4) developing a QF that can be integrated within probabilistic cancer risk projections and existing spaceflight dosimetry systems.

Along with a longstanding desire to clarify the exposure-to-risk relationship for spaceflight, there has been increased effort to directly mitigate radiation-induced health risks through the use of medical countermeasures [Dynan et al. 2022] and provide more individualized risk estimates [NASEM 2021]. Medical countermeasure strategies may include supplements or repurposing of existing pharmaceuticals. To support these activities, the NSCR model has been modified [Werneth et al. 2020, 2022] to facilitate risk projections within the context of medical countermeasures that may reduce incidence or mortality rates in the unexposed baseline population. These initial modifications have already provided key information to better understand the level of impact needed from such interventions to meaningfully reduce space radiation cancer risk. Additionally, modifications to NSCR geared toward providing more individualized risk estimates have been pursued in specific circumstances where data exist. Werneth et al. [2024] gathered data on a common somatic disorder and emerging cancer and CVD risk factor, Clonal Hematopoiesis of Indeterminate Potential (CHIP), and demonstrated a method for estimating space radiation risks for CHIP carriers. These model extensions have been incorporated into NSCR2025.

Finally, further updates to environment, physics, and transport models have been incorporated and will be discussed. Of particular note is the incorporation of two new nuclear interaction models. Relativistic Abrasion/Ablation/De-excitation FRaGmentation (RAADFRG) [Werneth et al. 2021] is a heavy ion fragmentation model based on the abrasion-ablation formulation with relativistic kinematics included in the 3D Lippman-Schwinger solution for the abrasion stage. Nuclear structure effects are expressed in the ablation stage, manifesting the even-odd behavior observed in experimental measurements. Double Differential FRaGmentation (DDFRG) [Norbury 2021, 2023, 2025] was developed to describe pion and light ion production on the basis of thermal nuclear models and coalescence scaling procedures. These two models have measurably enhanced the overall accuracy of nuclear models used to estimate tissue fluence spectra behind shielding in space, as will be shown.

Combined models for the space radiation environment, nuclear physics, and particle transport were successfully validated using data collected concurrently during Artemis-I [Slaba et al. 2025b]. The validation study was conducted blind – meaning that models were evaluated and predictions were made before measurement data were available – and included diverse shielding geometries (ISS, Orion, BioSentinel CubeSat, Martian surface) in destinations from low Earth orbit to Mars. Details of the study and results will be discussed later in this report.

This document aims to provide a complete description of NSCR2025 and is organized as follows. Models and data used to characterize the ambient space radiation environment in Earth orbit, deep space, the lunar surface, and Martian surface are described in Section 2. In Section 3, nuclear physics and radiation transport models employed to propagate the space radiation environment through shielding and tissue are discussed in detail. Extensive verification and validation efforts for combined environment, physics, and transport models are summarized in Section 4. The majority of the document is contained in Section 5 and includes updates to the cancer risk portion of NSCR2025. The new QF developed for the cancer risk model is described in detail, including experimental data sources, dose-response models, parameter selection, and uncertainty quantification. In Section 6, NSCR2025 is used to calculate exposure and risk estimates for representative mission architectures. Research capabilities that have been incorporated into the NSCR framework to quantify the impact of medical countermeasures and individualized factors are described in Section 7. A table or brief paragraph is provided at the beginning of each section to summarize the progression of advancements across NSCR2012, NSCR2020, and NSCR2025.

2. Ambient Space Radiation Environment

In this section, the major sources of radiation exposure for human missions to Low Earth Orbit (LEO), free space, the lunar surface, and Mars surface are summarized. The set of computational models used in NSCR2025 to characterize each of the sources is described, and recent advancements are highlighted along with validation and uncertainty quantification results.

The radiation environment in LEO is dependent on altitude, geographic location, and solar cycle phase and includes a geomagnetically modified form of the GCR as well as belts of lower energy trapped electrons and protons. In free space, GCR and SPE are the primary radiation hazards for human missions. GCR constitute a highly penetrating complex mixed field of ions that are difficult to shield and represent a continuous low dose-rate exposure. The GCR dose-rate varies with solar cycle phase and is approximately twice as large during solar minimum compared to solar maximum. SPE are episodic in nature lasting from several hours to several days and include low to medium energy protons that can be effectively shielded through spacecraft and storm-shelter design optimization strategies. SPE are most likely to occur during solar maximum. On the lunar and Martian surfaces, the GCR and SPE environments can penetrate into the surface and interact with regolith, giving rise to an induced albedo field comprising mostly neutrons. The high biological effectiveness of albedo neutrons requires they be accounted for in mission exposure and health risk projections.

2.1. Galactic Cosmic Rays

♦ *Summary of GCR model updates in NSCR2025* ♦

Risk model	GCR model	Notes
NSCR2012	BON2011	Systematically over-estimates Z > 1 ion fluxes. Time-delayed monthly sunspot number used to determine solar modulation. Developed before new data from ACE/CRIS, BESS, AMS-02, and PAMELA were available.
NSCR2020	BON2020	Average model error compared to all available data <1% with no known systematic errors. Daily ACE/CRIS oxygen flux is used to determine solar modulation. Accounts for new data from ACE/CRIS, BESS, AMS-02, and PAMELA.
NSCR2025	BON2020	ACE/CRIS databases used to determine solar modulation have been updated to allow calculations to the present date.

The free space GCR environment is characterized by a nearly continuous flux of fully ionized particles from H to Ni and beyond with kinetic energies spanning several orders of magnitude reaching up to TeV/n. The spectrum of these particles varies slowly with time over an approximate 11-year cycle between solar minimum and solar maximum. During solar minimum, the Sun's magnetic field strength is diminished, allowing greater penetration of GCR through the heliosphere. While at solar maximum, enhancement in the heliospheric magnetic field reduces GCR intensity below ~5 GeV/n. The GCR environment gives rise to a chronic low dose-rate exposure, varying by approximately a factor of two between solar minimum and solar maximum. A graphical summary of the GCR environment characteristics is provided in Figure 2.

Various GCR models have been developed over the past 30 years. Liu et al. [2024] summarized and compared models used in space radiation protection and risk assessment applications. Among these was the well-known Badhwar-O'Neill (BON) model developed and used by NASA, originally conceived by Badhwar and O'Neill [1996]. The BON model is based on a numerical solution to the Fokker-Planck equation accounting for diffusion, convection, and adiabatic deceleration under the assumptions of a quasi-steady state and spherically symmetric interplanetary medium [Badhwar and O'Neill 1996; O'Neill 2006, 2010]. Details of the Fokker-Planck formulation and Crank-Nicholson numerical solution employed within BON can be found elsewhere [Slaba and Whitman 2019].

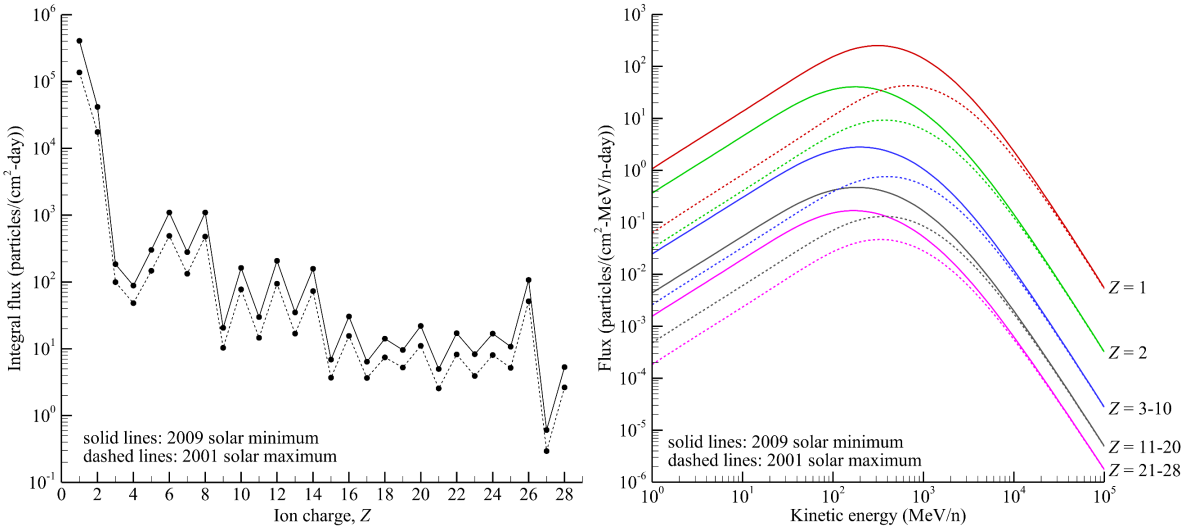

Figure 2. GCR environment at 1 AU for different ions during the 2009 solar minimum (solid lines) and 2001 solar maximum (dashed lines). The left panel shows the integral for all ions from $Z = 1$ to $Z = 28$; the right panel shows energy spectra for specific ions and ion groups.

Here, we highlight comparisons between the BON2011 [O'Neill 2013] model developed for NSCR2012 and the BON2020 [Slaba and Whitman 2020] model integrated into NSCR2020 [Simonsen and Slaba 2021] and NSCR2025. The two key distinguishing features of BON2011 and BON2020 are the data sources used for calibration and validation, and the time-dependent solar modulation parameter, Φ (MV). New measurement data collected after BON2011 development greatly enhanced overall accuracy in BON2020, as will be demonstrated.

GCR measurement data used for BON2011 and BON2020 are summarized in Table 1. Many of the datasets were used for both models, but it can be seen that some data from Balloon-borne Experiment with a Superconducting Spectrometer (BESS) [Abe et al. 2016] and Payload for Antimatter Matter Exploration and Light-nuclei Astrophysics (PAMELA) [Adriani et al. 2017, Martucci et al. 2018] were unavailable at the time BON2011 was developed. More than 10 years of continuous data from Advanced Composition Explorer (ACE) and Cosmic Ray Isotope Spectrometer (CRIS) [Stone et al. 1998], and the high-precision monthly measurements from Alpha Magnetic Spectrometer-02 (AMS) [Aguilar et al. 2015a,b, 2017, 2018a-c] were unavailable for consideration in BON2011 as well. The additional ACE/CRIS and AMS-02 data represent a substantial number of particle- and energy-specific observations.

The time-dependent solar modulation parameter, Φ (MV), is the primary input parameter for the BON models. It describes the state of the heliosphere within the Fokker-Planck equation, which uniquely determines the level of modulation manifested in the GCR energy spectrum for each ion. Detailed explanation of the methods for calculating Φ in BON2011 and BON2020 can be found elsewhere [O'Neill 2013, Slaba and Whitman 2020]. Here, only a brief summary is given.

In BON2011, Φ is calculated separately for protons ($Z = 1$) and heavier ions ($Z > 1$) for a given mission scenario (e.g., start and end dates) through a time-delayed empirical relationship dependent on SunSpot Number (SSN). The time-delay [Nymmik 2000] accounts for the lag between the observed solar activity (sunspots) and the time required for such activity to reach into the heliosphere and modulate GCR flux near 1 AU. For the prescribed mission, time-delayed SSN values are calculated and empirically scaled to arrive at Φ, with separate scaling applied for protons and heavy ions.

In BON2020, the approach for determining Φ depends on the prescribed mission dates. If the mission dates overlap with availability of ACE/CRIS data (~1997 – present date), then Φ is calculated using a multistep process based fundamentally on ACE/CRIS daily integral oxygen flux data. First, the average integral oxygen flux for the input mission dates is calculated directly from ACE/CRIS daily data. Second, the mission integral flux for all other ions is estimated using regression methods derived from analysis of the entire ACE/CRIS dataset. Finally, the integral flux values are converted to Φ values for each ion using empirical relationships. If the mission dates do not overlap with ACE/CRIS data (e.g., before 1997), then SSN data are used to estimate integral oxygen flux as a surrogate for ACE/CRIS data. The same process just outlined is then used to compute Φ for each ion.

Significant advancements in model formulation and data availability occurred between BON2011 and BON2020, resulting in notable changes in model accuracy. In Figure 3, calculated Fe integral flux rates from BON2011 and BON2020 are compared to ACE/CRIS data. Results from both models are well correlated with the data; however, BON2020 exhibits superior correlation (R^2 = 0.98 compared to R^2 = 0.87) and better represents data on the ascending and descending solar cycle phases.

Table 1. Summary of GCR measurement data used to develop and calibrate BON2020. Bold/italic text identifies data that were unavailable/partially-available at the time of BON2011 development, respectively.

Name	Flight	Time	Ions (Z)	Energy (GeV/n)	Data points	Median Error
ACE/CRIS[1]	Satellite	1998-present	5-28	0.05 – 0.5	12446	9%
AMS[2]	STS-91	1998	1, 2	0.1 – 200	58	11%
AMS-02[3]	ISS	2011-2017	1-9	0.4-10^3	7170	3%
ATIC-2[4]	Balloon	2002	1, 2, 6, 8, 10,…,14, 26	4.6 – 10^3	61	33%
BESS[5]	Balloon	1997-2000, 2002, 2004, 2007	1, 2	0.2 – 22	479	11%
CAPRICE[6]	Balloon	1994, 1998	1, 2	0.15 – 350	93	6%
CREAM-II[7]	Balloon	2005	6-8, 10, 12, 14, 26	18 – 10^3	42	25%
HEAO-3[8]	Satellite	1979	4-28	0.62 – 35	332	9%
IMAX[9]	Balloon	1992	1, 2	0.18 – 208	56	18%
MASS[10]	Balloon	1991	1, 2	1.6 – 100	41	9%
PAMELA[11]	Satellite	2006-2009	1, 2	0.08 – 10^3	6614	5%
TRACER[12]	Balloon	2003	8, 10, 12,…,20, 26	0.8 – 10^3	60	10%
Garcia-Munoz[13]	Satellite	1974	6, 8, 10, 12, 14	0.05 – 1	57	27%
Lezniak[14]	Balloon	1974	4-14, 16, 20, 26	0.35 – 52	114	11%
Minagawa[15]	Balloon	1975	26, 28	1.3 – 10	16	8%
Simon[16]	Balloon	1976	5-8	2.5 – 10^3	46	32%

[1][Stone et al. 1998], [2][Alcaraz et al. 2000a, 2000b], [3][Aguilar et al. 2015a,b, 2017, 2018a-c], [4][Panov et al. 2009], [5][Shikaze et al. 2008, Abe et al. 2016], [6][Boezio et al. 1999, Boezio et al. 2003], [7][Ahn et al. 2009], [8][Engelmann et al. 1990], [9][Menn et al. 2000], [10][Bellotti et al. 1999], [11][Adriani et al. 2011, 2013, 2017; Martucci et al. 2018], [12][Ave et al. 2008], [13][Garcia-Munoz et al. 1977], [14][Lezniak and Webber 1978], [15][Minagawa 1981], [16][Simon et al. 1980]. ATIC: Advanced Thin Ionization Calorimeter; CAPRICE: Cosmic AntiParticle Ring Imaging Cherenkov Experiment; CREAM-II: Cosmic Ray Energetics And Mass II; HEAO-3: High Energy Astronomical Observatory 3. IMAX: Isotope Matter-Antimatter eXperiment; MASS: Matter Antimatter Spectrometer System; TRACER: Transition Radiation Array for Cosmic Energetic Radiation.

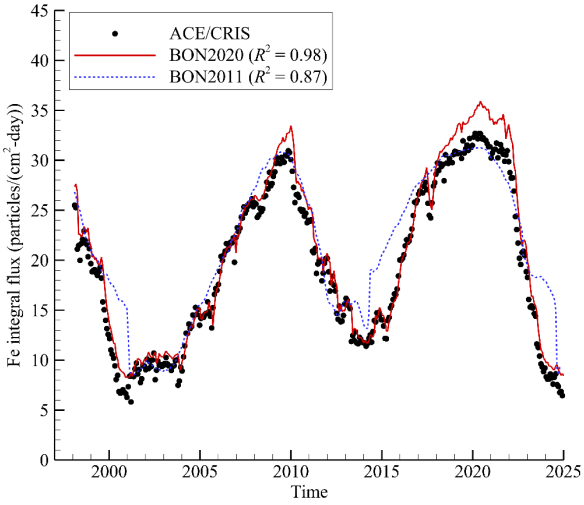

Figure 3. Fe integral flux calculations compared to ACE/CRIS data. The R^2 value is the Pearson correlation coefficient between the model and measurements shown in the plot.

The average model errors determined using all available measurements are shown in Figure 4 and have been separated according to energy and charge groups. It can be seen that BON2020 errors are close to 0% in most cases and generally fall within ±15%. The BON2011 errors are much larger, especially for the energetic portions (>500 MeV/n) of $Z > 2$ spectra. For reference, the BON2020 average model error calculated against all available data was found to be <1% [Slaba and Whitman 2020].

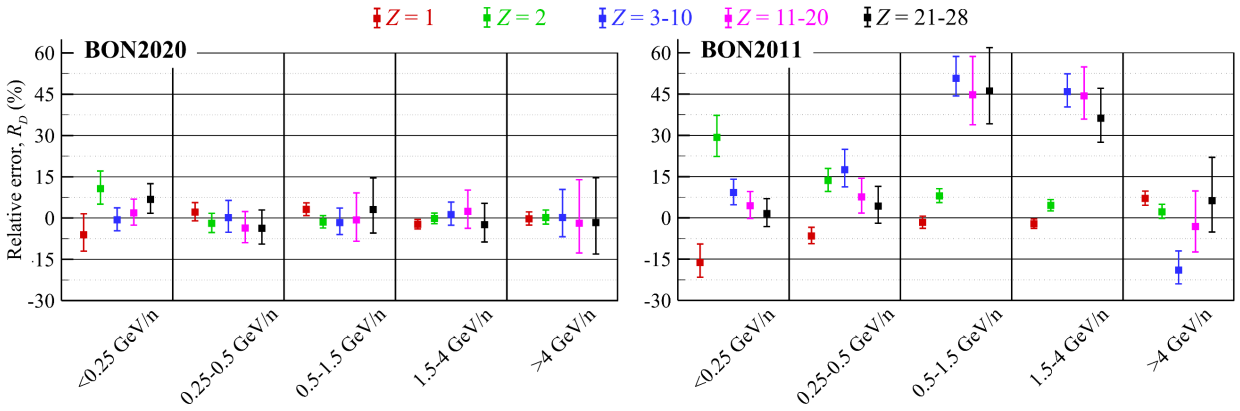

Figure 4. Average model relative error (%) separated into energy groups (x-axis) and charge groups (colored symbols). The error bars are closely related to measurement uncertainty.

2.2. Solar Particle Events

♦ *Summary of SPE model and capability updates in NSCR2025* ♦

NSCR2012, NSCR2020, and NSCR2025 have the ability to evaluate lifetime cancer risk associated with a given SPE determined from historical fits (e.g., design reference October 1989 event [Townsend et al. 2018, NASA 2022]) or probabilistic models [Xapsos et al. 1999, Feynman et al. 2002, Kim et al. 2011]. The ARRT tool [Mertens et al. 2018; Mertens and Slaba 2019; Hu et al. 2020, 2025] has also been developed to provide a real-time in-flight exposure and acute radiation risk assessment capability.

The term SPE is used here to refer to solar flares or coronal mass ejections in which protons may be produced and accelerated from the Sun. Such events are episodic in nature, with widely varying temporal, spatial, and spectral characteristics. It is known that SPE are more likely to occur during solar maximum and can give rise to intense dose-rates capable of instigating acute biological responses if adequate shielding is not provided. These acute responses represent an in-flight health risk, for which acute response models distinct from NSCR2025 are required. Nevertheless, the elevated exposure received by crewmembers during an SPE still contributes to their career exposure and associated lifetime excess risk of cancer incidence and/or mortality and needs to be evaluated. Both NSCR2012 and NSCR2025 include the ability to evaluate the exposure and lifetime risk of cancer incidence and mortality due to exposure from one or more SPE during a mission. Attention is drawn in this section to research since NSCR2012 that enabled SPE shielding design requirements to be defined and real-time in-flight acute risk models to be developed.

Assessment and mitigation of SPE exposure and health risks for crew can be thought of as having three components, which are described as follows. First, prior to mission launch, there may be a desire to estimate the likelihood of SPE occurrence or the probability that a safety limit will be exceeded. Such information is needed for mission planning and engineering design activities. Townsend et al. [2018] summarized various probabilistic models that could be used to calculate SPE worst-case scenarios [Tylka et al. 1997] and mission fluence spectra associated with prescribed confidence levels [Xapsos et al. 1999, Feynman et al. 2002]. Kim et al. [2011] also demonstrated an approach to estimate the probability of crewmembers behind shielding to exceed an exposure threshold. Probabilistic fluence models were used by Townsend et al. [2018] to ultimately recommend the cumulative October 1989 event as the design basis SPE for shielding requirements, which was later adopted in NASA STD 3001 [NASA 2022]. Other historical events are sometimes analyzed as well in terms of their overall magnitude [Townsend et al. 2006], spectral shape [Singleterry et al. 2016], and heavy ion components [Kim et al. 1999]. All of these approaches either have been or can be coupled to NSCR2025, thereby enhancing shield design and mission planning capabilities by enabling possible SPE contributions to crewmember cancer incidence and mortality to be evaluated pre-flight.

Second, during spaceflight, there is a possibility for one or more SPE to occur which could give rise to acute biological consequences distinct from carcinogenesis. The ability to assess exposures and possible acute health

consequences in real-time provides valuable information for crewmembers and mission control to determine if mitigation strategies or other actions need to be initiated. Mertens et al. [2018, 2019] developed a real-time computational tool for estimating human organ doses in space during an SPE. The tool combines HZETRN2020 [Slaba et al. 2020a] calculations with a real-time stream of data from active spaceflight dosimetry to estimate organ dose-rates. The organ dose-rates are used as input to a suite of acute radiation response models described by Kim et al. [2010] and Hu et al. [2020]. The resulting toolset, known as Acute Radiation Risks Tool (ARRT), generates "… severity scales and incidence of early neurovascular effects such as nausea, vomiting, fatigue and weakness, as well as blood cell kinetics, hematopoietic injury grades, and performance degradation, all synchronized with the real-time data stream [Hu et al. 2020]." Recent work has extended ARRT to include SPE forecasting models, providing a degree of advanced warning capability for upcoming Artemis missions [Hu et al. 2025].

Third, after spaceflight, crew exposures must be included into career records to facilitate risk communication and flight certification for subsequent missions. Personally worn dosimetry and area monitors are able to provide mission absorbed dose and dose equivalent. Tissue specific particle fluence spectra for the mission are needed to evaluate cancer risk metrics and NASA effective dose [NASA 2022], requiring the use of physics, transport, and human phantom models [Slaba et al. 2010a]. Methods have been developed and implemented to ensure these model calculations are consistent with spaceflight dosimetry for ISS missions [Cucinotta et al. 2008]. Additional work is needed to develop analogous model normalization techniques for upcoming missions beyond LEO where one or more SPE could occur during a mission.

2.3. Lunar Surface

♦ *Summary of lunar surface environment modeling updates in NSCR2025* ♦

Risk model	Notes
NSCR2012	Lunar surface environment calculations were not explicitly included in NSCR2012.
NSCR2020	Lunar surface environment capability was included in NSCR2020 based on advancements in physics and transport models described in Section 3. The lunar environment calculations were verified against available Monte Carlo simulations.
NSCR2025	Same capability as in NSCR2020 but with updated nuclear interaction models described in Section 3.1.

The lunar surface radiation environment differs from free space in two ways. First, the Moon blocks approximately half of the free space radiation environment impinging from below, thereby reducing the GCR or SPE intensity by a factor of two. Second, in the absence of shielding, incoming GCR or SPE can penetrate into regolith from above and instigate nuclear collisions from which neutrons and other secondary radiation may be produced. The SPE-induced lunar albedo environment is generally not considered significant, since shielding provided by human rated landers and habitats notably reduces the energy and intensity of incoming solar protons before they can reach regolith and initiate backscatter. GCR, on the other hand, are capable of penetrating through shielding and reaching deep into the surface. The GCR-induced albedo environment accounts for 10% - 30% of the crew exposure on the surface, depending on shielding architecture and heliospheric conditions and therefore cannot be ignored [Slaba et al. 2011, Matthia and Berger 2024].

NSCR2012 did not include the necessary physics and transport models to enable exposure and risk calculations on the lunar surface. Major advancements in space radiation physics and transport methods were achieved since NSCR2012, resulting in 3D methods that enable lunar environment calculations to be performed. These advancements are summarized in Section 3 and have been incorporated into NSCR2025.

To determine the lunar surface environment for a given mission, the BON2020 model is used to calculate the free space GCR spectrum, and a factor of one-half is applied to account for celestial shielding. The scaled GCR spectrum is assumed to be incident onto the top of a large lunar regolith [Jolliff et al. 2006] cylinder used to represent the Moon. The scaled GCR spectrum is propagated through the cylinder with HZETRN2020 using 3D physics and transport (described in Section 3.2), and the radiation field evaluated at a point just above the cylinder is used to represent the lunar albedo spectrum. Sensitivity studies have been performed to ascertain geometric parameters required to achieve equilibrium in the calculated lunar surface spectrum [Slaba et al. 2011, Slaba and Stoffle 2017]. Shielding effects have also been studied to provide initial information to guide engineering and design optimization [Slaba et al. 2011, Matthia and Berger 2024]. Example albedo lunar surface environment calculations are shown in Figure 5 for the 2009 solar minimum. Of particular note from a human health risk perspective is the albedo neutron spectrum, which can extend up to 100 MeV and beyond.

Limited measurements have been made on the lunar surface to facilitate model validation. Woolum et al. [1975] measured lunar neutron density within the first 400 g/cm^2 of the surface during Apollo 17. Data were obtained using ^{235}U-mica fission detectors and ^{10}B capture detectors. McKinney et al. [2006] later compared Monte Carlo N-

Particle eXtended (MCNPX) simulations to the Woolum et al. [1975] measurements and found good overall agreement at all depths.

The Chang'E 4 lander included a neutron dosimetry experiment [Zhang et al. 2020] that measured the total absorbed dose-rate and neutral particle (i.e., neutrons and gammas) dose-rate in silicon. The reported neutral particle dose-rate was substantially higher than what would be expected based on comparable measurements made on the Martian surface [Matthia et al. 2016, 2017]. It is believed that the on-board radioisotope thermoelectric generator power source may have contaminated and artificially inflated the neutral particle measurement reported by the Chang'E 4 experiment.

Finally, the Lunar Reconnaissance Orbiter (LRO) / Cosmic RAy Telescope for the Effects of Radiation (CRATER) instrument has been orbiting the Moon at 50 km since 2009 [Spence et al. 2010]. CRATER collects total absorbed dose-rate as well as LET spectra behind various levels of shielding associated with free space GCR and SPE but does not directly measure the lunar surface environment or albedo neutrons. The BON2014 model [O'Neill et al. 2015] was compared to CRATER observations [de Wet et al. 2020], and good agreement was found. While the study confirmed accuracy of the free space GCR model, little insight was gained regarding the lunar albedo components.

Limited verification studies have been performed through inter-code comparisons [Slaba et al. 2011, Matthia and Berger 2024]; albedo neutron spectra calculated with HZETRN for both SPE and GCR environments were found to agree well with Monte Carlo simulation results extracted from the open literature. Further verification studies are needed along with new measurements to facilitate direct validation and uncertainty quantification.

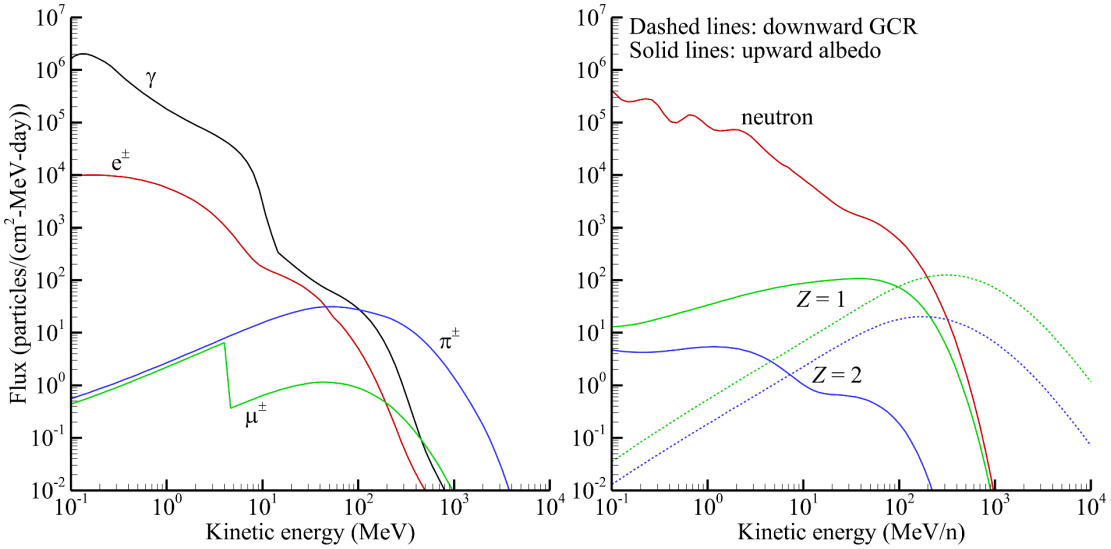

Figure 5. Lunar albedo environment for the 2009 solar minimum. The left panel shows spectra for γ, $e^{\pm}$, $\mu^{\pm}$, $\pi^{\pm}$. The right panel shows spectra for neutrons, Z = 1, and Z = 2 (solid lines) along with the downward directed GCR ions (free space GCR scaled by 0.5 to account for celestial shielding).

2.4. Martian Surface

♦ *Summary of Martian surface environment modeling updates in NSCR2025* ♦

Risk model	Notes
NSCR2012	Mars surface environment calculations were not explicitly included in NSCR2012.
NSCR2020	Mars surface environment capability was included in NSCR2020 based on advancements in physics and transport models described in Section 3. The Mars environment calculations were validated against MSLRAD data and verified against available Monte Carlo simulations.
NSCR2025	Same capability as in NSCR2020 but with updated nuclear interaction models described in Section 3.1.

The Martian surface environment is in many ways similar to the situation on the lunar surface. Extra complexity is introduced by the presence of a thin carbon dioxide atmosphere (~15-25 g/cm^2) expressing geographic, diurnal, and seasonal variability. Nevertheless, as on the lunar surface, the free space environment is reduced by a factor of two on Mars due to planetary shielding below. In the absence of lander/habitat shielding, incoming GCR or SPE can penetrate through the atmosphere and into regolith from above and instigate nuclear collisions, from which

neutrons and other secondary radiation may be produced. The SPE-induced Martian albedo environment is generally not considered significant, since shielding provided by the atmosphere along with lander/habitat shielding appreciably reduces the energy and intensity of incoming solar protons before they can reach regolith and initiate backscatter. GCR on the other hand are capable of penetrating through the atmosphere and lander/habitat shielding and reaching deep into the surface.

NSCR2012 did not include the necessary physics and transport models to enable exposure and risk calculations on the Martian surface. Major advancements in space radiation physics and transport methods were completed since NSCR2012, resulting in 3D methods that enable Mars environment calculations to be performed. These advancements are summarized in Section 3 and have been incorporated into NSCR2025.

To determine the Mars surface environment for a given mission, the BON2020 model is used to calculate the free space GCR spectrum, and a factor of one-half is applied to account for planetary shielding. The scaled GCR spectrum is assumed to be incident on the top of a large cylinder with 26 layers. The top 25 layers encompass a vertical height of 100 km and are composed of carbon dioxide. The density of each layer is determined from an atmospheric vertical density profile obtainable from models such as the Mars Climate Database (MCD) [Forget et al. 1999, Millour et al. 2018] or MarsGram [Justus and Johnson 2001]. The bottom layer is composed of Martian regolith [De Angelis et al. 2004]. The scaled GCR spectrum is propagated through the cylinder with HZETRN2020 using 3D physics and transport (described in Section 3.2), and the radiation field evaluated at a point just above the regolith layer is used to represent the Martian albedo spectrum. Sensitivity studies have been performed to ascertain geometric parameters required to achieve equilibrium in the calculated Mars surface spectrum [Slaba and Stoffle 2017], and initial shielding analyses were completed [Slaba et al. 2013a] but need to be revisited and expanded given advancements in nuclear physics and transport that were not yet available when the initial study was conducted.

Example Mars surface environment calculations are shown in Figure 6 for the 2009 solar minimum. The MCD model was used to assess Martian atmospheric shielding characteristics using a latitude of -4.76°, longitude of 137.4°, and a solar longitude of 338.6°. These conditions yielded a vertical column shielding thickness of 22.4 g/cm^2. It can be seen that all spectra extend to higher energies, compared to the lunar surface. The high energy components of the γ, $e^{\pm}$, $\mu^{\pm}$, $\pi^{\pm}$, and neutron spectra are forward directed secondaries produced by GCR interactions in the atmosphere, while the lower energy components include backscatter from nuclear interactions in regolith. The high energy $Z = 1$ and $Z = 2$ components include both primary GCR ions penetrating through the atmosphere as well as secondary particles (protons, ^{2}H, ^{3}H, ^{3}He, ^{4}He) produced from atmospheric interactions initiated by any of the primary GCR ions (i.e., $Z = 1$ to $Z = 28$).

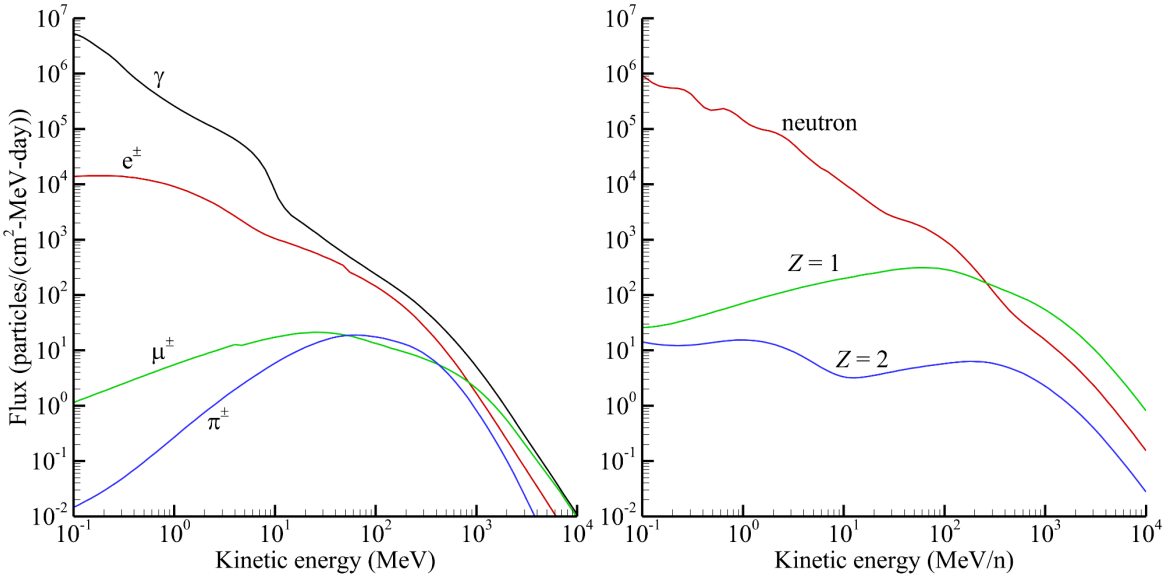

Figure 6. Mars surface environment for the 2009 solar minimum. The left panel shows spectra for γ, $e^{\pm}$, $\mu^{\pm}$, $\pi^{\pm}$. The right panel shows spectra for neutrons, Z = 1, and Z = 2. The MCD model was used to assess Martian atmospheric shielding characteristics using a latitude of -4.76°, longitude of 137.4°, and a solar longitude of 338.6°.

Significant effort has been invested to verify and validate Mars surface radiation environment calculations. Following the first Mars surface radiation measurements [Hassler et al. 2014], Matthia et al. [2016] compared multiple transport codes to Mars Science Laboratory Radiation Assessment Detector (MSLRAD) surface measurements of the absorbed dose-rate and energy spectra for gammas, neutrons, protons, ^{2}H, ^{3}H, ^{3}He, and ^{4}He. The initial study motivated modeling workshops in 2016 and 2018 involving blind comparisons between MSLRAD data and multiple transport code calculations. Participants were only given initial information needed to drive model calculations (e.g., measurement time interval, MSLRAD coordinates, and vertical atmospheric column density thickness) but were not given access to the observational data until the workshop. Workshop proceedings and findings were also peer-reviewed and published [Hassler et al. 2017, Matthia et al. 2017].

A consistent finding from the workshops and publications was that the models are in good agreement with each other and with measurements for the absorbed dose-rate, neutron energy distribution, and gamma energy distribution. The models also agreed well with each other for protons and ^{4}He above ~300 MeV/n, but larger discrepancies were seen at lower energies. Substantial disagreement was found between all models and measurements for ^{2}H, ^{3}H, and ^{3}He. Areas of disagreement were attributed mainly to nuclear production model uncertainty, traceable to significant gaps in ground-based experimental cross section measurements [Norbury and Miller 2012, Norbury et al. 2012].

A comparison between HZETRN2020 calculations and MSLRAD measurements of absorbed dose-rate is shown in Figure 7 [Slaba 2021]. The model calculations are within 7% of the measurements on average, with bounding errors of -19% and 3%. The largest model errors appear near the 2014 solar maximum when solar activity is more dynamic, and the dose-rate is minimal. The corresponding GCR modulation near Mars may not be as accurately described by the near-Earth data-driven empirical models incorporated into BON2020. Nonetheless, the combined models agree well with measured data overall and accurately describe the highest dose-rates observed in the 2019–2020 solar minimum.

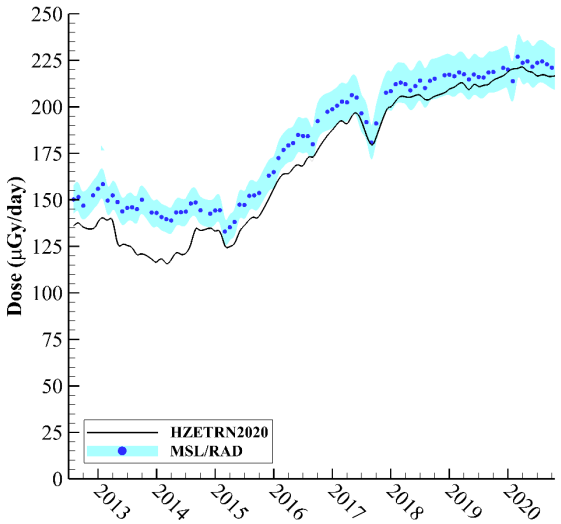

Figure 7. Comparison of model calculations from HZETRN2020 to MSLRAD measurements of dose-rate on the surface of Mars. Figure reproduced from [Slaba 2021].

2.5. Low Earth Orbit

♦ *Summary of LEO environment modeling updates in NSCR2025* ♦

LEO environment models in NSCR2012, NSCR2020, and NSCR2025 are similar, with two exceptions. First, the BON2020 model was used in NSCR2020 instead of BON2011 to calculate the geomagnetically attenuated GCR spectrum in Earth orbit. The BON2020 is used in NSCR2025 as well, as discussed in Section 2.1. Second, the AP9/AE9 [Ginet et al. 2013] model can now optionally be used in NSCR2025 in place of the dynamic [Badavi 2012] AP8/AE8 [Vette 1966; Sawyer and Vette 1976; Vette 1991; Heynderickx et al. 1996a, 1996b] model to calculate the trapped proton and electron spectra.

In low Earth orbit, the primary sources of human exposure come from geomagnetically attenuated GCR and trapped protons in the inner Van Allen belt. Energetic SPE are capable of reaching humans behind shielding in LEO, but the exposures are generally not an immediate concern provided crewmembers are inside the vehicle and not

engaged in extravehicular activities. There are also atmospheric albedo neutrons produced near the top of the Earth's atmosphere by GCR interactions [Wilson 1989]. These neutrons can reach LEO and penetrate shielding; however, their contribution to human exposures is generally small.

The LEO environment models incorporated into NSCR2025 are in many ways similar to what was included in NSCR2012, with two key distinctions. First, BON2011 was replaced with BON2020 in the calculation of the LEO GCR spectra. Second, the updated AP9/AE9 [Ginet et al. 2013] model can be optionally used to calculate the trapped proton spectrum.

A collection of models is used to determine the ambient LEO environment at any point along an orbital trajectory. First, the BON2020 model is used to calculate the free space GCR spectrum, which is then modified to account for planetary [Badavi et al. 2006] and geomagnetic shielding effects [Badavi 2012]. The planetary shielding affects all particles and energies and depends on the altitude at each trajectory point. The geomagnetic shielding effects depend on the altitude and geographic location of each trajectory point and yield cutoff energies below which charged particles are rejected by the Earth's magnetic field.

The trapped proton spectrum can be evaluated using either the dynamic/anisotropic model of Badavi [2012] based on the static AP8/AE8 datasets [Vette 1966, 1991; Sawyer and Vette 1976; Heynderickx et al. 1996a, 1996b] or the updated AP9/AE9 [Ginet et al. 2013] model which does not explicitly include solar cycle dependence. In either case, the spectrum depends on the altitude and geographic location at each point along a trajectory. The atmospheric albedo neutron spectrum [Wilson 1989] can also be evaluated, although it accounts for a small portion of the overall exposure in LEO.

The LEO radiation environment components for a circular orbit trajectory (altitude 400 km, inclination 51.6°) during the 2009 solar minimum is shown in Figure 8. Validation and uncertainty quantification for the LEO environmental models has been studied extensively. For further details, see the references in the preceding paragraphs along with the works of Badavi [2012] and Badavi et al. [2006; 2014a,b].

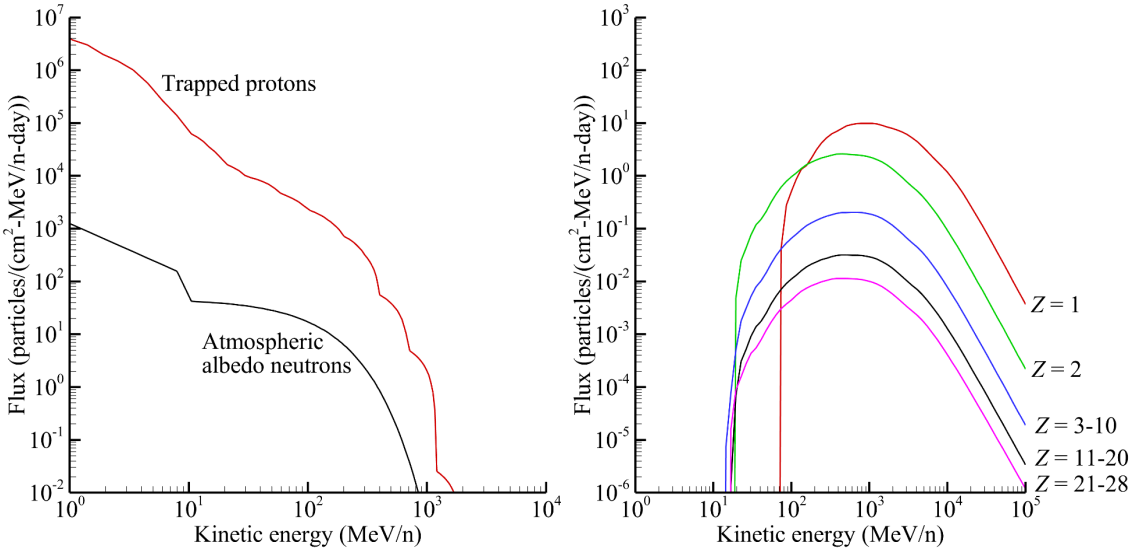

Figure 8. LEO radiation environment for a circular orbit at 400 km and 51.6° inclination during the 2009 solar minimum. The left panel shows the trapped proton and atmospheric albedo neutron spectra. The right panel shows cutoff GCR energy spectra for specific ions and ion groups.

3. Physics and Transport

In this section, the nuclear interaction and particle transport models used to propagate the space radiation environment through complex shielding and tissue are described. NASA's deterministic transport code, HZETRN, is utilized within NSCR2012, NSCR2020 and NSCR2025. However, major updates to nuclear physics models and transport methods have occurred in recent years, influencing both the magnitude and qualitative features of the calculated radiation field behind shielding, as will be shown. These updates are described, and results from benchmark comparisons are presented to demonstrate the overall impact on exposure quantities of interest to human risk assessment.

Ambient space radiation environments are modified as they pass through shielding and tissue due to a collection of atomic interactions, decay processes, and nuclear collisions [Wilson et al. 1991]. Atomic interactions are often quantified in terms of the LET or stopping power within the Continuous Slowing Down Approximation (CSDA) by the Bethe-Bloch formula [Bethe 1930, Bloch 1933], with ion-dependent corrections at low or high energy. Tai et al. [1997] compared various stopping power models and found negligible differences (<5%) for the ions and energies of interest to space radiation transport. It is generally understood that ion stopping powers are well known and not a significant source of uncertainty for space radiation protection. Relevant decay processes for space radiation are mainly limited to pions and muons, for which lifetimes and decay products are well known and therefore do not constitute an important source of uncertainty either.

Far less certain are the nuclear interactions which involve large energy transfers, secondary particle production, and 3D scattering. Models must be relied upon to quantify nuclear interaction cross sections, since experimental data are sparse [Norbury and Miller 2012, Norbury et al. 2012] compared to the expansive range of ions and energies found in space.

These atomic, decay, and nuclear interaction models are utilized within radiation transport codes to quantify how ambient radiation fields are modified as they propagate through complex shielding and human tissue. There are two main types of transport codes that can be used for this purpose – stochastic and deterministic. Stochastic methods are often referred to as Monte Carlo simulations, wherein individual particle trajectories in shielding media are explicitly simulated by sampling interaction cross sections to determine mean free path lengths, energy loss, and secondary particle production. These general-purpose tools are widely used in radiation analysis applications but can be associated with high computational costs, especially for space radiation environments. For that reason, NASA pursued the development of deterministic solutions many years ago [Wilson and Lamkin 1975, Wilson 1977]. Deterministic methods are based on solutions to the Boltzmann transport equation. NASA's transport code, HZETRN, employs perturbative methods and a converging sequence of physical approximations to produce highly efficient and accurate numerical solutions to the Boltzmann transport equation.

3.1. Nuclear Physics

♦ *Summary of nuclear physics modeling updates in NSCR2025* ♦

Nuclear physics models have been substantially updated, verified, and validated in NSCR2025. Major advancements include the heavy ion fragmentation model, RAADFRG [Werneth et al. 2021], the pion, nucleon, and light ion production model DDFRG [Norbury 2021, 2023, 2025], and an intranuclear Serber transport formulation for nucleon production below 300 MeV [Wilson et al. 2020]. External cross section databases from ENDF [Wilson et al. 2021] or generated from general purpose Monte Carlo codes can now also be optionally used [Slaba et al. 2020a].

Radiation transport codes utilize nuclear cross sections to determine mean free path lengths, secondary particle production, and secondary particle emission spectra. A multitude of nuclear interaction models have been developed for such purposes, and each of them is restricted to specific interaction types, particles, targets, or energy ranges. Space radiation transport codes therefore require a collection of nuclear models to ensure all relevant interactions, particles, targets, and energy ranges can be evaluated.

The nuclear models implemented in HZETRN2020 are summarized in this section; a visual summary is given in Table 2 to help guide discussion. Werneth et al. [2025] provided a more thorough discussion of the models, including references to available verification, validation, and uncertainty quantification results.

Table 2. Summary of nuclear interaction models used for projectile and secondary combinations in HZETRN2020.

<table>
<tr><th colspan="2" rowspan="2"></th><th colspan="4">Secondary</th></tr>
<tr><th>Pions
$\pi^{\pm}$</th><th>Nucleons
n, p</th><th>Light ions
^{2}H, ^{3}H, ^{3}He, ^{4}He</th><th>Heavy ions
$Z > 2$</th></tr>
<tr><td rowspan="4">Projectile</td><td>Pions
$\pi^{\pm}$</td><td rowspan="4">DDFRG2</td><td rowspan="2">Serber &
Ranft/Bertini</td><td>N/A</td><td>N/A</td></tr>
<tr><td>Nucleons
n, p</td><td>Ranft/Bertini &
NASA TP 3354</td><td rowspan="2">RAADFRG*</td></tr>
<tr><td>Light ions
^{2}H, ^{3}H, ^{3}He, ^{4}He</td><td>Ranft/Bertini &
NASA TP 3354</td><td>DDFRG1</td></tr>
<tr><td>Heavy ions
$Z > 2$</td><td colspan="3">RAADFRG</td></tr>
</table>

*Inverse kinematics are used to assess heavy ions produced from nucleon and light ion induced target fragmentation

The RAADFRG model is used to evaluate total fragmentation cross sections for nucleus-nucleus collisions as well as heavy ion production from target fragmentation. The model is based on an abrasion-ablation theoretical framework and has replaced NUClear FRaGmentation (NUCFRG) 3 [Adamczyk et al. 2012] used in prior versions of HZETRN. The initial abrasion stage accounts for secondary particles liberated promptly from the projectile at impact and is described by the 3D Lippman-Schwinger equation with an interaction potential derived from multiple scattering theory. The 3D Lippman-Schwinger equation is solved in momentum space, allowing relativistic kinematics to be incorporated.

Following the abrasion stage, there is an ablation stage associated with the excited pre-fragment formed by the overlap of projectile and target nuclei. Ablation is described using Weisskopf-Ewing theory and a modified version of the Dostrovsky et al. [1959] model. The Weisskopf-Ewing formalism requires a nuclear partition function to govern decay probabilities of particles ablated from the pre-fragment. RAADFRG employs a unique partition function based on the liquid drop nuclear binding energy model, leading to the production of even-odd structure that has been observed in numerous experimental cross section data.

Along with the abrasion-ablation processes, abraded nucleons from the projectile may coalesce to form heavier ions. Nucleons with momenta that are approximately equivalent are more likely to aggregate and form light nuclei. RAADFRG utilizes a coalescence model [de Wet et al. 2017], where particle assimilation may occur in each abrasion channel, and the final coalescence cross section is found by summing over all channels. An electromagnetic dissociation model [Norbury 2013] is also included for peripheral interactions that stimulate the emission of light ions.

RAADFRG and NUCFRG3 predictions of the elemental fragmentation cross section for 1 GeV/n ^{35}Cl incident on ^{27}Al are compared in Figure 9. The even-odd nuclear structure is clearly seen in the experimental data and RAADFRG results, while NUCFRG3 predicts the overall fragment spectrum trend on average but lacks nuclear structure effects. Uncertainty quantification analyses have shown that RAADFRG is in better agreement with experimental data than NUCFRG3 [Werneth et al. 2021].

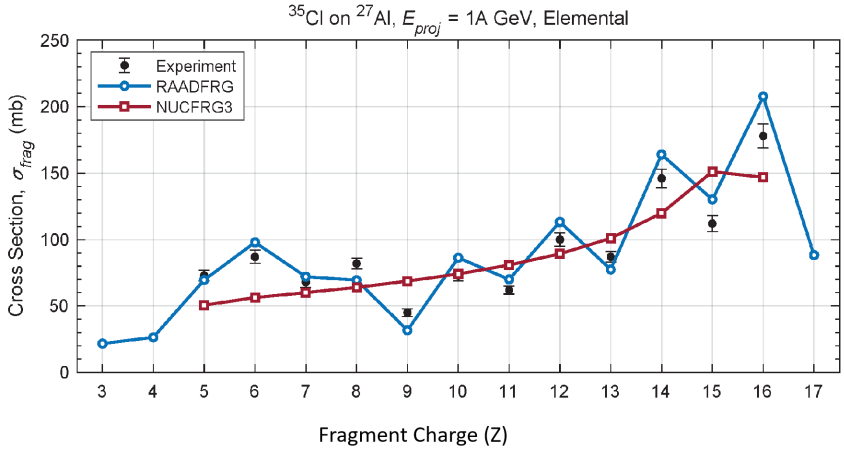

Figure 9. Elemental fragmentation cross section for a 1 GeV/n ^{35}Cl ions incident on ^{27}Al.

DDFRG1 and DDFRG2 use a thermal nuclear model to produce semi-empirical closed-form expressions for charged pion and light ion double differential production cross sections. Thermal models describe the region known as the fireball—a hot ensemble of hadrons—where the projectile and target nuclei overlap during nuclear collisions. Energy is liberated from the fireball by the emission of particles with a Lorentz-invariant double-differential cross section that follows a Boltzmann distribution.

The DDFRG1 model [Norbury 2021] consists of two components. The first component is a double-differential cross section model for proton production from nucleus-nucleus collisions, where protons are produced from sources related to the projectile, target, central fireball, and quasi-elastic direct knockout. The second part of the DDFRG1 model applies coalescence scaling parameters to the proton model to obtain a complete light ion production model [Norbury 2021]. The DDFRG2 model [Norbury 2023] uses only the fireball region for pion production and includes corrections to account for low energy negative pions produced in the forward direction, as these mesons may be absorbed more easily than higher energy pions.

A combination of models is used to describe nucleon production from charged pion and nucleon projectiles. The semi-empirical, parametric Bertini/Ranft model [Wilson et al. 1991] is used for projectile energies above 300 MeV. Below 300 MeV, the Wilson et al. [2020] implementation of the Serber intranuclear transport model is used.

The model employs a one-dimensional (1D) solution to a Boltzmann particle transport equation (but at the nuclear scale instead of the macroscopic scale) to describe the propagation of the multiple-scattering (projectile nucleons) and multiple-recoil nucleons as function of energy and depth through the nuclear medium. The quasi-elastic spectral distribution is found by averaging the multiple scattering fluence over the impact plane while applying Bertini/Ranft quasi-elastic branching ratios [Wilson et al. 1991]. The multiple production spectra nucleons exiting the media are found by averaging the multiple-recoil fluences over the impact plane at each impact parameter, applying the Bertini/Ranft multiplicities, and dividing by the multiplicity of nucleons that do not become trapped in the nuclear potential well. The quasi-elastic and multiple production cross sections are obtained by scaling each by the total absorption cross section [Tripathi et al. 1997, 1998, 1999], and the evaporation cross section is obtained by scaling the evaporation spectrum by the absorption cross section [Wilson et al. 2020]. The quasi-elastic component is assumed to move in the forward direction; the multiple production cross section utilizes the Ranft angular dependence [Wilson et al. 1991], and the evaporation cross section is assumed to be isotropic. The double differential fragmentation cross section is then found by summing these three components.

For light ion production or light ion projectile fragmentation, the Bertini/Ranft model is used to describe target de-excitation/evaporation contributions to the double differential cross section. The projectile break-up in these interactions is handled using the parametric model described in NASA TP 3354 by Cucinotta [1993].

Beyond these nuclear model updates, additional work has been completed to allow external cross section databases to be optionally used within HZETRN. Slaba et al. [2020a] generated spectral and double differential cross sections from GEometry ANd Tracking 4 (Geant4) [Allison et al. 2016] for all combinations of nucleons or pions producing nucleons or pions in selected target media. The primary purpose of the work was to demonstrate that HZETRN2020 could reproduce Monte Carlo simulation transport results provided the same nuclear cross sections are used; however, a computational infrastructure was also established that allows any externally generated cross section database to be used in the future.

The Evaluated Nuclear Data Files (ENDF)/B database [ENDF 2016] is a repository of nuclear cross section data which includes both experimental neutron cross section data and theoretical simulations of nuclear models [ENDF 2018]. These databases have been widely used in Monte Carlo simulation codes for many years. Methods to utilize ENDF/B within HZETRN for neutron elastic interactions were established by Wilson et al. [2021].

3.2. Radiation Transport

♦ *Summary of transport code updates in NSCR2025* ♦

Risk model	Transport code	Notes
NSCR2012	HZETRN2005 with modifications[3]	Systematically under-estimates exposures behind moderate and thick shielding. All particles restricted to 1D straight-ahead approximation. Lacked 3D scattering effects. Pion, muon, and electromagnetic cascade components were included as an empirical correction to the absorbed dose.
NSCR2020	HZETRN2020	Able to reproduce full Monte Carlo simulations when the same nuclear cross sections are used. Both 1D and 3D transport options can be used and includes coupled pion/nucleon interactions and low energy transport solutions for neutrons, recoil protons, negative pion capture, surface muons, and target fragments.
NSCR2025	HZETRN2020	Same as in NSCR2020 but with updated nuclear interaction models described in Section 3.1.

NASA's radiation transport code, HZETRN, has been discussed in various publications. The most comprehensive and detailed description of physical interaction models and transport theory was provided by Wilson et al. [1991]. A progression of advancements pertaining to numerical methods and theoretical formulation have followed since that seminal work, yielding the most current version – HZETRN2020 [Slaba et al. 2020a]. Here, the major updates and versions are summarized in a condensed form.

HZETRN2005 [Wilson et al. 2006] ♦ *Approximate version used in NSCR2012*[3] ♦

- All particles transported within the 1D straight-ahead approximation
  - Numerical transport algorithms could exhibit unstable behavior from neutron elastic interactions [Slaba et al. 2010b]
- Lacked 3D scattering effects
- Lacked pion, muon, and electromagnetic cascade components
- NUCFRG2 heavy ion fragmentation model [Wilson et al. 1994]

[3] The version of HZETRN used in NSCR2012 utilized straight-ahead 1D transport algorithms from HZETRN2005 for all particles along with the Quantum Multiple Scattering Fragmentation heavy ion fragmentation model. Pion, muon, and electromagnetic cascade contributions to dose were added through the use of an empirical parametric correction. Further details can be found in the NSCR2012 report.

HZETRN2010 [Slaba et al. 2010c,d]

- 1D straight-ahead approximation used for most particles
  - Faster (up to 100x) and more robust numerical methods [Slaba et al. 2010c, Slaba 2013]
- Bi-directional neutron transport option [Slaba et al. 2010d]
- Lacked pion, muon, and electromagnetic cascade components
- NUCFRG3 heavy ion fragmentation model [Adamczyk et al. 2012]

HZETRN2015 [Wilson et al. 2014, 2015a; Slaba et al. 2016]

- 1D straight-ahead approximation option
- Pseudo-3D transport option for neutrons and light ions [Wilson et al. 2014, 2015a]
- Pion, muon, and electromagnetic cascade components included but decoupled from nucleons [Norman et al. 2013, Slaba et al. 2013b]
- NUCFRG3 heavy ion fragmentation model
- Added capability to perform 3D transport in complex combinatorial [Wilson et al. 2016] or ray-trace [Slaba et al. 2016] mass shielding geometries.

HZETRN2020 [Slaba et al. 2020a] ♦ *Used in NSCR2025* ♦

- 1D straight-ahead approximation option
- 3D transport options for pions, nucleons, and light ions
- Pion, muon, and electromagnetic cascade components fully coupled to nucleon transport in 1D and 3D options
- RAADFRG [Werneth et al. 2021] or NUCFRG3 heavy ion fragmentation model options
- Incorporated surface muons, negative pion capture, low energy recoil protons, heavy ion target fragments
- Added capability to utilize cross section databases from ENDF or external models and codes such as Geant4

Many inter-code comparisons have been performed between versions of HZETRN and Monte Carlo simulations [Bahadori et al. 2013; Matthia et al. 2016, 2017; Norbury et al. 2019; Shavers et al. 2024a; Slaba et al. 2010d, 2011, 2013b, 2016, 2017, 2020a; Wilson et al. 2014, 2015a,b, 2016, 2020, 2021]. The general finding from these studies was that HZETRN agrees with the Monte Carlo simulations to the extent they agree with each other, and further improvements to nuclear interaction models, guided by new experimental cross section measurements, are needed to resolve remaining discrepancies.

A stronger conclusion was reached in work that occurred shortly after the Norbury et al. [2019] review paper. Cross section databases for nucleons, pions, and gammas were extracted from Geant4 [Allison et al. 2016] for several target materials and used within HZETRN2020 [Slaba et al. 2020a]. Benchmark comparisons in simple geometry were then used to demonstrate that HZETRN2020 could reproduce Geant4 simulation results when both codes used the same nuclear cross sections, thereby verifying the accuracy of the 3D deterministic transport methods in HZETRN2020.

Select results are shown in Figure 10 for a slab geometry with infinite lateral dimensions and 60 g/cm^2 aluminum shielding in front and behind the target point location. The boundary condition is the November 16-25, 2013 LEO GCR proton spectrum evaluated at cutoff rigidities between 14-16 GV, normally incident on the front face of the slab geometry. Results labeled as HZETRN2020$_{G4}$ were obtained by using nucleon, pion, and gamma cross sections from Geant4 within the 3D transport algorithms of HZETRN2020. Near ~10^4 MeV, a bump can be seen in the proton spectrum. Above 10^4 MeV, the spectrum is dominated by primary LEO GCR protons, while protons below 10^4 MeV constitute secondary particles produced from nuclear interactions. It can be seen that results for protons and neutrons between the two codes are almost overlapping, with minor remaining discrepancies attributable to differing stopping power formulae (for low energy protons), elastic cross sections (for low energy neutrons), and total reaction cross sections.

A final set of benchmark results is shown in Figure 11. In this plot, the geometry is a slab with infinite lateral dimensions and equal amounts of aluminum in front and behind a thin (0.03 mm) water layer. The target point is situated in the middle of the water layer, and the boundary condition is the GCR spectrum evaluated with BON2010 [O'Neill 2010] using a solar modulation parameter of 475 MV for solar minimum. The BON2010 model is used here for historical reasons to match the boundary condition used by the Monte Carlo codes included in the original benchmark study [Slaba et al. 2017].

It is clear from the figure that significant and quantifiable improvements in accuracy have occurred in going from HZETRN2005 to HZETRN2020. The HZETRN2020 results fall well within the Monte Carlo simulations for both dose and ICRP 60 dose equivalent [ICRP 1991]. Dose equivalent values from HZETRN2020 appear toward the upper end of the Monte Carlo results due to a systematic error in low energy (< 0.1 MeV) neutron transport related to leakage effects [Wilson et al. 2015, 2021] which artificially increases low energy proton recoils in the thin water layer. The impact on dose equivalent is noticeable but likely on the order of <10%. Further terms in the perturbation sequence for low energy neutron transport would be needed to resolve the issue more accurately.

Results labeled as "HZETRN2005+$\pi_{NSCR2012\text{-}fit}$" approximately correspond to the physics and transport used in NSCR2012. It is observed that those results substantially underestimate more likely values found in the gray shaded region encompassing Monte Carlo simulations and HZETRN2020 calculations. The under-estimate is now understood to be an expected result since transport procedures used in HZETRN2005 lacked 3D interactions and coupled pion/nucleon physics – both of which make key contributions to dose and dose equivalent behind moderate and thick shielding.

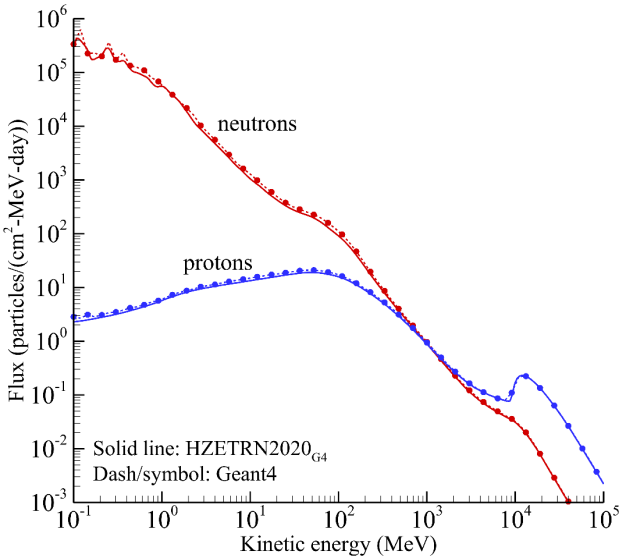

Figure 10. Comparison between Geant4 simulations and HZETRN2020$_{G4}$ (i.e., Geant4 cross sections used in HZETRN2020) for neutrons and protons in a slab with infinite lateral dimensions and 60 g/cm^2 aluminum shielding in front and behind the target point location. The boundary condition is the November 16-25, 2013 LEO GCR proton spectrum evaluated at cutoff rigidities between 14-16 GV, normally incident on the front face of the slab geometry. Figure reproduced from Slaba et al. [2020a].

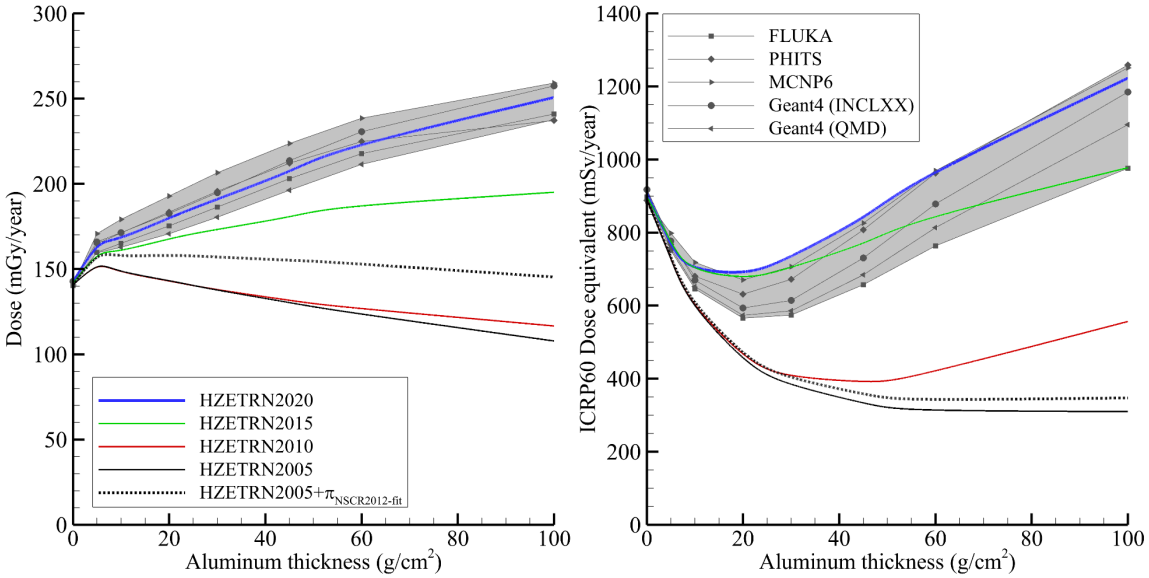

Figure 11. Total annual dose (mGy/year) (left) and dose equivalent (mSv/year) (right) as a function of aluminum thickness in slab geometry exposed to a solar minimum (Φ = 475 MV) GCR environment calculated with the BON2010 model. The x-axis indicates the amount of aluminum shielding in front and behind a 0.03 mm water layer. All values are calculated in the middle of the water layer. The range of Monte Carlo simulation results is indicated by the shaded region. Results labeled as "HZETRN2005+$\pi_{NSCR2012\text{-}fit}$" approximately correspond to the physics and transport used in NSCR2012. Figure modified from Slaba et al. [2017].

4. Combined Environment, Physics, and Transport Spaceflight Validation

♦ *Summary of physics and transport spaceflight validation for NSCR2025* ♦

Environment, physics, and transport models have been significantly updated for NSCR2025, resulting in notable and quantifiable improvements in overall accuracy against spaceflight data. On average, combined models used in NSCR2025 were shown to be within 5% of free space measurements, 7% of Mars surface measurements, and 25% of LEO measurements on ISS all collected during Artemis-I. Slightly larger errors on ISS are attributed to imprecise knowledge of the dynamic mass shielding geometry, high energy physics, and 3D Compton scattering effects associated with electrons below 10 MeV.

In this section, combined environment, physics, and transport models used in NSCR2025 are compared to available spaceflight data. Several validation studies have been conducted in recent years [George et al. 2024; Matthia et al. 2016, 2017; Norbury et al. 2019; Norman et al. 2013; Rahmanian et al. 2025a; Slaba et al. 2013b, 2020a, 2021, 2025b]. Good overall agreement was found between models and measurements in these studies.

Here, we focus on the most recent set of comparisons [Slaba et al. 2025b] in which combined models were compared to active dosimeter measurements of absorbed dose in silicon collected simultaneously during Artemis-I aboard ISS in LEO, in the BioSentinel CubeSat in free space, in the Orion capsule in free space, and on the surface of Mars. This particular validation study was performed blind, meaning that the model calculations were performed without prior knowledge of the measured values.

An important aspect of the Artemis-I validation study was the use of highly detailed and complex shielding geometry for the ISS and Orion, as shown in Figure 12 and Figure 13. The geometries were developed in a Computer-Aided Design (CAD) software environment and then exported to a ray-trace format compatible with HZETRN2020. The ray-trace analysis capability retains not only the mass shielding distribution surrounding a detector location but also the material composition and correct spatial orientation of objects placed within the CAD model. Even more important is that computational efficiency is retained in HZETRN2020 despite the enormous geometric complexity.

Results from the Artemis-I validation study are shown in Figure 14. Model calculations were within 5% of the available free space measurements, 7% of MSLRAD data, and 12-24% of ISS data depending on location within the station. Slightly larger model errors found for the ISS comparison are attributed to imprecise knowledge of the ISS mass shielding geometry, high energy physics, and 3D Compton scattering effects associated with electrons below 10 MeV [Slaba et al. 2020a, 2025b].

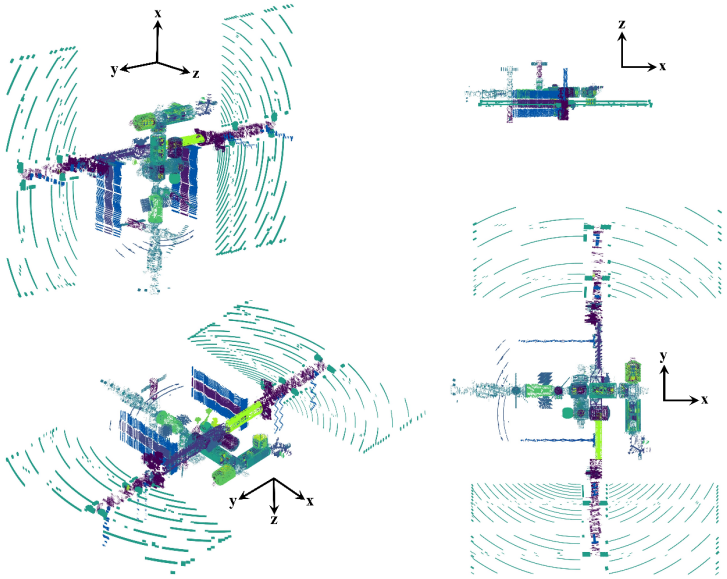

Figure 12. Scatter plot rendering of the ISS geometry used for model calculations; colors are used to identify unique objects retained in radiation transport analyses. A detailed CAD model of the ISS containing over 11,000 objects is ray-traced from a dosimeter location within the Cupola (observation module), and the ray-trace information is used as input into HZETRN2020. The scatter plot is a rendering of the geometry as interpreted and used by HZETRN2020 in transport analyses. Figure is reproduced from [Slaba et al. 2025b].

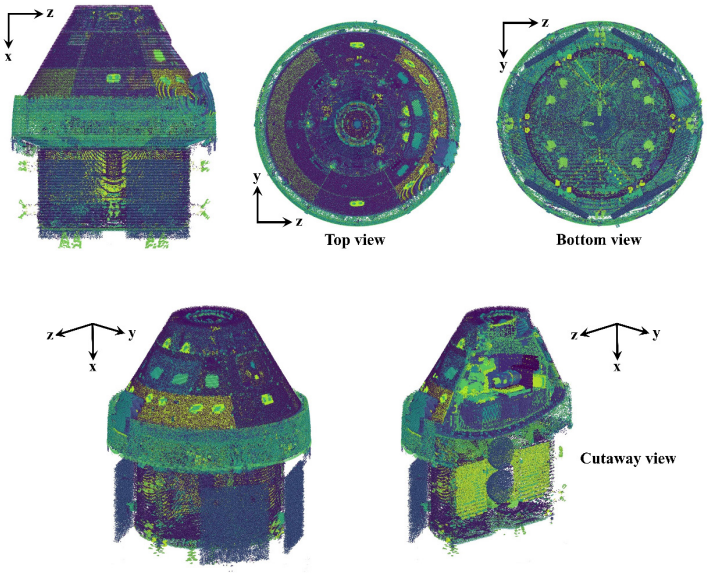

Figure 13. Scatter plot rendering of the Orion geometry used for model calculations; colors are used to identify unique objects retained in radiation transport analyses. A detailed CAD model of the Orion module containing over 20,000 objects is ray-traced from a dosimeter location within Orion, and the ray-trace information is used as input into HZETRN2020. The scatter plot is a rendering of the geometry as interpreted and used by HZETRN2020 in transport analyses. Figure is reproduced from [Slaba et al. 2025b].

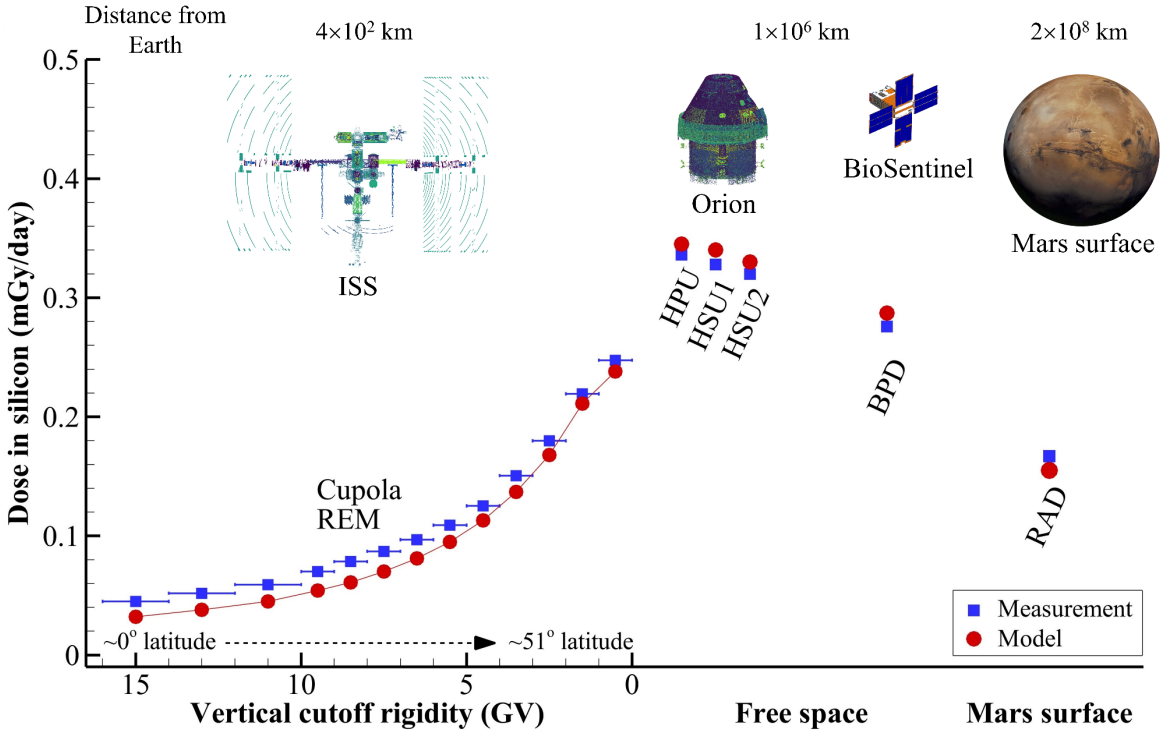

Figure 14. Comparison of model calculations to measurement data for the ISS, Orion module, BioSentinel CubeSat, and Mars surface during the Artemis-I mission. Approximate distances of each shielding geometry from the Earth are given at the top of the figure. Calculations and data for the ISS only include the GCR contributions. Exposure from trapped protons during passes through the South Atlantic Anomaly is not included in this comparison. ISS data are also binned according to vertical cutoff rigidity to show the trend associated with geomagnetic shielding. Figure is reproduced from [Slaba et al. 2025b].

5. Cancer Risk Model

In this section, the NASA space cancer risk model is described. Details of the model can be found in several other reports [Cucinotta et al. 2013b; Simonsen and Slaba 2020, 2021]; only a high-level overview is given here with an emphasis on updates and improvements incorporated into NSCR2025.

The NSCR model was primarily developed to calculate the excess lifetime Risk of Exposure-Induced Cancer (REIC) and Death (REID). These quantities are calculated by integrating the product of a hazard rate (λ) and survival function (bracketed term) over attained age (a) according to [Vaeth and Pierce 1990; Cucinotta et al. 2013b]

$$\mathrm{REIC} = \sum_T \int_{a_E}^{\infty} \lambda_i^{(T)}(a, a_E, H_T) \left[\frac{S_0(a)}{S_0(a_E)} e^{-\sum_{T'} \int_{a_E}^{a} \lambda_m^{(T')}(a', a_E, H_{T'}) da'} \right] da \,, \tag{1}$$

$$\mathrm{REID} = \sum_T \int_{a_E}^{\infty} \lambda_m^{(T)}(a, a_E, H_T) \left[\frac{S_0(a)}{S_0(a_E)} e^{-\sum_{T'} \int_{a_E}^{a} \lambda_m^{(T')}(a', a_E, H_{T'}) da'} \right] da \,. \tag{2}$$

In equations (1) and (2), H_T is the tissue dose equivalent (Sv), a_E is the age at exposure, S_0 is the survival probability for the unexposed baseline population, and the summation is taken over all radiosensitive tissue types, T. The integration variables labeled a' and T' have the same conceptual meaning as a and T, respectively. The ratio term in brackets is the conditional probability of survival to age a given exposure at age a_E in the unexposed baseline population. The exponential term accounts for decreased survival due to radiation exposure.

The terms $\lambda_i^{(T)}$ and $\lambda_m^{(T)}$ are the radiation-induced cancer incidence (i) and mortality (m) rates, dependent on dose, age at exposure, attained age, tissue type, and sex. They are calculated from models derived from the LSS of the atomic bomb survivor cohort; details of the LSS cohort, exposure characteristics, and epidemiological considerations can be found elsewhere [Grant et al. 2017; Preston et al. 2004, 2007; Stegeman et al. 2025]. The radiation-induced cancer incidence and mortality rates include a weighted mixture of absolute and relative excess risk terms to facilitate risk transfer from the LSS population to a target population more representative of modern-day astronauts. Adjustments are applied to account for differences in dose-rate and radiation quality (QF used in H_T) as well as latency between the age at exposure and appearance of cancer.

The radiation-induced solid cancer incidence rate can be written as

$$\lambda_i^{(T)}(a, a_E, H_T) = C_T(\tau) \Big[\nu_T \, \mathrm{ERR}_T(a, a_E) \lambda_{0,i}^{(T)}(a) + (1 - \nu_T) \, \mathrm{EAR}_T(a, a_E) \Big] \frac{H_T}{\mathrm{DDREF}}, \tag{3}$$

where $\lambda_{0,i}^{(T)}(a)$ is the age-dependent, sex- and site-specific cancer incidence rate for the unexposed baseline population of interest, DDREF is the Dose and Dose-Rate Effectiveness Factor, υ_T is the population transfer weight defining the contributions of the relative and absolute risks to the total, and $C_T(\tau)$, with $\tau = a - a_E$, is the latency factor used to describe the time-lag between age at exposure and first appearance of cancer. The terms ERR_T and EAR_T are the age-dependent, sex- and site-specific excess relative and absolute risk functions, respectively, derived from the LSS cohort for radiation-induced cancer incidence based on a linear dose-response.

The radiation-induced solid cancer mortality rates are obtained by scaling the corresponding incidence rates from equation (3). This incidence-to-mortality approximation is used to help circumvent classification and statistical uncertainties in the LSS dataset for site-specific radiation-induced solid cancer deaths [Cucinotta et al. 2013b]. The radiation-induced solid cancer mortality rate can be written as

$$\begin{aligned} \lambda_m^{(T)}(a, a_E, H_T) &= \frac{\lambda_{0,m}^{(T)}(a)}{\lambda_{0,i}^{(T)}(a)} \lambda_i^{(T)}(a, a_E, H_T) \\ &= C_T(\tau) \left[\nu_T \, \mathrm{ERR}_T(a, a_E) \lambda_{0,m}^{(T)}(a) + (1 - \nu_T) \, \mathrm{EAR}_T(a, a_E) \frac{\lambda_{0,m}^{(T)}(a)}{\lambda_{0,i}^{(T)}(a)} \right] \frac{H_T}{\mathrm{DDREF}} \end{aligned}, \tag{4}$$

where $\lambda_{0,m}^{(T)}(a)$ is the age-dependent, sex- and site-specific cancer mortality rate for the unexposed baseline population of interest, and ERR_T and EAR_T are the same incidence-based excess risk functions from equation (3).

For leukemia (L), the ERR and EAR functions are derived directly from LSS mortality data using a linear-quadratic dose response [Little et al. 2008]. The linear-quadratic model is presumed to implicitly account for adjustments at low dose and/or low dose-rate, thereby removing the need to apply a DDREF [Cucinotta et al. 2013b; NCRP 2000, 2006; NRC 2006; UNSCEAR 2006]. Thus, the mortality rate for leukemia is calculated without a DDREF using the linear component of the linear-quadratic ERR and EAR as

$$\lambda_m^{(L)}(a,a_E,H_L) = C_L(\tau)\Big[\nu_L\,\mathrm{ERR}_L(a,a_E)\lambda_{0,m}^{(L)}(a) + (1-\nu_L)\,\mathrm{EAR}_L(a,a_E)\Big]H_L\,, \tag{5}$$

and the incidence rate is calculated by inverting equation (4), yielding

$$\begin{aligned}\lambda_i^{(L)}(a,a_E,H_L) &= \frac{\lambda_{0,i}^{(L)}(a)}{\lambda_{0,m}^{(L)}(a)}\lambda_m^{(L)}(a,a_E,H_L) \\ &= C_L(\tau)\left[\nu_L\,\mathrm{ERR}_L(a,a_E)\lambda_{0,i}^{(L)}(a) + (1-\nu_L)\,\mathrm{EAR}_L(a,a_E)\frac{\lambda_{0,i}^{(L)}(a)}{\lambda_{0,m}^{(L)}(a)}\right]H_L\,.\end{aligned} \tag{6}$$

The models, methods, and data sources used to calculate terms appearing in equations (3) - (6) are described in the following sections.

5.1. Tissue Exposures

♦ *Summary of human phantom and tissue exposure assessment updates in NSCR2025* ♦

Tissue exposure uncertainties used in NSCR2012 and NSCR2020 have been updated based on recent validation studies described in Section 4. The relative uncertainty distribution applied to calculated tissue fluences in NSCR2025 intended to represent combined errors for environment, physics, transport, and shield geometry models is Gaussian with a mean of one and standard deviation of 0.2.

Risk model	Human Phantoms	Notes
NSCR2012	CAM/CAF	Initially developed in 1970s with limited computational resources to match the 50th percentile US Air Force personnel. Locations and masses of certain radiosensitive tissues were found to be unrealistic, introducing errors in calculated tissue exposures in some cases.
NSCR2020	MAX/FAX	High-resolution voxel-based models developed from CT scans of human cadavers and calibrated to match reference ICRP standards for human anatomical models.
NSCR2025	MAX/FAX	Same as NSCR2020.

Tissue exposures are calculated using the environment, physics, and transport models described in Sections 2 and 3, combined with detailed human phantoms placed inside complex vehicle or habitat mass shielding geometries. NSCR2012 utilized the CAM [Billings and Yucker 1973] and CAF [Yucker and Huston 1990, Yucker and Reck 1992] phantoms intended to match 50th percentile 1970s US Air Force personnel. The CAM/CAF phantoms are based on combinatorial quadric surfaces and were developed using limited computational resources by modern standards.

The high-resolution Male Adult VoXel (MAX) [Kramer et al. 2003] and Female Adult VoXel (FAX) [Kramer et al. 2004] human phantom models are incorporated into NSCR2025. The MAX/FAX phantoms are voxel-based (3.6 mm cubes) and derived from Computed Tomography (CT) scans of human cadavers with tissue masses, materials, and densities calibrated to ICRP reference standard values [ICRP 2001]. Methods for coupling human phantoms to HZETRN have been described [Slaba et al. 2010a] and independently verified with Monte Carlo simulations [Bahadori et al. 2013].

A visual comparison of the phantoms is provided in Figure 15. It can be seen that the FAX phantom contains greater detail and realism compared to the stylized and simplified CAF. Further comparisons are given in Table 3. The FAX masses are in excellent agreement with the ICRP reference values. Although MAX/FAX did not explicitly include bone marrow, target points were placed along the axial center of relevant bones to enable exposure calculations [Slaba et al. 2010a]. CAF tissue masses show large discrepancies with ICRP reference values, some of which (Blood Forming Organs (BFO), bladder, muscle) are unrealistically large.

The mass and location of tissues within the body affects calculated exposure quantities. Tissue dose equivalent values for the King model of the August 1972 SPE [King 1974] behind 10 g/cm^2 aluminum shielding are provided in the right two columns of the table. Values calculated in CAF and FAX differ by anywhere from -102% to 25%. In the case of the CAF thyroid, it was found that the absence of an outer skin and soft tissue layer around the phantom decreases the self-shielding for all internal organs and increases calculated exposure quantities. The thyroid exhibits larger sensitivity than other tissues since it is located just under the skin.

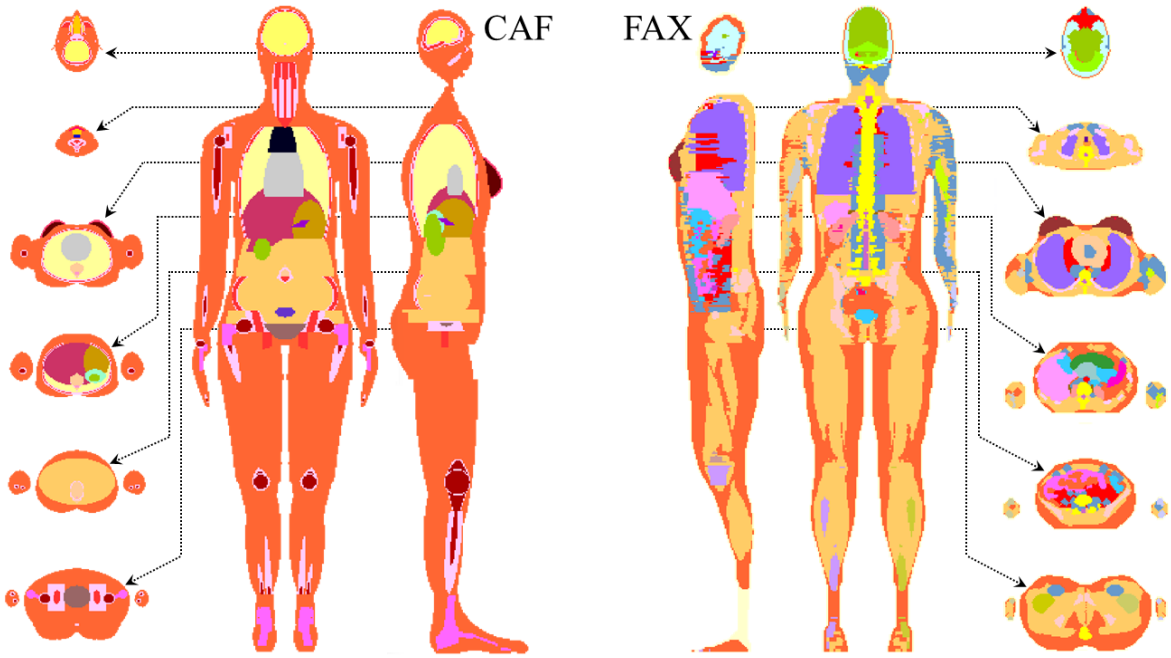

Figure 15. Visual comparison of CAF and FAX human phantoms. The different colors correspond to tissue types articulated in the phantoms.

Table 3. Tissue masses in CAF and FAX compared to ICRP reference values [ICRP 2001]. The symbol "-" indicates that the tissue type was not represented in the phantom. The right two columns are tissue dose equivalent (mSv) values behind 10 g/cm^2 aluminum shielding during the King 1972 SPE [King 1974]. Table values were extracted from Slaba et al. [2010a].

Tissue	Tissue mass (g)			Tissue dose equivalent (mSv)	
	CAF	FAX	ICRP	CAF	FAX
BFO	3074	-	900	256	300
Colon	-	680	680	-	176
Lung	871	950	950	246	307
Stomach	445	370	370	141	146
Breast	610	500	500	558	496
Bladder	173	40	40	134	113
Esophagus	0	35	35	462	150
Liver	1549	1400	1400	125	161
Thyroid	9	17	17	718	356
Brain	1076	1300	1300	290	303
Adrenals	-	13	13	161	98
Kidneys	415	275	275	162	129
Muscle	37635	17553	17500	440	375
Pancreas	73	120	120	159	96
Small Intestine	-	880	880	227	146
Spleen	69	130	130	145	166
Thymus	-	20	20	259	274
Uterus	50	80	80	129	87
Ovaries	19	11	11	137	100

The uncertainties associated with estimating tissue exposures stem from combined uncertainties associated with environment, physics, transport, mass shielding, and human phantom models. In NSCR2012, relative uncertainties (U_{phys}) were subjectively assigned to the tissue fluence spectrum for light and heavy particles as

$$U_{phys} \sim \begin{cases} N(\mu = 1.05, \sigma = 0.33) \ , \ A \leq 4 \\ N(\mu = 1, \sigma = 0.25) \quad , \ A > 4 \end{cases}, \tag{7}$$

where A is the particle mass, and $N(\mu,\sigma)$ represents a Gaussian distribution with mean μ and standard deviation σ. This same distribution was carried into NSCR2020.

Combined verification, validation, and uncertainty quantification studies discussed in the prior section justify revising equation (7) for NSCR2025. First, there is insufficient evidence to support the continued use of a 5% bias ($\mu = 1.05$) in the light ion tissue spectra. Verification comparisons against Monte Carlo simulations and validation studies (discussed in Section 4) do not indicate the presence of systematic errors in updated environment, physics, and transport models. Second, for LEO missions, model correction/normalization methods have been developed [Cucinotta et al. 2008] and deployed operationally to ensure calculated exposure quantities on ISS agree with measurement data to within ±15% on average. Lastly, a broad view of the verification and validation results summarized in Section 4, with particular emphasis on the Artemis-I study [Slaba et al. 2025b] and MSLRAD studies [Matthia et al. 2016, 2017], support the re-definition of U_{phys} as $N(\mu = 1, \sigma = 0.2)$ for all particles.

5.2. Unexposed Baseline Population Data

♦ *Summary of baseline population updates in NSCR2025* ♦

The baseline population databases for cancer incidence, cancer mortality, and survival probabilities have been updated for NSCR2025 using combined data from 2018, 2019, and 2021 [Rahmanian et al. 2025b]. These updates occur periodically [Cucinotta et al. 2013b; Chappell 2014, 2015, 2020]; the data sources and analysis methods have remained largely similar.

Radiogenic risks derived from the LSS cohort must be transferred to a population more representative of US astronauts and commercial crew. The transfer methodology used in NSCR requires cancer incidence rates, $\lambda_{0,i}^{(T)}$, cancer mortality rates, $\lambda_{0,m}^{(T)}$, and survival probabilities, S_0, in an unexposed baseline population of interest. Additional data and adjustments have also been introduced [Cucinotta et al. 2013b] to estimate rates and survival probabilities for a US never smoker population, deemed more representative of the healthy astronaut corps. All of the required datasets are obtained from US national cancer and health databases and are periodically revised in NSCR to reflect the current health status relevant for crewmembers.

Sex- and site-specific cancer incidence and mortality data are often made available in 5-year intervals (e.g., rates for individuals between the ages of 40-45). Numerical analysis methods must be applied to translate the 5-year interval data to 1-year intervals and extrapolate as needed to age 101 – the upper age integration limit in the REIC and REID integrals. A description of the numerical methods can be found in Chappell [2014, 2015, 2020] and Rahmanian et al. [2025b].

Rahmanian et al. [2025b] provided the most recent update to the baseline databases for use in NSCR2025. Cancer incidence and mortality rates for the average US population were obtained from the Centers for Disease Control and prevention (CDC) Wide-ranging ONline Data for Epidemiologic Research (WONDER) database [CDC 2024] and the NCI DevCan software [NCI 2024]. WONDER is the more comprehensive source, encompassing all cancer sites assessed in NSCR, but the Probability of Developing or Dying of Cancer (DevCan) software provides additional information for ages beyond 85 to guide extrapolations up to age 101. Data collected over the years 2018, 2019, and 2021 were used from both sources for consistency. The year 2020 was not included due to the COrona VIrus Disease (COVID), which confounded data collection, rate analysis, and overall survival [NCI 2024]. Survival probabilities were obtained from the National Vital Statistics Reports (NVSR) US life tables, published by the CDC National Center for Health Statistics (NCHS) [Arias and Xu 2022].

The never smoker adjustments to average US population data are guided by recommendations from the 2014 Surgeon General's report [Surgeon General 2014]. Site-specific and age-dependent relative risks for smoking induced mortality are extracted from the report and combined with updated smoking prevalence information for the years 2018, 2019, and 2021 from the CDC Behavioral Risk Factor Surveillance System (BRFSS) web-enabled analysis tool [CDC 2025]. These data are used to estimate the smoking attributable fraction which is then applied to cancer incidence rates, cancer mortality rates, and survival probabilities to estimate corresponding never smoker quantities. The solid cancer sites for which never smoker adjustments are applied include stomach, bladder, lungs, esophagus,

oral cavity, uterus, and remainder. Acute myeloid leukemia (AML) is also affected by smoking status [Surgeon General 2014]. Further details of the data sources, numerical methods, and never smoker model can be found in [Cucinotta et al. 2013b, Chappell 2014, 2015, 2020; Rahmanian et al. 2025b].

Relative uncertainties associated with the never smoker adjustment model, U_{NS}, were specified in NSCR2012 and retained in NSCR2025 as a standard normal distribution with a standard deviation of 15%.

5.3. Excess Risk Models

♦ *Summary of low LET excess risk models in NSCR2025* ♦

The excess risk models (ERR/EAR) and uncertainties implemented in NSCR2012 were retained in NSCR2020 and NSCR2025 without modification.

The ERR and EAR terms appearing in equations (3) - (6) quantify the excess cancer risk, above the baseline levels observed in an unirradiated population, attributable to radiation exposure. As discussed at the beginning of this section, the excess risk models used in NSCR for solid cancer are based on incidence data from the LSS cohort. Solid cancer mortality is quantified using an incidence-to-mortality scaling approximation given by equation (4). Excess risks for leukemia are based on mortality data from the LSS cohort, and the corresponding incidence rate is determined using the mortality-to-incidence scaling approximation given by equation (6).

The excess risk models implemented in NSCR2012 were based on a combination of Biological Effects of Ionizing Radiation (BEIR) VII [NRC 2006], United Nations Scientific Committee on the Effects of Atomic Radiation (UNSCEAR) [UNSCEAR 2006], Preston et al. [2007], and Little et al. [2008] analyses within the linear no-threshold framework. A generalized form used to represent the excess risk (ER) models can be found in Stegeman et al. [2025] and is simplified here as

$$\mathrm{ER}_T(a, a_E) = \beta_T H_T e^{f_T(a,a_E)}, \tag{8}$$

where β_T is the sex- and site-specific dose effect modifier, and $f_T(a,a_E)$ describes the dependency structure for attained age and age at exposure. Excess risk model uncertainties were subjectively assigned to β_T to align with parameter uncertainty estimates identified in each of the aforementioned reports. A summary of the models used for each cancer site is provided in Table 4. The same set of excess risk models implemented in NSCR2012 are used in NSCR2025.

Excess risk model relative uncertainties (U_{ER}) were treated in NSCR2012 by subjectively assigning Gaussian distributions with unity mean and tissue-dependent standard deviations. The term U_{ER} was used to collectively account for various sources of uncertainty (statistical, dosimetry, etc.) related to equation (8). Further details of the excess risk model uncertainties can be found elsewhere [Cucinotta et al. 2013b; Simonsen and Slaba 2020, 2021] and are retained in NSCR2025 without modification.

Table 4. Tissue specific excess risk model sources used in NSCR2012 and NSCR2025.

Tissue	Source	Tissue	Source
Bladder	UNSCEAR [2006]	Oral cavity	Preston et al. [2007]
Brain	UNSCEAR [2006]	Other	UNSCEAR [2006]
Breast	NRC [2006]	Ovary	Preston et al. [2007]
Colon	UNSCEAR [2006]	Pancreas	Preston et al. [2007]
Esophagus	UNSCEAR [2006]	Prostate	Preston et al. [2007]
Gall bladder	Preston et al. [2007]	Rectum	Preston et al. [2007]
Kidney	Preston et al. [2007]	Stomach	UNSCEAR [2006]
Leukemia	Little et al. [2008]	Thyroid	NRC [2006]
Liver	UNSCEAR [2006]	Uterus	Preston et al. [2007]
Lung	UNSCEAR [2006]		

5.4. Population Transfer Weights

♦ *Summary of population transfer weights in NSCR2025* ♦

The population transfer weights and uncertainty distribution used in NSCR2012 were retained in NSCR2020 and NSCR2025 without modification.

Transfer weights, υ_T, are used to combine absolute and relative excess risk models derived from the LSS cohort to enable risk projections for a different population of interest. A value of $\upsilon_T = 0$ indicates excess risks transfer independently across populations in a purely additive manner (i.e., the total risk in a population is the baseline risk in the population plus the excess additive risk obtained from the LSS cohort). Alternatively, a value of $\upsilon_T = 1$ indicates excess risks scale proportionally to the baseline rates in a given population.

For NSCR2012, Cucinotta et al. [2013b] generally followed BEIR VII [NRC 2006] in assigning population transfer weights except for lung and leukemia. Thus, $\upsilon_T = 0$ for breast cancer (purely EAR model), $\upsilon_T = 0.5$ for leukemia and lung cancer, $\upsilon_T = 1$ (purely ERR model) for thyroid cancer, and $\upsilon_T = 0.7$ for all other cancer sites. Uncertainties for the population transfer weights are represented by a Bernoulli distribution about the assigned values. The NSCR2012 transfer model and uncertainty distribution is used in NSCR2025.

5.5. Latency

♦ *Summary of cancer latency models in NSCR2025* ♦

The latency factor used in NSCR2012 was retained in NSCR2020 and NSCR2025 without modification.

The latency factor accounts for the time-lag between radiation exposure and the appearance of solid cancer or leukemia. The latency factor used in NSCR2012 and NSCR2025 was obtained from BEIR VII [NRC 2006] and is defined as

$$C_T(\tau) = \begin{cases} 0, \tau < \tau_0 \\ 1, \tau \geq \tau_0 \end{cases}, \tag{9}$$

with $\tau_0 = 2$ years for leukemia, and $\tau_0 = 5$ years for solid cancer. No uncertainties are assigned to the value of τ_0.

5.6. Dose and Dose-Rate Effectiveness Factor

♦ *Summary of DDREF models in NSCR2025* ♦

The DDREF nominal value and uncertainty distribution used in NSCR2012 was retained in NSCR2020 and NSCR2025 without modification.

The DDREF is used to adjust excess risks derived from acute exposures associated with the LSS cohort to the chronic low dose-rates in the space environment. Cucinotta et al. [2013b] considered data from multiple sources and selected the BEIR VII [NRC 2006] point-estimate value of 1.5 for all solid cancers. The DDREF is excluded (i.e., no dose-rate effects) for leukemia. For the uncertainty distribution, Bayesian analyses were conducted on several different dataset combinations. They considered LSS data along with various experimental datasets involving mouse irradiations. The final DDREF distribution is based on a subjective assessment of the different Bayesian posterior results.

The DDREF distribution used in NSCR2012 and NSCR2025 for uncertainty propagation is defined as a Student's t-distribution with 5 degrees of freedom [Cucinotta et al. 2013b]. This distribution may be written as

$$f(\delta) = \frac{1000 N_c a'(\delta)}{3\pi[a^2(\delta) + 5]^3}, \qquad a(\delta) = \sqrt{\tfrac{5}{s}} \ln\left(\tfrac{\delta}{1.5}\right), \tag{10}$$

where $s = 0.251$, and δ is used to denote the DDREF value. The symbol N_c is a normalization constant defined so that the integral of $f(\delta)$ from 0.2 to 6 is unity.

5.7. Space Radiation Quality Factor

♦ *Summary of space radiation quality factor updates in NSCR2025* ♦

Quality factor	Notes
NSCR2012	• Dependent on $(Z^*/\beta)^2$. • Based on Katz biological action cross section [Katz et al. 1971, Wilson et al. 1993]. • Subjectively assigned parameter values and uncertainties guided by experimental data and analyses encompassing multiple endpoints.
NSCR2020	• Largely identical to what was implemented in NSCR2012, with some minor modifications to parameter correlations and uncertainty distributions, as described by Simonsen and Slaba [2020].
NSCR2025	• Dependent on ion LET. • Based on biological action cross section inspired by a combination of the Katz model [Katz et al. 1971] and LET-based formulations from Borak et al. [2014] and Xu et al. [2026]. • Objectively assigned parameter values, uncertainties, and correlations guided by experimental data. • Performance is quantitatively assessed against experimental data and shown to be superior to its predecessor.

In this section, a generalized approach for QF development is summarized along with basic quantities, concepts, and key assumptions. Then, a detailed description of the NSCR2012 and NSCR2025 quality factors is presented, which includes data sources, underlying dose-response model specification, QF mathematical formulae, and uncertainty quantification.

The QF is used to translate between the biological effectiveness of the predominately low LET exposure received by the LSS cohort and the complex mixed-particle space radiation environment. The QF currently enters into cancer risk projections through the dose equivalent, H_T (Sv), according to [Cucinotta et al. 2013b; ICRP 1991, 2007; NCRP 2000, 2006]

$$H_T = \frac{10^{-8}}{6.24\rho}\sum_j \int_0^\infty \phi_j^{(T)}(E)\, Q\, L\, dE\,, \tag{11}$$

where $\phi_j^{(T)}(E)$ (particles/(cm^2-MeV/n)) is the fluence in tissue T of type j ions with kinetic energy E (MeV/n), L is the ion LET (keV/μm), and $\rho = 1$ g/cm^3 is the density of water. The constants appearing in front of the integral are related to unit conversion (1 Gy = 6.24×10^9 MeV/g). The symbol Q is the space radiation QF.

The general process for developing a space radiation QF for carcinogenesis involves: (1) collection of relevant ground-based experimental data, (2) application of dose-response models to describe the data, (3) calculation of radiation quality metrics from the dose-response models, and (4) selection of a functional form to describe radiation quality over all particle types comprising the space environment. The final step provides the QF for use in equation (11). Also included in steps (1) – (4) is the characterization and propagation of uncertainties to facilitate probabilistic evaluation of QF within the NSCR model.

5.7.1. Basic Quantities, Concepts, and Assumptions

Foundational information and background regarding the use of QF for space radiation risk assessment can be found in NCRP reports 132 [NCRP 2000] and 153 [NCRP 2006] and Cucinotta et al. [2013b]. Here, emphasis is placed on those details needed to guide discussion specific to the QF used in NSCR2012 and NSCR2025.

Radiation quality for an ion dose, D_Z (Gy), can be characterized using the RBE, defined as [ICRP 2003]

$$\mathrm{RBE} = \frac{D_\gamma}{D_Z}, \tag{12}$$

where D_γ (Gy) is the dose of gamma radiation yielding the same biological effect as D_Z. Evaluation of equation (12) generally requires dose-response models calibrated to observational data (experimental or epidemiological) over a range of doses for both the ion and gamma radiations. The RBE depends on D_Z and the selected dose-response models along with several other factors such as the endpoint, tissue type, and experimental system (e.g., animals vs. cells).

For the particles comprising the space environment, the RBE for cancer-related endpoints generally increases as D_Z decreases. If the dose-response models involved are approximately linear at low dose, RBE will reach an

asymptotic upper bound as $D_Z \to 0$ Gy [ICRP 2003]. The upper bound is denoted as $\mathrm{RBE}_{\max}$ and may be calculated as

$$\mathrm{RBE}_{\max} = \frac{\alpha_Z}{\alpha_\gamma}, \tag{13}$$

where α_Z and α_γ are the linear induction coefficients (i.e., initial dose-response slopes at low dose) associated with the ion and gamma exposures, respectively. $\mathrm{RBE}_{\max}$ was used as the basis for QF in NSCR2012 and will remain the basis for QF in NSCR2025.

Related to equation (13) is the concept of the biological action cross section. In the low dose regime, characterized by less than one ion traversal per sensitive volume (e.g., cell nucleus), one can write [Cucinotta et al. 2013b]

$$\alpha_Z D_Z = \sigma F_Z, \tag{14}$$

where σ (μm^2) is the biological action cross section, and F_Z ($1/\mu m^2$) is the ion fluence corresponding to the dose D_Z. Equations (13) and (14) can be rearranged to establish a relationship between $\mathrm{RBE}_{\max}$ and σ, given by [Cucinotta et al. 2013b]

$$\mathrm{RBE}_{\max} = \frac{6.24\sigma}{\alpha_\gamma L}, \tag{15}$$

where L is the ion LET (keV/μm), and the factor of 6.24 is a unit conversion (1 Gy = 6.24×10^9 MeV/g) in the fluence-to-dose relationship for water (ρ = 1 g/cm^3, not explicitly written in equations (15) and (16))

$$D_Z = \frac{LF_Z}{6.24}. \tag{16}$$

Equation (15) may be combined with particle-type dependent forms for σ to establish a QF.

Alternative metrics such as the Relative Effects Ratio (RER) [Shuryak et al. 2017a] have been proposed. While RBE is a ratio of doses yielding the same biological effects, RER is calculated as the ratio of effects at a fixed dose according to

$$\mathrm{RER} = \frac{R_Z(D)}{R_\gamma(D)}, \tag{17}$$

where R_Z and R_γ are the ion and gamma biological responses at the same dose, D (Gy). Shuryak et al. [2017a] argued that RER provides a more practical radiation quality metric when dose-effect curves exhibit complex non-linear behavior or even thresholds. Ground-based experimental costs may also be eased if RER is considered instead of RBE. As indicated in equation (17), only one common dose is needed for RER, which may be directly associated with an expected mission exposure level. RBE calculations, on the other hand, require data at several dose points to support dose-response model calibration [Shuryak et al. 2017b].

Practical application of RBE and RER in risk assessment leads to distinct but related expressions. Let $\boldsymbol{\mathcal{R}}_Z$ represent the cancer risk associated with ion exposure needing to be estimated. Let $\boldsymbol{\mathcal{R}}_\gamma$ denote the cancer risk associated with gamma exposure that can be estimated from terrestrial epidemiological data or models (e.g., LSS cohort). Then

$$\Re_Z \sim \Re_\gamma(\mathrm{RBE}\cdot D_Z), \tag{18}$$

$$\Re_Z \sim \mathrm{RER}\cdot \Re_\gamma(D_Z). \tag{19}$$

Both RBE and RER allow unknown risks for a given ion exposure to be estimated in terms of quantified gamma exposure risks. RBE provides the estimate based on dose-scaling, while RER is based on risk-scaling. Note that in cases where the underlying dose-response functions and $\mathcal{R}_\gamma$ are linear with respect to dose, then it can be shown that RBE = RER. Differences between RBE and RER occur in the presence of non-linearities and have been initially studied in other work [Shuryak et al. 2017b, Slaba et al. 2026]. Further investigation is needed to determine the impact, limitations, and suitability of RER for use in space radiation-induced cancer risk assessment for humans.

There is also the high-dose method [ICRP 2003, Kocher et al. 2005] for calculating RBE_{max} which involves the DDREF and evaluation of RBE at a higher dose (e.g., 1 Gy). The high-dose method provides an estimate for RBE_{max} according to

$$\mathrm{RBE}_{\mathrm{max}} = \mathrm{RBE}_{\mathrm{H}} \cdot \mathrm{DDREF} \tag{20}$$

where RBE_H is the high-dose RBE, typically estimated at a dose near 1 Gy. The primary advantage to RBE_H lies in the ability to more accurately estimate biological responses at higher doses where statistical uncertainties in experimental and epidemiological data are smaller compared to the low dose data needed for RBE_{max} evaluations.

Cucinotta [2015] combined the concepts of RBE and DDREF, yielding a quantity referred to as $RBE_{\gamma\text{-acute}}$. Further assumptions were made to neglect DDREF for high LET ions in the space environment, but it was demonstrated nevertheless that an uncertainty reduction of about 40% in REID was achieved by considering high dose and dose-rate gamma exposure data (as in the ICRP high-dose method). As with RER, further work is needed to better understand the impact, limitations, and suitability of possibly using the high-dose method or $RBE_{\gamma\text{-acute}}$ in space radiation-induced cancer risk assessments for humans.

Complexity is introduced into these concepts when the ion exposures of interest manifest nonlinear biological responses at low dose. Nonlinear low-dose responses are attributed to nontargeted effects (NTE) which generally refer to biological outcomes originating from unirradiated cell nuclei through microenvironment perturbations or other signaling pathways [Shuryak and Brenner 2020]. Much has been studied on this topic [Cucinotta and Chappell 2010, Cucinotta et al. 2013b, Cucinotta and Cacao 2017, Chang et al. 2016, Chappell et al. 2020, Shuryak and Brenner 2020]. Cucinotta and Cacao [2017], in particular, attempted to estimate the impact of NTE on space cancer risk projections. They demonstrated that NTE could possibly significantly increase cancer risks for Mars missions by as much as factor of two. Further discussion of NTE is provided in Section 5.7.3.2.

It is simply noted here that NTE dose-response model corrections were not included in the NSCR2012 QF and are not included in the updated NSCR2025 QF. Further ground-based measurements and mechanistic insights are needed before such terms are included in risk assessment models used to set permissible exposure limits and communicate health risks.

Equation (11) is based on the concept of simple additivity, where it is assumed that the total dose equivalent for a mixed field can be obtained by summing (over particle type and energy) the dose equivalents associated with the components comprising the field. Such an approximation is presumed to be reasonably accurate if the dose-responses for each component of the mixed field are approximately linear. Feiveson et al. [2021] presented data on chromosome aberrations in blood samples extracted from 43 crewmembers who participated in ISS missions. Those measurements were compared to aberration yields associated with acute gamma exposure of pre-flight blood samples in the same individuals. An average RBE of 3.09 ± 0.24 was calculated, with values for individual crewmembers ranging from 2.4 to 4.7. These estimates agree well with an average QF of ~2-3 determined by models based on simple additivity [Cucinotta et al. 2008, Simonsen et al. 2020].

NASA developed a ground-based GCRsim at the NSRL to provide a means of assessing biological effects of the complex mixed-particle space radiation environment in an experimental setting. Prior to GCRsim commissioning in 2018, experimental studies and modeling activities were conducted to investigate possible mixed-field effects, including simple additivity, synergy (combined effects more than additive), and antagonism (combined effects less than additive). Sachs and colleagues developed a theoretical and computational framework to assess the validity of simple additivity in comparison to synergy or antagonism in mixed-particle exposures [Ham et al. 2017; Huang et al. 2019, 2020]. Xu et al. [2026] developed a multilevel probabilistic dose-response model that can predict single ion and mixed field exposures without the a priori assumption of simple additivity. The models and experimental data relevant for assessing these mixed field effects were reviewed by Huff et al. [2023] in the context of ground-based GCR simulation [Simonsen et al. 2020]. It was concluded that available experimental data and computational models show heterogeneous results with respect to evidence for synergy/antagonism. Although a substantial deviation from simple additivity was not found in the available data when viewed collectively, further

work is needed to assess the uncertainties that may be introduced into risk projections. Nevertheless, equation (11) and the embedded use of simple additivity are the basis for computing dose equivalent in NSCR2012 and NSCR2025.

Finally, it is assumed within the risk projection formulation and equations (11) and (18) that biological outcomes originating from HZE and gamma irradiations are qualitatively similar. Possible sources and evidence for qualitative differences between these two radiation types were discussed in section 5.2 of the NSCR2012 report [Cucinotta et al. 2013b]. Trani et al. [2010] and Datta et al. [2013] found that the spectrum of gastrointestinal tumors arising from HZE exposures were both greater in number and more aggressive than their gamma-induced counterparts. Conversely, Edmonson et al. [2020] considered a genetically diverse mouse model and found the spectrum of HZE and gamma-induced tumors to be similar. Further experiments need to be conducted to improve mechanistic understanding and bring clarity in this area.

5.7.2. NSCR2012 Formulation

The development process for the NSCR2012 QF relied moderately upon expert opinion and subjective judgements, which can be necessary in cases where data are sparse compared to the range of variables needing to be represented by predictive models. Here, an attempt is made to summarize the data sources and dose-response models underlying the NSCR2012 QF. The information in this section was obtained from section 5 of the NSCR2012 report [Cucinotta et al. 2013b], where the interested reader can find further details.

5.7.2.1. Data Sources

Data were considered from two main sources: animal tumorigenesis experiments and cellular studies assessing radiation-induced chromosome aberrations and mutations. The use of human epidemiological data collected from high LET exposures to inform RBE and QF specification was also discussed (section 5.1.1 of the NSCR2012 report), and two key limitations associated with such data were identified. First, such data are extremely sparse and limited mainly to analyses of the neutron component of the atomic bomb fallout in the LSS cohort along with additional data from α emitter exposures. Second, there are key differences between high LET space radiation and terrestrial sources. Energetic heavy ions found in the space environment elicit energy deposition and damage in a localized manner along distinct tracks through biological tissues and cell nuclei. Terrestrial sources such as low energy neutrons and α emitters on the other hand leave a very different spatial distribution of energy deposition and damage. This may include relatively homogeneous whole-body exposures or more localized tissue exposures (e.g., lung exposure due to inhalation). It is surmised that human epidemiological data involving high LET terrestrial exposures had minimal direct influence in defining the NSCR2012 QF.

Animal carcinogenesis studies are performed at ground-based facilities using accelerated heavy ion beams or neutron sources. Although limited in number, they do provide a terrestrial analog for humans exposed to space radiation. The animal studies are summarized in Tables 5.1 and 5.2 of the NSCR2012 report, which includes neutrons and HZE ions, mouse and rat models, tumorigenesis and life-shortening endpoints, along with RBE_{max} and RBE at different dose levels. The impact of dose-rate effects on RBE estimates elucidated through fractionated exposures are mentioned as well. The RBE data were mainly used to estimate the maximum value of QF and guide specification of the Σ_0/α_γ parameter in the NSCR2012 QF (discussed in Section 5.7.2.3).

Cellular studies are also performed at ground-based facilities to quantify cancer-related endpoints such as chromosome aberrations, cell transformation, and mutations. These experiments can be performed at a much lower cost than animal studies. Translation of these endpoints to carcinogenesis can be difficult though, especially in the absence of mechanistic understanding. Table 5.3 and Figure 5.4 of the NSCR2012 report provide the cellular data available at that time. The chromosome aberration data were obtained from human blood lymphocytes, and transformation data were obtained in C3H10T1/2 mouse fibroblast cells. The available data provided insights into the particle type dependency of RBE which informs specification of the κ parameter in the NSCR2012 QF (discussed in Section 5.7.2.3).

5.7.2.2. Dose-Response Model

RBE is a calculated quantity originating from dose-response models calibrated to experimental data. The choice of dose-response model, calibration approach, and inclusion/exclusion of high-dose observations can all influence the magnitude of calculated RBE. One would ideally use a consistent set of such choices to minimize ambiguity and aid interpretation and clarity, but this may not always be possible when data are sparse and/or extracted from disparate sources. For NSCR2012, not all of the relevant information was available or provided in the report. It

was noted that parameter estimates for the maximum biological effectiveness (i.e., maximum value of QF for a particle) were obtained from RBE_{max} values calculated from "… a linear dose response at low particle dose, ignoring NTEs or other possible mechanisms …" [Cucinotta et al. 2013b].

5.7.2.3. Quality Factor

The space radiation QF developed for NSCR2012 [Cucinotta et al. 2013b] was based on the Katz biological action cross section and an initiation-promotion model of tumor induction [Katz et al. 1971, Wilson et al. 1993]. The cross section can be written as

$$\Sigma(Z,E) = \Sigma_0 P(Z,E) + \frac{\alpha_\gamma L}{6.24}[1 - P(Z,E)]s_{sparse}\,, \tag{21}$$

$$P(Z,E) = \left(1 - e^{-\frac{X_{tr}}{\kappa}}\right)^m [1 - e^{-E/0.2}]\,. \tag{22}$$

Replacing σ in equation (15) with $\Sigma(Z,E)$ from equation (21) yields

$$Q_{NASA}(Z,E) = [1 - P(Z,E)]s_{sparse} + \frac{6.24\Sigma_0}{\alpha_\gamma L} P(Z,E)\,, \tag{23}$$

where E (MeV/n) is the ion kinetic energy, L is LET (keV/μm), $X_{tr} = (Z^*/\beta)^2$ is the track-structure parameter with Z^* being the effective charge [Barkas 1963], and β the ion velocity relative to the speed of light. The term in brackets in equation (22) is intended to account for the narrowing (thindown) of ion tracks as the ion comes to rest; the value of 0.2 MeV is referred to as the thindown energy. The symbols s_{sparse}, m, κ, and Σ_0/α_γ are adjustable parameters. The parameter s_{sparse} represents the value of Q for low LET ions when $P \rightarrow 0$ (i.e., high energy protons and helium). It was noted in the NSCR2012 report that "[the] interpretation of the parameters is quite general, and is not tied to a particular track structure model per se, but rather is an efficient parameterization of radiobiology data for particles." [Cucinotta et al. 2013b]. Preferred values for the adjustable parameters are given in Table 5.

Table 5. NSCR2012 QF adjustable parameter definitions.

Parameter	Nominal value	Uncertainty distribution
s_{sparse}	1	Relative uncertainty specified as $N(\mu = 1, \sigma = 0.15)$
m	3	Discrete distribution for m = {2, 2.5, 3, 3.5, 4} with probabilities {0.2, 0.2, 0.35, 0.2, 0.05}
κ	1000 ($Z > 4$); 550 ($Z \leq 4$)	[(a)]Relative uncertainty specified as log-$N[\mu = \ln(0.95), \sigma = \ln(1.4)]$
Σ_0/α_γ	7000/6.24 (solid cancer); 1750/6.24 (leukemia)	Relative uncertainty specified as log-$N[\mu = \ln(0.9), \sigma = \ln(1.4)]$ for solid cancers and log-$N[\mu = \ln(1), \sigma = \ln(1.6)]$

[(a)] The uncertainty distribution for κ was originally defined in the NSCR2012 report as being $N(\mu = 1, \sigma = 0.33)$ with constrained sampling intervals and an empirically designated correlation to m. Simonsen and Slaba [2020] modified the uncertainty distribution to be log$N[\mu = \ln(0.95), \sigma = \ln(1.4)]$ and redefined the correlation to m to improve robustness of parameter sampling.

A discussion of parameter estimation is provided in section 5.6.1 of the NSCR2012 report. The parameters were specified by broadly considering available RBE data, biophysical considerations, and historical studies with the Katz model focused on various cancer-related endpoints and cell inactivation. Justification to introduce distinct Σ_0/α_γ values for solid cancer and leukemia and distinct κ values for $Z > 4$ and $Z \leq 4$ was provided. The uncertainty distributions were subjectively assigned and are described in Table 5.

5.7.3. NSCR2025 Formulation

The QF developed for NSCR2025 is described in this section. Throughout the development process, emphasis was placed on (1) maintaining clarity and traceability to underlying experimental datasets; (2) utilization of ensemble global dose-response models capable of recapitulating experimental data and predicting responses where no data exist; (3) providing objective and robust QF uncertainty estimates accounting for dose-response model errors, experimental data uncertainty, and variation across endpoints; (4) developing a QF that can be integrated within probabilistic cancer risk projections and existing spaceflight dosimetry systems.

Items (1) and (3) are key components of NASA STD 7009 for models and simulations which "… establishes requirements and recommendations for the development and use [of models] … while ensuring the credibility of the results from [a model] is assessed and clearly conveyed, especially for critical decisions." [NASA 2024]. Data pedigree and uncertainty quantification, in particular, explicitly appear as factors involved in the formal model assessments contained within the standard and are therefore emphasized in the NSCR2025 QF development process.

Along with these formal requirements, a NASEM committee was formed in ~2020 at the behest of NASA to "assess [NASA's] processes for long-term risk assessment and management for currently anticipated crewed missions with respect to cancer … due to space radiation" [NASEM 2021]. The committee recommended that NASA improve and expand the methods used to communicate space radiation-induced health risks to the general public, astronauts, and decision/policymakers [NASEM 2021]. Compliance with this recommendation necessarily includes items (1) and (3) to ensure risk projections and their uncertainties can be reasonably linked to underlying ground-based experimental data and models.

Item (2) is a key feature of the NSCR2025 QF made possible by new data [George et al. 2013, Hada et al. 2014, Chang et al. 2016] and global dose-response models [Xu et al. 2026; Slaba et al. 2025a, 2026] that were not available at the time of the NSCR2012 report. Global dose-response models are calibrated to available data spanning a representative range of particle types and can predict responses where no data exist. This predictive feature enables RBE_{max} calculations to be made over the full range of particles comprising the space environment from a consistent global dose-response model framework. Uncertainties attributable to experimental data, theoretical assumptions, and prediction error can also be propagated through global dose-response models and RBE_{max} calculations, providing a robust foundation for generating QF uncertainties.

Item (4) recognizes the importance of in-flight measurements that are both biologically informative and relatable to risk metrics while accounting for practical constraints associated with current spaceflight dosimetry systems. Pixel-based instruments [George et al. 2024], combined silicon and scintillator stacks [Zeitlin et al. 2016, 2023], and tissue equivalent proportional counters [Hayes et al. 2022] are capable of measuring the absorbed dose-rate and LET (or lineal energy transfer) spectrum. Some of these hardware systems have demonstrated the ability to discriminate Z and E in narrow intervals [Zeitlin et al. 2016]. In-flight mass and volume constraints limit their ability to resolve the full Z and E range needed to support in situ integration and evaluation of the NSCR2012 QF based on $(Z^*/\beta)^2$.

Simplifications to the NSCR2012 QF have been proposed to facilitate integration into measurement systems [Borak et al. 2014, Naito and Kodaira 2026]. Borak et al. [2014] presented an approach wherein the $(Z^*/\beta)^2$ dependence of the NSCR2012 QF was replaced with LET alone. The mean quality factor (evaluated as dose-equivalent divided by dose) was computed as a function of shielding thickness for representative GCR environments. It was demonstrated that the LET-dependent form agreed with the NSCR2012 QF within 5% across the broad range of cases studied. This rather small error can be compared to overall QF uncertainties which have been estimated to drive a 2.7-fold (170%) uncertainty in risk projections [Cucinotta et al. 2013b, Simonsen and Slaba 2021]. Borak et al. [2014] therefore demonstrated that QF accuracy is not appreciably altered if the $(Z^*/\beta)^2$ dependence is replaced with LET alone in practical space calculations.

There are important theoretical and experimental considerations surrounding the use of $(Z^*/\beta)^2$ or LET in QF development that must be discussed as well. It was stated in the NSCR2012 report that "… initial DNA damage and the non-DNA damage, such as the production of various oxidative species, is dependent on Z and LET or alternatively Z and E, and is not well described by LET alone." [Cucinotta et al. 2013b]. This statement is supported by track-structure and radio-chemical simulations for cellular-scale targets and experiments focused on cell inactivation at medium and high doses (see Figures 5.8-5.11 in the NSCR2012 report).

Without seeking to contradict these statements, there exist data and analyses offering a different perspective. First, a well-known figure from Thacker et al. [1979] suggests that plotting cell inactivation RBE as a function of $(Z^*/\beta)^2$ instead of LET "reconcile[s] some of the differences in effectiveness between helium and heavier ions." [Thacker et al. 1979]. It needs to be noted however that their analysis combines RBE from two different cell lines (V79 hamster cells and T1 human cells) and is based on an endpoint (cell inactivation) that is less relevant to space

radiation carcinogenesis than mutagenesis, thereby weakening the impact of their conclusions for the present purpose. In that regard, a figure is provided later in the same paper showing mutagenesis RBE as a function of LET with no apparent charge branching that might be resolved through the use of $(Z^*/\beta)^2$.

Second, Waligorski et al. [1987] analyzed available transformation data from C3H10T1/2 cells within the context of the Katz action cross section. They found a "nonunique dependence of RBE on LET" [Waligorski et al. 1987] but also noted that considering RBE as a function of $(Z^*/\beta)^2$ did not fully resolve the dependency structure either (see text around Figure 7 in their paper).

Third, Kiefer et al. [2001] summarized an extensive set of experiments conducted at Gesellschaft für Schwerionenforschung (GSI) with over 40 different beams with energies between ~1 MeV/n up to ~1 GeV/n and charges between $Z = 2$ and $Z = 92$. They clearly state: "A unique dependence of mutation induction cross sections on LET or any other physical parameter of the particles cannot be found." [Kiefer et al. 2001].

Lastly, limited animal tumorigenesis data [Fry et al. 1985, Alpen et al. 1993, Chang et al. 2016] do not clearly demonstrate a preference between $(Z^*/\beta)^2$ or LET dependency structures. Chromosome aberration experiments encompassing a wider range of particle types, wherein time is allowed for repair processes to take place after the initial damage, are similarly inconclusive on this matter [George et al. 2003, 2007, 2013; Hada et al. 2014]. RITCARD simulation results are provided in Section 5.7.3.3 indicating that RBE charge branching depends on the endpoint being considered. The simulations reflect charge branching in the RBE for complex double strand break (DSB) formation, but such dependence is no longer apparent in the RBE for total exchanges, wherein repair processes are accounted for after irradiation. Analogously, Sridharan et al. [2015] found marked differences in the γH2AX intensity induced by ions with either similar LET or $(Z^*/\beta)^2$ at 2 h post-irradiation that were largely absent at 24 h post-irradiation. They also found that "… both LET and $(Z^*/\beta)^2$ provide a fairly good indicator of γH2AX response …" [Sridharan et al. 2015] and conclude that $(Z^*/\beta)^2$ provided only a "… slightly better fit … " [Sridharan et al. 2015] for describing γH2AX intensity as a function of particle type. It bears noting though that even this latter conclusion was drawn from data taken at a high dose of 2 Gy where direct relevance to space radiation protection can be difficult to establish.

In summary, evidence favoring $(Z^*/\beta)^2$ instead of LET dependent RBE behavior rests mainly within the realms of initial DNA damage, certain track-structure simulations, and cell inactivation data at medium and high doses. Cell transformation and mutational RBE provide mixed conclusions [Thacker et al. 1979, Waligorski et al. 1987, Kiefer et al. 2001]. RBE derived from animal [Fry et al. 1985, Alpen et al. 1993, Chang et al. 2016] and in vitro chromosome aberration [George et al. 2003, 2007, 2013; Hada et al. 2014] experimental data that directly underpin QF do not demonstrate the need for $(Z^*/\beta)^2$ dependency to explain global trends across particle types. Moreover, the $(Z^*/\beta)^2$ dependent NSCR2012 QF cannot be directly integrated into spaceflight dosimetry systems. Simplifications to the NSCR2012 QF were studied [Borak et al. 2014], and it was demonstrated that calculated results are negligibly altered by replacing $(Z^*/\beta)^2$ dependence with LET alone. It is therefore unclear whether possible benefits in accuracy or uncertainty reduction outweigh the additional complexity imposed by $(Z^*/\beta)^2$dependent QF.

A visual description of the NSCR2025 QF development strategy can be found in Figure 16 and will be referred to throughout the remainder of this section which is organized as follows. Experimental data are described and classified as either global or individual, as shown in the orange boxes in the figure. An ensemble dose-response model is presented and calibrated separately to the global datasets; performance is assessed both with and without NTE corrections. The track-structure based DNA damage and repair simulation tool RITCARD is described. The ensemble dose-response model and RITCARD are used to calculate RBE_{max} values for multiple endpoints over a broad range of particle types (and nuclear radii in the case of RITCARD). A parametric QF is presented and calibrated using results from the ensemble dose-response model, RITCARD simulations, and additional experimental data spanning charged particles and fission neutrons, animals and cells, and multiple carcinogenic related endpoints. The same information is used to assign QF uncertainties and parameter correlations for use in probabilistic cancer risk projections. The blue boxes in the figure identify important QF components derived from both experimental data and modeling results. Lastly, the NSCR2025 QF performance is quantitatively assessed and compared to other QF models.

5.7.3.1. Data Sources

There are two classes of experimental data appearing within the NSCR2025 development flowchart shown in Figure 16. Global datasets encompass observations collected in the same experimental system over a broad range of doses and particle types relevant to space radiation-induced carcinogenesis. Global dose-response models contained within the ensemble framework (discussed in Section 5.7.3.2) can be calibrated directly to these datasets, allowing RBE_{max} values to be calculated for any relevant particle type as an initial foundation for establishing the magnitude, behavior, and uncertainty of QF. Three datasets exist with sufficient dose and particle-type coverage to support such

efforts. They are Harderian gland tumorigenesis [Fry et al. 1985, Alpen et al. 1993, Chang et al. 2016], human blood lymphocyte chromosome aberrations [George et al. 2003, 2007, 2013; Hada et al. 2014], and human skin fibroblast chromosome aberrations [Hada et al. 2014]. Additional complexity surrounds cell transformation and mutational data and are discussed later in this section.

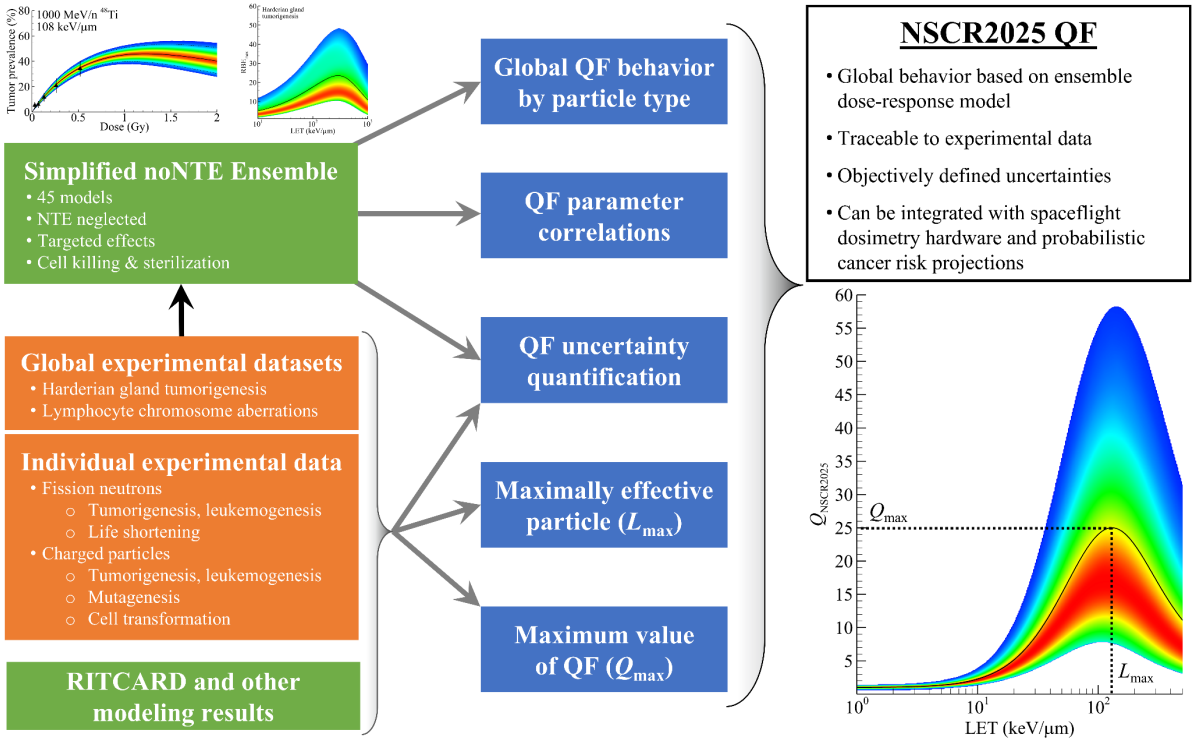

Figure 16. NSCR2025 QF development strategy flowchart. Global experimental datasets are used in conjunction with a simplified noNTE ensemble dose-response model to provide global RBE_{max} estimates (i.e., covering the range of particle types found in space). Global and individual experimental data are used to identify the maximally effective particle (L_{max}) and maximum QF (Q_{max}) and guide parameter correlations and uncertainty assignments.

The global experimental datasets used to calibrate the ensemble dose-response model are listed in Table 6. Key experimental data were made available after completion of the NSCR2012 report. Chang et al. [2016] extended the Harderian gland tumorigenesis dataset by including additional measurements for 260 MeV/n ^{28}Si (LET = 75 keV/μm), 1 GeV/n ^{48}Ti (LET = 108 keV/μm), 600 MeV/n ^{56}Fe (LET = 174 keV/μm), and gamma exposures. George et al. [2013] and Hada et al. [2014] measured chromosome aberrations in blood lymphocytes and skin fibroblasts for over 20 different particle types spanning a broad range of highly relevant ions, energies, and LET values. RBE_{max} values will be calculated directly from the calibrated ensemble for each dataset over a range of particle types in the next section. The calculated values provide initial foundational information for establishing QF parameter values and uncertainties.

Table 6. Global experimental datasets used for ensemble dose-response model calibration. References in bold text indicate data that were either unpublished or unavailable when the NSCR2012 report was completed.

Endpoint	# of obs.	Ion range (Z)	Energy range (MeV/n)	LET range (keV/μm)	Dose range (Gy)
Murine Harderian gland tumorigenesis[1, 2, 3]	41	10 – 41	260 – 1000	25 – 433	0.03 – 1.6
Human blood lymphocyte CA[4, 5, 6, 7]	159	6 – 26	55 – 5000	13 – 305	0.005 – 2
Human skin fibroblast CA[7]	44	8 – 26	55 – 600	75 – 239	0.005 – 1.2
Total	244	6 – 41	55 – 5000	13 – 433	0.005 – 2

[1][Fry et al. 1985], [2][Alpen et al. 1993], **[3][Chang et al. 2016]**, [4][George et al. 2003], [5][George et al. 2007], **[6][George et al. 2013]**, **[7][Hada et al. 2014]**

The Harderian gland tumorigenesis data and some of the chromosome aberrations measured in lymphocytes from the aforementioned datasets were utilized for the development of the NSCR2012 QF, preserving continuity by anchoring the NSCR2025 QF with data from its predecessor. Harderian glands are located within the eye socket and do not exist in humans. However, they are made of epithelial and secretory cells and can form spontaneous tumors – primarily adenomas and to a lesser extent carcinomas [Alpen et al. 1993, Chang et al. 2016] – originating from epithelial cell transformation, thus constituting a relevant model of epithelial-driven tumorigenesis. The Harderian gland has been considered a good model for evaluating high-LET RBE and radiation quality effects due to the high sensitivity to radiation, short latency to tumor formation, and low spontaneous incidence rates. Limitations include lack of a direct human counterpart and formation of adenomas as the primary tumor, which may be a more relevant marker of early cancer induction versus full carcinogenesis. Tissue-specific tumor models could provide more translational relevance, but these data sets are currently limited.

As previously mentioned, chromosome aberration experiments are cost-efficient and contrary to animal models, can be assessed directly in cells of human origin. Aberrations measured at the first metaphase arise from the misrepair of radiation-induced DNA damage and are reflective of track structure effects and clustered DNA damage associated with high-LET radiation. Chromosome aberrations constitute an early biological endpoint relevant to carcinogenesis, as aberration formation relates to the fate of the cell [Sridharan et al. 2016]. Causal connection between gross chromosomal abnormalities and the formation of tumors during the multi-stage process of carcinogenesis has been suggested by various studies [Bailey et al. 2024, Hanahan 2026]. One epidemiological study showed correlation between chromosome aberration frequency measured in lymphocytes and the risk of cancer [Bonassi et al. 2008]. Chromosome aberrations are also sensitive to the dose-rate [ICRP 2026] and could be used for future DDREF development, as animal studies with low dose-rate exposures remain challenging and costly to perform. Another key advantage of chromosome aberrations lies in their suitability for predictive modeling with tools like RITRACKS/RITCARD. Predictive models can complement experimental data for ion charge/energies, doses and dose-rates for which no measurement exists. They can also be used to provide insights into key early biological events driving carcinogenesis that remain difficult to evaluate experimentally, as will be illustrated in Section 5.7.3.3. Together, studies of chromosome aberrations and Harderian gland tumor formation provide complementary approaches capturing early DNA damage and repair (mis)repair and early stages of tumor formation.

In contrast to the global datasets of Table 6, individual experimental data refer to studies wherein dose-responses and/or RBE values were reported for one or a limited number of particle types. These data generally lack the necessary particle type coverage needed to support calibration of global dose-response models but nevertheless provide an additional source of discrete RBE values that can influence specific QF components and uncertainty quantification. Examples of individual data include the work of Weil et al. [2009] assessing leukemia and hepatocellular carcinoma in mice exposed to 1 GeV/n ^{56}Fe or the Suman et al. [2016] experiments quantifying gastrointestinal and colon tumors per mouse exposed to four different energetic ion beams.

Cell transformation and mutagenesis experimental datasets represent an exception to the individual/global classification scheme. While several experiments have been conducted for these endpoints over a broad range of doses and particle types, additional complexity surrounds the quantified RBE and associated interpretation. X-rays were frequently used as a reference radiation instead of ^{60}Co or ^{137}Cs, potentially causing a reduction in RBE estimates by a factor of two or more [Kocher et al. 2005, NCRP 2018]. Non-human cell lines such as V79 hamster cells or C3H10T1/2 mouse cells were used in some of the more expansive datasets, simultaneously introducing both in-vivo/in-vitro and animal/human translational uncertainties. Cell survival and inactivation were frequently studied alongside transformation or mutagenesis, sometimes shifting focus toward higher doses and away from the low doses needed to refine RBE_{max} estimates. Given these complexities, transformation and mutation data are considered as individual experimental datasets in this work. RBE reported for these endpoints nevertheless provide key information to help identify the most effective particle type where QF is maximized and support uncertainty quantification, as will be shown. Global analysis of these datasets within the ensemble framework may be considered in future work.

The individual experimental datasets collected for this work are summarized in Table 7. RBE were extracted from plots or tables in the publications listed. Efforts were made to retain only RBE_{max} values for consistency, but in some cases, only alternative metrics could be extracted (e.g., RER, RBE at a specified dose value, or RBE at a specified cell survival level). In cases where X-rays were used as a reference radiation, an upper error bar of a factor of two will be applied in plots [Kocher et al. 2005, NCRP 2018].

An additional set of data needing to be addressed involves neutron exposures. For this, consideration is given to analyses of fission neutron exposure data from Edwards et al. [1999], Kocher et al. [2005] and Table 5.2 of the NSCR2012 report. The information extracted from these three sources can be found in Table 8. RBE_{max} estimates and associated uncertainties vary widely depending on the endpoint, animal model, sex, and analysis methods employed. These data will be primarily used to guide QF uncertainties at an LET of ~70 keV/μm. The average RBE_{max} for life-

shortening and solid cancer in Table 8 (i.e., excluding leukemia and lymphocytic cancers) yields ~31, although individual results vary between 4 and 140.

Table 7. Individual experimental data used within the NSCR2025 QF development and uncertainty quantification procedures.

Animal Tumorigenesis and Leukemogenesis (16 RBE)				
Source	**Radiation**	**Ref.**	**Metric**	**Endpoint (System)**
Dicello et al. [2004]	250 MeV protons, 1 GeV/n ^{56}Fe	^{60}Co/^{137}Cs	RBE (D_{ref} = 1.6 Gy)	Mammary tumorigenesis (Female SD rats)
Weil et al. [2009]	1 GeV/n ^{56}Fe	^{137}Cs	RBE_{max}	HCC, AML (Male CBA/CaJ mice)
Suman et al. [2016](1)	Z = 6, 14, 26 E = 290 – 1000 MeV/n		RER (0.1 Gy)	GI and colon tumors/mouse (Male/Female APC$^{1638N/+}$ mice)
Chang et al. [2022](1)	Z = 8, 14, 22, 26 E = 260 – 1000 MeV/n		RBE (D_{ref} = 0.4 Gy)	Lung tumorigenesis (Female CB6F1/Hsd mice)
Neoplastic Cell Transformation (34 RBE)				
Source	**Radiation**	**Ref.**	**Metric**	**Cell line**
Yang et al. [1985]	Z = 6, 10, 14, 18, 26, 92 E > 300 MeV/n	X-rays	RBE (50% surv.)	C3H10T1/2, embryonic mouse cells
Miller et al. [1995]	Z = 1, 2, 6, 8, 9 E < 7 MeV/n		RBE_{max}	
Han et al. [1998]	19 – 290 MeV/n ^{12}C, 27 – 95 MeV/n ^{28}Si			SHE, Primary SHE cells
Bettega et al. [2009](2)	11, 100, 270 MeV/n ^{12}C	15 MeV photons		CGL1, HeLa X HSF cells
HGPRT-locus Mutagenesis (97 RBE)				
Source	**Radiation**	**Ref.**	**Metric**	**Cell line**
Thacker et al. [1979]	Z = 2, 5, 7 E < 11 MeV/n	^{60}Co	RBE_{max}	V79, hamster lung fibroblast cells
Kranert et al. [1990]	Z = 8,10,20,22,28,54,82,92 E < 16 MeV/n	X-rays		
Stoll et al. [1995](2)	2 – 396 MeV/n ^{16}O 8 – 395 MeV/n ^{20}Ne			
Stoll et al. [1996](2)	Z = 28, 79, 82 E = 2 – 980 MeV/n			
Belli et al. [1998](2)	E < 5 MeV protons			
Kiefer et al. [2001]	Z = 2 – 92 E = 1 – 980 MeV/n			
Suzuki et al. [1996](2)	E = 7 – 129 MeV/n ^{12}C	^{137}Cs	RBE (100×10^{-6} MF)(3)	HE20, HE fibroblast-like cells
Suzuki et al. [2003](2)	15, 30 MeV/n ^{12}C 54, 123 MeV/n ^{20}Ne			
Suzuki et al. [2006](2)	E = 15 – 123 MeV/n ^{20}Ne		RBE (30×10^{-6} MF)(3)	
Hei et al. [1988](2)	E < 4 MeV/n ^{2}H E < 2 MeV/n ^{3}He		RBE_{max}	Primary diploid HSF
Cox and Masson [1979]	Z = 2, 5, 7 E < 11 MeV/n	X-rays		HF19, human diploid lung fibroblast
Chen et al. [1984](2)	0.7 MeV/n ^{4}He			GM10, diploid embryonic HSF
Chen et al. [1994]	Z = 10, 18, 26, 57 E = 94 – 603 Mev/n	^{60}Co		Primary normal HSF
Tsuruoka et al. [2009](2)	E = 134 – 427 MeV/n ^{56}Fe	X-rays	RBE (50×10^{-6} MF)(3)	NB1RGB, normal HSF

(1) Not available when NSCR2012 report was completed.
(2) Not referenced in the NSCR2012 report.
(3) RBE calculated at a specified mutation frequency (MF) level.

Table 8. Fission neutron data extracted from Edwards et al. [1999], Kocher et al. [2005] and Table 5.2 of the NSCR2012 report. Values in brackets are the 66% confidence interval, approximately corresponding to one standard deviation. Values in parentheses for Grahn et al. [1992] correspond to the number of days after irradiation when tumors were assessed. Multiple RBE values for the same system arise from differing analysis methods.

Source	Endpoint	System	RBE_{max}
Upton et al. [1967][1,2]	Life-shortening	Male RF/Un mice	40 [10, ∞] 140 [30, ∞]
		Female RF/Un mice	3.5 [2, 4.5] 15 [5, 55]
Storer et al. [1979][1,2]		RFM mice	7.5 [6.7, 8.3]
Storer and Ullrich [1983][1,2]		BALB/c mice	15 [12, 18]
Carnes et al. [1989][1-3]		Male B6CF1 mice	50 [35, 65]
		Female B6CF1 mice	45 [34, 56]
Di Majo et al. [1996][3,4]		Male CBA/Cne mice	24 [16, 31]
		Female CBA/Cne mice	8.6 [8.0, 9.2]
Edwards et al. [1999][1-3]	Myeloid leukemia	RF/Un mice	19 [9, 38]
	Lymphoma		4.7 [2.7, 5.6]
	Thymic leukemia	Female RFM mice	29 [12, 64]
	Harderian gland tumor		33 [22, 47]
	Pituitary tumor		120 [17, ∞]
	Lung adenocarcinoma	Female BALB/c mice	20 [12, 30]
	Mammary tumor	Female BALB/c mice	27 [18, 41]
	Myeloid leukemia	CBA/H mice	21 [14, 36]
Grahn et al. [1992][1-3]	Lymphocytic tumors	Male B6CF1 mice (600-799)	6.6 [4.8, 8.4] 20 [15, 25] 12 [8, 16] 36 [23, 49]
		Female B6CF1 mice (600-799)	8.4 [7.7, 9.1] 17.8 [16.3, 19.3]
		Male B6CF1 mice (800-999)	9.7 [8.2, 11.2] 25.2 [22, 28.4]
		Female B6CF1 mice (600-799)	8.5 [6.7, 10.3] 15.8 [13.2, 18.4]
	Vascular tissue tumors	Male B6CF1 mice (600-799)	13.9 [11.3, 16.5]
		Female B6CF1 mice (600-799)	7.2 [4.0, 10.4]
		Male B6CF1 mice (800-999)	13.7 [12.1, 15.3]
		Female B6CF1 mice (800-999)	8.9 [6.9, 10.9]
	All epithelial tissue or ovarian tumors	Male B6CF1 mice (600-799)	23 [18, 28] 45 [38, 52]
		Female B6CF1 mice (600-799)	23 [19, 27]
		Male B6CF1 mice (800-999)	14.4 [11.5, 17.3] 31 [26, 36]
		Female B6CF1 mice (800-999)	19 [13, 25]
Wolf et al. [2000][3]	Lethal tumors	Male SD rats	>50
Lafuma et al. [1989][3]	Lung tumors	Male SD rats	>50
Shellabarger et al. [1980][3]	Mammary tumors	Female SD rats	>50

[1] Also found in Edwards et al. [1999].
[2] Also found in Kocher et al. [2005].
[3] Also found in Table 5.2 of the NSCR2012 report.
[4] 250 kVp X-rays were used as a reference radiation for RBE_{max} calculations.

Another source of information allowing inferences to be made about the biological effectiveness of neutrons can be found within the LSS cohort - a human population exposed to a mixed gamma-neutron exposure. The dose-response for cancer incidence or mortality in the LSS cohort is based on the estimated colon dose as [Cordova and Cullings 2019]

$$D_{colon} = D_{\gamma} + w_n D_n, \tag{24}$$

where D_γ is the gamma dose (Gy), D_n is the neutron dose (Gy), and the neutron weighting factor, or RBE, is traditionally taken as $w_n = 10$. Walsh [2013] found more accurate ERR models were achieved with a neutron RBE of 65 with a 95% confidence interval of 11 – 170. Cordova and Cullings [2019] also analyzed the LSS cohort and found a neutron RBE of 80 with a 95% confidence interval of 20 – 190 yielded the most accurate ERR. Though informative, it is important to remember that these inferences represent indirect and uncertain measures of neutron effectiveness.

Lastly, limited high LET human exposure data are considered for comparative purposes. Human epidemiological data associated with high LET radiation are sparse and primarily confined to previously discussed LSS neutron exposures and α emitters such as uranium, plutonium, and radon. There are key differences in the exposure profiles associated with space radiation and terrestrial α emitter exposures, as discussed previously in Section 5.7.2.1 and the NSCR2012 report. Nevertheless, available RBE for α radiation derived from human epidemiological data will be compared to the NSCR2025 QF in a later section.

In ICRP 150 [ICRP 2021], the biological effectiveness of α particles produced from plutonium for lung cancer mortality was estimated on the basis of the Mayak worker cohort [Gillies et al. 2017]. Their estimates range from 16 – 21 for acute intakes depending on whether absolute or relative risk models are assumed. Biological effectiveness for α particles produced from radon was estimated in the same report as 14. These values will be compared to NSCR2025 QF at an LET of 90 keV/μm, corresponding to a 1.15 MeV/n ^{4}He ion, later in this report.

5.7.3.2. Multi-Model Ensemble Dose-Response Model

Various global dose-response models have been developed to describe experimental data obtained from exposures involving mono-energetic ions of interest to space radiation carcinogenesis [Katz et al. 1971, Cucinotta et al. 2013b, Chang et al. 2016, Slaba et al. 2025a, Xu et al. 2026]. Ideally, one global dose-response model exhibiting superior performance could be identified, providing clear justification for its use as the basis for RBE_{max} calculations and QF development. This requires either a single standard dataset upon which the performance of all dose-response models can be evaluated systematically, or a single dose-response model that performs optimally across a range of experimental systems and endpoints. At this time, neither of these requirements have been realized due to incomplete mechanistic understanding [Patel et al. 2020] and data limitations discussed in the previous section.

Multi-model ensemble methodologies offer an alternative solution to the one-model paradigm with several advantages [Simonsen and Slaba 2021; Stabilini et al. 2023]. Multi-model ensembles offer a means to robustly determine central tendencies for sparse biological response data across the relevant range of doses and particle types. An ensemble framework provides a foundation to objectively propagate uncertainties originating from experimental data and dose-response models into RBE_{max} calculations and QF. New data and models can be integrated into the ensemble, allowing emerging knowledge and evidence to be incorporated as they become available.

In this section, an ensemble dose-response model framework is presented, calibrated, and compared to the three global experimental datasets identified in Table 6. A simplified ensemble (noNTE) is considered where NTE contributions and microdosimetric (μD) models [Slaba et al. 2025a] are excluded. Both NTE and μD models give rise to non-linear behavior at low dose such that calculated RBE often increase without bound at the lowest doses. The use of RBE_{max} as the basis for QF therefore necessitates that these terms be excluded. Performance comparisons are then made between the full and simplified noNTE ensembles to provide an assessment of the impact of low dose non-linearity within the context of available models and experimental data used for QF development. Finally, the simplified noNTE ensemble is used to calculate RBE_{max} over a broad range of particle types for each of the three experimental datasets.

The ensemble dose-response model employed in this work is described in detail by Slaba et al. [2026]; a condensed summary is provided throughout this section. The ensemble is based on a generalized framework that includes three biologically interpretable components: targeted effects (TE), NTE, and cell-killing/sterilization (CK). TE refer to biological responses originating from sensitive targets such as cell nuclei that received non-zero energy deposition from the exposure. NTE refer to biological responses originating from unirradiated targets through microenvironment perturbations or other signaling pathways [Shuryak and Brenner 2020]. CK refers to sensitive targets that were sufficiently irradiated to inhibit proliferative processes, thereby removing their ability to contribute directly to observable carcinogenic outcomes.

The generalized dose-response model, R_G, quantifies an observable excess biological response (e.g., tumorigenesis above unirradiated controls) as a function of ion beam dose, D (Gy), and is written as

$$R_G(D;\mathbf{B}) = [R_{TE}(D;\mathbf{B}) + R_{NTE}(D;\mathbf{B})]R_{CK}(D;\mathbf{B}), \tag{25}$$

where **B** denotes the set of information describing the ion beam (energy, mass, charge, LET, etc.). In equation (25), R_{TE}, R_{NTE}, and R_{CK} are the dose-response components representing TE, NTE, and CK, respectively. The response functions R_G, R_{TE}, and R_{NTE} have the same units carried by experimental data, while R_{CK} is dimensionless. As an example, in the case of Harderian gland tumorigenesis, the response units would be prevalence (%).

An ensemble member is defined by selecting a TE, NTE, and CK model from a prescribed set of options. There are 21 TE, 5 NTE, and 2 CK model options available for consideration within equation (25). Every ensemble member contains a TE component, since dose-response models including only NTE and CK can be generally viewed as implausible within the context of experimental datasets analyzed herein. Consideration is given to cases where NTE and/or CK contributions are neglected, as studied elsewhere [Chappell et al. 2020; Slaba et al. 2025a, 2026]. Combining all possible combinations of TE, NTE, and CK models along with the cases where NTE and CK are neglected yields 378 ensemble members. Subsets of the full ensemble are considered which neglect NTE contributions and μD models for gamma and ion exposures allowing evaluation of RBE_{max}. The simplified noNTE ensemble contains 45 dose-response model members for ion exposures and 4 dose-response model members for gamma exposures. Details for all of the ensemble components and member models can be found in Appendix A.

Two key features distinguish the various model options. First, the models for each component may depend on beam dose, beam fluence, or microdosimetric quantities, inducing distinct dose-response shapes and affecting the overall magnitude of calculated RBE. Second, the models for each component may contain distinct particle type and energy dependencies, affecting the global behavior of calculated RBE as a function of particle type.

The TE models can be organized into groups according to their underlying dose-dependence. There are linear dose (L_D), linear-quadratic dose (LQ_D), and linear fluence (L_ϕ) models. The L_D and LQ_D options include various forms of an LET-dependent linear-induction coefficient, α, inspired by the work of Chang et al. [2016]. The linear fluence options utilize forms of the Katz cross section [Katz et al. 1971] where one or more parameters have been fixed to values used in the NSCR2012 quality factor [Cucinotta et al. 2013b]. The μD model is based on an integral equation involving a biological weighting function folded with energy deposition spectra [Slaba et al. 2025a]. The spectra are calculated from extensive track structure simulations using RITRACKS [Plante and Cucinotta 2011] and represent the distribution of energy depositions received by microscopic spherical targets (1 μm – 10 μm) in ion beam irradiations. The model produces non-linear dose-responses, and beam dependency is embedded in the underlying μD quantities derived from track structure simulations. The μD options reflect different cell nuclei population groupings and spherical nuclear radii. The multilevel probability (mP) model considers probabilistic arguments at both cell and tissue niche levels, resulting in a non-linear fluence-based model with an LET dependency [Xu et al. 2026].

The NTE models include dose-independent step functions (sharp turn-on of NTE effects for non-zero doses) with beam-independent (Step) and beam-dependent ($Step_{LET}$) options [Chang et al. 2016]. The Asymptotic model is a beam-independent exponential dose function that saturates at high dose [Shuryak et al. 2017a, 2022]. The mP models are based on multilevel probabilistic concepts including both dose and beam dependencies [Xu et al. 2026]. Finally, in the case of CK, the commonly used exponentially decaying dose model is used with both beam-independent (Exp) and beam-dependent (ExpLET) forms [Chang et al. 2016].

Performance-based objective weighting factors [Stabilini et al. 2023] are used to combine members and their uncertainties. The weighting factors are based on the Akaike Information Criterion (AIC) [Akaike 1972] that quantifies model performance against experimental data and includes penalty terms associated with the number of adjustable parameters (i.e., models are increasingly penalized as the number of adjustable parameters grows). The ensemble dose-response for a specific biological endpoint is calculated as a weighted sum of the member models according to

$$R_{ensemble}(D;\mathbf{B}) = \sum_m w_m R_G^{(m)}(D;\mathbf{B}), \tag{26}$$

where $R_G^{(m)}(D;\mathbf{B})$ is the m^{th} ensemble member and w_m is the corresponding member model weight. The weights are defined as [Stabilini et al. 2023]

$$w_m = \frac{\exp[-\frac{1}{2}(\mathrm{AIC}_m - \mathrm{AIC}_{\min})]}{\sum_k \exp[-\frac{1}{2}(\mathrm{AIC}_k - \mathrm{AIC}_{\min})]}, \tag{27}$$

where AIC_m is the Akaike Information Criterion [Akaike 1972] value for ensemble member model m, and AIC_{min} is the minimum AIC_m value over all ensemble members. The denominator ensures that the sum of all ensemble member

model weights is unity. Each AIC_m value is obtained by comparing the calibrated ensemble member model to experimental dose-response data for the biological endpoint of interest. The AIC is related to the logarithm of the sum of square errors (SSE) and includes a penalty term for the number of adjustable model parameters.

Parameter calibration and uncertainty quantification for each ensemble member was performed separately for each experimental dataset using the same method described in previous work [Slaba et al. 2025a]. The final uncertainty distribution for the ensemble accounts for statistical measurement error as well as the spread in member model predictions (sometimes referred to as model-form error), and parameter correlations are retained.

Results from calibration of the full ensemble and simplified noNTE ensemble to three available datasets are provided in Figure 17 - Figure 19. The top panel in each plot is for the full ensemble, and the bottom panel is for the simplified noNTE ensemble. The three dose-response components (TE, NTE, CK) appear as headers at the top of each plot. Model options for each component are arranged in columns beneath the appropriate header. Boxes under the NTE and CK components labeled as "None" indicate these components were excluded. Each line in the plot represents an ensemble member passing through a set of component model options. The color of each line reflects the member weight, w_m; numerical values for the colors are shown in the contour legend in each plot. Gray lines correspond to ensemble members with negligible weight (i.e., low performance). Numbers appearing above (beside, in the case of TE) component options represent the cumulative weight of all ensemble members passing through the option. Accordingly, the numbers in a given column sum to unity.

In Table 9, summary performance statistics are provided to facilitate a quantitative comparison between the full and noNTE ensembles. The full ensemble dose-response model provides marginally better performance, as indicated by consistently lower SSE values and higher correlation coefficients (R^2) for all three datasets. The magnitude of the average relative difference (R_d) and Chi-square (χ^2) values are smaller for the noNTE ensemble for some endpoints. These seemingly mixed performance results are attributable to scatter and sparsity in the data along with experimental gaps at both low and high dose [Slaba et al. 2025a].

The full ensemble member weights for Harderian gland tumorigenesis (Figure 17A) are broadly distributed across the available model options. The largest single member weight was found to be 0.07 – associated with a μD TE model combined with the LET-dependent mP NTE model and a simple exponential CK model. Additionally, 159 members were needed to achieve a cumulative weight of 0.99 (i.e., 99% of the ensemble). These findings are reflective of sparse and uncertain experimental data allowing disparate dose-response model formulations to achieve comparable performance.

It can also be seen in Figure 17A that the μD model options account for a significant fraction of the TE member weights (0.658), and ensemble members with NTE corrections included account for 0.938 of the total ensemble weight as compared to only 0.062 for the None NTE option. These features collectively imply that models with non-linear low dose behavior, arising either from μD or NTE considerations, outperform models lacking such features for this dataset. This finding is confirmed in Table 9, where it is seen that the full ensemble performance metrics are generally superior to the simple noNTE ensemble metrics.

The simplified noNTE ensemble weights for Harderian gland tumorigenesis (Figure 17B) are broadly distributed across the available TE options and tightly clustered through a single CK option (Exp). The linear dose and mP TE models combined account for 0.73 of the member weights, while the linear-quadratic and fluence-based approaches contribute smaller individual fractions. RBE_{max} values derived from the simplified noNTE ensemble will therefore be heavily influenced by the linear and mP TE models – both of which express particle type dependency with LET-based functions.

In Figure 18A, full ensemble member weights for blood lymphocyte chromosome aberrations are tightly clustered to linear and linear-quadratic TE options, accounting for 0.999 of the total weight. The largest single member weight was found to be 0.228 – associated with a linear dose TE model without any NTE or CK corrections. Only 15 members were required to achieve a cumulative weight of 0.99. Weights are focused through the None CK option, likely reflecting the fact that aberrations are assessed before first cell division, where significant cell killing occurs due to lethal aberrations, and the lack of high-dose experiments in the dataset which would elicit greater impacts from interphase cell death. The necessity of NTE corrections is difficult to ascertain in this dataset. The None option is the single largest weight for the NTE component (0.342), but all other NTE options combined account for 0.658 of the total weight.

Performance metrics in Table 9 are also mixed for this endpoint. The full ensemble has a lower SSE and marginally higher R^2 compared to the simplified noNTE ensemble, but the χ^2 value is lower for the simplified noNTE ensemble. These mixed performance results reflect uncertainty and scatter in the underlying experimental data. One notable source of uncertainty is the use of different blood donors for experiments conducted years apart [Poignant et al. 2025].

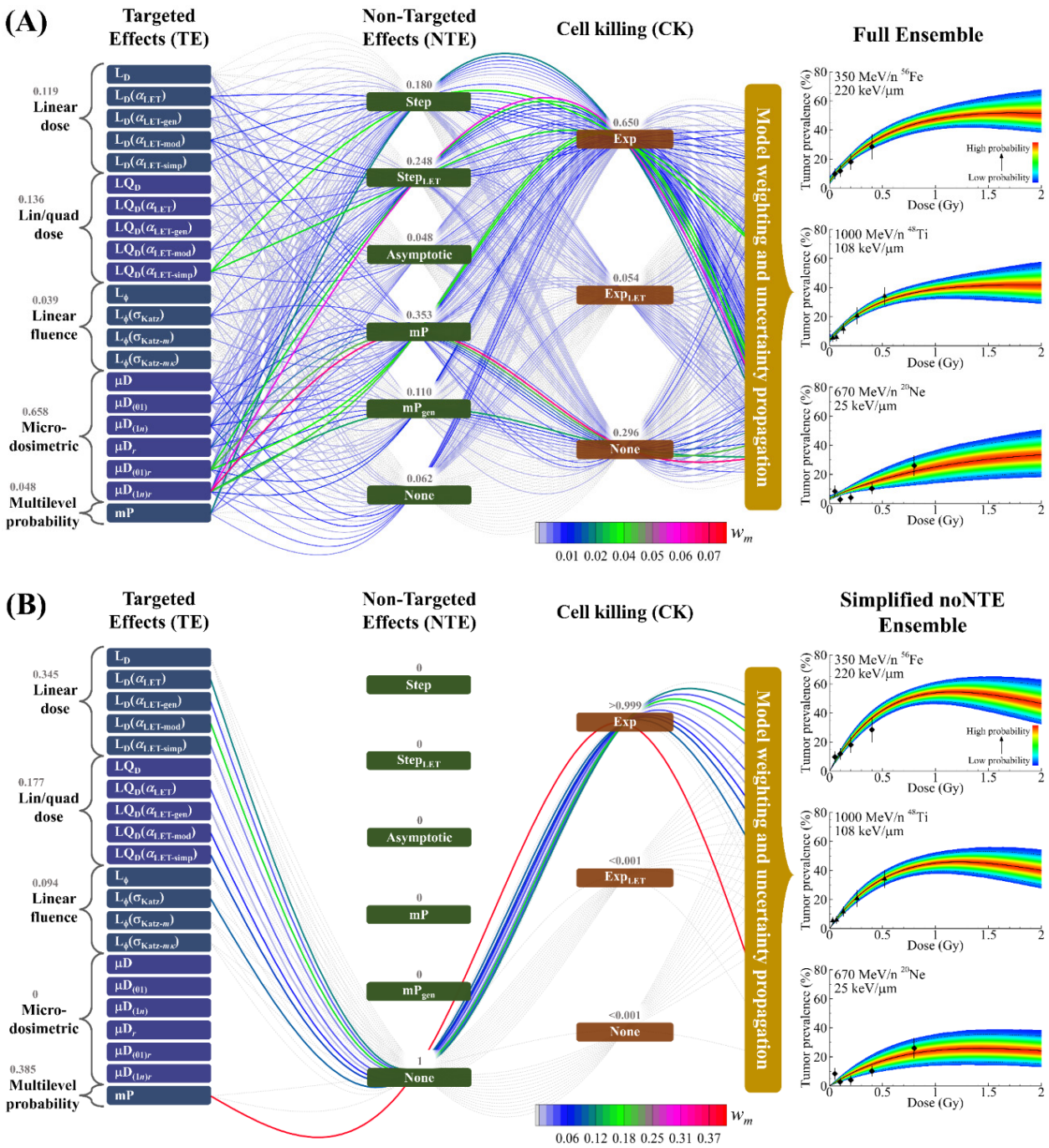

Figure 17. Ensemble dose-response model map for Harderian gland tumorigenesis. Results for the full ensemble are in the top panel (A), and results for the simplified noNTE ensemble are in the bottom panel (B). Each line in a map represents an individual ensemble member as a path through the model options for each component. Colors indicate the member weight value, w_m. Dashed gray lines represent ensemble members with a weight in the lowest 1st percentile. Numbers appearing above (beside, in the case of TE) component options represent the cumulative weight of all ensemble members passing through the option. The three plots on the right illustrate the mean (solid line) and 95% confidence level (dashed lines near the boundary of the blue regions) ensemble dose-response results along with dose-dependent uncertainty distributions (contour heat map) and corresponding experimental data from Alpen et al. [1993] (diamonds) and Chang et al. [2016] (triangles) for selected beams.

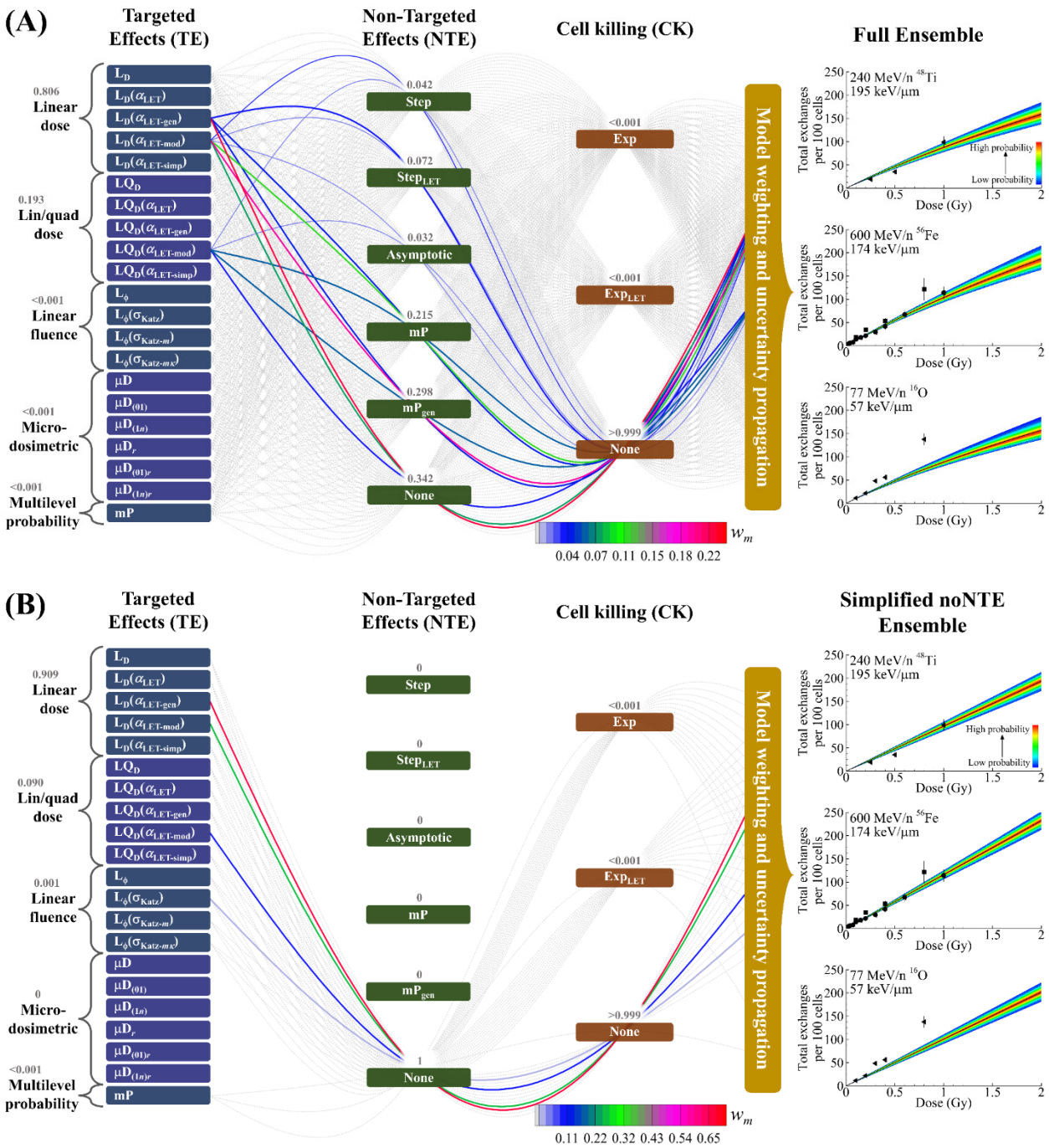

Figure 18. Same as Figure 17 but for total chromosome aberrations in human blood lymphocytes. Experimental data are from George et al. [2007] (squares), George et al. [2013] (left triangles), and Hada et al. [2014] (circles).

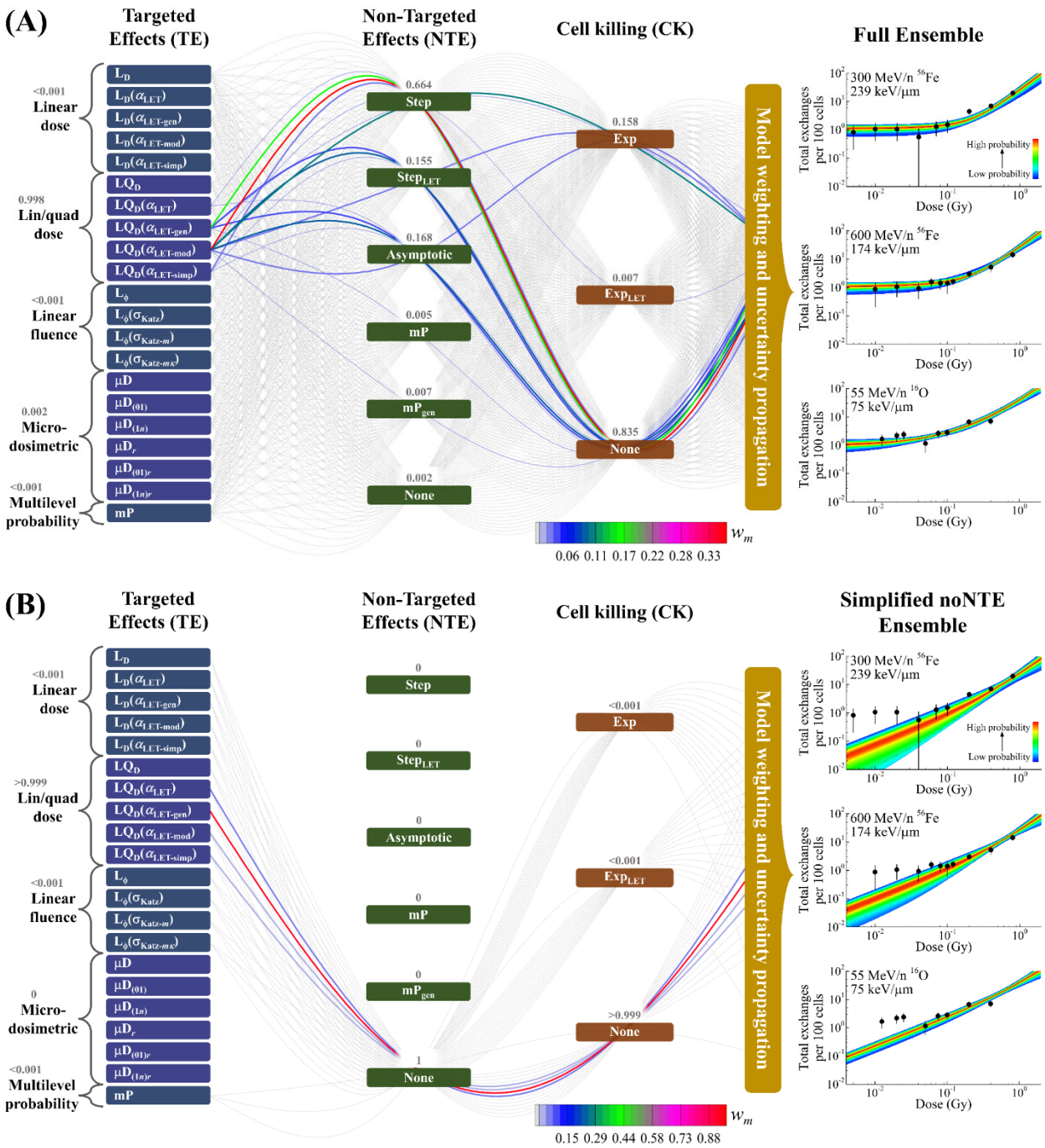

Figure 19. Same as Figure 17 but for total chromosome aberrations in human skin fibroblasts. Experimental data are from Hada et al. [2014] (circles).

Table 9. Summary performance statistics for the full and simplified noNTE ensembles. SSE is the sum of square errors, R^2 is the correlation coefficient, χ^2 is the Chi-square value, and R_d is the average relative difference.

Statistics	Harderian gland tumorigenesis		Blood lymphocyte chromosome aberrations		Skin fibroblast chromosome aberrations	
	Full	noNTE	Full	noNTE	Full	noNTE
SSE	861.7	1109.5	62941.2	64439.9	62.9	84.5
R^2	0.894	0.864	0.890	0.887	0.981	0.975
χ^2	40.5	57.5	2286.9	2175.0	94.8	79.3
R_d	0.10	-0.02	0.20	0.16	0.13	-0.32

The simplified noNTE ensemble weights for blood lymphocyte chromosome aberrations (Figure 18B) are dominated by a linear dose TE model with no NTE or CK corrections. Thus, the RBE_{max} values derived from the simplified noNTE ensemble in this case will be driven by the linear dose model and associated LET-dependent induction coefficient.

Results for skin fibroblast chromosome aberrations are provided in Figure 19. The weights for the full ensemble (Figure 19A) are tightly clustered through linear-quadratic TE options (0.998) combined with various NTE options. The largest single member weight was found to be 0.366 – associated with a linear-quadratic dose TE model with a simple NTE model and no CK correction. Only 18 members were required to achieve a cumulative weight of 0.99. Enhanced performance of the linear-quadratic dose-response models is likely a consequence of data limitations. The quadratic dose term is often attributed to responses at higher doses where the probability of more than one event (ionization, track, etc.) occurring in a sensitive biological site is amplified [UNSCEAR 1993]. In this case though, experimental emphasis in the low-dose regime causes a response shape that is apparently best described by a linear-quadratic response. Correlations between the linear and quadratic components suppress the linear coefficient in favor of the quadratic term, which allows the upward curvature near 0.1 Gy to be described. For the CK component, a majority of the weight passes through the None option (0.835), although CK corrections cannot be completely ignored. A possible preference towards excluding the CK option is again likely attributable to the experimental endpoint estimated prior to first cell cycle and the experimental data which were focused in the low-dose regime characterized by less than one ion traversal per cell nucleus where cell-killing/sterilization effects are minimal [Hada et al. 2014]. The NTE component is mainly focused through three options, accounting for 0.987 of the total weight. Here again, it is surmised that emphasis in the low-dose regime for this dataset enhances the need for NTE corrections to describe biological responses that cannot be adequately explained by a TE-only paradigm. In Table 9, mixed performance results are once again found. The full ensemble has a lower SSE and marginally higher R^2 compared to the simplified noNTE ensemble, but the χ^2 value is lower for the simplified noNTE ensemble.

The simplified noNTE ensemble weights for skin fibroblast chromosome aberrations (Figure 19B) are dominated by a linear-quadratic dose TE model. Thus, the RBE_{max} values derived from the simplified noNTE ensemble in this case will be driven by the linear-quadratic dose model and associated LET-dependent linear induction coefficient.

There has been considerable analysis published on the topic of NTE [Cucinotta and Chappell 2010, Cucinotta et al. 2013b, Cucinotta and Cacao 2017, Chang et al. 2016, Chappell et al. 2020, Shuryak and Brenner 2020]; the present discussion will therefore be limited to the results in Figure 17 - Figure 19. It is observed that the None option (i.e., NTE component excluded) never dominates the cumulative NTE component weight, suggesting that the available NTE options enhance dose-response model accuracy, particularly at low-dose. Simultaneously, the None option is modestly weighted for the Harderian gland tumorigenesis and blood lymphocyte chromosome aberration datasets, suggesting that a purely TE paradigm cannot be discarded either. In the case of skin fibroblast chromosome aberrations, the None option is negligible. This finding may be influenced by the nature of the fibroblast dataset, which includes a large number of low-dose experiments but lacks mid- to high-dose observations that could enhance the relative impact of TE and CK components. Combining these observations and findings, we find that: (1) the ensemble weights are suggestive that NTE low-dose corrections provide enhanced accuracy for some datasets, but (2) models considering only TE cannot be fully disregarded, and (3) additional low-dose experimental data (less than one ion traversal per cell nucleus) and corresponding NTE model development efforts are needed to bring clarity.

The available experimental data for all three endpoints are sparse in comparison to the range of doses and particle types being represented by the various dose-response models, and the data are moderately scattered due to statistical and unquantified systematic uncertainties. Sparse and uncertain data obscure model calibration and subsequent performance assessments. The ensemble framework was developed for these reasons to robustly

characterize the central tendency of the available experimental data and de-emphasize the need for a single global optimal model across all relevant endpoints. If new datasets become available or advancements in mechanistic understanding are achieved, the ensemble framework also provides an infrastructure to assess the impact of such progress.

For gamma exposures, the ensemble was simplified to consider only linear and linear-quadratic TE options in conjunction with the Exp and None CK options. NTE options were not considered for gamma exposures, consistent with many prior analyses [George et al. 2003, Chang et al. 2016, Chappell et al. 2020]. This choice is also justified by experimental data limitations. Gamma doses in the three datasets were generally greater than or equal to 0.1 Gy, where NTE contributions likely make limited discernable contributions to biological responses. The gamma ensemble dose-response results are shown in Figure 20. For Harderian gland tumorigenesis, the ensemble was dominated by the linear-quadratic (w_m = 0.725) and linear (w_m = 0.245) TE options with the simple exponential dose CK option. For blood lymphocyte chromosome aberrations, the ensemble was dominated by the linear-quadratic TE models without (w_m = 0.525) and with (w_m = 0.456) the exponential dose CK option. For skin fibroblast chromosome aberrations, the ensemble was dominated by the linear TE models without CK (w_m = 0.994).

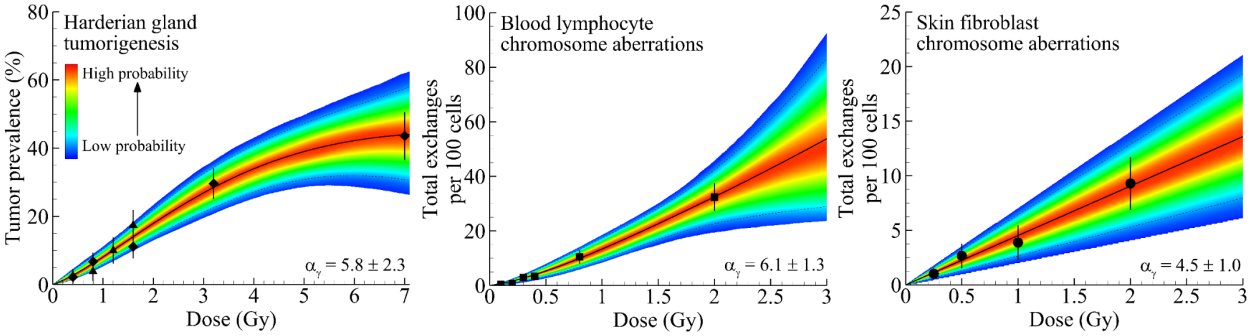

Figure 20. Ensemble dose-response model for gamma exposures for three different experimental datasets. The ensemble mean (solid black line) and 95% confidence level (dashed lines) are shown along with dose-dependent uncertainty distributions (contour heat map). The initial slopes for each endpoint used in RBE_{max} calculations are shown in the bottom right corner of each plot as the mean ± one standard deviation. Symbols with error bars represent experimental data from Alpen et al. [1993] (diamonds), and Chang et al. [2016] (triangles) for Harderian gland tumorigenesis; George et al. [2007] (squares) for blood lymphocyte chromosome aberrations; and Hada et al. [2014] (circles) for skin fibroblast chromosome aberrations.

The most striking feature is the apparently strong linear behavior of the skin fibroblast chromosome aberration response. The linear gamma response is surprising and inconsistent with other experimental results involving fibroblasts [Cornforth et al. 2002, George et al. 2009, Loucas et al. 2013]. Furthermore, the fibroblast dataset was developed specifically to focus on the dose-regime corresponding to ion fluences with <1 hit per cell nuclei [Hada et al. 2014]. The dataset lacks mid- to high-dose datapoints [Slaba et al. 2025a] that would influence the relative importance of TE, NTE, and CK components. Further discussion on the RBE_{max} values derived from the fibroblast dataset is provided in Section 5.7.3.4.

Lastly, the simplified noNTE ensemble was used to calculate dose-responses and RBE_{max} over a broad range of doses and particle types for each of the three endpoints. The mean RBE_{max} values (solid black lines) from the simplified noNTE ensemble dose-response model are provided in Figure 21 for all three endpoints. Contour distributions are used to visualize RBE_{max} uncertainties originating from experimental data and dose-response models within the ensemble. Dashed lines indicate the LET range encompassed by the underlying experimental data to identify regions where extrapolation is occurring.

The uncertainty contours in Figure 21 were obtained by utilizing the information generated within the calibration process for the ensemble dose-response model framework. Recall that each ensemble member was fit separately to 10^4 experimental data realizations which yielded the same number of correlated parameters sets. For gamma radiation, initial slopes are calculated from the ensemble using each of the 10^4 parameter sets, yielding a distribution of α_γ values. The process is repeated for ion exposures, but the result is a distribution of $\alpha_Z(L)$ curves over a prescribed LET range. A distribution of RBE_{max} curves is subsequently calculated by randomly sampling from the α_γ and $\alpha_Z(L)$ distributions and performing the calculation in equation (13).

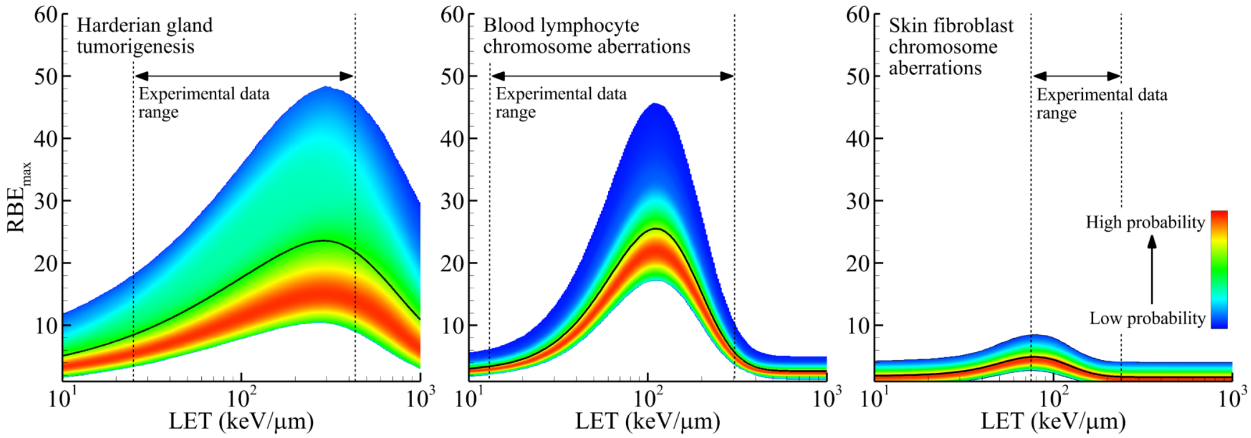

Figure 21. RBE_{max} as a function of LET calculated from the noNTE ensemble dose-response for Harderian gland tumorigenesis (left), blood lymphocyte chromosome aberrations (middle), and skin fibroblast chromosome aberrations (right). The dashed lines indicate the range of LET values encompassed by the underlying experimental data. The solid black line is the mean ensemble result. The contour is plotted within the 95% confidence level bounds for the mean ensemble result and is provided to help visualize the calculated RBE_{max} uncertainty distribution accounting for both statistical errors in the experimental measurements and variation of dose-response model results within the ensemble.

The Harderian gland results exhibit a peak RBE_{max} of about 23 near 274 keV/µm. Similar results are seen for blood lymphocyte chromosome aberrations, with the peak value being 26 near 111 keV/µm. The skin fibroblast chromosome aberration results appear markedly different, with a much smaller peak value of 4 near 70 keV/µm. For all three endpoints, the ratio between the upper 95% confidence level (top of the contour) and mean RBE_{max} values was found to be approximately a factor of two, with some dependence on endpoint and particle type.

The significantly smaller RBE_{max} values for skin fibroblasts are attributed to two main causes. First, the underlying gamma dose-response data exhibited a linear behavior, as shown in Figure 20. The linearity was found to be inconsistent with other fibroblast gamma radiation data [Cornforth et al. 2002, George et al. 2009, Loucas et al. 2013] and leads to an amplified linear induction coefficient compared to what would be obtained from data exhibiting the more expected linear-quadratic response. Second, the fibroblast ion data was highly focused in the low-dose regime corresponding to less than one hit per cell nuclei on average. This low-dose emphasis produced response shapes favoring linear-quadratic models, as shown in Figure 19 and discussed in Section 5.7.3.2. The quadratic dose term for ions is typically associated with multi-track interactions occurring at high dose [UNSCEAR 1993], but in this case mainly provides flexibility to describe curvature in the available data. Correlations between the linear and quadratic components suppress the linear coefficient in favor of the quadratic term, which allows the upward curvature near 0.1 Gy to be described. Combining these two causes, we find an unexpectedly reduced linear coefficient for ions and enhanced linear coefficient for gammas. It is clear from equation (13) then that such conditions necessarily yield smaller RBE_{max} values.

The fibroblast dataset encompasses particles ranging in LET from 75 – 239 keV/µm. Results in Figure 21 suggest a peak in the RBE_{max} curve exists near the lower end of this interval. Considering the limited LET range over which the fibroblast data exist along with the issues surrounding artificially reduced RBE_{max} values, it is concluded that the fibroblast dataset should not be used to guide or inform QF development at this time.

5.7.3.3. RITCARD

The simulation tool RITCARD [Plante et al. 2019a], formerly NASA Radiation Track Image (NASARTI) [Ponomarev and Cucinotta 2006; Ponomarev et al. 2008, 2010, 2012, 2014], has been developed for more than 20 years at NASA with the goal of better understanding and quantifying the effect of heavy ions on cellular endpoints related to cancer incidence, including DNA damage and the formation of chromosome aberrations.

RITCARD is a simulation-based tool and is therefore fundamentally different than the dose-response models incorporated in the ensemble framework described in the previous section. The tool provides a means of simulating biological responses such as chromosome aberrations for radiation conditions (i.e., different particle types, mixed fields, and dose-rates) where no data exists. By formulating hypotheses and evaluating endpoints that are

complementary to measurable quantities with current experimental techniques, RITCARD can also potentially refine the mechanistic understanding of the biological processes driving carcinogenesis, and the physical and biological parameters affecting radiation-induced responses.

In this section, RITCARD is described and a summary comparison to experimental dose-response data involving chromosome aberrations in cellular irradiations is provided. RITCARD is then used in Section 5.7.3.4 to simulate chromosome aberration yields for a range of doses, particle types, and cell nucleus sizes to facilitate RBE_{max} calculations.

In its original version, NASARTI used a random walk polymer model, with loop structures and chromosome domain constraints, to compute the 3D DNA distribution in nuclei, combined with an amorphous ion track model to compute DNA double strand breaks [Ponomarev et al. 2001; Ponomarev and Cucinotta 2006]. Early calculations showed that NASARTI could reproduce DNA fragment size distributions as measured by pulsed field gel electrophoresis following exposure to different ions [Ponomarev 2001, Ponomarev and Cucinotta 2006]. NASARTI was further utilized to investigate DNA DSB multiplicity for different radiation qualities within Radiation-Induced Foci (RIF) [Ponomarev et al. 2008, 2010], which are structures formed by proteins involved in the DNA damage response. RIF are experimentally measured by fluorescence microscopy, which lacks the resolution to quantify multiple clustered DSB within [Penninckx et al. 2021]—a marker of high LET radiation. NASARTI was also used to analyze DSB patterns for different radiation qualities within the HGPRT locus [Ponomarev and Cucinotta 2006, Ponomarev et al. 2008], a gene commonly used to evaluate somatic mutations in mammalian cells [Suzuki et al. 1996, 2003, 2006]. DNA damage repair models were later included in NASARTI, allowing for the computation of chromosome aberrations as measured by Fluorescence In Situ Hybridization (FISH) for normal human cells and repair-deficient human cells [Ponomarev et al. 2012, 2014].

RITCARD emerged as new software following extensive restructuring of NASARTI [Plante et al. 2019a]. One of the major advancements in RITCARD was the use of the track-structure simulation tool RITRACKS [Plante and Cucinotta 2008] in place of the amorphous track-structure model employed in NASARTI. In subsequent work, the model of DNA repair was updated [Plante et al. 2019b], improving the predictions of simple exchanges (chromosome exchanges involving two breaks) in human fibroblasts for both monoenergetic ions [Plante et al. 2019b] and mixed field exposure behind shielding [Slaba et al. 2020b]. Recent research efforts have since focused on improving RITCARD predictions of aberrations measured by FISH in both fibroblasts and lymphocytes [George et al. 2003, 2007, 2013, 2015; Hada et al. 2014].

In a preliminary benchmarking study [Poignant et al. 2022], the effect of nuclear geometry and DNA distribution within the nucleus were shown to have a major impact on aberration yields, suggesting such nuclear properties—which vary with cell types—are key biological factors influencing radiation-induced cell response. Nevertheless, the yield of complex exchanges (exchanges involving more than two breaks) was found to be overestimated by RITCARD for fibroblasts and lymphocytes. It was suggested that such discrepancies might be due to the experimental use of partial staining of the whole genome and detection limitations of small chromosome fragments not accounted for in RITCARD. Subsequent work introduced these experimental features, as well as a new model of DNA distribution relying on High-throughput Chromosome Conformation Capture (Hi-C) experimental data, providing a more realistic 3D DNA architecture [Poignant et al. 2025]. With these improvements, RITCARD demonstrated excellent predictions of total exchange yields, with the exception of low LET radiation. Remarkably, large differences between the aberration yields of lymphocytes and fibroblasts that are experimentally observed were, in the simulation, driven primarily by the differences in nuclear geometries.

In the current RITCARD version [Poignant et al. 2025, 2026], the 3D distribution of the Topological Associated Domains (TAD) within a nuclear geometry is generated with G-NOME using Hi-C data [Ingram et al. 2020] and is then combined with a random expansion algorithm within TAD structures to obtain the distribution of cubical DNA voxels (side length: 20 nm, DNA content: 2,000 bp) utilized by RITCARD. In parallel, RITRACKS is used to generate the irradiation of a water volume encompassing cell nuclei by monoenergetic, monodirectional ion beams. For a given irradiation dose D (Gy), the number of ion tracks is sampled from a Poisson distribution with mean value $\lambda = 6.24DA/L$, where L is the LET (keV/μm), and A (μm^2) is the irradiation area. Periodic boundary conditions are applied to secondary electrons to mimic the contribution of long range δ-electrons generated by distant tracks not explicitly simulated. At the end of the simulation, energy deposition events (ionization or excitation of water molecules by ions and secondary electrons) located within DNA voxels are recorded.

Next, DNA damages are computed following an algorithm proposed by others [Francis et al. 2011]. First, energy deposition events are randomly sampled to account for the fact that not all energy deposition events interact with the DNA structure, using a probability $p_s = 0.3$ (0 means no events are selected, 1 means all events are selected). For selected events, the probability of inducing a strand break (SB) is equal to 0 for energy less than 5 eV and linearly increases to 1 up to an energy of 37.5 eV. SB are randomly assigned one of the two DNA strands with equal

probability. SB within 3.2 nm from one another (~10 bp) are clustered together. A DSB is formed if a cluster contains at least two SB on opposite strands and within 10 bp. A DSB is considered complex if it contains more than two SB in the cluster.

Finally, the repair of DNA DSB is modeled during a time period following a bi-exponential decay. Simple and complex breaks each generate two free ends that are repaired with fast ($\tau_1 = 1.7$ h) and slow ($\tau_2 = 23.7$ h) time repair constants, respectively [Plante et al. 2019b]. The repair algorithm proceeds by small time steps δt during which repair attempts are made for all free ends. Simple free ends are assumed to either repair properly with a probability equal to $\delta t/\tau_1$ or remain unrepaired. Complex free ends can either repair with any other complex free ends with a probability equal to $\delta t/\tau_2$, or remain unrepaired. The rate, I, of any two complex free ends to repair is a function of their Euclidian distance, r,

$$I = e^{-r/\sigma}, \tag{28}$$

where $\sigma = 0.5$ μm. The misrepair rates between a given free and all other free ends is computed according to equation (28) and stored in a list. During a repair event, a pair of free ends is randomly chosen based on that list. At the end of the repair time, chromosome fragment sequences are analyzed for aberrations, as detailed elsewhere [Poignant et al. 2025]. To accurately reproduce experimentally measured aberrations, different techniques and technical limitations can be implemented, including a detection threshold (any chromosome fragment below that threshold is considered undetected and not accounted for in an exchange), or the use of different painting probes (e.g., solid stain for Giemsa or chromosome painting of the whole genome [Loucas et al. 2013, 2016] or a subset of the genome [George et al. 2003, 2013, 2015; Hada et al. 2014; Plante et al. 2019a] for FISH).

Ongoing research efforts have focused on updating the RITCARD DSB model—described in the previous paragraph—to better align with predictions of track-structure tools with atomic scale DNA models [Thompson et al. 2024] and performing a parameter optimization to improve low LET predictions [Poignant et al. 2026]. The results obtained from RITCARD with the new DNA damage model and parameter optimization are displayed in Figure 22. Simulation predictions match experimental data well, especially for high LET (darker purple symbols) radiation. Discrepancies are seen for low LET radiation (yellow/green symbols), as already discussed, and for cases at very low dose, where experimental data exhibit larger error bars due to statistical uncertainties. Additional parameters are currently being tested to further improve RITCARD predictions.

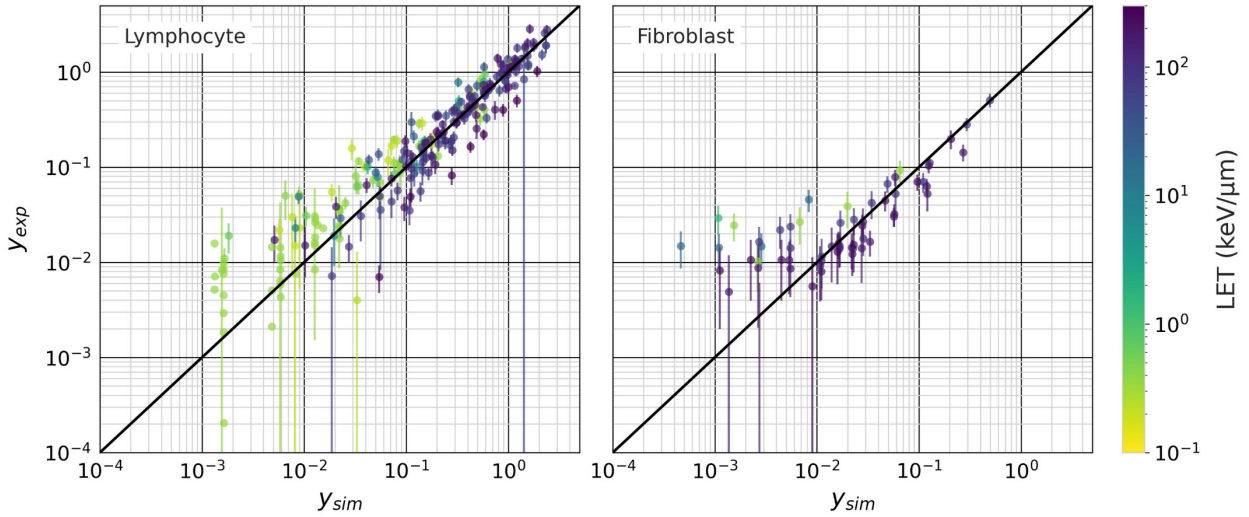

Figure 22. RITCARD simulation results (y_{sim}) vs. experimental data (y_{exp}) for the yield of total exchanges per cell for lymphocytes (left) and fibroblasts (right). Experimental data are from [George et al. 2003, 2007, 2013, 2015; Hada et al. 2014, Plante et al. 2019a].

In this work, RITCARD simulations were performed over a broad range of doses, particles, spherical cell nucleus size, and aberration types (see Appendix B for details). The simulated dose-response results from RITCARD were then analyzed to facilitate RBE_{max} calculations. Three different nuclei were considered, using human B-

lymphocyte GM12878 Hi-C data and spherical geometries with radii, r_s = 3, 4 and 6 µm. DNA damage repair was modeled for a time period of 48 hours post-irradiation. Two endpoints were considered: (1) true first-metaphase total exchanges, calculated as the sum of simple and complex exchanges in all irradiated cells and (2) true stable total exchanges, calculated as the sum of simple and complex exchanges in cells carrying non-lethal aberrations only. The term "true" refers to the fact that all exchanges were accounted for, including those involving small fragments or intra-chromosomal rearrangements (e.g., inversion) that are typically undetectable with FISH but are relevant for cancer risk assessment, as these structural changes might be transmissible [Bailey et al. 2024]. Aberrations were classified as lethal when they induced asymmetrical structural changes to the chromosomes (dicentrics, rings and large (> 5 Mbp) fragments) [Loucas et al. 2022]. First-metaphase aberrations are aberrations measured prior to the cell going through the first cycle. Many of these aberrations are lethal for the cell and eliminated from the cell population due to failure at completing first or later mitosis due to incorrect separation of the genetic material. Measuring aberrations in cells containing only stable aberrations thus assesses genomic alterations that are transmissible.

RBE_{max} values obtained from RITCARD are displayed as a function of LET in Figure 23. Similar trends are obtained for first-metaphase and stable aberration RBE_{max}. Both the peak RBE_{max} values and LET at which this value is attained are dependent on the size of the nucleus. For first-metaphase exchanges, RBE_{max} peak values are in the range 27 (r_s = 3 µm) to 92 (r_s = 6 µm), closely matching estimates obtained by the ensemble model for FISH aberration data for lymphocyte cells for r_s = 3 µm. Results significantly differ from the ensemble model for FISH aberration data for fibroblast, arising from differences in nuclear geometry (fibroblasts have flattened ellipsoidal nuclei), the absence of a quadratic response for γ-irradiation for fibroblasts responsible for a high linear coefficient value, and the inclusion of aberrations in RITCARD that are typically not detectable by conventional FISH technique.

Stable exchanges have consistently lower RBE_{max}, with RBE_{max} peak values in the range 15 (r_s = 3 µm) to 67 (r_s = 6 µm). The complexity of an aberration, which is heavily influenced by ion LET, is a crucial factor determining its lethality. With a high rate of very complex aberrations, high LET ions are more likely to promptly kill the cells compared to low LET radiation, giving rise to lower RBE_{max} values compared to first-metaphase aberrations. RBE_{max} values obtained for r_s = 3 µm are close to those obtained for Harderian gland tumorigenesis (nuclear radius estimated at 2.76 µm), though the peak is found for a lower LET value. Many aberrations are lethal and thus non-transmissible, likely playing a limited role in carcinogenesis. Assessing stable aberrations might be a more relevant endpoint for cancer estimates.

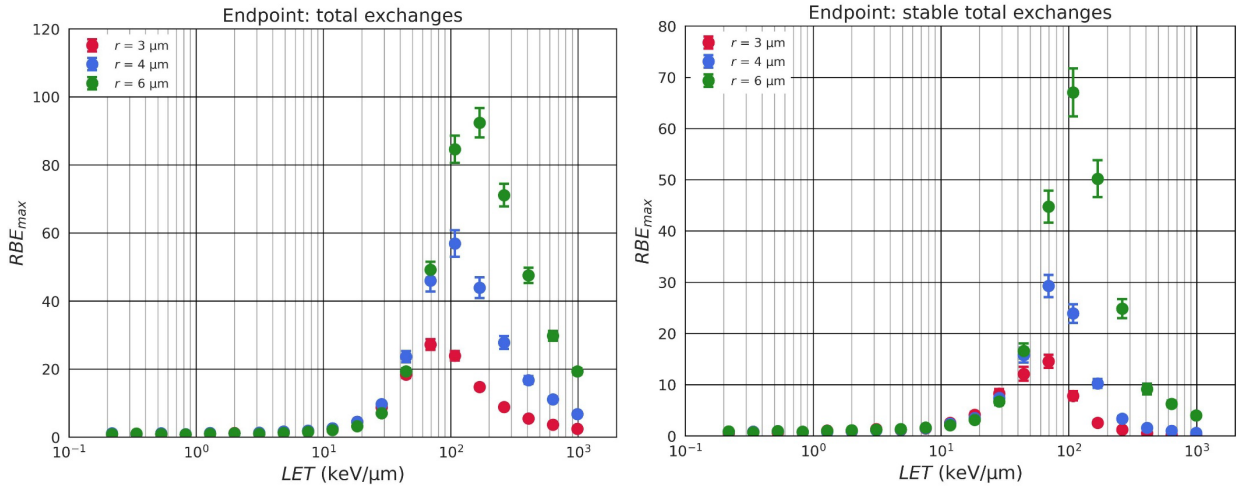

Figure 23. RBE_{max} as a function of ion LET displayed for first-metaphase true first-mitosis total exchanges (left) and true stable total exchanges (right). Results for the three different nucleus sizes are displayed in different colors.

The increase in RBE_{max} peak values for larger nuclear size is driven by two factors. For low LET, the yield of exchanges is systematically higher for smaller radii, resulting in larger α_γ values, due to a higher DNA density that favors misrepairs over proper repair. For high LET, higher yields are generally obtained for bigger radii, leading to larger α_Z values. A complex exchange counts as one exchange regardless of how many chromosomes are involved. A high-LET ion track generates clustered DSB within multiple chromosomes. For small nuclei, this favors intra-chromosomal misrepairs that form a small number of exchanges with many chromosomes. For larger nuclei, DSB generated along ion track created in distinct chromosomes are more likely to be farther from one another as the

chromatin is more spread out. This favors the formation of a higher number of separate exchanges, each involving a lesser number of chromosomes compared to smaller radii. Both small and larger nuclei are found to generally have a similar number of chromosomes involved in exchanges and only differ in the clustering of chromosomes within one exchange. The combination of larger α_γ—due to a higher rate of misrepair—and lower α_Z—due to a reduced number of exchanges with increased complexity—for smaller radii yields large differences in the amplitude of RBE_{max} values.

LET values at which the RBE_{max} peaks are also dependent on the nucleus size and obtained at 70.0 keV/µm for r_s = 3 µm, 70.0 – 109.0 keV/µm for r_s = 4 µm and 109.0 – 169.8 keV/µm for r_s = 6 µm for the set of simulated ions. The decline beyond a given LET threshold is due to two factors. First, an increased amount of energy is deposited along the ion track that, rather than creating additional aberrations, creates aberrations that are increasingly complex and involve an increased number of breakpoints. Second, a decreasing number of ion tracks is required to reach a dose for increasing LET, leading to an increasing number of cells not being traversed by ions. This effect is size dependent, as the cross-sectional area of the nucleus is proportional to the squared radius. This combination creates the decline in α_Z values, and thus RBE_{max} values beyond a LET value, that depends on the nuclear radius.

The combined effects of ion charge, LET, and endpoint are illustrated in Figure 24. The figure displays RBE_{max} as a function of LET for ions with energy in the range 1 MeV/n – 1.6 GeV/n. For complex DSB (left panel), the LET value at which RBE_{max} peaks is ~300 keV/µm and not strongly affected by *Z*. However, the RBE_{max} amplitude notably varies with ion charge for similar LET, peaking at values in the range 10 (Fe ion) to 14 (C ion). This charge dependence is significantly reduced when looking at RBE for total exchanges (right panel). For this endpoint, the RBE_{max} peaks at 24 – 27 for all ions and at a lower LET value of about 70 keV/µm. These RITCARD simulation results are suggestive that the presence or absence of charge branching in RBE depends on the endpoint. In this case, the endpoint related to initial damage caused by the ion energy deposition (complex DSB) exhibits some degree of charge branching, while the endpoint allowing repair to occur after irradiation (total exchanges) exhibits no apparent charge branching. Similar results were demonstrated in Figure 2 of Sridharan et al. [2015], where ions with similar LET or $(Z^*/\beta)^2$ elicited γH2AX intensity dose-responses that were notably different at 2 h post-irradiation but highly similar at 24 h post-irradiation.

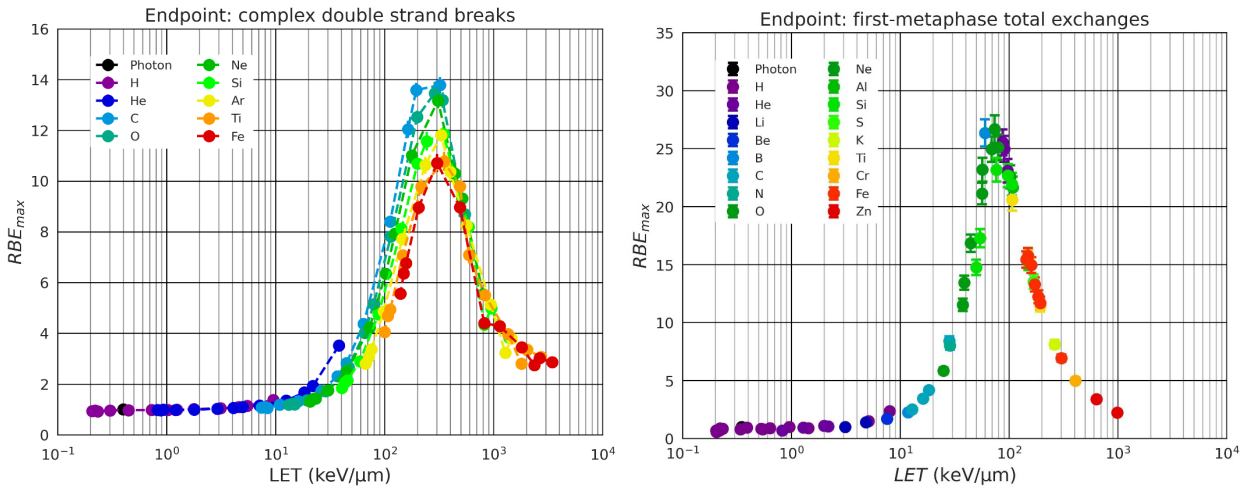

Figure 24. RBE_{max} as a function of ion LET displayed for complex DNA DSB (left) and first-metaphase true first-mitosis total exchanges (right). Results for the three different nucleus sizes are displayed in different colors. Results are provided for r_s = 3 µm.

5.7.3.4. Quality Factor

QF development proceeds by first adopting a parametric equation for $Q_{NSCR2025}$ to account for the four points of emphasis discussed at the beginning of Section 5.7.3 – particularly items (3) and (4) addressing the need for a QF with objective and robust uncertainties that can be integrated within probabilistic cancer risk projections and existing spaceflight dosimetry systems. Equation (15) is used for this purpose but with a modified action cross section inspired by a combination of the Katz model [Katz et al. 1971] along with LET-based formulations developed by Borak et al. [2014] and Xu et al. [2026] after the NSCR2012 report. The action cross section used here is written as

$$\Sigma(L) = \Sigma_0 P(L) + s_{sparse} \frac{\alpha_\gamma L}{6.24}, \tag{29}$$

$$P(L) = (1 - e^{-L/k})^\mu, \tag{30}$$

where k, μ, Σ_0, and s_{sparse} are adjustable parameters that will be discussed shortly. Replacing σ in equation (15) with $\Sigma(L)$ from equation (29) yields

$$Q_{\mathrm{NSCR\,2025}}(L) = \Sigma_{sparse} + \frac{6.24\Sigma_{0\gamma}}{L} P(L), \tag{31}$$

where $\Sigma_{0\gamma} = \Sigma_0/\alpha_\gamma$ (Gy-μm^2) controls the maximum value of QF, referred to hereafter as $Q_{\max}$. The location parameter k (keV/μm) primarily influences the LET value where $Q_{\max}$ is found, referred to as $L_{\max}$ (keV/μm). The shape parameter μ controls the decreasing slope of QF away from $Q_{\max}$. The parameter s_{sparse} represents the value of QF for sparsely ionizing radiation such as high energy protons with sufficiently low LET where $P(L) \to 0$. A nominal value of $s_{sparse} = 1$ is prescribed with a Gaussian uncertainty distribution having unity mean and standard deviation $\sigma = 0.15$, consistent with NSCR2012 [Cucinotta et al. 2013b]. This prescription is also conceptually consistent with the ICRP 60 QF where $Q = 1$ below 10 keV/um [ICRP 1991].

Equations (29) – (31) appear similar to the NSCR2012 equations (21) – (23) but differ in two ways. First, the $(1 - P)$ term previously attached to the sparsely ionizing component of the action cross section in equation (21) has been removed. It was determined through analysis and calibration to the global experimental datasets that the $(1 - P)$ term had no discernable impact on accuracy. Second, $P(Z,E)$ is replaced with a similarly formed $P(L)$. This replacement follows from previous discussion regarding the inability to distinguish between $(Z^*/\beta)^2$ or LET dependencies in the data directly underlying QF as well as the desire to develop a QF that can be integrated with existing spaceflight dosimetry systems.

Initial estimates for $\Sigma_{0\gamma}$ and k are guided by $L_{\max}$ and $Q_{\max}$ values obtained from the information collected in Table 10 from various sources. Rows with gray text indicate that the $Q_{\max}$ value is based on one or more alternative metrics such as RER, RBE at 50% survival, and/or RBE relative to X-rays. For example, RBE reported by Suman et al. [2016] were determined to be dose-dependent RER estimates for gastrointestinal tumors per mouse. RBE values from Yang et al. [1985] for neoplastic cell transformation in C3H10T1/2 cells were calculated at 50% survival relative to 250 kVp X-rays. Both Kiefer et al. [2001] and Cox and Masson [1979] utilized X-rays as the reference radiation for RBE calculations. These data are nevertheless utilized to inform $L_{\max}$, as differences in radiation quality metrics or reference radiation types are not expected to heavily influence identification of the most biologically effective particle.

$\Sigma_{0\gamma}$ is guided by relevant $Q_{\max}$ values presented in Table 10. It can be seen that $Q_{\max}$ derived from the ensemble dose-response analyses of the Harderian gland tumorigenesis and lymphocyte chromosome aberration datasets are quite similar (24 vs. 26). Lung tumorigenesis data from Chang et al. [2022] suggest a lower $Q_{\max}$ value of 9; further study is needed to determine if this is a tissue- and/or model-dependent outcome. The fission neutron data extracted from Table 8 corresponds to LET of ~70 keV/μm, but experiments suggest neutrons elicit responses commensurate with maximally effective charged particles [Borek et al. 1978, Fry et al. 1985]. Averaging $Q_{\max}$ values from the Harderian gland tumorigenesis and lymphocyte chromosome aberration ensemble analyses with the lung tumorigenesis and fission neutron results yields $Q_{\max} = 25$.

Remaining experimentally derived $Q_{\max}$ results in Table 10 associated with cell transformation and mutagenic endpoints are considered in uncertainty quantification procedures. Model-based assessments are similarly considered within uncertainty assignments. RITCARD $Q_{\max}$ estimates depend on the nuclear radius (and nuclear geometry, in general [Poignant et al. 2022]) and can extend to relatively large values. The ICRP 60 [ICRP 1991] definition of $Q_{\max} = 30$ is based on a more expansive set of doses, endpoints, and experimental systems that may not be as directly relevant for space radiation-induced carcinogenesis.

Table 10. L_{max} and Q_{max} values obtained from various sources. Q_{max} entries in bold text are obtained from RBE_{max} calculations; gray non-bold Q_{max} values are based on one or more alternative metrics such as RER, RBE at 50% survival, and/or RBE relative to X-rays.

Source		L_{max} (keV/μm)	Q_{max}
HG tumor prevalence (Figure 21, left)		274	**24**
Lymphocyte CA (Figure 21, middle)		111	**26**
GI tumors per mouse [Suman et al. 2016]		69	3 – 13[(1)]
Lung tumorigenesis [Chang et al. 2022]		108	**9**
Fission neutron tumorigenesis [mean from Table 8]		-	**29**
Fission neutron life-shortening [mean from Table 8]		-	**35**
C3H10T1/2 cell transformation [Yang et al. 1985]		142	6 – 10[(2)]
C3H10T1/2 cell transformation [Miller et al. 1995]		90	**19**
V79 Mutagenesis [Thacker et al. 1979]		155 ± 45	**18**
V79 Mutagenesis [Kiefer et al. 2001]		116	24[(3)]
HF19 Mutagenesis [Cox and Masson 1979]		90	7[(3)]
HSF Mutagenesis [Chen et al. 1994]		178	**6**
HE20 Mutagenesis [Suzuki et al. 1996, 2003, 2006]		131	**8**
RITCARD[(4)]	Total exchanges	69 – 168	**27 – 92**
	Stable exchanges	69 – 108	**15 – 67**
ICRP 60 [ICRP 1991]		100	**30**
Shafirkin et al. [2022]		100 – 200	**50**
NSCR2012	$Z = 1$	62[(5)]	**41**
	$Z = 2 – 8$	115 – 177[(6)]	**29 – 42**
	$Z = 9 – 14$	137 – 153[(7)]	**31 – 35**
	$Z = 15 – 28$	156 – 200[(8)]	**25 – 31**

[(1)] RBE reported in Suman et al. [2016] are dose-dependent RER estimates.
[(2)] RBE were calculated by Yang et al. [1985] for neoplastic cell transformation at 50% survival relative to 250 kVp X-rays.
[(3)] RBEmax values were calculated relative to X-rays.
[(4)] The range of RITCARD results encompass target radii, $r = 3 – 6$ um.
[(5-8)] Kinetic energies ranging from [(5)]0.3 MeV, [(6)]0.8 – 27 MeV/n, [(7)]34 – 92 MeV/n, [(8)]108 – 617 MeV/n.

NSCR2012 results have been separated into charge and energy groups to guide discussion. Q_{max} values of 25 – 31 are found for $Z = 15 – 28$ ions with kinetic energies between 108 MeV/n – 617 MeV/n. Reasonable agreement in Q_{max} values derived from the ensemble-analyses in this work and NSCR2012 is encouraging but also expected. Track structure effects are quite similar for these energetic $Z = 15 – 28$ ions and those underlying the Harderian gland and lymphocyte chromosome aberration datasets. The NSCR2012 QF values were also guided in part by a portion of the Harderian gland and lymphocyte aberration data available at that time, as already mentioned. At the same time, the Harderian gland and chromosome aberration RBE_{max} values for 600 MeV/n ^{56}Fe plotted in Figure 5.15 of the NSCR2012 report ($RBE_{max} = 27$ and 41) were found to be moderately larger than estimates from the ensemble analyses ($RBE_{max} = 22$). Such differences are small compared to overall QF uncertainties, but the systematic trend bears noting in relation to the initial assignments for $\Sigma_{0\gamma}$ and Q_{max}.

The NSCR2012 results for $Z < 15$ require further discussion. The Q_{max} values of 31 – 35 for $Z = 9 – 14$ occur between 34 – 92 MeV/n, corresponding to relatively high LET between 137 keV/μm – 153 keV/μm. No Harderian gland data were collected in this charge/energy domain, but there are three data points for lymphocyte chromosome aberrations. The beams are 64 MeV/n ^{20}Ne (103 keV/μm), 89 MeV/n ^{20}Ne (80 keV/μm), and 93 MeV/n ^{28}Si (152 keV/μm). RBE_{max} values calculated directly from the lymphocyte ensemble dose-response model for these beams fell between 22 – 25. In Table 5.3 of the NSCR2012 report, the RBE_{max} for 93 MeV/n ^{28}Si for the same endpoint is similarly reported as 22.1 ± 1.8. Thus, despite the larger predictions from NSCR2012 QF for lower energy $Z = 9 –14$ beams, the underlying data reflect RBE_{max} values closer to 22 – 25.

The Q_{max} values of 29 – 42 for $Z = 2 – 8$ occur between 0.8 – 27 MeV/n, also corresponding to relatively high LET between 115 keV/μm – 177 keV/μm. The closest data point in either experimental dataset was 55 MeV/n ^{16}O (75 keV/μm) for lymphocyte chromosome aberrations for which $RBE_{max} = 22$ is predicted by the ensemble dose-response model for this beam. Cox and Masson [1979] and Kiefer et al. [2001] investigated mutagenesis induced by low energy (<15 MeV/n) ion beams. Among their $Z = 2 – 8$ ion data, RBE_{max} values were found to be less than 25.

Complicating interpretation is the fact that both of these experimental datasets utilized X-rays as a reference radiation source; however, this issue is not expected to account for a factor of 3 – 4 uncertainty required to enhance mutational RBE up to the NSCR2012 QF values of 29 – 42.

Track structure and biophysical arguments were also put forward in the NSCR2012 report to support enhanced RBE_{max} values for these lower energy heavy ions. While these arguments are not without merit, the overall hypothesis of increasing Q_{max} for low energy ions between $Z = 2 – 8$ is not clearly validated by the experimental datasets underlying QF development, nor is it validated by the preponderance of low energy mutagenesis data.

It should also be noted that low energy (< 27 MeV/n) ions with $Z = 2 – 8$ primarily appear within humans behind shielding in space as a result of target fragmentation in sensitive tissues induced by energetic nucleons. The target fragmentation events produce an instantaneous multiplicity of low energy ions, neutrons and other particles that deposit significant energy within microns of the interaction site, leading to a spatial distribution of cellular damage different from what is elicited by the monoenergetic beams used in experimental studies. The impact of these differences on biological outcomes and RBE is not well known at this time but nevertheless represent an additional source of uncertainty that further clouds Q_{max} determination.

For $Z = 1$ ions, it is found that $Q_{max} = 42$ occurs at an energy of 0.3 MeV (62 keV/μm). There are no low energy proton data contained within the Harderian gland or lymphocyte datasets. Belli et al. [1998] assessed mutagenesis in low energy proton beams between 0.88 MeV and 3.24 MeV, yielding RBE_{max} values between 3 – 6. An X-ray reference source was also used in these experiments but is not expected to account for a factor of 5 – 10 uncertainty in RBE_{max} required to reach the NSCR2012 specification of 42.

Approximately half of the low energy protons found within humans behind shielding in space originate from neutron-induced elastic collisions in tissue (i.e., proton recoils). Neutron exposure data can therefore, in principle, be leveraged to provide ancillary estimates of RBE and Q_{max} for low energy protons. The fission neutron RBE_{max} values contained in Table 8 vary widely and carry substantial uncertainty in some cases, as evidenced by the bracketed 66% confidence intervals. The all solid-cancer incidence and life-shortening data from the table range between 4 and 140 with a mean value of 31. A comprehensive assessment of neutron exposure data, RBE, and weighting factors was compiled in ICRP 92 [2003]. The maximally effective neutron was identified at 1 MeV and assigned a radiation weighting factor of $w_R = 20$ for stochastic effects. Kocher et al. [2005] analyzed similar datasets and recommended a median high-dose effectiveness factor for neutrons of 10 for use in assigning probability of causation for radiogenic cancers. Translating this high-dose median to a mean and extrapolating to low dose and dose-rate would yield a neutron RBE_{max} closer to 20 [Kocher et al. 2005].

The use of $Q_{max} = 42$ for low energy $Z = 1$ ions within NSCR2012 conservatively falls within the bounds of information drawn from available neutron exposure data. However, a similar body of evidence has been used by the ICRP [ICRP 2003] and Kocher et al. [2005] to justify neutron effectiveness factors that are a factor of 2 – 4 smaller. The initial estimate of $Q_{max} = 25$ discussed earlier in this section is anchored by both charged particle and neutron exposure data and is therefore suitable for the present application.

The L_{max} values in Table 10 extracted from experimental data exhibit heterogeneity depending on the endpoint and system. The average L_{max} value obtained from all experimental data is ~130 keV/μm which is used as a guide for k. It is demonstrated later in this section that objectively defined parameter uncertainties and correlations for $\Sigma_{0\gamma}$ and k yield Q_{max} and L_{max} distributions that encompass all experimental values from Table 10.

The NSCR2012 QF used $m = 3$ based on various experimental datasets involving mutations in human and hamster cell lines, analysis of neoplastic transformation in C3H10T1/2 cells [Waligorski et al. 1987], and lymphocyte chromosome aberrations. Analysis of the mutation and transformation datasets from Table 10 suggest μ in the range of 2 – 3 depending on the fitting procedure. Combining the mean RBE_{max} curves from Figure 21 for both endpoints over the LET range supported by experimental data yields $\mu = 3$, almost exactly. Given these results and their agreement with m from NSCR2012, an initial value of $\mu = 3$ is selected.

A brute-force search algorithm was implemented with $\mu = 3$ to find that values of $\Sigma_{0\gamma}$ and k that yield $Q_{max} = 25$ and $L_{max} = 130$ keV/um. The algorithm produced parameter estimates of $\Sigma_{0\gamma} = 811.3$ Gy-μm^2 and $k = 68.3$ keV/um. The value of $\Sigma_{0\gamma} = 811.3$ Gy-μm^2 is ~28% smaller than the corresponding NSCR2012 parameter, $\Sigma_0/\alpha_\gamma = 1122$ Gy-μm^2. It is important to note that these fixed parameter values were not prescribed directly; they were inferred from the range of Q_{max} and L_{max} values in Table 10 encompassing multiple cancer-related endpoints, experimental systems, and radiation types.

Results obtained by evaluating these three fixed parameters in the $Q_{NSCR2025}$ functional form of equation (31) are shown in Figure 25. In the left plot, $Q_{NSCR2025}$ approximately balances RBE_{max} curves derived from ensemble analysis of the Harderian gland and lymphocyte datasets. Reasonable agreement is also seen between the ICRP 60 [ICRP 1991] and $Q_{NSCR2025}$ curves in the middle plot. The QF from Shafirkin et al. [2022] is considerably larger than

$Q_{NSCR2025}$ and ICRP 60 [1991], perhaps due to consideration of endpoints including CNS effects, tissue damage, and cataract formation.

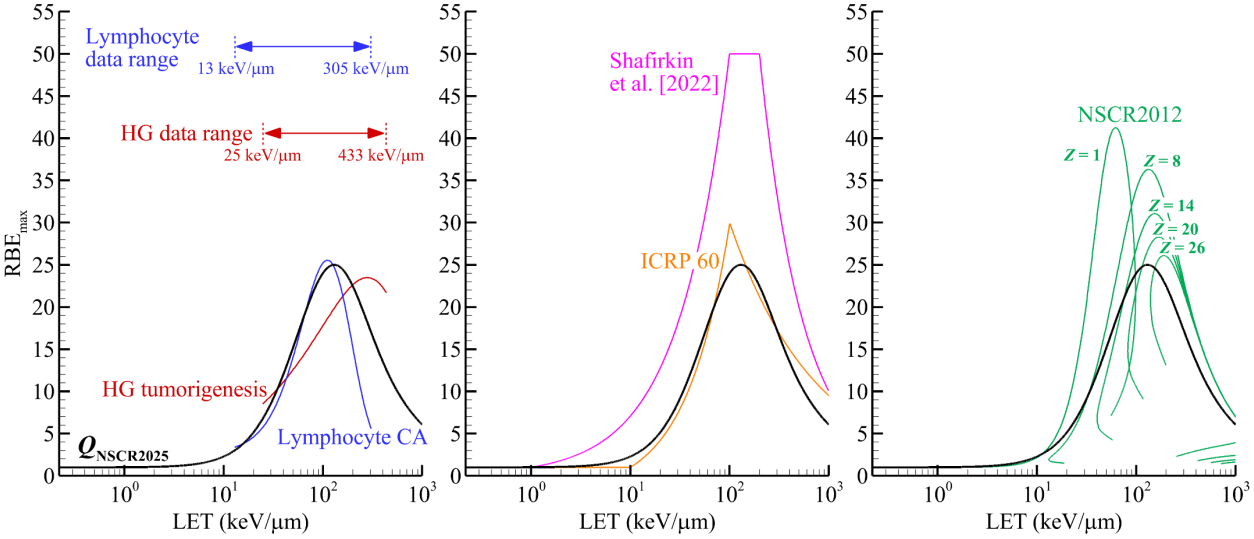

Figure 25. The NSCR2025 QF with $s_{sparse} = 1$, $\Sigma_{0\gamma} = 811.3$ Gy-μm^2, $k = 68.3$ keV/um, and $\mu = 3$ is compared to mean ensemble RBE$_{max}$ curves from Figure 21 for Harderian gland tumorigenesis (red, left) and lymphocyte chromosome aberrations (blue, left), ICRP 60 QF [ICRP 1991] (orange, middle), Shafirkin et al. [2022] QF (pink, middle), and NSCR2012 QF [Cucinotta et al. 2013b] for $Z = 1 – 26$ (green, right).

Despite similar mathematical formulae and baseline parameters, qualitative and quantitative differences are found in the right plot between the NSCR2012 and NSCR2025 QF. Qualitative differences arise from the use of $(Z^*/\beta)^2$ in NSCR2012 compared to the LET dependency structure in the NSCR2025 QF. Quantitative differences are especially pronounced for $Z = 1$, 8, and 14 ions. The larger QF values from NSCR2012 were discussed in the prior section in the context of available experimental data involving ions and neutrons. While experimental evidence exists to support these amplified values in some cases, there are additional data suggesting the opposite, particularly for neutron exposures.

The value for $\Sigma_{0\gamma}$ for leukemia is taken to be 4x smaller than $\Sigma_{0\gamma}$ for solid cancer, consistent with the NSCR2012 report. In their review of the NASA cancer risk model, the NRC noted "… that it is reasonable to make such a distinction on the basis of the limited animal and human data available." [NRC 2012]. The specific evidence brought forward in the NSCR2012 report for a modified leukemia QF is quoted here without modification:

> "ICRP Publication 92 [ICRP 2003] noted that studies with α-emitters have estimated a low RBE compared to human studies for leukemia with γ-rays and x rays. Boice [1993] estimates, from a study of 1003 patients exposed to thorotrast resulting in α-particle exposure to the bone marrow, an effectiveness of α-particles 1.33 times greater than that of γ-rays in the LSS of A-bomb survivors. In contrast, analysis of studies of liver cancer in thorotrast patients suggests RBE of about 20 relative to the LSS results [Grogan et al. 2001]. These estimates carry large uncertainties."
>
> "Weil et al. [2009] reported the RBE for Fe nuclei at 1 GeV/u for hepatocellular carcinoma (liver tumors) was 50.9 ± 9.9 in CBA [carcinoma-bearing animal] mice. In contrast, the RBE for AML for Fe nuclei was 0.48 ± 0.007 (Figure 5.2 [in NSCR2012 report]). The small RBE found for Fe-induced leukemia is similar to the values for α-particles suggested by the thorotrast patient data and with neutron RBE studies of AML in mice that showed maximum RBE of about 3 [Mole et al. 1983, Ullrich and Preston 1987]. In considering leukemia risks, the congruence of modest RBE from human data, heavy ion, and neutron leukemogenesis studies along with studies of cell killing for progenitor cells for leukemias [Griffiths et al. 1994] or loss of deletions with time after exposure [Peng et al. 2009] lends support to a much lower QF assignment for leukemia compared to solid cancers."

Uncertainties and correlations are now assigned to the $Q_{NSCR2025}$ parameters to support evaluation within probabilistic cancer risk projections. The process through which uncertainties are assigned was developed to account for dose-response model-form errors, statistical errors associated with the Harderian gland tumorigenesis and lymphocyte chromosome aberration datasets, variation between the RBE_{max} values derived from these datasets, and variation in RBE_{max} values from individual experiments (Table 7) and fission neutron exposures (Table 8) encompassing a broader range of tissues and endpoints. It is also desired that parameter correlations and uncertainty distributions are objectively derived and traceable to analysis of experimental data to the extent possible.

To accomplish these aims, additional information is first gleaned from the contour distributions shown in Figure 21 for Harderian gland tumorigenesis (left panel) and lymphocyte chromosome aberrations (middle plane). The contours were derived by calibrating the ensemble dose-response model framework separately to 10^4 experimental data realizations, yielding the same number of discrete global RBE_{max} curves. To utilize this data for uncertainty quantification, equation (31) was calibrated separately to each of the 10^4 discrete RBE_{max} curves for Harderian gland tumorigenesis and lymphocyte chromosome aberrations in the LET range supported by experimental data. Since the data sets extend down to only 25 keV/μm (Harderian gland tumorigenesis) and 13 keV/μm (lymphocyte chromosome aberrations), $s_{sparse} = 1$ was held fixed in this step. These calibrations yield sets of correlated $Q_{NSCR2025}$ parameters for each experimental endpoint, as shown in Figure 26.

Parameter distributions, correlations, and average values for the two datasets are generally distinct. Certain trends can nevertheless be connected to the contour distributions from Figure 21. The location parameter k primarily influences L_{max}, the LET value at which Q_{max} is found, with larger values of k shifting L_{max} to higher LET. It is seen in Figure 26, that the distribution of k values for Harderian gland tumorigenesis ranges between 10^2 keV/μm and 10^4 keV/μm with a mean value of 371 keV/μm. These are notably larger than what is found for lymphocyte chromosome aberrations where k ranges from 25 keV/μm to 40 keV/μm with a mean value of 33 keV/μm. These observations are consistent with Figure 21, where $L_{max} = 274$ keV/μm and $L_{max} = 111$ keV/μm for Harderian gland tumorigenesis and lymphocyte chromosome aberrations, respectively.

The shape parameter μ controls the slope of QF away from the maximum value. It is seen in Figure 26, that the distribution of μ values for Harderian gland tumorigenesis ranges between 1 – 3 with a mean value of 1.8. These are notably smaller than what is found for lymphocyte chromosome aberrations where μ ranges from 4 – 10 with a mean value of 5.7. These observations are also consistent with Figure 21, where the overall shape of the RBE_{max} curve is broader (smaller μ) for Harderian gland tumorigenesis than the more narrowly peaked (larger μ) lymphocyte chromosome aberration curve.

The biological interpretation of the differences in L_{max} and μ observed in the two experimental datasets may be related to multiple factors and is not precisely known. There are in vivo vs. in vitro considerations since the Harderian gland involved irradiation of mice, while blood lymphocyte chromosome aberrations were assessed from irradiated cells in medium contained in flasks. Harderian gland tumors were assessed well after irradiation, allowing ample time for repair, misrepair, and tumor growth, while lymphocyte chromosome aberrations were assessed at a much earlier timepoint as the cell enters mitosis for the first time after irradiation.

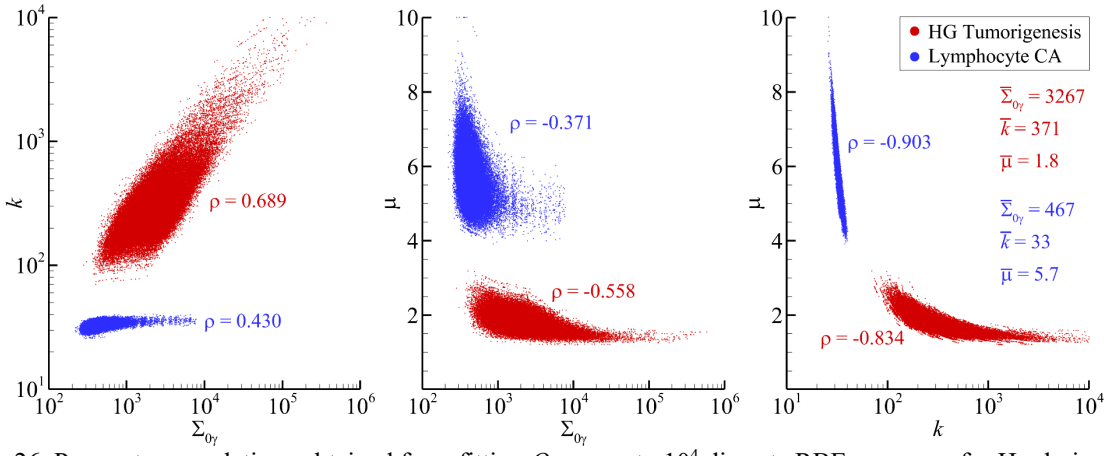

Figure 26. Parameter correlations obtained from fitting $Q_{NSCR2025}$ to 10^4 discrete RBE_{max} curves for Harderian gland tumorigenesis (red) and lymphocyte chromosome aberrations (blue). The rank correlation coefficient (ρ) is shown beside each parameter point cloud with the text color for the associated dataset. Mean parameter values are shown in the right panel with the text color for the associated dataset.

Marginal parameter distributions can be extracted from Figure 26 and placed on a common foundation to guide QF uncertainty quantification. The marginal parameter distributions are transformed to a relative scale by dividing each parameter sample by the corresponding mean. This transformation allows the shape and relative scale of each marginal parameter distribution to be visualized without altering correlations. Results are shown in Figure 27. The marginal relative distributions for $\Sigma_{0\gamma}$ and k are broad and skewed right for Harderian gland tumorigenesis, while the skewness and width of the distributions are diminished for lymphocyte chromosome aberrations. The relative distributions for μ are quite similar for both endpoints and appear nearly symmetric.

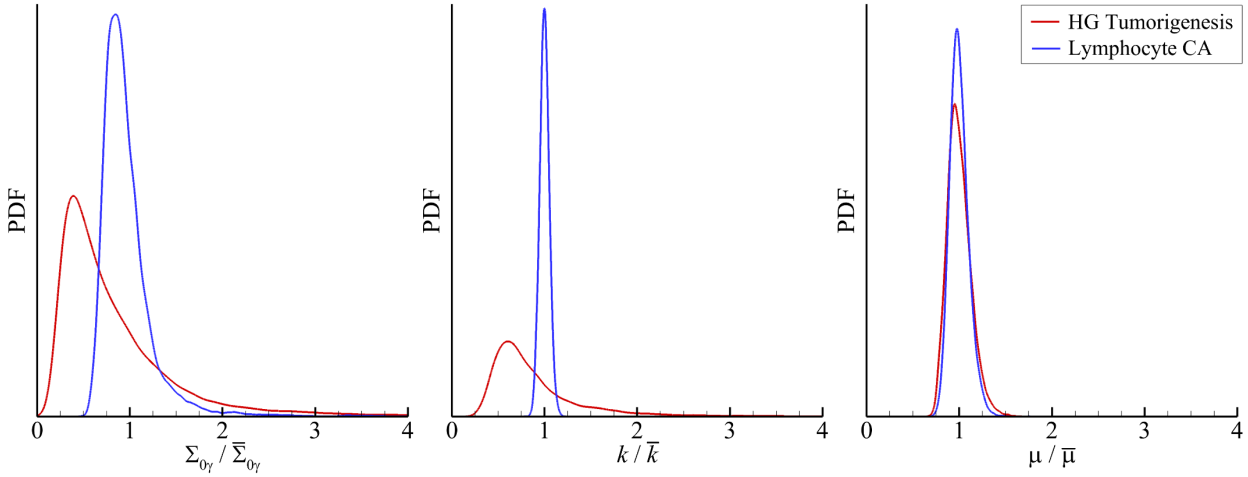

Figure 27. Marginal relative uncertainty distributions for QF parameters for Harderian gland tumorigenesis (red) and lymphocyte chromosome aberrations (blue) derived from the ensemble dose-response RBE_{max} contours shown in Figure 21.

Given the results in Figure 27, lognormal distributions were chosen to represent the skewed relative uncertainty distributions for $\Sigma_{0\gamma}$ and k. A standard normal distribution was chosen to represent the relative uncertainty distribution for μ. A brute-force optimization procedure was implemented to define relative uncertainty distributions and correlations for $\Sigma_{0\gamma}$, k, and μ. The parameter $s_{sparse} = 1$ was held fixed in the optimization. Within the optimization procedure, rank correlation coefficients are randomly and independently selected for each parameter pair as generally guided by Figure 26 (e.g., $\rho > 0$ for $\Sigma_{0\gamma}$ and k pair and $\rho < 0$ for all other pairs). Correlations were resampled if the resulting correlation matrix was not positive definite – a necessary condition to ensure the existence of a Cholesky decomposition for the correlation matrix. Shape parameters for the relative uncertainty distributions were also randomly and independently sampled from a broad range of possibilities as generally guided by Figure 27.

The randomly sampled correlations and relative uncertainty distributions are used to produce a set of 10^5 simulated QF parameters. The simulated parameters were then evaluated through equation (31), allowing various quantities to be calculated: L_{max} distribution, Q_{max} distribution, and mean QF. The following optimization constraints were imposed:

- The simulated mean QF agrees with the baseline NSCR2025 QF from Figure 25.
- The simulated mean QF produces $L_{max} = 130$ and $Q_{max} = 25$.
- The simulated L_{max} distribution has a mean of 130 keV/μm and encompasses values from Table 10.
- The simulated Q_{max} distribution has a mean of 25 and an upper 95th confidence interval bound exceeding 60 – guided by larger RBE_{max} values observed for fission neutron exposures (Table 8) and hepatocellular carcinoma in mice [Weil et al. 2009].

The process was repeated a large number of times to arrive at a set of correlation coefficients and relative uncertainty distribution parameters that best met the aforementioned constraints. Results from the optimization procedure are provided in Table 11, Table 12, Figure 28, and Figure 29.

Table 11. Preferred values and marginal relative uncertainty distributions for $Q_{NSCR2025}$ parameters.

Parameter	Preferred value	Relative uncertainty distribution
$\Sigma_{0\gamma}$ (Gy-μm^2)	811.3 (solid cancer)	Lognormal (μ = -0.131, σ = 0.643)
	811.3/4 (leukemia)	Lognormal (μ = -0.645, σ = 1.286)
k (keV/μm)	68.3	Lognormal (μ = -0.008, σ = 0.354)
μ	3.0	Normal (μ = 1, σ = 0.127)
s_{sparse}	1.0	Normal (μ = 1, σ = 0.150)

Note that the location parameter μ appearing in the argument of the Normal and Lognormal functions should not be confused with the QF parameter μ.

Table 12. Rank correlation matrix for $Q_{NSCR2025}$ parameters. s_{sparse} is treated as uncorrelated from $\Sigma_{0\gamma}$, k, and μ.

	$\Sigma_{0\gamma}$	k	μ
$\Sigma_{0\gamma}$	1.0	0.491	-0.123
k	0. 491	1.0	-0.856
μ	-0.123	-0.856	1.0

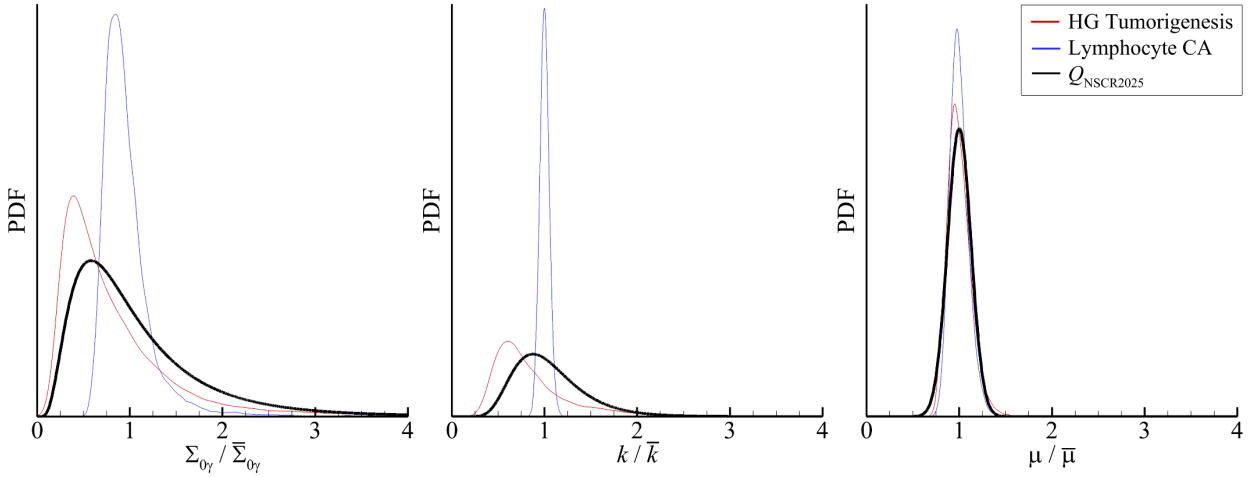

Figure 28. Same as Figure 27, but the $Q_{NSCR2025}$ relative uncertainty distributions are included (black).

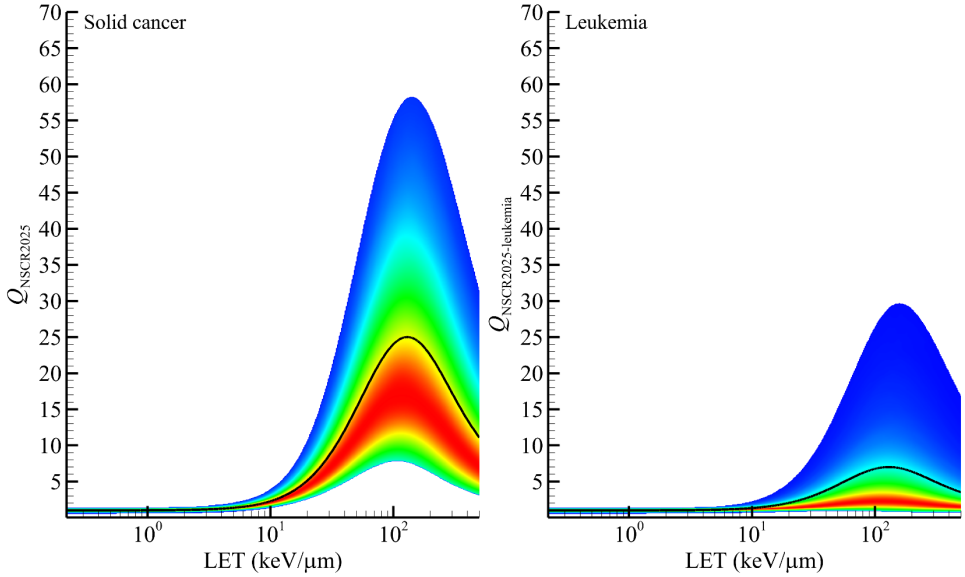

Figure 29. $Q_{NSCR2025}$ mean (solid black line) and 95% confidence interval (contour heat map) for solid cancer (left) and leukemia (right).

5.7.3.5. Verification and Validation

In this section, the NSCR2025 QF and its uncertainties are compared to RBE_{max} values from the experimental data sources identified in Tables Table 6 – Table 8. Quantitative performance metrics are provided to facilitate comparison between the Shafirkin et al. [2022], ICRP 60, NSCR2012, and NSCR2025 QF.

In the bottom left panel of Figure 30, the simulated L_{max} vs. Q_{max} distribution from NSCR2025 is shown. Data in the plot were generated using Monte Carlo methods. Briefly, 10^5 correlated parameters were sampled using the preferred values, relative uncertainty distributions, and correlation coefficients from Table 11 and Table 12. Each of the 10^5 correlated parameters yields a separate QF curve from which L_{max} and Q_{max} can be extracted. The set of L_{max} and Q_{max} values are plotted as scatter points in Figure 30, and a contour histogram has been superimposed to help visualize the joint probability distribution. Marginal probability distributions for L_{max} (top left) and Q_{max} (bottom right) are compared to corresponding experimental data and modeling results from Table 10. Both marginal distributions broadly encompass the range of experimental data covering charged particle and fission neutron exposures, cellular and animal systems, and multiple endpoints including tumorigenesis, life shortening, cell transformation, mutagenesis, and chromosome aberrations. The distributions are also well placed amongst the experimental data; approximately the same number of data points appear above and below the median (near the peak) of each distribution.

In Table 13, QF model performance is quantitatively assessed against available experimental data. The NSCR2025 QF has the lowest χ^2 value in all datasets and the lowest Root Mean Square Error (RMSE) value in all datasets except fission neutrons. It needs to be remembered that experimental data are sparse and uncertain in some cases (e.g., large error bars). Thus, RMSE for fission neutrons of 33.8 (NSCR2012) and 34.3 (ICRP 60 and NSCR2025) could be considered as comparable. The ICRP 60 and NSCR2025 RMSEs of 8.9 and 8.7, respectively, for charged particle tumorigenesis should similarly be considered as nearly indistinguishable. It is found that the ICRP 60 and NSCR2025 performance is quite similar for several other datasets and metrics.

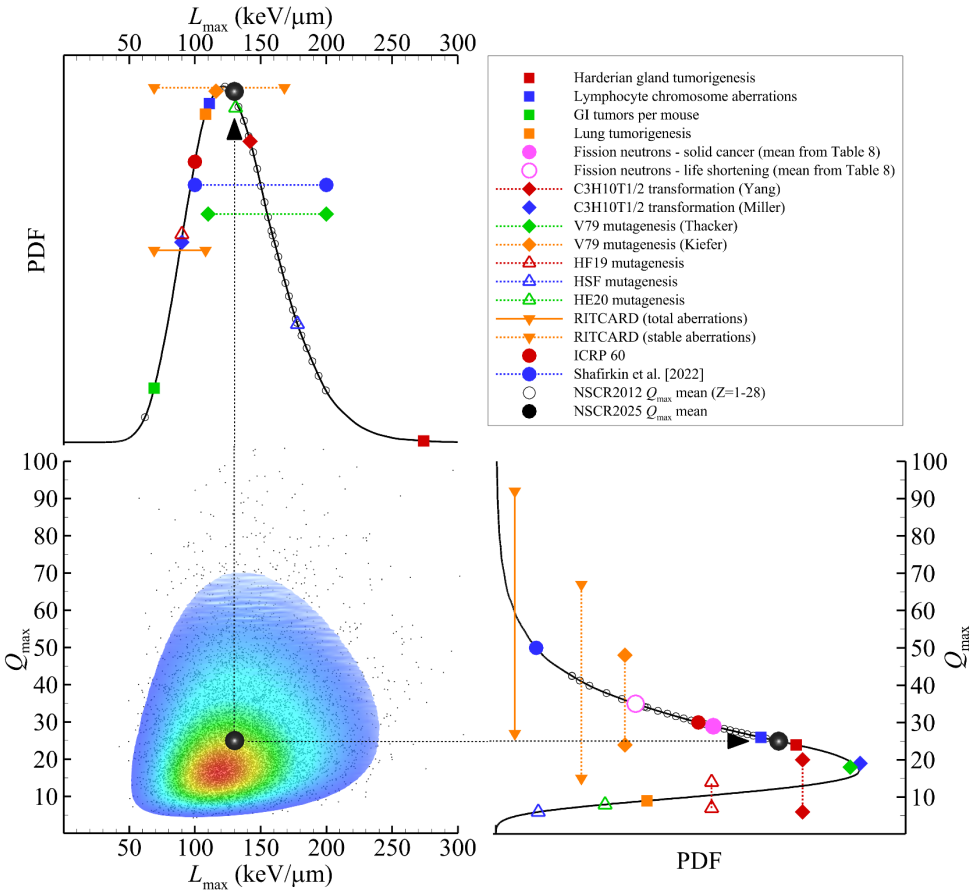

Figure 30. Simulated L_{max} and Q_{max} distributions using the NSCR2025 preferred parameters, relative uncertainty distributions (Table 11) and correlation matrix (Table 12). The contour heat map in the lower left plot is used to help visualize the joint probability distribution expressed by the light gray scatter points for L_{max} and Q_{max}.

Table 13. Comparative performance metrics for the ICRP 60, NSCR2012, NSCR2025, and Shafirkin et al. [2022] QF. Entries in bold denote the model with optimal performance for the given dataset (columns) and metric (RMSE or χ^2).

Metric	Model	Charged particles			Fission neutrons	All
		Tumorigenesis	Mutagenesis	Transformation		
RMSE	ICRP 60	8.9	11.8	12.4	34.3	15.9
	NSCR2012	9.2	17.9	17.3	33.8	18.9
	NSCR2025	**8.7**	**11.1**	**12.0**	34.3	**15.5**
	Shafirkin	25.5	27.8	29.7	**33.0**	28.3
χ^2	ICRP 60	17.2	38.9	37.1	17.5	30.9
	NSCR2012	16.7	73.3	59.0	56.8	55.5
	NSCR2025	**16.5**	**34.8**	**36.1**	**17.4**	**28.6**
	Shafirkin	92.8	174.4	193.1	46.7	142.8

All experimentally derived RBE values are plotted with the NSCR2025 QF in Figures 31 – 39 for completeness and qualitative comparison purposes. The Q_{NSCR2025} mean aligns with Harderian gland tumorigenesis and lymphocyte chromosome aberration data well in Figure 31, as expected. Both of these datasets were used to establish the global behavior of the NSCR2025 QF as a function of LET and to inform both $Q_{\max}$ and $L_{\max}$.

Tumor incidence data in Figure 32 exhibit scattered results with somewhat large error bars, though a majority of the data fall within the Q_{NSCR2025} 95% confidence interval. Colon and gastrointestinal tumor multiplicity in APC1638N/+ mice and lung tumor incidence in CB6F1 mice show lower $\text{RBE}_{\max}$ values than the Q_{NSCR2025} mean, while hepatocellular carcinoma incidence in CBA/CaJ mice and mammary tumor incidence in Sprague-Dawley (SD) rats are larger than the Q_{NSCR2025} mean. As previously mentioned, these sets of studies investigated different tumor types, in different animal models, using different quantities (tumor incidence vs. multiplicity), all of which could contribute to significant differences in the estimate of biological effectiveness. While scattered, fission neutron $\text{RBE}_{\max}$ values for both life shortening and tumorigenesis in Figure 33 also mostly fall within Q_{NSCR2025} 95% confidence interval.

$\text{RBE}_{\max}$ values for leukemia endpoints are shown in Figure 34. The vast majority of data were obtained for neutron exposure, using various animal systems, leukemia subtypes, and experimental protocols (Table 8). One datapoint was obtained for acute myeloid leukemia incidence in male CBA/CaJ mice exposed to 1 GeV/n ^{56}Fe ions [Weil et al. 2009]. Averaged fission neutron data and HZE ion data exhibit larger and smaller values, respectively, than the $Q_{\text{NSCR2025-leukemia}}$ 95% confidence interval. As noted in the previous section, additional human data supports the assignment of a lower QF for leukemia, compared to solid cancer [ICRP 2003]. Measurements with additional heavy ions would bring clarity on in vivo $\text{RBE}_{\max}$ values.

Cell transformation data are compared to QNSCR2025 in Figure 35. Apart from the data from Miller et al. [1995], which notably used very low energy HZE ions (Table 7), the majority of cell transformation data exhibit systematically lower values compared to the Q_{NSCR2025} 95% confidence interval. Part of this discrepancy might be attributed to the fact that X-rays were used as reference radiation in most cases (Table 7). However, even with a factor of two correction applied to account for the use of X-rays, calculated $\text{RBE}_{\max}$ values still peak typically around 10 and remain below the Q_{NSCR2025} mean.

Transformation assays (Figure 35) in the different cell systems measure the ability of cells to grow uncontrollably in vitro, by assessing anchorage-independent growth which is an early marker of neoplastic growth (SHE cells), integrin-associated protein (CD47) expression which enables immune cell evasion and promotes tumor growth and motility (CGL1 cells), or by visually evaluating morphological transformation in fibroblasts that are able to grow tumors when injected into immunocompromised mice (C3H10T1/2 cells). These assays thus capture some (epi)genetic changes that allow cells to acquire cancerous phenotypes. They however do not fully capture the complex tumor microenvironment that exerts pressure on tumor growth in vivo—including, but not limited to, inflammation and immune system response, multi-cellular systems and cell-cell communication, influence of the tissue architecture—possibly resulting in systematically lower $\text{RBE}_{\max}$ values. It is also worth noting that these three cell lines are fibroblast (C3H10T1/2), fibroblast-like (SHE) or fibroblast hybrid (CGL1) types, which could exhibit lower $\text{RBE}_{\max}$ values as observed for the 82-6 hTERT cell line (see the right panel of Figure 21 for fibroblasts).

With the exception of the V79 cell line, $\text{RBE}_{\max}$ values are also systematically below the Q_{NSCR2025} mean for the HGPRT-locus mutagenesis assay (Figure 36 - Figure 39) peaking typically around 5. As for the transformation assay, the assessment of a specific mutation in a monolayer cell system does not capture the complexity of the tumor

microenvironment in vivo. Additionally, a shortcoming of this assay is the evaluation of mutations of a locus located on a chromosome that has a single copy in the cell system (i.e., the HGPRT-locus is located on the single X chromosome in male cells). Following exposure to radiation, nearby vital genes may be inactivated at the same time resulting in cell death, complicating the interpretation of mutation induction in viable cells [Kronenberg 1994]. The assay does not necessarily capture well the qualitative complexity of mutations induced by heavy ions as compared to reference radiation. One study of mutation of the S1 locus in a human x hamster hybrid cell system, where a hamster cell contains a single, non-vital human chromosome 11, showed a modest RBE of 1.6 between ^{137}Cs and ^{56}Fe 600 MeV/n ions, but the complexity of mutations was nine-fold higher for Fe ions compared to gamma radiation. Complex mutations were linked with increased genomic instability, one of the hallmarks of cancer [Waldren et al. 1998].

The V79 cell line (Figure 38 and Figure 39) has a mutated p53 gene that creates a non-functional p53 protein [Chaung et al. 1997]. This protein plays a central role in regulating cell cycle and apoptosis following DNA damage. Heavy ions are particularly capable of forming complex DNA lesions, triggering cell cycle delays and interphase cell death that heavily depend on the ion LET [George et al. 2003]. Chromosome aberration studies have shown that a much larger proportion of V79 cells are able to progress through the first cell cycle, in comparison to normal human fibroblasts [Nasonova et al. 2004]. This reduced ability of cells to control damage propagation to progeny cells might explain the increased RBE_{max} observed for the V79 cell line, compared to the other fibroblast cells that do not carry mutation in the p53 gene. Confirming mutation sensitivity to the p53 gene status, WTK1 cells, deficient in p53 expression, were considerably more sensitive for radiation-induced mutation than the wildtype TK6 [Phillips et al. 1995].

It is also worth mentioning that transformation and mutation in vitro assays are typically performed by exposing monolayers of adherent fibroblasts that exhibit flattened nuclei to monodirectional ion beams. Such geometrical properties—which, as previously discussed, influence the formation of aberrations—are likely to affect other endpoints and significantly differ from in vivo conditions [ICRP 2003]. Solid tumors mostly arise from epithelial cells, which typically have near-spherical nuclei. However, similar RBE_{max} values are obtained for mutation in TK6 lymphoblast cells [Kronenberg 1994], which are grown in suspension and likely exhibit round nuclei.

Lastly, the NSCR2025 QF can be compared to biological effectiveness for lung cancer mortality derived from human exposure to α emitters. Using a representative value of 90 keV/μm, corresponding to a 1.15 MeV/n ^{4}He ion, the NSCR2025 QF has a mean value of 23 with a 95% confidence interval of 8 - 53. The corresponding biological effectiveness of plutonium α particles was estimated in ICRP 150 [2021] to be in the range of 16 – 21, and the biological effectiveness of radon α particles was estimated as 14. It was concluded in ICRP 150 [2021] that these estimates were consistent with the ICRP radiation weighting factor, $w_R = 20$, assigned to α [ICRP 2007]. It is similarly concluded here that the NSCR2025 QF is reasonably consistent with the biological effectiveness of α emitters derived from human epidemiological data in ICRP 150 [2021].

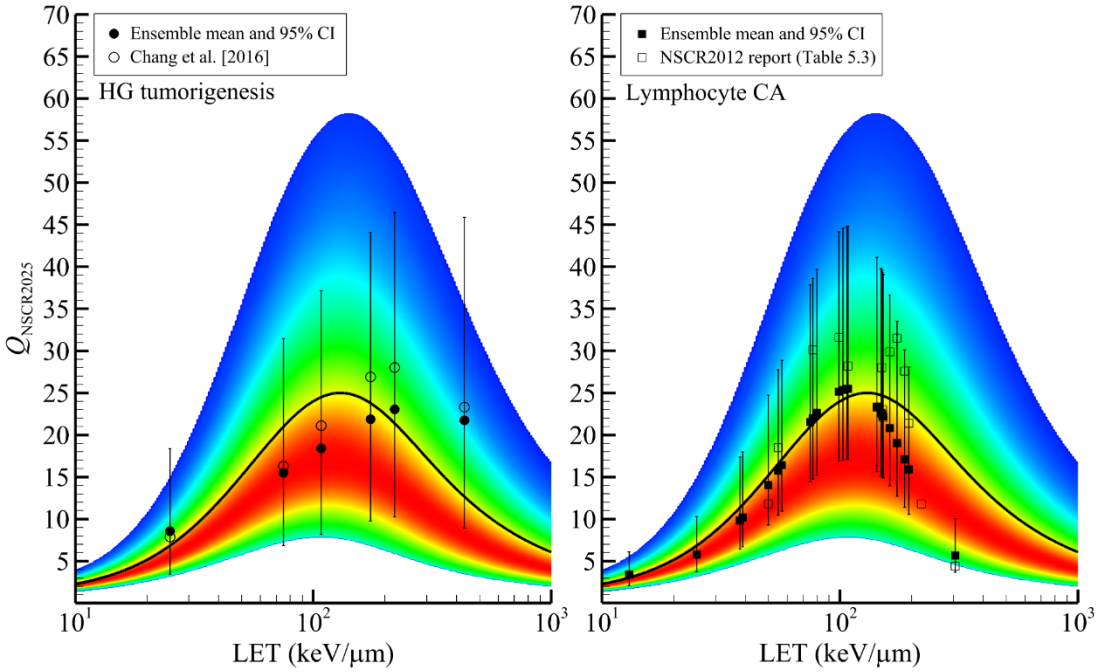

Figure 31. Comparison of $Q_{NSCR2025}$ mean (black line) and 95% confidence interval (contour) to RBE_{max} values derived from the ensemble dose-response models for Harderian gland tumorigenesis (left) and lymphocyte chromosome aberrations (right). RBE_{max} calculations were performed only for the ions contained within each dataset. Closed symbols and error bars represent the ensemble mean and 95% confidence interval (CI). Open symbols were extracted from specific publications.

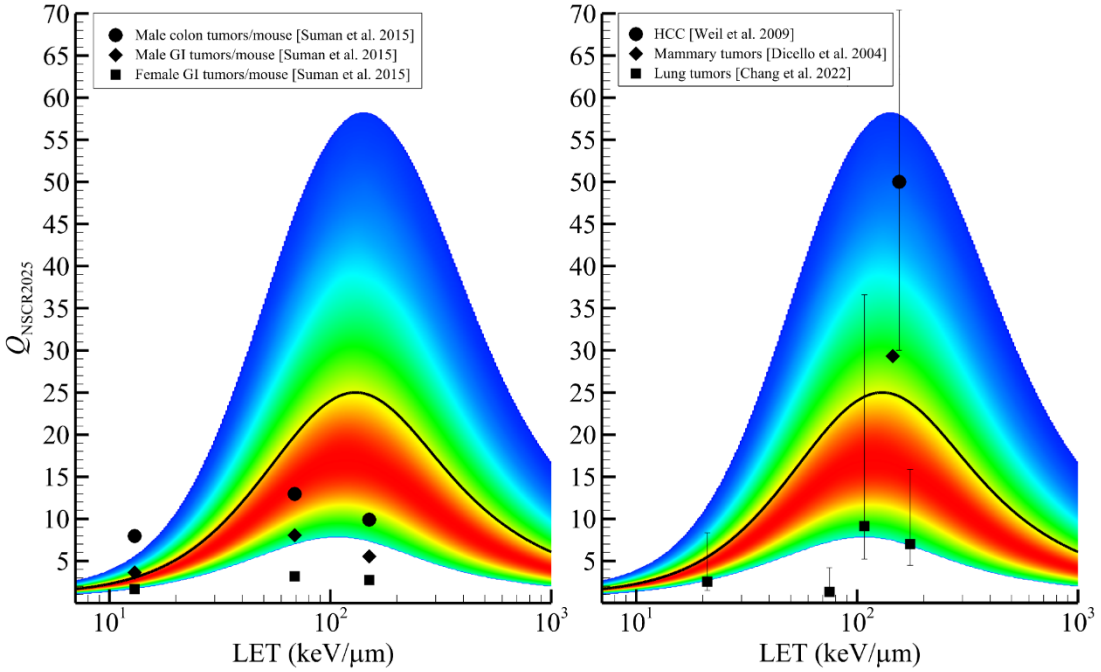

Figure 32. Comparison of $Q_{NSCR2025}$ mean (black line) and 95% confidence interval (contour) to RBE_{max} values for colon and gastrointestinal tumor multiplicity in $APC^{1638N/+}$ mice [Suman et al. al 2016] (left), hepatocellular carcinoma incidence in CBA/CaJ mice [Weil et al. 2009] (right), mammary tumor incidence in SD rats [Dicello et al. 2004] (right), and lung tumor incidence in CB6F1 mice [Chang et al. 2022] (right). Error bars represent one standard deviation.

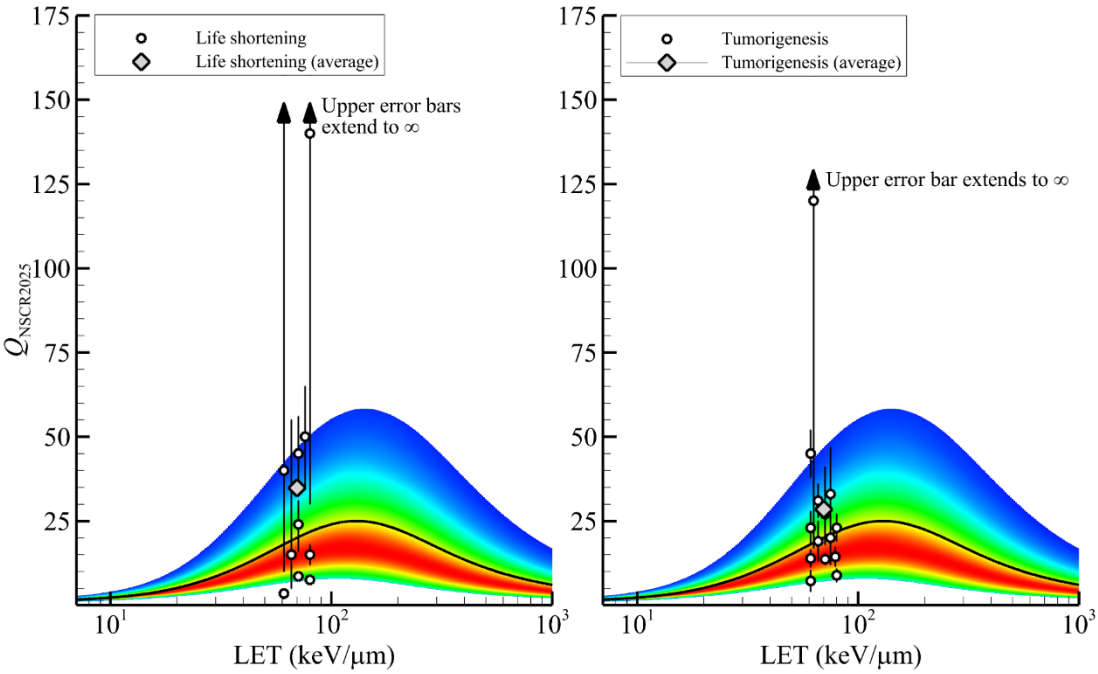

Figure 33. Comparison of $Q_{NSCR2025}$ mean (black line) and 95% confidence interval (contour) to RBE_{max} values for life shortening (left) and tumorigenesis (right). Fission neutron RBE values and error bars representing one standard deviation can be found in Table 8. Upper error bars extending to ∞ are denoted with an upward arrow.

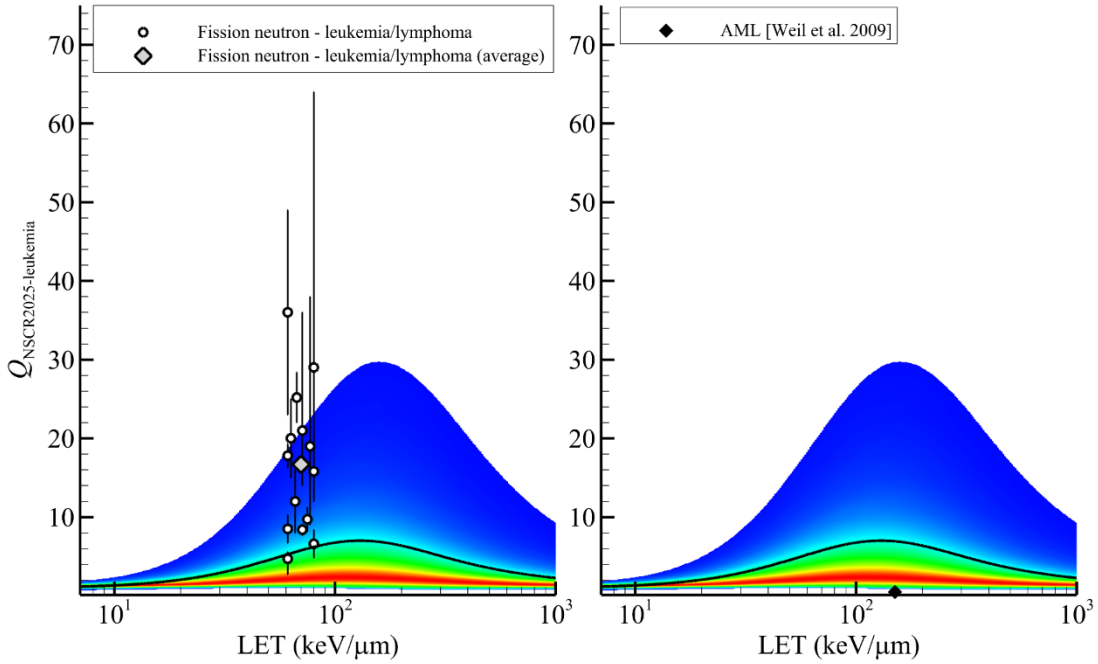

Figure 34. Comparison of $Q_{NSCR2025\text{-}leukemia}$ mean (black line) and 95% confidence interval (contour) to RBE_{max} values for leukemia/lymphoma from fission neutrons (left) and AML [Weil et al. 2009] (right). Fission neutron RBE values and error bars representing one standard deviation can be found in Table 8.

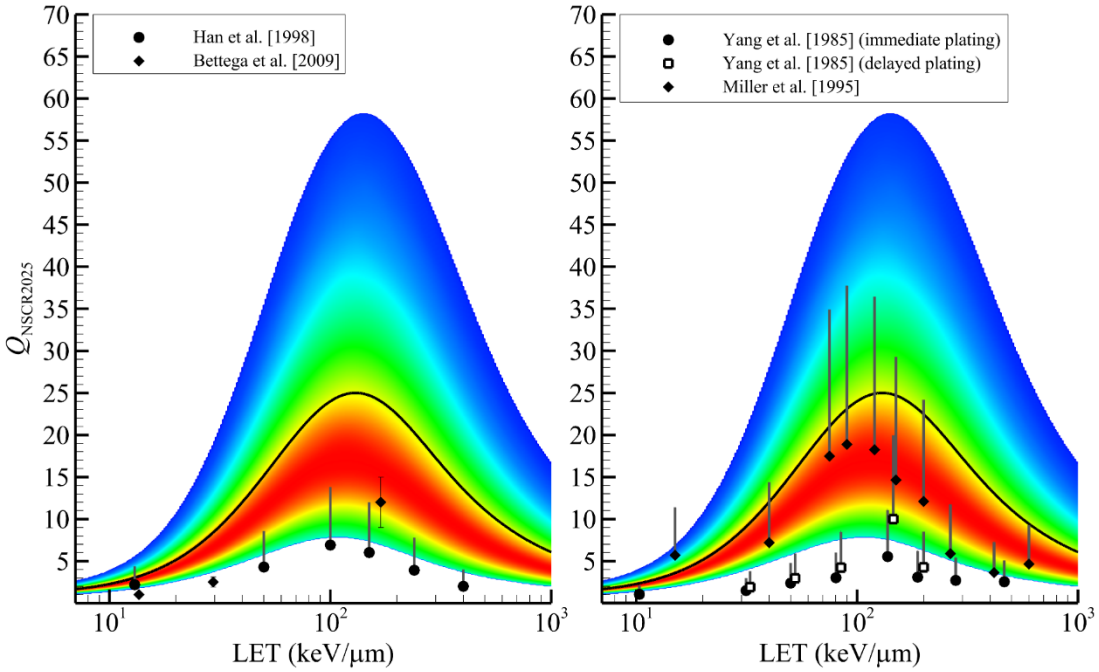

Figure 35. Comparison of $Q_{NSCR2025}$ mean (black line) and 95% confidence interval (contour) to RBE_{max} values for neoplastic cell transformation in SHE cells [Han et al. 1998] (left), CGLI cells [Bettega et al. 2009] (left), and C3H10T1/2 cells [Yang et al. 1985, Miller et al. 1995] (right). Error bars were extracted from the publications and represent one standard deviation. Symbols with a dark gray upper error bar indicate a factor of 2 uncertainty attributable to the use of X-rays instead of gamma rays as a reference radiation in the RBE calculation.

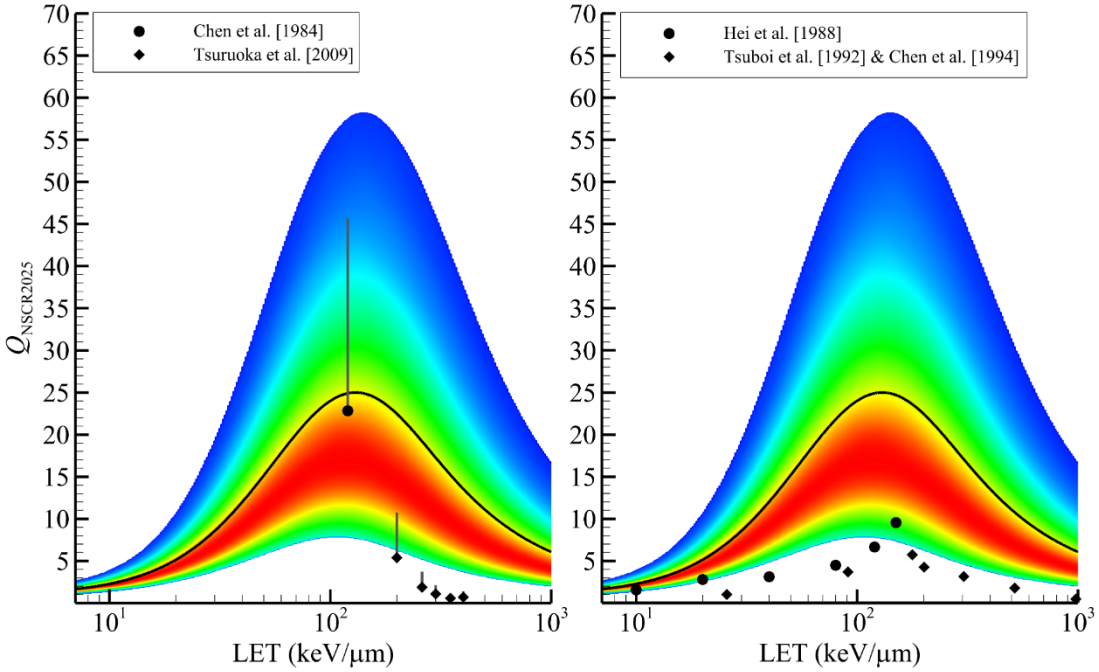

Figure 36. Comparison of $Q_{NSCR2025}$ mean (black line) and 95% confidence interval (contour) to RBE_{max} values for mutagenesis in GM10 cells [Chen et al. 1984] (left), NB1RGB cells [Tsuruoka et al. 2009] (left), HSF cells [Hei et al. 1988, Tsuboi et al. 1992, Chen et al. 1994] (right). Symbols with a dark gray upper error bar indicate a factor of 2 uncertainty attributable to the use of X-rays instead of gamma rays as a reference radiation in the RBE calculation.

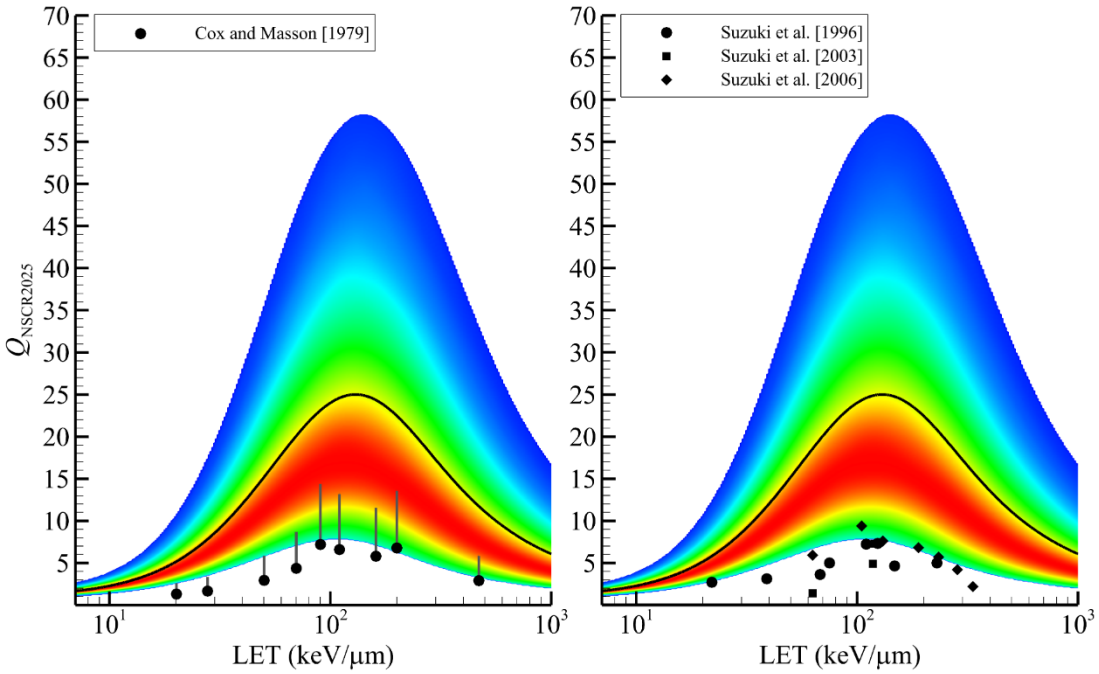

Figure 37. Comparison of $Q_{NSCR2025}$ mean (black line) and 95% confidence interval (contour) to RBE_{max} values for mutagenesis in HF19 cells [Cox and Masson 1979] (left), HE20 cells [Suzuki et al. 1996, 2003, 2006] (right). Symbols with a dark gray upper error bar indicate a factor of 2 uncertainty attributable to the use of X-rays instead of gamma rays as a reference radiation in the RBE calculation.

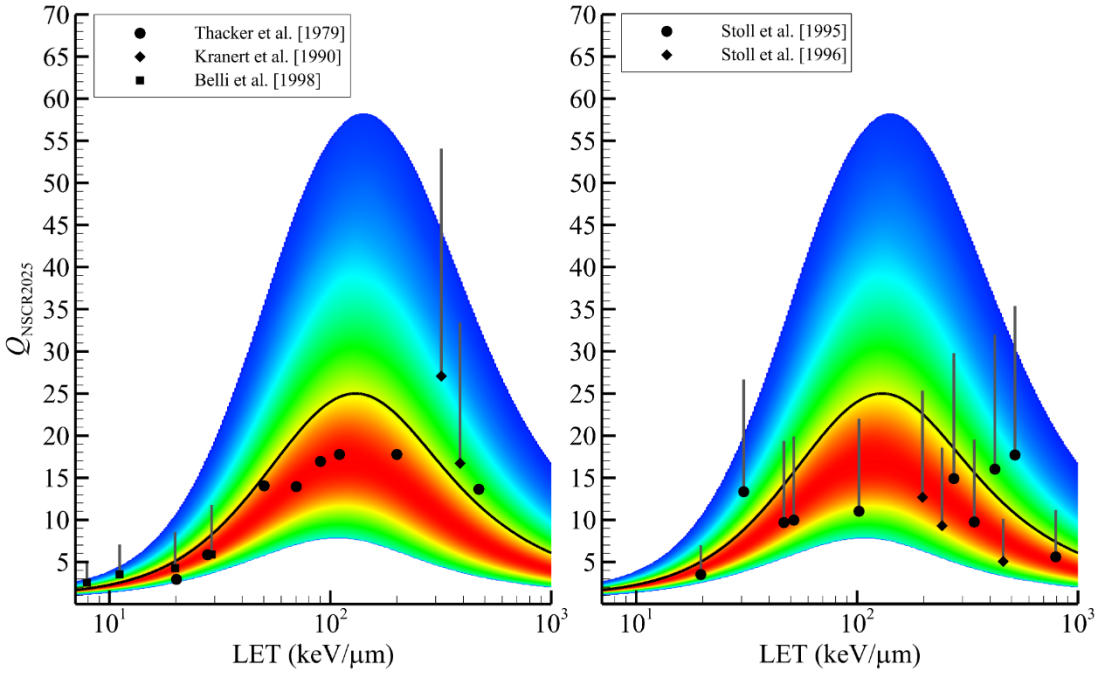

Figure 38. Comparison of $Q_{NSCR2025}$ mean (black line) and 95% confidence interval (contour) to RBE_{max} values for mutagenesis in V79 cells [Thacker et al. 1979; Kranert et al. 1990; Belli et al. 1998; Stoll et al. 1995, 1996]. Symbols with a dark gray upper error bar indicate a factor of 2 uncertainty attributable to the use of X-rays instead of gamma rays as a reference radiation in the RBE calculation.

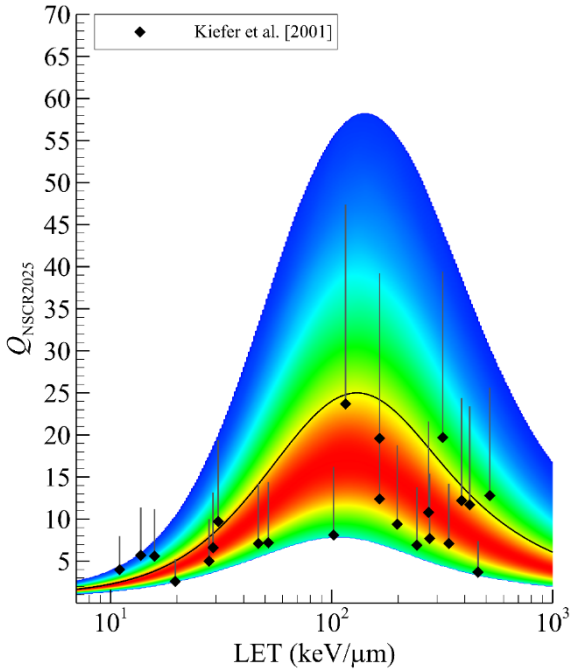

Figure 39. Comparison of $Q_{NSCR2025}$ mean (black line) and 95% confidence interval (contour) to RBE_{max} values for mutagenesis in V79 cells [Kiefer et al. 2001]. Symbols with a dark gray upper error bar indicate a factor of 2 uncertainty attributable to the use of X-rays instead of gamma rays as a reference radiation in the RBE calculation.

6. Mission Exposure and Probabilistic Cancer Risk Projections

In this section, a select set of end-to-end calculations are performed with NSCR2025 utilizing all of the data and models described in the previous sections. Uncertainties included in NSCR2020 and NSCR2025 probabilistic risk projections were described throughout Section 5. The same information is provided in Appendix C in condensed form for comparative and documentation purposes. Emphasis is placed in this section on scenarios related to the astronaut career PEL of 600 mSv NASA effective dose [NASA 2022]. The limiting value corresponds to a 3% mean REID for a 35 year old female never smoker, based on the NSCR2012 QF and tissue weighting factors derived from the NSCR2012 model (Table 6.3 of the NSCR2012 report). Numerous updates and improvements have obviously occurred between NSCR2012 and NSCR2025. However, the new QF and updated baseline population disease rates and survival probabilities have the potential to influence both the exposure-to-risk relationship and NASA effective dose tissue weights. It is found that:

- The collection of updates and improvements that have been incorporated into NSCR2025 do not modify the exposure-to-risk relationship significantly enough (i.e., beyond the 30% variation threshold noted in NASA STD 3001 [NASA 2022]) to warrant a re-evaluation of the PEL at this time.

- The updated NSCR2025 QF and NASA effective dose tissue weights derived from NSCR2025 represent a collection of validated, evidence-based model advancements anchored by ground-based experimental data, epidemiological data, and spaceflight measurements and should therefore be adopted for use at NASA as a replacement for the NSCR2012 quantities.

In Table 14 and Table 15, tissue-specific and total REID projections from NSCR2025 are given for males and females, respectively. Calculations were performed for a 35 year old on a 1 year deep space mission behind 20 g/cm^2 aluminum shielding during the 2009 solar minimum GCR environment. General trends across tissues, sexes, and smoking history are consistent with past analyses [Cucinotta et al. 2013; Simonsen and Slaba 2020, 2021]. It is worth noting as well that point estimate (Pt. Est.) and mean values are well aligned. The point estimate calculation which utilizes fixed parameter values can be considered as a practical surrogate for the mean probabilistic result.

Table 14. NSCR2025 REID calculations for a 35 year old male on a 1 year deep space mission behind 20 g/cm^2 aluminum shielding exposed to the 2009 solar minimum GCR environment.

Site	Average US population			Never smoker population		
	Pt. Est.	Mean	95th CL	Pt. Est.	Mean	95th CL
Bladder	0.158	0.155	0.450	0.136	0.134	0.366
Brain	0.034	0.034	0.093	0.039	0.038	0.105
Colon	0.149	0.146	0.404	0.173	0.170	0.469
Esophagus	0.069	0.068	0.337	0.028	0.028	0.127
Liver	0.124	0.122	0.317	0.148	0.146	0.388
Lung	0.362	0.355	1.143	0.255	0.250	1.093
Oral cavity	0.035	0.034	0.119	0.016	0.015	0.048
Remainder	0.153	0.151	0.429	0.184	0.181	0.523
Stomach	0.119	0.117	0.583	0.134	0.132	0.688
Thyroid	0.005	0.005	0.015	0.007	0.007	0.019
Leukemia	0.137	0.127	0.292	0.145	0.134	0.312
Prostate	0.039	0.039	0.121	0.052	0.051	0.159
Total	1.385	1.353	3.371	1.318	1.286	3.267

Table 15. NSCR2025 REID calculations for a 35 year old female on a 1 year deep space mission behind 20 g/cm^2 aluminum shielding exposed to the 2009 solar minimum GCR environment.

Site	Average US population			Never smoker population		
	Pt. Est.	Mean	95th CL	Pt. Est.	Mean	95th CL
Bladder	0.079	0.078	0.197	0.080	0.079	0.223
Brain	0.031	0.030	0.093	0.033	0.033	0.099
Colon	0.142	0.140	0.371	0.159	0.157	0.423
Esophagus	0.021	0.021	0.092	0.013	0.013	0.054
Liver	0.108	0.106	0.389	0.121	0.119	0.438
Lung	1.036	1.012	3.743	0.544	0.532	1.859
Oral cavity	0.017	0.017	0.052	0.013	0.013	0.041
Remainder	0.156	0.153	0.441	0.178	0.175	0.514
Stomach	0.132	0.129	0.700	0.145	0.142	0.779
Thyroid	0.014	0.014	0.039	0.016	0.016	0.045
Leukemia	0.089	0.082	0.189	0.091	0.084	0.198
Breast	0.188	0.184	0.467	0.217	0.213	0.541
Ovaries	0.094	0.092	0.266	0.101	0.100	0.286
Uterus	0.021	0.020	0.052	0.022	0.022	0.055
Total	2.129	2.079	5.826	1.735	1.696	4.370

REID uncertainties attributable to major components of the NSCR model are shown in Figure 40. The DDREF contribution to REID uncertainty has not changed between NSCR2020 and NSCR2012 since the same underlying DDREF model developed for NSCR2012 has been retained without modification. The "Excess Risk" row in Figure 40 includes uncertainties associated with absolute and relative risk models from the LSS cohort as well as the population transfer weights. These models have not changed since NSCR2012; the slight uncertainty reduction in Figure 40 is a consequence of updated cancer incidence and mortality rates in the baseline population (US never smokers). These updated rates reflect current health profiles, improved surveillance, and treatment modalities, which affect the incidence-to-mortality ratio and absolute/relative excess risk contributions to the overall hazard rate in equations (3) - (6). Uncertainties are similarly affected, which produces the slight modification observed in Figure 40.

Tissue exposure and physics uncertainties have been modestly reduced in NSCR2025. Relative uncertainties assigned for this term in NSCR2012 were mainly applicable for ISS missions in LEO, where area dosimetry and model correction methods were employed [Cucinotta et al. 2008]. Various intercode comparisons and spaceflight validation studies discussed in Sections 3 and 4 demonstrate that combined environment, physics, and transport models utilized in NSCR2012 likely carried much larger uncertainties for missions beyond LEO. Substantial updates have occurred

over the past decade, as described in Section 3. The model updates and extensive verification and validation studies have provided greater clarity for uncertainty assignment with enhanced applicability beyond LEO to support deep space, lunar, and Mars missions.

The uncertainty introduced in REID due to radiation quality effects has been reduced in NSCR2025 as compared to NSCR2020. The reduction follows directly from refined QF development and uncertainty quantification methods aimed at enhancing performance, objectivity, and traceability to experimental data. It was shown in the previous section that the updated NSCR2025 QF has improved performance compared to the NSCR2012 QF (carried into NSCR2020) when assessed against subsets or the entirety of relevant RBE data. It is also important to recognize that uncertainties in the NSCR2012 QF were subjectively assigned [Cucinotta et al. 2013b], while ensemble analyses of supportive global experimental datasets as well as individual data encompassing a broader set of endpoints, experimental conditions, and radiation types including fission neutrons, were used to assign NSCR2025 QF uncertainties in a more objective and rigorous manner.

Improved QF development and uncertainty quantification procedures embodied in NSCR2025 lead to a similar reduction in overall uncertainty for total REID. Nevertheless, it is important to understand that several important unquantified uncertainties are not represented in Figure 40. This includes the impact of NTE, which has been studied extensively with limited data [Cucinotta and Chappell 2010, Cucinotta et al. 2013b, Cucinotta and Cacao 2017, Chang et al. 2016, Chappell et al. 2020, Shuryak and Brenner 2020]. Substantial low dose experimental investments are needed to better understand the mechanisms for NTE to support model development and inclusion in cancer risk projections. Further discussion of experimental data needs is provided in the last section of this report.

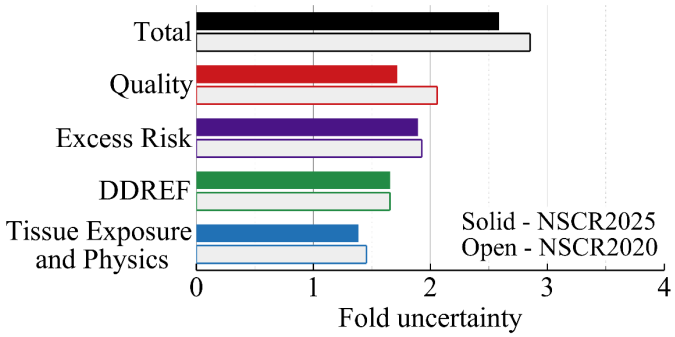

Figure 40. Uncertainty assessment for key components of REID using the NSCR2020 and NSCR2025 models. Calculations are for a 35 year old female (never smoker) behind 20 g/cm^2 aluminum shielding on a 1 year mission exposed to the 2009 solar minimum GCR environment. Fold uncertainty is calculated as the ratio of the upper 95th CL and mean REID values using 10^6 simulation histories.

Tissue weights can be derived from NSCR2025 by dividing tissue-specific REID values by the total REID for a given exposure. Weights calculated from NSCR2025 are compared to ICRP and NSCR2012 tissue weights in Table 16. The NSCR2012 and NSCR2025 tissue weights are in reasonable qualitative agreement, but it can be seen that results differ by more than 30% for some tissue sites (bold text). The source of differences observed in the table between the two NSCR versions cannot be precisely stated, since the calculational details used to generate the NSCR2012 weights were not provided. Nevertheless, one can see that the lung weight remains one of the single largest contributions to overall radiation-induced cancer mortality, driven by excess risk models derived from the LSS cohort as well as baseline disease rates from the US population and associated never smoker adjustments. The NCRP provided a commentary on the sex-dependent nature of lung cancer risks [NCRP 2022]. Recommendations to improve the lung cancer component of the NASA risk model involving targeted reanalysis of the LSS cohort and consideration of occupationally exposed cohorts in the Million Person Study (MPS) [Boice 2022] were provided and are being addressed in ongoing work.

ICRP weights are sex averaged and originate from a broader range of experimental and epidemiological data sources including information at high dose which is deemed less relevant for spaceflight risk projections. Nevertheless, when the various weights and QF are used to calculate effective dose-like quantities (ICRP effective dose in comparison to NASA effective dose), as shown in Figure 41, results are quite similar. This level of agreement was unintentional, but it is nevertheless considered advantageous when exposure and risk metrics used by various space agencies are in reasonable agreement [Shavers et al. 2024b].

NASA effective doses calculated with NSCR2025 are up to 19% lower than the NSCR2020 values. This systematic trend traces back to the QF updates, for which it was shown in the previous section that the more conservatively defined NSCR2012 QF (used in NSCR2020) tends to overestimate experimentally derived RBE in some cases. This assessment is also objectively supported in Table 13, where it was shown that even with limited and uncertain data, the NSCR2025 QF has superior performance compared to the NSCR2012 QF.

The NASA effective dose value yielding a 3% mean REID is provided in Table 17. It is important to understand that the results in Table 17 were calculated for a specific GCR environment and shielding configuration, while the 600 mSv PEL corresponding to 3% mean REID in NASA STD 3001 [NASA 2022] is a summary relationship accounting for a broad range of shielding and solar modulation configurations. The overall trends shown in Table 17 are nevertheless informative. For the specific example of 2009 solar minimum GCR conditions and 20 g/cm^2 aluminum shielding, the NSCR2020 effective dose yielding 3% mean REID is ~10% lower than 600 mSv, while the corresponding NSCR2025 effective dose is ~10% higher than 600 mSv. It can also be seen that uncertainty in REID has been reduced in going from NSCR2020 and NSCR2025. Both of these findings are traceable to QF updates, for which it was shown in the previous section that the NSCR2012 QF (used in NSCR2020) was conservative within the context of available experimentally derived RBE.

Table 16. Tissue weights from ICRP 60 [ICRP 1991], ICRP 103 [ICRP 2007], NSCR2012 [Cucinotta et al. 2013b] and NSCR2025. The NSCR2012 tissue weights were extracted from Table 6.3 of the NSCR2012 report. The NSCR2025 weights are calculated by dividing site-specific REID values by the total REID for a uniform 1 Sv exposure to all tissues. Weights calculated from NSCR2025 were found to be insensitive to the assumed exposure level and are therefore applicable for a range of human mission scenarios. Entries in bold text reflect NSCR2025 values differing from NSCR2012 by more than 30%.

Site	ICRP		NSCR2012				NSCR2025			
			Avg. US		Never smokers		Avg. US		Never smokers	
	60	103	M	F	M	F	M	F	M	F
Bladder	0.05	0.04	0.079	0.034	0.068	0.047	**0.109**	0.038	**0.098**	0.047
Bone	0.01	0.01	-	-	-	-	-	-	-	-
Brain	[1]	0.01	0.017	0.010	0.024	0.017	0.022	**0.014**	0.026	0.018
Colon	0.12	0.12	0.103	0.059	0.118	0.097	0.102	0.068	0.124	0.092
Esophagus	0.05	0.04	0.051	0.010	0.021	0.007	0.047	0.010	0.020	0.008
Liver	0.05	0.04	0.071	0.049	0.084	0.055	0.085	0.052	0.106	0.070
Lung	0.12	0.12	0.305	0.513	0.212	0.336	0.235	0.458	0.172	0.290
Oral cavity	-	0.01	0.016	0.006	0.003	0.003	**0.023**	**0.008**	**0.011**	**0.007**
Remainder	0.05	0.12	0.094	0.082	0.081	0.087	0.105	0.074	**0.131**	0.101
Skin	0.01	0.01	-	-	-	-	-	-	-	-
Stomach	0.12	0.12	0.090	0.063	0.138	0.090	0.082	0.063	**0.096**	0.084
Thyroid	0.05	0.04	0.002	0.003	0.002	0.004	**0.004**	**0.006**	**0.005**	**0.009**
Leukemia	0.12	0.12	0.150	0.070	0.210	0.100	0.159	0.073	0.175	0.090
Prostate	-	[2]	0.022	-	0.039	-	0.028	-	0.038	-
Breast	0.05	0.12	-	0.055	-	0.087	-	**0.080**	-	0.111
Ovaries	0.2	0.08	-	0.046[3]	-	0.070[3]	-	0.047	-	0.061
Uterus	[1]	[2]	-		-		-	0.010	-	0.013
Total solid cancer	0.88	0.88	0.850	0.930	0.790	0.900	0.841	0.927	0.825	0.910

[1] Brain and uterus are considered as part of the remainder within the ICRP 60 effective dose tissue weights.
[2] Prostate and uterus are considered as part of the remainder within the ICRP 103 effective dose tissue weights.
[3] Only the combined weight for "Ovary/Uterus or Testis" was provided in the NSCR2012 report.

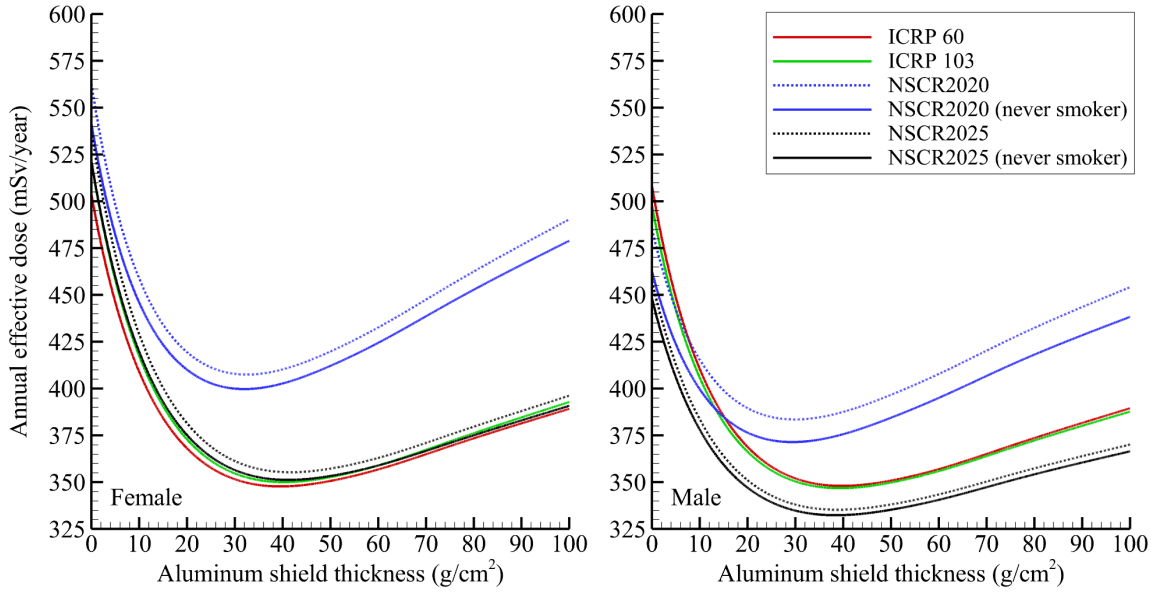

Figure 41. NASA and ICRP annual effective dose (mSv/year) versus aluminum shield thickness for males and females during the 2009 solar minimum GCR environment.

Table 17. NASA effective dose (mSv) yielding a 3% mean REID for a 35 year old female astronaut (never smoker) behind 20 g/cm^2 aluminum shielding during the 2009 solar minimum GCR environment.

	NASA effective dose (mSv)	REID (%)		REIC (%)	
		Mean	Upper 95% CL	Mean	Upper 95% CL
NSCR2020	541	3.0	8.7	6.5	17.9
NSCR2025	661	3.0	7.5	7.0	17.3

7. Medical Countermeasures and Individualized Risk Evaluation

♦ *Summary of medical countermeasure and individualized risk capability in NSCR2025* ♦

A methodology to assess the impact of MCM on space radiation risk reduction was developed [Werneth et al. 2020]. NSCR2025 includes the capability for users to define sex- and age-dependent scaling factors for cancer mortality rates, cancer incidence rates, and baseline US population survival curves. Relative risks used for defining scaling factors often reported in epidemiological studies with confidence limits may also be propagated in NSCR2025. Additional work was performed to extend the MCM methodology for the assessment of individualized risk with CHIP as a feasible risk factor for some crewmembers [Werneth et al. 2024].

NASA envisions an integrated approach to safeguard crewmembers from space radiation that encompasses physical protection to minimize exposures and also biological protection through post-mission surveillance for early detection, evaluating the role of individual risk factors including those controlling baseline risk and radiation sensitivity/susceptibility [Feiveson et al. 2021], and the use of medical countermeasures. A methodology to assess the impact of medical countermeasures on space radiation risk reduction was recently developed [Werneth et al. 2020], and a follow up study [Werneth et al. 2022] showed that substantial MCM reductions of all cancer mortality rates would be required to meet the NASA PEL for long duration spaceflight missions. NSCR2025 now includes the capability for users to define age-dependent scaling factors of cancer mortality rates, cancer incidence rates, and baseline US population survival curves. Relative risks used for defining scaling factors often reported in epidemiological studies with confidence limits may also be propagated in NSCR2025. Additional work was performed to extend the MCM methodology for the assessment of individualized risk with CHIP as a possible risk factor for some crewmembers [Werneth et al. 2024].

As mentioned in Section 1, increased emphasis has been placed on directly mitigating space radiation risks through medical countermeasures [Dynan et al. 2022]. Diet, exercise, and other lifestyle factors, as well as possible clinical interventions such as increased monitoring are also being considered. Means of quantifying the impact of

these interventions on long term health consequences need to be developed to allow risk/benefit analyses before, during, and after spaceflight. Within the context of existing risk assessment models, the impact of reduced disease rates attributable to MCM administration can be estimated by modifying the unexposed population data used within projection models. This approach has been previously applied within the NSCR model to differentiate between the average US population and a never smoker population more indicative of the astronaut corps [Cucinotta and Chappell 2011]. Werneth et al. [2020] utilized a similar approach and as a proof of concept developed a methodology to estimate the impact on REID of long-term aspirin regimens, which have been linked with decreased colorectal cancer incidence [Bibbins-Domingo 2016]. These examples are based on the observation that changes in the baseline population disease rates will also change radiation specific risks in cases where the underlying epidemiological data follow an excess relative risk model. Further refinement using this approach may be attained by consideration of the impact of healthy modifiable lifestyle factors (such as low-alcohol consumption, low excess body fat, physical activity level, etc.) on baseline disease rates.

It should also be noted that evaluation of MCM efficacy and more individualized risk are intimately connected to the metric of interest. Werneth et al. [2020] showed that although long-term aspirin regimens are linked with notable decreases in colorectal cancer incidence rates [Bibbins-Domingo 2016], the impact on REID, which represents the summation of all tissue-specific cancers, is almost negligible. Further analysis [Werneth et al. 2022] established the requirements for MCMs to appreciably reduce REID for a Mars mission. Substantial, and currently unrealistic, reduction of all solid cancer risks would be needed for a single MCM to reduce REID below the prior NASA PEL for a Mars mission. These studies provide useful information regarding the current risk mitigation strategy in the context of exposure-induced death. Yet, radiation-induced death is a high consequence, binary classification neglecting a multitude of factors that may influence accepting/rejecting risk and mitigation strategies for crew and stakeholders. It is reasonable to assume there exists MCM, dietary or lifestyle interventions capable of reducing incidence and non-mortality risks deemed important on an individual basis, and consideration of multiple risk metrics for both cancer and CVD is therefore required.

The methodology developed to investigate the potential risk reduction achieved with MCM may also be used to project more individualized risk profiles for crewmembers, which is important for risk communication, informed consent and medical decision making. A common blood disorder known as CHIP was found to affect some persons with an ageing hematopoietic system, where there is greater propensity for hematopoietic stem cells to acquire somatic mutations [Uddin et al. 2022]. Individuals with CHIP have no symptoms of disease yet have an increased risk of 1% per year of developing a hematological malignancy; a person diagnosed with CHIP at age 50 would have approximately a 20% chance of developing a blood malignancy by age 70. In a human cohort study, Jaiswal et al. [2014] found that CHIP has ties to significant increases in risk of leukemia, coronary heart disease, incident ischemic stroke, and all-cause mortality as compared to non-CHIP carriers. The NSCR model was modified, as it was for studying MCM, by scaling cancer, CHD, and stroke hazard rates by the hazard ratio data provided by Jaiswal et al. [2014]. As such, this case study would exemplify additional individualized risk projection information beyond REID that is relevant for both in-mission and post-mission risk assessment and should be communicated to crewmembers by flight surgeons.

The importance of considering individualized risks is illustrated in Figure 42, which shows the increased risk associated with CHIP carriers for a 2-year deep space mission for crewmembers behind 20 g/cm^2 of spherical aluminum shielding exposed at age 50 to the 2001 solar maximum GCR environment and the August 1972 SPE. The stroke (panels a and b) and total (panels c and d) REID are shown for CHIP carriers in comparison to the REID projected with the unmodified baseline mortality rates. Sex differences in risk may be attributed to other risk factors such as larger baseline risks for females due to radiation-induced lung cancer in the NSCR model.

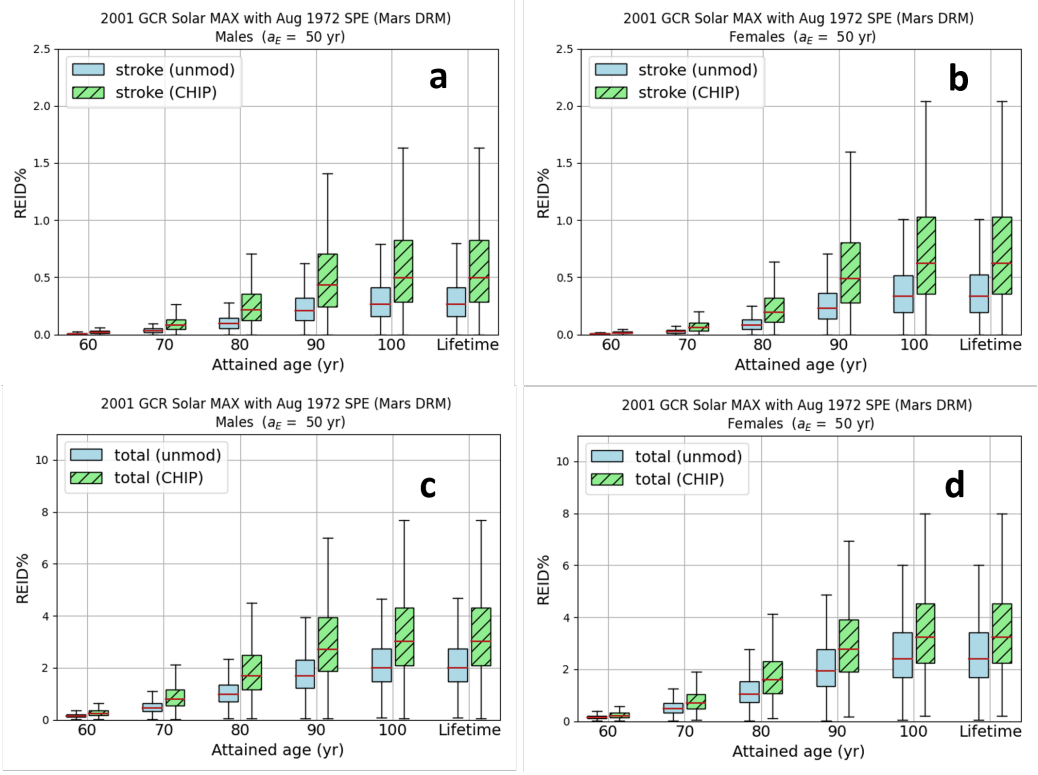

Figure 42. Risk of exposure-induced death (%) for male (panel a) and female (panel b) stroke showing a large increase for CHIP carriers (hashed green boxes) as compared to non-CHIP carriers. Likewise, the total REID for males (panel c) and females (panel d) is increased appreciably for CHIP carriers. Age of radiation exposure for both sexes is 50 yr.

8. Summary and Recommendations

The NSCR2025 model embodies a collection of research accomplishments providing objective and quantifiable improvements in radiation exposure estimates and probabilistic cancer risk projections. The updated model exhibits modestly reduced REID uncertainty compared to its predecessor, attributable mainly to a new space radiation carcinogenesis QF aided by new experimental data, robust ensemble dose-response models, and uncertainty quantification methods. Extensions to the NSCR model include the ability to evaluate medical countermeasure efficacy and individualized risk factors along with an enhanced physics uncertainty assessment applicable for deep space, the Moon, and Mars.

The overall computational framework can be thought of as having three major components: ambient space radiation environment, nuclear physics and transport, and probabilistic cancer risk assessment. The cancer risk assessment portion includes a combination of experimental data, epidemiological data, and theoretical models. A summary of the components that have been updated and improved in NSCR2025 is provided along with future research and experimental data recommendations.

Ambient Space Radiation Environment

<u>Updates:</u>

- The updated and highly accurate BON2020 GCR model is used in NSCR2025 and is a key advancement for future long duration missions where exposure to GCR represents the primary radiation hazard for crewmembers. BON2020 accounts for two decades of ACE/CRIS observations and high-precision measurements from AMS-02 and PAMELA along with historical balloon-borne and satellite data. The

BON2020 model has been shown to be within ±15% of the vast majority (95%) of available measurements with an average model error of <1%.

- A lunar surface environment capability can be used in NSCR2025 that will be critical for sustaining human presence on the Moon. The lunar environment model provides estimates for the GCR or SPE induced albedo spectra for inclusion in cancer risk projections. Initial verification of the lunar surface environment model has been completed through inter-code comparisons.
- A Mars surface environment capability can be used in NSCR2025 and is required to assess crew exposure and health risks for potential surface operations in the future. The Mars environment model accounts for time- and location-dependent atmospheric effects as well as the induced albedo contributions. The model has been successfully verified through inter-code comparisons and validated using MSLRAD data.

Prioritized research and data needs:

1. The lunar neutron spectrum has never been directly measured and therefore represents a critical gap for crew health and safety. A precise measurement of the lunar albedo neutron spectrum extending up to 100 MeV is therefore needed to validate computational models used to predict crew exposures and optimize shielding for sustained human habitation mission architectures. In the absence of such a measurement, human exposure estimates for long duration surface missions will be based solely on theoretical predictions with limited analogous information to ensure accuracy or estimate uncertainty.
2. Integral flux data from ACE/CRIS are currently used to estimate solar modulation effects within BON2020 and are essential to support overall model accuracy. If the satellite is decommissioned or no longer provides required data, the only viable alternative at this time is to revert back to SSN data. Although SSN can be used to estimate solar modulation within BON2020, overall model accuracy will be notably diminished. It is therefore important that ACE/CRIS remain operational in lieu of an equivalent data stream.
3. Additional high energy and high precision GCR measurements would be useful to further enhance BON2020 accuracy. The impact of such improvements may be difficult to discern against larger uncertainties stemming from physics, transport, radiobiology, and epidemiological considerations factoring into space radiation risk projections. Nevertheless, AMS-02 has been collecting data for many years and represents a unique opportunity to extract high-precision, time-resolved ion energy spectra with minimal cost.

Physics and Transport

Updates:

- New nuclear physics models for heavy ion fragmentation and production of pions, nucleons, and light ions have been developed and incorporated into HZETRN2020 and NSCR2025. These nuclear models are essential to accurately estimate secondary radiation fields induced by GCR interactions in moderate and thick shielding anticipated for long duration deep space transit and surface exploration. The RAADFRG heavy ion fragmentation model includes relativistic kinematics and predicts even-odd nuclear structure effects observed in experimental data. DDFRG is based on a multi-source thermal model representation of the Lorentz invariant double differential cross section with coalescence scaling for light production. Both models have been successfully validated against available experimental data.
- HZETRN2020 is a state-of-the-art space radiation transport code that has been extensively verified against Monte Carlo simulations and validated with available spaceflight measurements. The code includes both 1D and 3D analysis options with established methods for analyzing simple and highly complex CAD-based mass shielding geometries. It has been shown that HZETRN2020 can precisely reproduce full scale Monte Carlo simulations, provided the same nuclear interaction data are used in both codes.

Prioritized research and data needs:

1. Significant uncertainties in excess of 100% have been shown for model predictions of ^{2}H, ^{3}H, and ^{3}He in both benchmark verification studies and validation against MSLRAD measurements. These uncertainties

stem from nuclear models used to address the break-up of heavy ion GCR primaries at high energy and nucleon-induced target fragmentation at lower energies. Ground-based nuclear cross section measurements at accelerator facilities are needed to ameliorate the problem.

2. The HZETRN2020 transport code systematically underestimates Compton electrons below ~10 MeV. The systematic error was established through comparison to Monte Carlo simulations and stems from inadequate treatment of 3D scattering effects for these low energy electrons within HZETRN2020. The impact can be seen mainly in comparison to ISS data, where geomagnetic shielding removes a portion of the GCR environment and subsequently enhances the relative contribution of low energy electrons to total dose. Methods to address this systematic error could be developed but would likely have only a minor impact on the accuracy of estimated human exposures beyond LEO.

Combined Environment, Physics, and Transport Spaceflight Validation

Updates:

- An extensive set of benchmark verification and spaceflight validation studies have been successfully completed over the past decade. The most recent validation study provided a comprehensive assessment of the accuracy of combined models using data collected simultaneously at LEO, free space, and Mars during the Artemis-I mission. It was demonstrated that models are in excellent agreement with measurements in free space and on the surface of Mars, providing confidence for planned human exploration missions beyond LEO. Slightly larger differences were found when models were compared to ISS measurements and were attributed to known systematic errors with low energy (<10 MeV) electron transport in HZETRN2020 and imprecise knowledge of the dynamic ISS mass shielding.

Prioritized research and data needs:

1. Precise measurement of the secondary neutron spectrum up to ~100 MeV is a key gap needing to be addressed. Neutrons contribute significantly to human exposures behind moderate and thick shielding in free space. They also represent the primary component of induced albedo environments on the lunar and Martian surfaces, as discussed previously in this section.

Cancer Risk Model

Updates:

- The detailed voxel-based MAX/FAX phantoms based on CT scans of human cadavers and calibrated to ICRP reference quantities are used in NSCR2025 to facilitate tissue-specific exposure estimates.
- The relative uncertainty assigned to calculated tissue fluence spectra, representing combined uncertainty originating from environment, physics, and transport models, has been updated on the basis of numerous improvements and verification and validation studies conducted over the past decade. The updated relative uncertainties are taken to be Gaussian with a mean of one and standard deviation of $\pm$20% and are deemed applicable for missions from LEO to Mars.
- Baseline cancer incidence, mortality, and all-cause survival probabilities for the average US population and never smoker subpopulation have been updated to the most recently available data from CDC and NCI. Never smoker adjustments to the average US population data are guided by Surgeon General recommendations.
- The space radiation QF has been updated to account for new experimental data and multi-model ensemble dose-response analyses with rigorous uncertainty quantification methods. The new QF is based on LET alone, a departure from the $(Z^*/\beta)^2$ dependent structure of its predecessor. Evidence favoring $(Z^*/\beta)^2$ dependence over LET rests in cellular inactivation data and track-structure considerations; no clear evidence was found in experimentally derived RBE directly underlying space radiation QF definitions. More importantly, regardless of the manner in which experimental data supporting LET vs. $(Z^*/\beta)^2$ are interpreted, the updated QF exhibits objectively enhanced performance compared to its predecessor when evaluated against

experimentally derived RBE data. Uncertainties and correlations assigned to QF parameters were objectively drawn from individual experimental datasets and ensemble analysis of global experimental datasets. Lastly, the updated QF was found to align well with ICRP calculations and can also be directly integrated into existing spaceflight dosimetry hardware.

- A revised set of NASA effective dose tissue weights has been provided based on the updates collected within NSCR2025. The revised weights account for QF updates along with current cancer incidence and mortality rates in the US population.
- Extensions to the cancer risk model have been incorporated to allow the impact of medical countermeasures and specific individualized risk factors on REIC and REID to be evaluated. These extensions are in support of broader agency initiatives to directly mitigate space radiation-induced health risks and align with recommendations from the NASEM to provide more informative individualized risk projections to the extent possible.

Prioritized research and data needs:

1. Radiation quality and dose-rate effects remain the primary drivers of uncertainty in space radiation-induced cancer risk projections. Significant investment in ground-based experimental data with an emphasis on low dose (<100 mGy) and low dose-rates is needed to improve mechanistic understanding, guide model development, and reduce uncertainties. Similar recommendations were made in the NSCR2012 report and have been echoed within committee findings for many years [NCRP 2006, 2014; Fogtman et al. 2023]. A more narrowly focused set of experimental recommendations with potential near-term impacts are provided herein.
2. The NSRL GCRsim can be used to inform and improve multiple aspects of the NSCR framework.
    a. A GCRsim dose-response curve for in vivo tumorigenesis would allow the assumption of simple additivity implicit in dose equivalent to be tested more thoroughly within the context of theoretical models [Ham et al. 2017; Huang et al. 2019, 2020; Xu et al. 2026].
    b. If sufficiently low doses are included, information can potentially be gained regarding the significance of NTE originating from heavy ions within a mixed field dominated (>50%) by low LET protons.
    c. Given appropriate animal models, tissue-specific responses can possibly be extracted to enhance the fidelity of the current QF applied uniformly to all solid cancers.
3. It is important to continue developing theoretical dose-response models that can be validated against ground-based experimental data and predict responses where no data exist. RITCARD and the recently developed μD and mP models are extensible to complex mixed fields. Both RITCARD and the mP models have been successfully compared to mixed field experimental data [Slaba et al. 2020b, Xu et al. 2026] and may be useful to further analyze simple additivity in dose equivalent. RITCARD and the mP model may also be utilized to investigate dose-rate effects, a key driver of risk projection uncertainty, but further development and validation will be needed.
4. Excess risk models derived from the LSS cohort represent a significant source of uncertainty in space radiation risk projections. The site-specific ERR and EAR models assembled into NSCR2012 were drawn from multiple sources available between 2006-2008 [NRC 2006, UNSCEAR 2006, Preston et al. 2007, Little et al. 2008] with simplified uncertainties assigned to represent statistical fluctuations in the epidemiological data. Walsh and colleagues [Stabilini et al. 2023, Hafner and Walsh 2024] have utilized multi-model ensemble methods to produce solid cancer excess risk models with rigorously defined uncertainties accounting for correlations in the covariates involved. Such methods could be applied in a tissue-specific manner for integration into the NSCR model. This effort would notably improve the theoretical basis upon which low LET excess risks and uncertainties are quantified in NSCR [Fogtman et al. 2023].
5. The MPS represents a new opportunity to assess cancer risk induced by terrestrial radiation at low dose-rates within the US population. Individuals within the MPS were largely exposed occupationally over significantly longer time spans than what was experienced by the nearly instantaneous exposure associated with the LSS cohort, providing effective low dose-rates closer to the GCR environment encountered by astronauts. However, challenges arise when attempting to incorporate such data into the current NASA cancer risk

model, which requires information about the total mission dose, age at exposure, and attained age after exposure. The NCRP summarized a Bayesian approach to overcome such obstacles in which the sex-dependent dose-modifier is informed by MPS data, while the exposure and attained age modifiers are retained from LSS analyses [NCRP 2022]. Further research is needed to incorporate MPS data into NASA space radiation cancer risk projections and should be pursued so that risk projections are based fundamentally on exposure and population profiles more indicative of the US astronaut spaceflight experience.

6. Genetically susceptible animals are often used in experiments to enhance biological signals and reduce costs. Such genetic sensitivities may manifest equivalently in ion and gamma exposures and effectively cancel each other in RBE estimates; however, a residual bias is possible as well. QF models are developed using a wide range of experimental data and do not rely exclusively on experimental data utilizing genetically susceptible animals, thereby suppressing the impact of any possible bias. Nevertheless, targeted experiments could be performed with genetically diverse mice to assess such details and determine if current QF models carry systematic biases.
7. Cancer prevention and disease surveillance/screening may reduce cancer risk associated with space radiation exposure. For example, it is reported that approximately 40% of cancer cases and deaths in the general US population are potentially preventable by adoption of healthy lifestyle habits [Islami et al. 2024]. Baseline cancer rates in the NSCR can be adapted to assess the influence of these factors on REID for individual astronauts. Likewise, established cancer screening protocols and emerging methods of early cancer detection (e.g., multi-cancer early detection tests) provide a means to detect and intercept the disease at more treatable and curable stages. The potential impact of enhanced surveillance for individual cancer sites where screening data exists (stage shift and effect on mortality) should be investigated. The impact of new technologies such as multi-cancer early detection tests should also be studied when the appropriate data become available.
8. Artificial intelligence and machine learning (AI/ML) represent new approaches and opportunities for studying space radiation-induced cancer risk. These methods often require large quantities of data to support training and cross validation. Unfortunately, ground-based experiments are expensive, limiting the number of assays and output data needed for AI/ML. Omics (genomics, transcriptomics, proteomics, metabolomics) studies produce large quantities of data that lend to AI/ML analysis, particularly in the context of biomarker discovery and medical countermeasure assessments [da Silveira et al. 2020, Malkani et al. 2020]. Approaches to integrate AI/ML analysis of omics data into space radiation risk assessment need to be developed and should continue to be pursued, especially as the computational tools involved evolve rapidly.

9. Acknowledgements

This work was performed by the Multi-Model Ensemble Risk Assessment (MERA) project at NASA Langley Research Center and is supported by the NASA Langley Research Center contract 80LARC23DA003 and the Human Research Program under the Human Exploration and Operations Mission Directorate at NASA. The authors are grateful for the thoughtful reviews provided by: Iulian Apostoaei, Steve Blattnig, Martha Clowdsley, Francesca Luoni, John Norbury, Ryan Norman, Shirin Rahmanian, Janapriya Saha, Chris Sandridge, Eddie Semones, Luke Stegeman, Marshleen Yadav, and Janice Zawaski.

10. Software Availability

The computational models described in this report and contained in NSCR2025 can be utilized through the On-Line Tool for the Assessment of Radiation in Space (OLTARIS) website available at https://oltaris.nasa.gov. Source code for BON2020, HZETRN2020, and RITRACKS can be obtained through the NASA software repository at https://software.nasa.gov. Computational models and software contained in NSCR2025 are developed and maintained in compliance with NASA standard 7009.

11. References

Abe, K., et al., Measurements of cosmic-ray proton and helium spectra from the BESS-polar long-duration balloon flights over Antarctica. *Astrophys. J.* **822**: 1-16; 2016.

Adamczyk, A.M., Norman, R.B., Sriprisan, S.I., Townsend, L.W., Norbury, J.W., Blattnig, S.R., Slaba, T.C., NUCFRG3: light ion improvements to the nuclear fragmentation model. *Nuc. Instr. Meth. A* **678**: 21-32; 2012.

Adriani, O., et al., PAMELA measurements of cosmic-ray proton and helium spectra. *Science* **332**: 69-72; 2011.

Adriani, O., et al., Time dependence of the proton flux measured by PAMELA during the 2006 July – 2009 December solar minimum. *Astrophys. J.* **765**: 1-8; 2013.

Adriani, O., et al., Ten years of PAMELA in space. *Rivista del Nuovo Cimento* **40**: 473-522; 2017.

Aguilar, M., et al., Precision measurement of the helium flux in primary cosmic rays of rigidities 1.9 GV to 3 TV with the Alpha Magnetic Spectrometer on the International Space Station. *Phys. Rev. Lett.* **115**: 211101; 2015a.

Aguilar, M., et al., Precision measurement of the proton flux in primary cosmic rays from rigidity 1 GV to 1.8 TV with the Alpha Magnetic Spectrometer on the International Space Station. *Phys. Rev. Lett.* **114**: 171103; 2015b.

Aguilar, M., et al., Observation of the identical rigidity dependence of He, C, and O cosmic rays at high rigidities by the Alpha Magnetic Spectrometer on the International Space Station. *Phys. Rev. Lett.* **119**: 251101; 2017.

Aguilar, M., et al., Observation of new properties of secondary cosmic rays lithium, beryllium, and boron by the Alpha Magnetic Spectrometer on the International Space Station. *Phys. Rev. Lett.* **120**: 021101; 2018a.

Aguilar, M. et al., Precision measurement of cosmic-ray nitrogen and its primary and secondary components with the Alpha Magnetic Spectrometer on the International Space Station. *Phys. Rev. Lett.* **121**: 051103; 2018b.

Aguilar, M., et al., Observation of fine time structures in the cosmic proton and helium fluxes with the alpha Magnetic Spectrometer on the International Space Station. *Phys. Rev. Lett*., **121**:, 051101; 2018c.

Ahn, H.S., et al., Energy spectra of cosmic-ray nuclei at high energies. *Astrophys. J.* **707**: 593-603; 2009.

Akaike, H., Information theory and an extension of the maximum likelihood principle. Selected Papers of Hirotugu Akaike. Springer, New York, NY; 1972.

Alcaraz, J., et al., Cosmic protons. *Phys. Lett. B* **490**: 27-35; 2000a.

Alcaraz, J., et al., Helium in near earth orbit. *Phys. Lett. B* **494**: 193-202; 2000b.

Allison, J., et al., Recent developments in Geant4. *Nuc. Instr. Meth. A* **835**: 186-225; 2016.

Alpen, E.L., Powers-Risius, P., Curtis, S.B., DeGusman, R., Tumorigenic potential of high-Z, high-LET charged-particle radiations. *Rad. Res.* **136**: 382-91; 1993.

Arias, E., Xu, J., United States life tables, 2019. *National Vital VitalStatistics Reports*: 70(19), available at https://www.cdc.gov/nchs/data/nvsr/nvsr70/nvsr70-19.pdf; 2022.

Ave, M., Boyle, P.J., Gahbauer, F., Hoppner, C., Horandel, J.R., Ichimura, M., Muller, D., Romero-Wolf, A., Composition of primary cosmic-ray nuclei at high energies. *Astrophys. J.* **678**: 262-273; 2008.

Badavi, F.F., West, K.J., Nealy, J.E., Wilson, J.W., Abrahms, B.L., Luetke, N.J. A dynamic/anisotropic low Earth orbit (LEO) ionizing radiation model, NASA-TP-214533; 2006.

Badavi, F.F., A dynamic model for validation of cosmic rays anisotropy at low Earth orbit. *IEEE Trans. Nucl. Sci.* **59**: 447-455; 2012.

Badavi, F.F., Walker, S.A., Santos Koos, L., Evaluation of the new radiation belt AE9/AP9/SPM model for cislunar mission. *Acta Astro.* **102**: 156-168; 2014a.

Badavi, F.F., Validation of the new trapped environment AE9/AP9/SPM at low Earth orbit. *Adv. Space Res.* **54**: 917-928; 2014b.

Badhwar, G.D., and O'Neill, P.M., Galactic cosmic radiation model and its applications. *Adv. Space Res.* **17**: 7-17; 1996.

Bahadori, A.A., Sato, T., Slaba, T.C., Shavers, M.R., Semones, E.J., Van Baalen, M., Bolch, W.E., A comparative study of space radiation organ doses and associated cancer risks using PHITS and HZETRN. *Phys. Med. Bio.* **58**: 7183-7207; 2013.

Bailey, S.M., Kunkel, S.R., Bedford, J.S., Cornforth, M.N., The central role of cytogenetics in radiation biology. *Rad. Res.* **202**: 227-259; 2024.

Barcellos-Hoff, M.H., Blakely, E.A., Burma, S., Fornace, A.J., Gerson, S., Hlatky, L., Kirsch, D.G., Luderer, U., Shay, J., Wang, Y., Weil, M.M., Concepts and challenges in cancer risk prediction for the space radiation environment. *Life Sci. Space Res.* **6**: 92-103; 2015.

Barkas, W.H., *Nuclear Research Emulsions*. New York, NY, Academic Press Inc.; 1963.

Belli, M., Cera, F., Cherubini, R., Vecchia, M.D., Haques, A.M.I., Ianzini, F., Mschini, G., Sapora, O., Simone, G., Tabocchini, M.A., Tiveron, P., RBE-LET relationships for cell inactivation and mutation induced by low energy protons in V79 cells: further results at the LNL facility. *Int. J. Radiat. Biol.* **74**: 501-509; 1998.

Bellotti, R., et al., Balloon measurements of cosmic ray muon spectra in the atmosphere along with those of primary protons and helium nuclei over midlatitude. *Phys. Rev. D* **60**: 052002-1; 1999.

Benton, E.R., Benton, E.V., Space radiation dosimetry in low-Earth orbit and beyond. *Nuc. Instr. Meth. B* **184**: 255-294; 2001.

Bethe, H.A., Zur theorie des durchgangs Schneller korpuskularstrahlen durch materie. *Ann. Phys.* **397**: 325; 1930.

Bettega, D., Calzolari, P., Hessel, P., Stucchi, C.G., Weyrather, W.K., Neoplastic transformation induced by carbon ions. *Int. J. Radiation Oncology Biol. Phys.* **73**: 861-868; 2009.

Bibbins-Domingo, K., Aspirin Use for the Primary Prevention of Cardiovascular Disease and Colorectal Cancer: U.S. Preventive Services Task Force Recommendation Statement. *Ann. Intern. Med.* **164**, 836–84; 2016.

Billings, M.P., Yucker, W.R., The computerized anatomical man (CAM) model. Summary Final Report, MDC-G4655, McDonnell Douglas Company; 1973.

Bloch, F., Zur bremsung rasch bewegter teilchen beim durchgang durch materie. *Ann. Phys.* **408**: 285; 1933.

Boezio, M., et al., The cosmic-ray proton and helium spectra between 0.4 and 200 GV. *Astrophys. J.* **518**: 457-472; 1999.

Boezio, M., et al., The cosmic-ray proton and helium spectra measured with the CAPRICE98 balloon experiment. *Astroparticle Phys.* **19**: 583-604; 2003.

Boice, J.D., Leukemia risks in thorotrast patients. *Rad. Res.* **136**: 301-302; 1993.

Boice, J.D., The Million Person Study relevance to space exploration and Mars. *Int. J. Radiat. Biol* **98**: 551-559; 2022.

Bonassi, S., Norppa, H., Ceppi, M., Strömberg, U., Vermeulen, R., Znaor, A., Cebulska-Wasilewska, A., Fabianova, E., Fucic, A., Gundy, S., Hansteen, I., Knudsen, L.E., Lazutka, J., Rossner, P, Sram, R.J., Boffetta, P., Chromosomal aberration frequency in lymphocytes predicts the risk of cancer: results from a pooled cohort study of 22 358 subjects in 11 countries. *Carcinogenesis* **29**: 1178-1183; 2008.

Borak, T.B., Heilbronn, L.H., Townsend, L.W., McBeth, R.A., de Wet, W., Quality factors for space radiation: a new approach. *Life Sci. Space Res.* **1**: 96-102; 2014.

Borek, C., Hall, E.J., Rossi, H., Malignant transformation in cultured hamster embryo cells produced by X-rays, 430-keV monoenergetic neutrons, and heavy ions. *Cancer Res.* **38**: 2997-3005; 1978.

Carnes, B.A., Grahn, D., Thomson, J.F., Dose response modelling of the life shortening in a retrospective analysis of the combined data from the JANUS program at Argonne National Laboratory. *Rad. Res.* **119**: 39-56; 1989.

CDC, United States Cancer Statistics - Mortality Data: 1999-2021, WONDER Online Database. 2023 submission. Available at https://wonder.cdc.gov/cancermort-v2021.html; 2024.

CDC, Behavioral risk factor surveillance system (BRFSS) web enabled analysis tool (WEAT). Available at https://nccd.cdc.gov/weat/#/crossTabulation; 2025.

Chang, P.Y., Cucinotta, F.A., Bjornstad, K.A., Bakke, J., Rosen, C.J., Du, N., Fairchild, D.G., Cacao, E., Blakely, E.A., Harderian gland tumorigenesis: low-dose and LET response. *Rad. Res.* **185**: 449-460; 2016.

Chang, P.Y., Bakke, J., Rosen, C.J., Bjornstad, K.A., Mao, J.H., Blakely, E.A., Heavy-ion-induced lung tumors: dose- & LET-dependence. *Life* **12**: 907; 2022.

Chappell, L., Background cancer and mortality rates: documentation for background rates used by the NASA space cancer risk codes. SRAG-COM-RISK-2014-013; 2014.

Chappell, L., 2011 US cancer and mortality rates for use in space cancer risk codes. SRAG-COM-RISK-2015-018; 2015.

Chappell, L., Background cancer incidence and mortality rates update. SRAG-COM-RISK-2020; 2020.

Chappell, L.J., Elgart, S.R., Milder, C.M., Semones, E.J., Assessing nonlinearity in harderian gland tumor induction using three combined HZE-irradiated mouse datasets. *Rad. Res.* **194**: 38-51; 2020.

Chaung, W., Mi, L.J., Boorstein, R.J., The p53 status of Chinese hamster V79 cells frequently used for studies on DNA damage and DNA repair. *Nucleic Acids Res.* **25**: 992-994; 1997.

Chen, D.J., Strniste, G.F., Tokita, N., The genotoxicity of alpha particles in human embryonic skin fibroblasts. *Rad. Res.* **100**: 321-327; 1984.

Chen, D.J., Tsuboi, K., Nguyen, T., Yang, T.C., Charged-particle mutagenesis II. Mutagenic effects of high energy charged particles in normal human fibroblasts. *Adv. Space Res.* **14**: 347-354; 1994.

Cordova, K.A., Cullings, H.M., Assessing the relative biological effectiveness of neutrons across organs of varying depth among the atomic bomb survivors. *Rad. Res.* **192**: 380-387; 2019.

Cornforth, M.N., Bailey, S.M., Goodwin, E.H., Dose responses for chromosome aberrations produced in noncycling primary human fibroblasts by alpha particles, and by gamma rays delivered at sublimiting low dose rates. *Rad. Res.* **158**: 43-53; 2002.

Cox, R. and Masson, W.K., Mutation and inactivation of cultured mammalian cells exposed to beams of accelerated heavy ions. *Int. J. Radiat. Biol.* **36**: 149-160; 1979.

Cucinotta, F.A., Calculations of cosmic-ray helium transport in shielding materials. NASA TP 3354; 1993.

Cucinotta, F.A., Kim, M.Y., Willingham, V., George, K.A., Physical and biological organ dosimetry analysis for International Space Station astronauts. *Rad. Res.* **170**: 127-138; 2008.

Cucinotta, F.A., Chappell, L.J., Non-targeted effects and the dose response for heavy ion tumor induction. *Mutat. Res. Fund. Mol. Mech. Mutagen.* **687**: 49-53; 2010.

Cucinotta, F.A., Chappell, L.J., Updates to astronaut radiation limits: radiation risks for never-smokers. *Rad. Res.* **176**, 102–114; 2011.

Cucinotta, F.A., Kim, M.Y., Chappell, L.J., Space radiation cancer risk projections and uncertainties – 2010. NASA TP 2011-216155; 2011.

Cucinotta, F.A., Kim, M.Y., Chappell, L.J., Huff, J.L., How safe is safe enough? Radiation risk for a human mission to Mars. *Plos One* **8**: e74988; 2013a.

Cucinotta, F.A., Kim, M.Y., Chappell, L.J., Space radiation cancer risk projections and uncertainties – 2012. NASA TP 2013-217375; 2013b.

Cucinotta, F.A., A new approach to reduce uncertainties in space radiation cancer risk predictions. *PloS one* **10**: e0120717; 2015.

Cucinotta, F.A., Alp, M., Rowedder, B., Kim, M.Y., Safe days in space with acceptable uncertainty from space radiation exposure. *Life Sci. Space Res*. **5**: 31-38; 2015.

Cucinotta, F.A., Cacao, E., Non-targeted effects models predict significantly higher Mars mission cancer risk than targeted effects models. *Sci. Rep.* **7**: 1832; 2017.

Cucinotta, F.A., To, K., Cacao, E.E., Predictions of space radiation fatality risk for exploration missions. *Life Sci. Space Res.* **13**: 1-11; 2017.

Cucinotta, F.A., Cacao, E.E., Kim, M.Y., Saganti, P.B., Benchmarking risk predictions and uncertainties in the NSCR model of GCR cancer risks with revised low LET risk coefficients. *Life Sci. Space Res.* **27**: 64-73; 2020.

da Silveira, W.A., et al., Comprehensive multi-omics analysis reveals mitochondrial stress as a central biological hub for spaceflight impact. *Cell* **183**: 1185-1201; 2020.

Datta, K., Suman, S., Kallakury, B.V., Fornace, A.J., Heavy ion radiation exposure triggered higher intestinal tumor frequency and greater β-catenin activation than γ radiation in APC Min/+ mice. *PLoS One* **8**, e59295; 2013.

De Angelis, G., Clowdsley, M.S., Singleterry, R.C., Wilson, J.W., A new Mars radiation environment model with visualization. *Adv. Space Res.* **34**: 1328-1332; 2004.

de Wet, W.C., *Nuclear Fragmentation Cross Sections for Space Radiation Application,* Ph.D. thesis, University of Tennessee; 2017.

de Wet, W.C., Slaba, T.C., Rahmanifard, F., Wilson, J.K., Jordan, A.P., Townsend, L.W., Schwadron, N.A., Spence, H.A., CRaTER observations and permissible mission duration for human operations in deep space. *Life Sci. Space Res.* **26**: 149-162; 2020.

Dicello, J.F., Christian, A., Cucinotta, F.A., Gridley, D.S., Kathirithamby, R., Mann, J., Markham, A.R., Moyers, M.F., Novak, G.R., Piantadosi, S., Ricart-Arbona, R., Simonsen, D.M., Strandberg, J.D., Vazquez, M., Williams, J.R., Zhang, Y., Zhou, H., Huso, D., *In vivo* mammary tumourigenesis in the Sprague-Dawley rat and microdosimetric correlates. *Phys. Med. Biol.* **49**: 3817-3830; 2004.

Di Majo, V., Coppola, M., Rebessi, S., Saran, A., Pazzaglia, S., Pariset, L., Covelli, V., The influence of sex on life shortening and tumor induction in CBA/Cne mice exposed to X rays or fission neutrons. *Rad. Res.* **146**: 81-87; 1996.

Dostrovsky, I., Fraenkel, Z., Friedlander, G., Monte Carlo calculations of nuclear evaporation processes. III. Applications to low-energy reactions. *Phys. Rev.* **116**: 683–702; 1959.

Durante, M., Cucinotta, F.A., Heavy ion carcinogenesis and human space exploration. *Nat. Rev. Cancer* **8**: 465-472; 2008.

Dynan, W.S., Chang, P.Y., Sishc, B.J., Elgart, S.R., Breaking the limit: biological countermeasures for space radiation exposure to enable long duration spaceflight. *Life Sci. Space Res.* **35**: 1-3; 2022.

Edmondson, E.F., Gatti, D.M., Ray, F.A., Garcia, E.L., Fallgren, C.M., Kamstock, D.A., Weil, M.M., Genomic mapping in outbred mice reveals overlap in genetic susceptibility for HZE ion– and γ-ray–induced tumors. *Sci. Adv.* **6**: eaax5940; 2020.

Edwards, A.A., Neutron RBE values and their relationship to judgments in radiological protection. *J. Radiat. Prot.* **19**: 93-105; 1999.

ENDF, Evaluated Nuclear Datafile Database. Available at https://www-nds.iaea.org/exfor/endf.htm; 2016.

ENDF, ENDF/B-VIII.0: The 8th major release of the nuclear reaction data library with CIELO-project cross sections, new standards and thermal scattering data. *Nuclear Data Sheets* **148**: 1-142; 2018.

Engelmann, J.J., Ferrando, P., Soutoul, A., Goret, P., Juliusson, E., Koch-Miramond, L., Lund, N., Masse, P., Peters, B., Petrou, N., Rasmussen, I.L., Charge composition and energy spectra of cosmic-ray nuclei for elements from Be to Ni. Results from HEAO-3-C2. *Astron. Astrophys.* **233**: 96-111; 1990.

Feiveson, George, K., Shavers, M., Moreno-Villanueva, M., Zhang, Y., Babiak-Vazquez, A., Crucian, B., Semones, E., Wu, H., Predicting chromosome damage in astronauts participating in International Space Station missions. *Sci. Rep.* **11**: 5293; 2021.

Feynman, J., Ruzmaikin, A., Berdichevsky, V., The JPL proton fluence model: an update. J. Atmos. *Solar Terrestrial Phys.* **64**: 1679–1686; 2002.

Fogtman, A., Baatout, S., Baselet, B., Berger, T., Hellweg, C.E., Jiggens, P., La Tessa, C., Narici, L., Nieminen, P., Sabatier, L., Santin, G., Schneider, U., Straube, U., Tabury, K., Tinganelli, W., Walsh, L., Durante, M., Towards sustainable human space exploration – priorities for radiation research to quantify and mitigate radiation risks. *npj Micro* **8**: 9; 2023.

Forget, F., Hourdin, F., Fournier, R., Hourdin, C., Talagrand, O., Collins, M., Lewis, S.R., Read, P.L., Huot, J.P., Improved general circulation models of the Martian atmosphere from the surface to above 80 km. *J. Geo. Res.* **104**: 24155-24176; 1999.

Francis, Z., Villagrasa, C., Clairand, I., Simulation of DNA damage clustering after proton irradiation using an adapted DBSCAN algorithm. *Comput. Methods Programs Biomed.* **101**: 265-270; 2011.

Fry, R.J.M., Powers-Risius, P., Alpen, E.L., Ainsworth, E.J., High-LET radiation carcinogenesis. *Rad. Res.* **104**: 188-195; 1985.

Garcia-Munoz, M., Mason, G.M., Simpson, J.A., Wefel, J.P., Charge and energy spectra of heavy cosmic rays at intermediate energies. 15th International Cosmic Ray Conference, Plovdiv, Bulgaria; 1977.

George, K.A., Durante, M., Willingham, V., Wu, H., Yang, T.C., Cucinotta, F.A., Biological effectiveness of accelerated particles for the induction of chromosome damage measured in metaphase and interphase human lymphocytes. *Rad. Res.* **160**: 425-435; 2003.

George, K.A., Cucinotta, F.A., The influence of shielding on the biological effectiveness of accelerated particles for the induction of chromosome damage. *Adv. Space Res.* **39**: 1076-1081; 2007.

George, K.A., Hada, M., Jackson, L.J., Elliott, T., Kawata, T., Pluth, J.M., Cucinotta, F.A., Dose response of gamma rays and iron nuclei for induction of chromosome aberrations in normal and repair-deficient cell lines. *Rad. Res.* **171**: 752-763, 2009.

George, K.A., Hada, M., Chappell, L.J, Cucinotta, F.A., Biological effectiveness of accelerated particles for the induction of chromosome damage: track structure effects. *Rad. Res.* **180**: 25-33; 2013.

George, K.A., Hada, M., Cucinotta, F.A., Biological effectiveness of accelerated protons for chromosome exchanges. *Front. Oncol.* **5**: 226; 2015.

George, S., et al., Space radiation measurements during the Artemis I lunar mission. *Nature* **634**: 48-52; 2024.

Gillies, M., Kuznetsova, I., Sokolnikov, M., Haylock, R., O'Hagan, J., Tsareva, Y., Labutina, E., Lung cancer risk from plutonium: a pooled analysis of the Mayak and Sellafield worker cohorts. *Rad. Res.* **188**: 645-660; 2017.

Ginet, G.P., O'Brien, T.P., Huston, S.L., Johnston, W.R., Guild, T.B., et al., AE9, AP9 and SPM: new models for specifying the trapped energetic particle and space plasma environment. *Space Sci. Rev.* **179**: 579 - 615; 2013.

Grahn, D., Lombard, L.S., Carnes, B.A., The comparative tumorigenic effects of fission neutrons and cobalt-60 γ rays in the $B6CF_1$ mouse. *Rad. Res.* **129**: 19-36; 1992.

Grant, E.J., Brenner, A., Sugiyama, H., Sakata, R., Sadakane, A., Utada, M., Cahoon, E.K., Milder, C.M., Soda, M., Cullings, H.M., Preston, D.L., Mabuchi, K., Ozasa, K., Solid cancer incidence among the Life Span Study of atomic bomb survivors: 1958–2009. *Rad. Res.* **187**: 513-537; 2017.

Griffiths, S.D., Marsden, S.J., Wright, E.G., Greaves, M.F., Goodhead, D.T., Lethality and mutagenesis of B lymphocyte progenitor cells following exposures to α-particles and X-rays. *Int. J. Radiat. Biol*. **66**: 197-205; 1994.

Grogan, H.A., Sinclair, W.K., Voilleque, P.G., Risks of fatal cancer from inhalation of 239,240 plutonium by humans: a combined four-method approach with uncertainty evaluation. *Health Phys*. **80**: 447-461; 2001.

Hada, M., Chappell, L.J., Wang, M., George, K.A., Cucinotta, F.A., Induction of chromosomal aberrations at fluences of less than one HZE particle per cell nucleus. *Rad. Res.* **182**: 368-379; 2014.

Hafner, L., Walsh, L., Application of multi-method-multi-model inference to radiation related solid cancer excess risk models for astronaut risk assessment. *Z. Med. Phys.* **34**: 83-91; 2024.

Ham, D.W., Song, B., Gao, J., Yu, J., Sachs, R.K., Synergy theory in radiobiology. *Rad. Res.* **189**: 225–237; 2017.

Han, Z.B., Suzuki, H., Suzuki, F., Suzuki, M., Furusawa, Y., Kato, T., Ikenaga, M., Relative biological effectiveness of accelerated heavy ions for induction of morphological transformation in Syrian hamster embryo cells. *J. Radiat. Res.* **39**: 193-201; 1998.

Hanahan, D., Hallmarks of cancer – then and now, and beyond. *Cell* **189**: 2254-2277; 2026.

Hassler, D.M., Zeitlin, C., Wimmer-Scweingruber, R.R., Ehresmann, B., Rafkin, S., et al., Mars surface radiation environment measured with the Mars Science Laboratory's Curiosity rover. *Science* **343**: 6169; 2014.

Hassler, D.M., Norbury, J.W., Reitz, G., Mars science laboratory radiation assessment detector (MSL/RAD) modeling workshop proceedings. *Life Sci. Space Res.* **14**: 1-2; 2017.

Hayes, B.M., Causey, O.I., Gersey, B.B., Benton, E.R., Active tissue equivalent dosimeter: a tissue equivalent proportional counter flown onboard the International Space Station. *Nucl. Instr. Meth. A* **1028**: 166389; 2022.

Hei, T.K., Chen, D.J., Brenner, D.J., Hall, E.J., Mutation induction by charged particles of defined linear energy transfer. *Carcinogenesis* **9**: 1233-1236; 1988.

Heynderickx, D., Lemaire, J., Daly, E.J., Evans, H., Calculating low-altitude trapped particle fluxes with the NASA Models AP-8 and AE-8. *Rad. Meas.* **26**: 947-952; 1996a.

Heynderickx, D., Lemaire, J., Daly, E.J., Historical review of the different procedures used to compute the L-parameter. *Rad. Meas.* **26**: 325-331; 1996b.

Hu, S., Barzilla, J.E., Semones, E., Acute radiation risk assessment and mitigation strategies in near future exploration spaceflights. *Life Sci. Space Res.* **24**: 25-33; 2020.

Hu, S., Barzilla, J.E., Nunez, M., Semones, E., Real-time dose prediction for Artemis missions. J. *Space Weather Space Clim.* **15**: 1; 2025.

Huang, E.G., Lin, Y., Ebert, M., Ham, D.W., Zhang, C.Y., Sachs, R.K., Synergy theory for murine harderian gland tumours after irradiation by mixtures of high energy ionized atomic nuclei. *Rad. Env. Biophys.* **58**: 151–166; 2019.

Huang, E.G., Wang, R.-Y., Xie, L., Chang, P., Yao, G., Zhang, B., Ham, D.W., Lin, Y., Blakely, E.A., Sachs, R.K., Simulating galactic cosmic ray effects: synergy modeling of murine tumor prevalence after exposure to two one-ion beams in rapid sequence. *Life Sci. Space Res.* **25**: 107-118; 2020.

Huff, J.L., Plante, I., Blattnig, S.R., Norman, R.B., Little, M.P., Khera, A., Simonsen, L.C., Patel, Z.S., Cardiovascular disease risk modeling for astronauts: making the leap from Earth to space. *Front. Cardiovasc. Med.* **9**: 873597; 2022.

Huff, J.L., Poignant, F., Rahmanian, S., Khan, N., Blakely, E.A., Britten, R.A., Chang, P., Fornace, A.J., Hada, M., Kronenberg, A., Norman, R.B., Patel, Z.S., Shay, J.W., Weil, M.M., Simonsen, L.C., Slaba, T.C., Galactic cosmic ray simulation at the NASA space radiation laboratory – progress, challenges, and recommendations on mixed-field effects. *Life Sci. Space Res.* **36**: 90-104; 2023.

ICRP, International Commission on Radiological Protection. Recommendations of the international commission on radiological protection. ICRP Publication 60, Pergamon Press; 1991.

ICRP, International Commission on Radiological Protection. Basic anatomical and physiological data for use in radiobiological protection: reference values. ICRP Publication 89, Pergamon Press; 2001.

ICRP, International Commission on Radiological Protection. Relative biological effectiveness (RBE), quality factor (Q), and radiation weight factor (w_R). ICRP Publication 92, Pergamon Press; 2003.

ICRP, International Commission on Radiological Protection. The 2007 recommendations of the international commission on radiological protection. ICRP Publication 103, Pergamon Press; 2007.

ICRP, International Commission on Radiological Protection. Cancer risk from exposure to plutonium and uranium. ICRP Publication 150, Pergamon Press; 2021.

ICRP, International Commission on Radiological Protection. Scientific Evidence Relevant to the Assessment of Solid Cancer Radiation Risk at Low Dose and Low Dose Rate., in press; 2026.

Ingram, S.P., Henthorn, N.T., Warmenhoven, J.W., Kirkby, N.F., Mackay, R.I., Kirkby, K.J., Merchant, M.J., Hi-C implementation of genome structure for in silico models of radiation-induced DNA damage. *PLoS Comput. Biol.* **16**: e1008476; 2020.

Islami, F., Marlow, E.C., Thompson, B., McCullough, M.L., Rumgay, H., Gapstur, S.M., Patel, A.V., Soerjomataram, I., Jemal, A., Proportion and number of cancer cases and deaths attributable to potentially modifiable risk factors in the United States, 2019. *CA Cancer J. Clin.* **74**: 405-432; 2024.

Jaiswal, S., Fontanillas, P., Flannick, J., Manning, A., Grauman, P. V., Mar, B. G., et al., Age-related clonal hematopoiesis associated with adverse outcomes. *N. Engl. J. Med.* **371**, 2488–2498; 2014.

Jolliff, B.L., Wieczorek, M.A., Shearer, C.K., Neal, C.R., editors. New views of the Moon. *Rev. Mineral. Geochem.* **60**; 2006.

Justus, C.G., Johnson, D.L., Mars global reference atmospheric model 2001 version (Mars-GRAM 2001). NASA TM 2001-210961; 2001.

Katz, R., Ackerson, B., Homayoonfar, M., Sharma, S.C., Inactivation of cells by heavy ion bombardment. *Rad. Res.* **47**: 402-425; 1971.

Kiefer, J., Schmidt, P., Koch, S., Mutations in mammalian cells induced by heavy charged particles: an indicator for risk assessment in space. *Rad. Res.* **156**: 607-611; 2001.

Kim, M.Y., Wilson, J.W., Cucinotta, F.A., Simonsen, L.C., Atwell, W., Badavi, F.F., Miller, J., Contribution of high charge and energy (HZE) ions during solar-particle event of September 29, 1989. NASA TP 1999-209320; 1999.

Kim, M.Y., Hu, S., Nounu, H.N., Cucinotta, F.A., Development of graphical user interface for ARRBOD (acute radiation risk and BRYNTRN organ dose projection). NASA TP 2010-216116; 2010.

Kim, M.Y., De Angelis, G., Cucinotta, F.A., Probabilistic assessment of radiation risk for astronauts in space missions. *Acta Astronautica* **68**: 747-759; 2011.

King, J.H., Solar proton fluences for 1977-1983 space missions. *J Space. Rockets* **11**: 401-408; 1974.

Kocher, D.C., Apostoaei, A.I., Hoffman, F.O., Radiation effectiveness factors for use in calculating probability of causation of radiogenic cancers. *Health Phys.* **89**: 3-32; 2005.

Kramer, R., Vieira, J.W., Khoury, H.J., Lima, F.R.A., Fuelle, D., All about MAX: a male adult voxel phantom for Monte Carlo calculations in radiation protection dosimetry. *Phys. Med. Bio.* **48**: 1239-1262; 2003.

Kramer, R., Vieira, J.W., Khoury, H.J., Lima, F.R.A., Loureiro ECM, Lima VJM, Hoff G, All about FAX: a female adult voxel phantom for Monte Carlo calculations in radiation protection dosimetry. *Phys. Med. Bio.* **49**: 5203-5216; 2004.

Kranert, T., Schneider, E., Kiefer, J., Mutation induction in V79 Chinese hamster cells by very heavy ions. *Int. J. Radiat. Biol.* **58**: 975-987; 1990.

Kronenberg, A., Mutation induction in human lymphoid cells by energetic heavy ions. *Adv. Space Res.* **14**: 339-346; 1994.

Lafuma, J., Chmelevsky, D., Chameaud, J., Morin, M., Masse, R., Kellerer, A.M., Lung carcinomas in Sprague-Dawley rats after exposure to low doses of radon daughters, fission neutrons, or γ rays. *Rad. Res.* **118**: 230-245; 1989.

Lezniak, J.A., Webber, W.R., The charge composition and energy spectra of cosmic-ray nuclei from 3000 MeV per nucleon to 50 GeV per nucleon. *Astrophys. J.* **233**: 676-696; 1978.

Little, M.P., Hoel, D.G., Molitor, J., Boice, J.D., Wakeford, R., Muirhead, C.R., New models for evaluation of radiation-induced lifetime cancer risk and its uncertainty employed in the UNSCEAR 2006 report. *Rad. Res.* **169**: 660-676; 2008.

Liu, W., Guo, J., Wang, Y., Slaba ,T.C., A comprehensive comparison of various galactic cosmic-ray models to the state-of-the-art particle and radiation measurements. *Astrophys. J. Suppl.* **271**: 29; 2024.

Loucas, B.D., Durante, M., Bailey, S.M., Cornforth, M.N., Chromosome damage in human cells by γ rays, α particles and heavy ions: track interactions in basic dose-response relationships. *Rad. Res.* **179**: 9-20; 2013.

Loucas, B.D., Shuryak, I., Cornforth, M.N., Three-color chromosome painting as seen through the eyes of mFISH: another look at radiation-induced exchanges and their conversion to whole-genome equivalency. *Front. Oncol.* **6**: 52; 2016.

Loucas, B.D., Shuryak, I., Kunkel, S.R., Cornforth, M.N., Dose-dependent transmissibility of chromosome aberrations at first mitosis after exposure to gamma rays. I. Modeling and implications related to risk assessment. *Rad. Res.* **197**: 376-383; 2022.

Martucci, M., et al., Proton fluxes measured by the PAMELA experiment from the minimum to the maximum solar activity for solar cycle 24. *Astrophys. J. Lett.* **854**; 2018.

Matthia, D., Ehresmann, B., Lohf, H., Kohler, J., Zeitlin, C., Appel, J., Sato, T., Slaba, T.C., Martin, C., Berger, T., Boehm, E., Boettcher, S., Brinza, D.E., Burmeister, S., Guo, J., Hassler, D.M., Posner, A., Rafkin, S.C.R., Reitz, G., Wilson, J.W., Wimmer-Schweingruber, R.F., The Martian surface radiation environment – a comparison of models and MSL/RAD measurements. *J. Space Weather Space Cli.* **6**: A13; 2016.

Malkani, S., et al., Circulating miRNA spaceflight signature reveals targets for countermeasure development. *Cell Rep.* **33**: 108448; 2020.

Matthia, D., Hassler, D.M., de Wet, W., Ehresmann, B., Firan, A., Flores-McLaughlin, J., Guo, J., Heilbronn, L.H., Lee, K., Ratliff, H., Rios, R.R., Slaba, T.C., Smith, M., Stoffle, N.N., Townsend, L.W., Berger, T., Reitz, G., Wimmer-Schweingruber, R.F., Zeitlin, C., The radiation environment on the surface of Mars – summary of model calculations and comparison to RAD data. *Life Sci. Space Res.* **14**: 18-28; 2017.

Matthia, D., Berger, T., Radiation exposure and shielding effects on the lunar surface. *Space Weather* **22**: e2024SW004095; 2024.
McKinney, G.W., Lawrence, D.J., Prettyman, T.H., Elphic, R.C., Feldman, W.C., Hagerty, J.J., MCNPX benchmark for cosmic ray interactions with the Moon. *J. Geo. Res.* **111**: E06004; 2006.

Menn, W., et al., The absolute flux of protons and helium at the top of the atmosphere using IMAX. *Astrophys. J.* **533**: 281-297; 2000.

Mertens, C.J., Slaba, T.C., Hu, S., Active dosimeter-based estimate of astronaut acute radiation risk for real-time solar energetic particle events. *Space Weather* **16**: 1291-1316; 2018.

Mertens, C.J., Slaba, T.C., Characterization of solar energetic particle radiation dose to astronaut crew on deep-space exploration missions. *Space Weather* **14**: 1650-1658; 2019.

Miller, R.C., Marino, S.A., Brenner, D.J., Martin, S.G., Richards, M., Randers-Pehrson, G., Hall, E.J., The biological effectiveness of radon-progeny alpha particles. II. Oncogenic transformation as a function of linear energy transfer. *Rad. Res.* **142**: 54-60; 1995.

Millour, E., Forget, F., Spiga, A., Vals, M., Zakharov, V., Montabone, L., Lefevre, F., Montmessin, F., Chaufray, J.Y., Lopez-Valverde, M.A., Gonzalez-Galindo, F., Lewis, S.R., Read, P.L., Desjean, M.C., Cipriani, F., The Mars climate database (Version 5.3). From Mars Express to ExoMars Scientific Workshop. Madrid, Spain; 2018.

Minagawa, G., The abundances and energy spectra of cosmic ray iron and nickel at energy from 1 to 10 GeV per amu. *Astrophys. J.* **248**: 847-855; 1981.

Mole, R.H., Papworth, D.G., Corp, M.J., The dose-response for X-ray induction of myeloid-leukemia in male CBA/H mice. *Br. J. Cancer* **47**: 285–291; 1983.

Naito, M., Kodaira, S., Charge-weighted quality factors based on LET for practical dose assessment of space radiation. *Life Sci. Space Res.* **51**: 25-32; 2026.

NASA, NASA Space Flight Human System Standard. NASA STD 3001, Vol I; 2022.

NASA, NASA Standard for Models and Simulations. NASA STD 7009; 2024.

NASEM, National Academies of Sciences Engineering and Medicine. Space radiation and astronaut health: managing and communicating cancer risks. The National Academies Press; 2021.

Nasonova, E., Füssel, K., Berger, S., Gudowska-Nowak, E., Ritter, S., Cell cycle arrest and aberration yield in normal human fibroblasts. I. Effects of X-rays and 195 MeV u(−1) C ions. *Int. J. Radiat. Biol.* **80**: 621-634; 2004.

NCI, *DevCan: Probability of Developing or Dying of Cancer Software, Version 6.9.1*. National Cancer Institute: Statistical Research and Applications Branch. Available at http://surveillance.cancer.gov/devcan; 2024.

NCRP, National Council on Radiation Protection and Measurements. Radiation protection guidance for activities in low Earth orbit. NCRP Report 132, Bethesda, MD; 2000.

NCRP, National Council on Radiation Protection and Measurements. Information needed to make radiation protection recommendations for space missions beyond low Earth orbit. NCRP Report 153, Bethesda, MD; 2006.

NCRP, National Council on Radiation Protection and Measurements. Radiation Protection for Space Activities: Supplement to Previous Recommendations. NCRP Commentary 23, Bethesda, MD; 2014.

NCRP, National Council on Radiation Protection and Measurements. Evaluation of the Relative Effectiveness of Low-Energy Photons and Electrons in Inducing Cancer in Humans. NCRP Report 181, Bethesda, MD; 2018.

NCRP, National Council on Radiation Protection and Measurements. Evaluation of a sex-specific difference in lung cancer radiation risk and approaches for improving lung cancer radiation risk projection (with a focus on application to space activities). NCRP Commentary 32, Bethesda, MD; 2022.

Norbury, J.W., Miller, J., Review of nuclear physics experimental data for space radiation. *Health Phys.* **103**, 640-642; 2012.

Norbury, J.W., Miller, J. Adamczyk, A.M., Heilbronn, L.H., Townsend, L.W., Blattnig, S.R., Norman, R.B., Guetersloh, S.B., Zeitlin, C.J., Nuclear Data for Space Radiation. *Rad. Meas.* **47**: 315-363; 2012.
Norbury, J.W., Light ion and multiple nucleon removal due to electromagnetic dissociation. *Nuc. Instr. Meth. A* **703**: 220-243; 2013.

Norbury, J.W., Slaba, T.C., Aghara, S., Badavi, F.F., Blattnig, S.R., Clowdsley, M.S., Heilbronn, L.H., Maung, K.M., Mertens, C.J., Miller, J., Norman, R.B., Sandridge, C.A., Singleterry, R.C., Sobolevsky, N., Townsend, L.W., Werneth, C.M., Wilson, J.W., Xiaojing, X., Zeitlin, C., Advances in Space Radiation Physics and Transport. *Life Sci. Space Res.* **22**: 98-124; 2019.

Norbury, J.W., Double-differential fragmentation (DDFRG) models for proton and light ion production in high energy nuclear collisions. *Nuc. Instr. Meth. A* **986**: 164681; 2021.

Norbury, J.W., DDFRG2: double-differential fragmentation model for pion production in high energy nuclear collisions. *Nuc. Instr. Meth. A* **1053**: 168336; 2023.

Norbury, J.W., DDFRG3: double-differential fragmentation model for neutron production in high energy nuclear collisions. *Nuc. Instr. Meth. A* **1071**: 170056; 2025.

Norman, R.B., Slaba, T.C., Blattnig, S.R., An extension of HZETRN for cosmic ray initiated electromagnetic cascades. *Adv. Space Res.* **51**: 2251-2260; 2013.

NRC, National Research Council. Health risks from exposure to low levels of ionizing radiation. BEIR VII Phase 2 report. National Academies Press; 2006.

NRC, National Research Council. Technical evaluation of the NASA model for cancer risk to astronauts due to space radiation 2012. The National Academies Press; 2012.

Nymmik, R.A., Time lag of galactic cosmic ray modulation: conformity to general regularities and influence on particle energy spectra. *Adv. Space Res.* **26**: 1875-2000; 2000.

O'Neill, P.M., Badhwar-O'Neill galactic cosmic ray model updated based on advanced composition explorer (ACE) energy spectra from 1997 to present. *Adv. Space Res.* **37**: 1727-1733; 2006.

O'Neill, P.M., Badhwar-O'Neill galactic cosmic ray flux model – revised. *IEEE Trans. Nucl. Sci.* **57**: 3148 – 3153; 2010.

O'Neill, P.M., Badhwar-O'Neill 2011 galactic cosmic ray flux model description. NASA TP 2013-217376; 2013.

O'Neill, P.M., Golge, S., Slaba, T.C., Badhwar-O'Neill 2014 galactic cosmic ray flux model description. NASA TP 2015-218569; 2015.

Panov, A.D., et al., Energy spectra of abundant nuclei of primary cosmic rays from the data of ATIC-2 experiment: final results. *Russ. Acad. Sci. Phys.* **73**: 564-567; 2009.

Patel, Z.S., Brunstetter, T.J., Tarver, W.J., Whitmire, A.M., Zwart, S.R., Smith, S.M., Huff, J.L., Red risks for a journal to the red planet: The highest priority human health risks for a mission to Mars. *npj Micro* **6**: 33; 2020.

Peng, Y., Brown, N., Finnon, R., Warner, C.L., Liu, X., Genik, P.C., Callan, M.A., Ray, F.A., Borak, T.B., Badie, C., Bouffler, S.D., Ullrich, R.L., Bedford, J.S., Weill, M.M., Radiation leukemogenesis in mice: Loss of *PU.1* on chromosome 2 in CBA and C57BL/6 mice after irradiation with 1 GeV/nucleon 56Fe ions, X rays or gamma rays. Part I. experimental observations. *Rad. Res.* **171**: 474–483; 2009.

Penninckx, S., Pariset, E., Cekanaviciute, E., Costes, S.V., Quantification of radiation-induced DNA double strand break repair foci to evaluate and predict biological responses to ionizing radiation. *NAR Cancer* **3**: zcab046; 2021.

Phillips, E.N., Xia, F., Kelsey, K.T., Liber, H.L., Spectra of spontaneous and X-ray-induced mutations at the hprt locus in related human lymphoblast cell lines that express wild-type or mutant p53. *Rad. Res.* **143**: 255-262; 1995.

Plante, I., Cucinotta, F.A., Ionization and excitation cross sections for the interaction of HZE particles in liquid water and application to Monte Carlo simulation of radiation tracks. *New J. Phys.* **10**: 125020; 2008.

Plante, I., Cucinotta, F.A., Monte-Carlo Simulation of Ionizing Radiation Tracks in Applications of Monte Carlo Methods in Biology, Medicine and Other Fields of Science; Mode, C.B., Ed.; InTech: Rijeka, Croatia, pp. 315-56; 2011.

Plante, I., Ponomarev, A., Patel, Z., Slaba, T.C., Hada, M., RITCARD: radiation-induced tracks, chromosome aberrations, repair and damage. *Rad. Res.* **192**: 282-298; 2019a.

Plante, I., Slaba, T.C., Shavers, Z., Hada, M., A bi-exponential repair algorithm for radiation-induced double-strand breaks: Application to simulation of chromosome aberrations. *Genes* **10**: 936; 2019b.

Poignant, F., Plante, I., Patel, Z.S., Huff, J.L., Slaba, T.C., Geometrical properties of the nucleus and chromosome intermingling are possible major parameters of chromosome aberration formation. *Int. J. Mol. Sci.* **23**: 8638; 2022.

Poignant, F., Huff, J.L., Kunkel, S.R., Plante, I., Slaba, T.C., Effect of fluorescence in situ hybridization detection threshold on chromosome aberration counting: a simulation study. *Life Sci. Space Res.* **46**: 154-168; 2025.

Poignant, F., Huff, J.L., Plante, I., Slaba, T.C., RITCARD: a simulation tool for predicting space-radiation induced chromosome aberrations. Part 1: parameter sensitivity analysis and calibration. *Life Sci. Space Res.*, submitted; 2026.

Ponomarev, A.L., Cucinotta, F.A., Sachs, R.K., Brenner, D.J., Peterson, L.E., Extrapolation of the DNA fragment-size distribution after high-dose irradiation to predict effects at low doses. *Rad. Res.* **156**: 594-597; 2001.

Ponomarev, A.L., Cucinotta, F.A., NASA radiation track image GUI for assessing space radiation biological effects. NASA TP 2006-213719; 2006.

Ponomarev, A.L., Costes, S.V., Cucinotta, F.A., Stochastic properties of radiation-induced DSB: DSB distributions in large scale chromatin loops, the HPRT gene and within the visible volumes of DNA repair foci. *Int. J. Radiat. Biol.* **84**: 916-929; 2008

Ponomarev, A.L., Huff, J., Cucinotta, F.A., The analysis of the densely populated patterns of radiation-induced foci by a stochastic, Monte Carlo model of DNA double-strand breaks induction by heavy ions. *Int. J. Radiat. Biol.* **86**: 507-515; 2010.

Ponomarev, A.L., George, K., Cucinotta, F.A., Computational model of chromosome aberration yield induced by high-and low-LET radiation exposures. *Rad. Res.* **177**: 727-737; 2012.

Ponomarev, A.L., George, K., Cucinotta, F.A., Generalized time-dependent model of radiation-induced chromosomal aberrations in normal and repair-deficient human cells. *Rad. Res.* **181**, 284-292; 2014.

Preston, D.L., Pierce, D.A., Shimizu, Y., Cullings, H.M., Fujita, S., Funamoto, S., Kodama, K., Effect of recent changes in atomic bomb survivor dosimetry on cancer mortality risk estimates. *Rad. Res.* **162**: 377-389; 2004.

Preston, D.L., Ron, E., Tokuoka, S., Funamoto, S., Nisha, N., Soda, M., Mabuchi, K., Kodama, K., Solid cancer incidence in Atomic Bomb Survivors: 1958-1998. *Rad. Res.* **168**: 1-64; 2007.

Rahmanian, S., Slaba, T.C., George, S., Braby, L.A., Bhattacharya, S., Straume, T., Santa Maria, S.R., Galactic cosmic ray environment predictions for the NASA BioSentinel mission, part 2: post-mission validation. *Life Sci. Space Res.* **44**: 134-142; 2025a.

Rahmanian, S., Slaba, T.C., Werneth, C.M., Updated background incidence, mortality, and survival rates for the NASA cancer risk model: 2018, 2019, 2021 combined data. NASA TP 2025-0006549; 2025b.

Sawyer, D.M., Vette, J.I., AP-8 trapped proton environments for solar maximum and solar minimum. NSSDC/WDC-A-R&S 76–06; 1976.

Shafirkin, A.V., Grigoriev, Y.G. Ushakov, I.B., Shurshakov, V.A., Biological effectiveness of fast neutrons and accelerated multicharged ions for derivation of a new dependence of space radiation quality coefficients on linear energy transfer. *Hum. Physiol.* **48**: 871-880; 2022.

Shavers, M.R., Semones, E.J., Shurshakov, V., Dobynde, M., Sato, T., Komiyama, T., Tomi, L., Chen, J., El-Jaby, S., Straube, U., Li, C., Ruhm, W., Comparison of dose and risk estimates between ISS partner agencies for a 30-day lunar mission. *Zeitschift furMedizinische Physik* **34**: 31-43; 2024a.

Shavers, M.R., Semones, E.J., Tomi, L., Chen, J., Straube, U., Komiyama, T., Shurshakov, V., Li, C., Ruhm, W., Space agency-specific standards for crew dose and risk assessment of ionising radiation exposures for the International Space Station. *Zeitschift furMedizinische Physik* **34**: 14-30; 2024b.

Shellabarger, C.J., Chmelevsky, D., Kellerer, A.M., Stone, J.P., Holtzman, S., Induction of mammary neoplasms in the ACI rat by 430-keV neutrons, X-rays, and diethylstilbestrol. *JNCI* **69**: 1135-1146; 1982.

Shikaze, Y., et al., Measurements of 0.2-20 GeV/n cosmic-ray proton and helium spectra from 1997-2002 with the BESS spectrometer. *Astroparticle Phys.* **28**: 154-167; 2008.

Shuryak, I., Fornace, A.J., Datta, K., Suman, S., Kumar, S., Sachs, R.K., Brenner, D.J., Scaling human cancer risks from low LET to high LET when dose-effect relationships are complex. *Rad. Res.* **187**: 476-482; 2017a.

Shuryak, I., Loucas, B.D., Cornforth, M.N., Seeking beta: experimental considerations and theoretical implications regarding the detection of curvature in dose-response relationships for chromosome aberrations. *Rad. Res.* **187**: 7-19; 2017b.

Shuryak, I., Brenner, D.J., Review of quantitative mechanistic models of radiation-induced non-targeted effects (NTE). *Radiat. Prot. Dosimetry* **192**: 236-252; 2020.

Shuryak, I., Slaba, T.C., Plante, I.P., Poignant, F., Blattnig, S.R., Brenner, D.J., A practical approach for continuous in situ characterization of radiation quality factors in space. *Sci. Rep.* **12**: 1453; 2022.

Simon, M., Ormes, J.F., Balasubrahmanyan, V.K., Arens, J.F., Energy spectra of cosmic-ray nuclei to above 100 GeV per nucleon. *Astrophys. J.* **239**: 712-724; 1980.

Simonsen, L.C., Slaba, T.C., Ensemble methodologies for astronaut cancer risk assessment in the face of large uncertainties. NASA TP 2020-5008710; 2020.

Simonsen, L.C., Slaba, T.C., Guida, P., Rusek, A., NASA's first ground-based galactic cosmic ray simulator: enabling a new era in space radiobiology research. *Plos Biology* **18**: e3000669; 2020.

Simonsen, L.C., Slaba, T.C., Improving astronaut cancer risk assessment from space radiation with an ensemble model framework. *Life Sci. Space Res.* **31**: 14-28; 2021.

Singleterry, R.C., Walker, S.A., Clowdsley, M.S., A simple engineering analysis of solar particle event high energy tails and their impact on vehicle design. NASA TP 2016-219183; 2016.

Slaba, T.C., Qualls, G.D., Clowdsley, M.S., Blattnig, S.R., Walker, S.A., Simonsen, L.C., Utilization of CAM, CAF, MAX, and FAX for space radiation analyses using HZETRN. *Adv. Space Res.* **45**: 866-883; 2010a.

Slaba, T.C., Blattnig, S.R., Clowdsley, M.S., Walker, S.A., Badavi, F.F., An improved neutron transport algorithm for HZETRN. *Adv. Space Res.* **46**: 800-810; 2010b.

Slaba, T.C., Blattnig, S.R., Badavi, F.F., Faster and more accurate transport procedures for HZETRN. *J. Comp. Phys.* **229**: 9397-9417; 2010c.

Slaba, T.C., Blattnig, S.R., Aghara, S.K., Townsend, L.W., Handler, T., Gabriel, T.A., Pinsky, L.S., Reddell, B., Coupled neutron transport for HZETRN. *Rad. Meas.* **45**: 173-182; 2010d.

Slaba, T.C., Blattnig, S.R., Clowdsley, M.S., Variation in lunar neutron dose estimates. *Rad. Res.* **176**: 827-841; 2011.

Slaba, T.C., Faster heavy ion transport for HZETRN. NASA TP 2013-217803; 2013.

Slaba, T.C., Mertens, C.J., Blattnig, S.R., Radiation shielding optimization on Mars. NASA TP 2013-217983; 2013a.

Slaba, T.C., Blattnig, S.R., Reddell, B., Bahadori, A., Norman, R.B., Badavi, F.F., Pion and electromagnetic contribution to dose: comparisons of HZETRN to Monte Carlo results and ISS data. *Adv. Space Res.* **52**: 62-78; 2013b.

Slaba, T.C., Wilson, J.W., Badavi, F.F., Reddell, B.D., Bahadori, A.A., Solar proton exposure of an ICRU sphere within a complex structure: ray-trace geometry. *Life Sci. Space Res.* **9**: 77-83; 2016.

Slaba, T.C., Stoffle, N.N., Evaluation of HZETRN on the Martian Surface: Sensitivity tests and model results. *Life Sci. Space Res.* **14**: 29-35; 2017.

Slaba, T.C., Bahadori, A.A., Reddell, B.D., Singleterry, R.C., Clowdsley, M.S., Blattnig, S.R., Optimal shielding thickness for galactic cosmic ray environments. *Life Sci. Space Res.* **12**: 1-15; 2017.

Slaba, T.C., Whitman, K., The Badhwar-O'Neill 2020 Model. NASA TP 2019-220419; 2019.

Slaba, T.C., Whitman, K., The Badhwar-O'Neill 2020 Model. *Space Weather* **18**: e2020SW002456; 2020.

Slaba, T.C., Wilson, J.W., Werneth, C.M., Whitman, K., Updated deterministic radiation transport for future deep space missions. *Life Sci. Space Res.* **27**: 6-18; 2020a.

Slaba, T.C., Plante, I., Ponomarev, A., Patel, Z., Hada, M., Determination of chromosome aberrations in human fibroblasts irradiated by mixed fields generated with shielding. *Rad. Res.* **194**: 246-258; 2020b.

Slaba, T.C., Historical reconstruction of astronaut cancer risk: context for recent solar minima. *Space Weather* **19**: e2021SW002851; 2021.

Slaba, T.C., Poignant, F., Rahmanian, S., A microdosimetric dose response model for monoenergetic ions and doses relevant for space radiation carcinogenesis. *Rad. Res*. **204**: 81-100; 2025a.

Slaba, T.C., Rahmanian, S., George, S., Laramore, D., Norbury, J.W., Werneth, C.M., Zeitlin, C., Validated space radiation exposure predictions from Earth to Mars during Artemis-I. *npj Micro.* **11**: 1-9; 2025b.

Slaba, T.C., Poignant, F., An ensemble dose-response model for monoenergetic ions and doses relevant for space radiation carcinogenesis. *Life Sci. Space Res.* **51**: 71-82; 2026.

Spence, H. E., Case, A. W., Golightly, M. J., Heine, T., Larsen, B. A., Blake, J. B., … Charara, Y., CRaTER: the cosmic ray telescope for the effects of radiation experiment on the lunar reconnaissance orbiter mission. *Space Sci. Rev.* **150**: 243–284; 2010.

Sridharan, D.M., Chappell, L.J., Whalen, M.K., Cucinotta, F.A., Pluth, J.M., Defining the biological effectiveness of components of high-LET track structure. *Rad. Res.* **184**: 105-119; 2015.

Sridharan, D.M., et al., Evaluating biomarkers to model cancer risk post cosmic ray exposure. *Life Sci. Space Res.* **9**: 19-47; 2016.

Stabilini, A., Hafner, L., Walsh, L., Comparison and multi-model inference of excess risks models for radiation-related solid cancer. *Rad. Env. Bio.* **62**: 17-34; 2023.

Stegeman, L., Slaba, T.C., Huff, J.L., Semones, E., Zawaski, J.A., Saha, J., Utilizing the Life Span Study data in NASA astronaut cancer risk assessment. *Carcinogenesis*, **46**: bgaf076; 2025.

Stoll, U., Schmidt, A., Schnieder, E., Kiefer, J., Killing and mutation of Chinese hamster V79 cells exposed to accelerated oxygen and neon ions. *Rad. Res.* **142**: 288-294; 1995.

Stoll, U., Barth, B., Scheerer, N., Schneider, E., Kiefer, J., HRPT mutations in V79 Chinese hamster cells induced by accelerated Ni, Au and Pb ions. *Int. J. Radiat. Biol.* **70**: 15-22; 1996.

Stone, E.C., Frandsen, A.M., Mewaldt, R.A., Christian, E.R., Margolies, D., Ormes, J.F., Snow, F., The advanced composition explorer, *Space Sci. Rev.* **86**: 1-22; 1998.

Storer, J.B., Serrano, L.J., Darden, E.B., Jernigan, M.C., Ullrich, R.L., Life shortening in RFM and BALB/c mice as a function of radiation quality, dose and dose rate. *Rad. Res.* **78**: 122-161; 1979.

Storer, J.B., Ullrich, R.L., Life shortening in BALB/c mice following brief, protracted or fractionated exposures to neutrons *Rad. Res.* **96**: 335-347; 1983.

Suman, S., Kumar, S., Moon, B.H., Strawn, S.J., Thakor, H., Fan, Z., Shay, J.W., Fornace, A.J., Datta, K., Relative biological effectiveness of energetic heavy ions for intestinal tumorigenesis shows male preponderance and radiation type energy dependence in $APC^{1638N/+}$ mice. *Int. J. Radiat. Oncol. Biol. Phys.* **95**: 131-138; 2016.

Surgeon General, The health consequences of smoking—50 years of progress: a report of the surgeon general. National Center for Chronic Disease Prevention and Health Promotion (US) Office on Smoking and Health., Rockville, MD; 2014.

Suzuki, M., Watanabe, M., Kanai, T., Kase, Y., Yatagai, F., Kato, T., Matsubara, S., LET dependence of cell death, mutation induction and chromatin damage in human cells irradiated with accelerated carbon ions. *Adv. Space Res.* **18**: 127-136; 1996.

Suzuki, M., Tsuruoka, C., Kanai, T., Kato, T., Yatagai, F., Watanabe, M., Qualitative and quantitative difference in mutation induction between carbon-and neon-ion beams in normal human cells. *Biol. Sci. Space* **17**: 302-306; 2003.

Suzuki, M., Tsuruoka, C., Kanai, T., Kato, T., Yatagai, F., Watanabe, M., Cellular and molecular effects for mutation induction in normal human cells irradiated with accelerated neon ions. *Mut. Res.* **594**: 86-92; 2006.

Tai, H., Bichsel, H., Wilson, J.W., Shinn, J.L., Cucinotta, F.A., Badavi, F.F., Comparison of Stopping Power and Range Databases for Radiation Transport Study. NASA TP 3644; 1997.

Thacker, J., Stretch, A., Stephens, M.A., Mutation and inactivation of cultured mammalian cells exposed to beams of accelerated heavy ions II. Chinese hamster V79 cells. *Int. J. Radiat. Biol.* **36**: 137-148; 1979.

Thompson, S.J., Prise, K. M., McMahon, S.J., Monte Carlo damage models of different complexity levels predict similar trends in radiation induced DNA damage. *Phys. Med. Biol.* **69**: 215035; 2024.

Townsend, L.W., Stephens, D.L., Hoff, J.L., Zapp, E.N., Moussa, H.M., Miller, T.M., Campbell, C.E., Nichols, T.F., The Carrington event: possible doses to crews in space from a comparable event. *Adv. Space Res.* **38**: 226-231; 2006.

Townsend, L.W., Adams, J.H., Blattnig, S.R., Clowdsley, M.S., Fry, D.J., Jun, I., McLeod, C.D., Minow, J.I., Moore, D.F., Norbury, J.W., Norman, R.B., Reames, D.V., Schwadron, N.A., Semones, E.J., Singleterry, R.C., Slaba, T.C., Werneth, C.M., Xapsos, M.A., Solar Particle Event Storm Shelter Requirements for Missions Beyond Low Earth Orbit. *Life Sci. Space Res.* **17**: 32-39; 2018.

Trani, D., Datta, K., Doiron, K., Kallakury, B., Fornace, A.J., Enhanced intestinal tumor multiplicity and grade in vivo after HZE exposure: mouse models for space radiation risk estimates. *Rad. Env. Bio.* **49**: 389–396; 2010.

Tripathi, R.K., Cucinotta, F.A., Wilson, J.W., Universal parameterization of absorption cross sections, NASA TP 3621; 1997.

Tripathi, R.K., Wilson, J.W., Cucinotta, F.A., Nuclear absorption cross sections using medium modified nucleon–nucleon amplitudes. *Nuc. Instr. Meth. B* **145**: 277-282; 1998.

Tripathi, R.K., Cucinotta, F.A., Wilson, J.W., Universal parameterization of absorption cross sections – light systems, NASA TP-1999-209726; 1999.

Tsuboi, K., Yang, T.C., Chen, D.J., Charged-particle mutagenesis I. Cytotoxic and mutagenic effects of high-LET charged iron particles on human skin fibroblasts. *Rad. Res.* **129**: 171-176; 1992.

Tsuruoka, C., Suzuki, M., Furusawa, Y., Anzai, K., Okayasu, R., The influence of mutation induction in normal human fibroblasts irradiated with X rays and iron ions. *Biol. Sci. Space* **23**: 55-60; 2009.

Tylka, A.J., Adams, J.H., Boberg, P.R., Brownstein, B., Dietrich, W.F., Flueckiger, E.O., Peterson, E.L., Shea, M.A., Smart, D.F., Smith, E.C., CREME96: a revision of the cosmic ray effects on micro-electronics code. IEEE Trans. Nucl. Sci. 44: 2150–2160; 1997.

Uddin, M. M., Zhou, Y., Bick, A. G., Burugula, B. B., Jaiswal, S., Desai, P., et al. (2022). Longitudinal profiling of clonal hematopoiesis provides insight into clonal dynamics. *Immun. Ageing A* **19**, 23; 2022.

Ullrich, R.L., Preston, R.J., Myeloid leukemia in male RFM mice following irradiation with fission spectrum neutrons or gamma rays. *Rad. Res.* **109**: 165–170; 1987.

UNSCEAR, United Nations scientific committee on the effects of atomic radiation. Sources and effects of ionizing radiation. UNSCEAR 1993 report to the general assembly, with scientific annexes. United Nations, New York NY; 1993.

UNSCEAR, United Nations scientific committee on the effects of atomic radiation. Sources and effects of ionizing radiation. UNSCEAR 2006 report to the general assembly, with scientific annexes. United Nations, New York NY; 2006.

Upton, A.C., Randolph, M.L., Conklin, J.W., Kastenbaum, M.A., Slater, M., Melville, G.S.J., Conte, F.P., Sproul, J.A., Late effects of fast neutrons and gamma-rays in mice as influenced by the dose rate of irradiation: life shortening. *Rad. Res.* **32**: 493-509; 1967.

Vaeth, M., Pierce, D.A., Calculating excess lifetime risks in relative risk models. *Environ. Health. Per.* **87**: 83-94; 1990.

Vette, J.I., Models of the trapped radiation environment, volume 1: inner zone protons and electrons. NASA SP-3024; 1966.

Vette, J.I., The NASA/National Space Science Data Center Trapped Radiation Environment Model Program (TREMP) (1964–1991), NSSDC/WDC-A-R&S 91-29; 1991.

Waldren, C., Vannais, D., Drabek, R., Gustafson, D., Kraemer, S., Lenarczyk, M., Kronenberg, A., Hei, T., Ueno, A., Analysis of mutant quantity and quality in human-hamster hybrid A_L and A_L-179 cells exposed to ^{137}Cz-γ or HZE-Fe ions. *Adv. Space Res.* **22**: 579-585; 1998.

Waligorski, M.P., Sinclair, G.L., Katz, R., Radiosensitivity parameters for neoplastic transformations in C3H10T1/2 cells. *Rad. Res.* **111**: 424-437; 1987.

Walsh, L., Neutron relative biological effectiveness for solid cancer incidence in the Japanese A-bomb survivors: an analysis considering the degree of independent effects from γ-ray and neutron absorbed doses with hierarchical partitioning. *Radiat. Env. Biophys.* **52**: 29-36; 2013.

Weil, M.M., Bedford, J.S., Bielefeldt-Ohmann, H., Ray, F.A., Genik, P.C., Ehrhart, E.J., Fallgren, C.M., Hailu, F., Battaglia, C.L.R., Charles, B., Callan, M.A., Ullrich, R.L., Incidence of acute myeloid leukemia and hepatocellular carcinoma in mice irradiated with 1 GeV/nucleon ^{56}Fe ions. *Rad. Res.* **172**: 213-219; 2009.

Werneth, C. M., Slaba, T. C., Blattnig, S. R., Huff, J. L., and Norman, A methodology for investigating the impact of medical countermeasures on the risk of exposure induced death. *Life Sci. Space Res.* **25**, 72–102; 2020.

Werneth, C.M., de Wet, W.C., Townsend, L.W., Maung, K.M., Norbury, J.W., Slaba, T.C., Norman, R.B., Blattnig, S.R., Ford, W.P., Relativistic abrasion-ablation de-excitation fragmentation (RAADFRG) model. *Nuc. Instr. Meth. B* **502**: 118-135; 2021.

Werneth, C. M., Slaba, T. C., Huff, J. L., Patel, Z. S., and Simonsen, L. C., Medical Countermeasure Requirements to Meet NASA's Space Radiation Permissible Exposure Limits for a Mars Mission Scenario. *Health Phys.* **123**, 116–127; 2022.

Werneth, C.M., Patel, Z.S., Thompson, M.S., Blattnig, S.R., Huff, J.L. (2024). Considering Clonal Hematopoiesis of Indeterminant Potential in Space Radiation Risk Analysis for Hematologic Cancers and Cardiovascular Disease. *Commun. Med.* **4**, 105; 2024.

Werneth, C.M., Norbury, J.W., Slaba, T.C., Review of Nuclear Cross Section Models in HZETRN2020, NASA TP-2025-0009529; 2025.

Wilson, J.W., Lamkin, S.L., Perturbation theory for charged-particle transport in one dimension. *Nuc. Sci. Eng.* **57**: 292-299; 1975.

Wilson, J.W., Analysis of the theory of heavy ion transport. NASA TN D-8381; 1977.

Wilson, J.W., Cosmic ray neutron albedo dose in low Earth orbit, *Health Phys.* **57**: 665-668; 1989.

Wilson, J.W., Townsend, L.W., Schimmerling, W., Khandelwal, G.S., Khan, F., Nealy, J.E., Cucinotta, F.A., Simonsen, L.C., Shinn, J.L., Norbury, J.W., Transport methods and interactions for space radiations. NASA RP 1257; 1991.

Wilson, J.W., Cucinotta, F.A., Shinn, J.L., Cell kinetics and track structure. In: Swenberg CE, et al., *Biological Effects and Physics of Solar and Galactic Cosmic Rays*. Plenum Press. New York, NY; 1993

Wilson, J.W., Shinn, J.L., Townsend, L.W., Tripathi, R.K., Badavi, F.F., Chun, S.Y., NUCFRG2: a semiempirical nuclear fragmentation model. *Nuc. Instr. Meth. B* **94**: 95-102; 1994.

Wilson, J.W., Tripathi, R.K., Badavi, F.F., Cucinotta, F.A., Standardized radiation shield design method: 2005 HZETRN. SAE ICES 2006-18; 2006.

Wilson, J.W., Slaba, T.C., Badavi, F.F., Reddell, B.D., Bahadori, A.A., Advances in NASA radiation transport research: 3DHZETRN. *Life Sci. Space Res.* **2**: 6-22; 2014.

Wilson, J.W., Slaba, T.C., Badavi, F.F., Reddell, B.D., Bahadori, A.A., 3DHZETRN: shielded ICRU spherical phantom. *Life Sci. Space Res.* **4**: 46-61; 2015a.

Wilson, J.W., Slaba, T.C., Badavi, F.F., Reddell, B.D., Bahadori, A.A., 3DHZETRN: neutron leakage in finite objects. *Life Sci. Space Res.* **7**: 27-38; 2015b.

Wilson, J.W., Slaba, T.C., Badavi, F.F., Reddell, B.D., Bahadori, A.A., Solar proton exposure of an ICRU sphere within a complex structure: combinatorial geometry. *Life Sci. Space Res.* **9**: 69-76; 2016.

Wilson, J.W., Werneth, C.M., Slaba, T.C., Badavi, F.F., Reddell, B.D., Bahadori, A.A., Effects of the Serber first step in 3DHZETRN-v2.1. *Life Sci. Space Res.* **26**: 10-27; 2020.

Wilson, J.W., Slaba, T.C., Werneth, C.M., Badavi, F.F., Reddell, B.D., Bahadori, A.A., Neutron diffusion correction in 3DHZETRN-V2: ENDF/B. NASA TP 2021-0020403; 2021.

Wolf, C., Lafuma, J., Masse, R., Morin, M., Kellerer, A.M., Neutron RBE for induction of tumors with high lethality in Sprague-Dawley rats. *Rad. Res.* **154**: 412-420; 2000.

Woolum, D.S., Burnett, D.S., Furst, M., Weiss, J.R., Measurement of the lunar neutron density profile. *Moon* **12**: 231-250; 1975.

Xapsos, M.A., Summers, G.P., Barth, J.L., Stassinopoulos, E.G., Burke, E.A., Probability model for worst case solar proton event fluences. *IEEE Trans. Nucl. Sci.* **46**: 1481–1485; 1999.

Xu, X., Blattnig, S.R., Slaba, T.C., A multilevel probabilistic dose response model for radiation-induced harderian gland tumor prevalence – single beam and mixed field effects. *Life Sci. Space Res.* **51**: 11-24; 2026.

Yang, T.C., Craise, L.M., Mei, M.T., Tobias, C.A., Neoplastic cell transformation by heavy charged particles. *Rad. Res.* **104**: 177-187; 1985.

Yucker, W.R., Huston, S.L., The computerized anatomical female. Final Report, MDC-6107, McDonnell Douglas Company; 1990.

Yucker, W.R., Reck, R.J., Computerized anatomical female body self-shielding distributions. Report, MDC 92H0749, McDonnell Douglas Company; 1992.

Zeitlin, C., Hassler, D.M., Wimmer-Schweingruber, R.F., Ehresmann, B., Appel, J., Berger, T., Bohm, E., Bottcher, S., Brinza, D.E., Burmeister, S., Guo, J., Kohler, J., Lohf, H., Marin, C., Matthia, D., Posner, A., Rafkin, S., Reitz, G., Tyler, Y.D., Vincent, M., Weigle, G., Iwata, Y., Kitamura, H., Murakami, T., Calibration and characterization of the Radiation Assessment Detector (RAD) on Curiosity. *Space Sci Rev* **201**: 201–233; 2016.

Zeitlin, C., Castro, A.J., Beard, K.B., Abdelmelek, M., Hayes, B.M., Johson, A.S., Stoffle, N., Rios, R.R., Results from the radiation assessment detector on the International Space Station: Part 1, the charged particle detector. *Life Sci. Space Res.* **39**: 67-75; 2023.

Zhang, S., et al., First measurements of the radiation dose on the lunar surface. *Sci. Adv.* **6**: eaaz1334; 2020.

Appendix A

In this Appendix, references, mathematical expressions, and labeling conventions for the various TE, NTE, and CK options implemented within the ensemble dose-response model are provided. Details regarding the physical or biological interpretations of the models are not discussed; such information can instead be found in the references provided.

TE models

Linear dose-response models are labeled as L_D and may be generally written as

$$R_{TE}(D;\mathbf{B}) = \alpha(\mathbf{B})D\,, \tag{A1}$$

where D (Gy) is the beam dose, $\alpha(\mathbf{B})$ is a proportionality factor, and $\mathbf{B}$ denotes the set of information describing the ion beam (energy, mass, charge, LET, etc.). Forms for $\alpha(\mathbf{B})$ included in this work are given in Table A1; the labeling convention used in the main text is also provided.

Linear-quadratic dose-response models include an additional term, D^2, and may be generally written as

$$R_{TE}(D;\mathbf{B}) = \alpha(\mathbf{B})D + p_\beta D^2\,. \tag{A2}$$

The linear coefficient functions $\alpha(\mathbf{B})$ from Table A1 are used in equation (A2), and p_β is treated as an adjustable parameter. Labels for linear-quadratic dose-response models will be the same as for linear dose-response models except that L_D will be replaced with LQ_D.

Table A1. Coefficient functions for the linear dose-response model, where L is the beam LET (keV/μm), and p_i are the adjustable parameters with the restriction that $p_i > 0$.

$\alpha(\mathbf{B})$	Comment	Label
$p_1 + p_2 L^{p_3} e^{-p_4 L}$	Generalized form of Chang et al. [2016] linear coefficient	$L_D(\alpha_{\text{LET-gen}})$
$p_1 + p_2 L e^{-p_3 L}$	Chang et al. [2016] linear coefficient	$L_D(\alpha_{\text{LET}})$
$p_1 L^{p_2} e^{-p_3 L}$	Modified form of Chang et al. [2016] linear coefficient	$L_D(\alpha_{\text{LET-mod}})$
$p_1 L e^{-p_2 L}$	Simplified form of Chang et al. [2016] linear coefficient	$L_D(\alpha_{\text{LET-simp}})$
p_1	Constant dose coefficient	L_D

Fluence-based models are labeled as L_ϕ and may be written as

$$R_{TE}(D;\mathbf{B}) = \phi\sigma(\mathbf{B})\,, \tag{A3}$$

where ϕ (particles/μm^2) is the beam fluence, related to the beam dose and LET, L (keV/μm), through the relationship $\phi = 6.24D/L$, and $\sigma(\mathbf{B})$ is the biological action cross section. Forms for the action cross section included in this work are provided in Table A2 along with labels. The Katz cross section [Katz et al. 1971] is used, with simplifying variations informed by its application within the NSCR2012 QF and cancer risk projection models [Cucinotta et al. 2013b].

Table A2. Action cross section forms used in equation (A3), where Z^* is the ion effective charge [Cucinotta et al. 2013b], β is the ion velocity relative to the speed of light, and p_i are the adjustable parameters with the restriction that $p_i > 0$.

$\sigma(\mathbf{B})$	Comment	Label
$p_1[1 - e^{-(Z^*/\beta)^2/p_2}]^{p_3}$	Katz cross section	$L_\phi(\sigma_{Katz})$
$p_1[1 - e^{-(Z^*/\beta)^2/p_2}]^3$	Katz cross section with the main exponent fixed to 3, consistent with the NSCR2012 QF	$L_\phi(\sigma_{Katz\text{-}m})$
$p_1[1 - e^{-(Z^*/\beta)^2/550}]^3$	Katz cross section with the main exponent fixed to 3 and exponential coefficient fixed at 550, consistent with the NSCR2012 QF	$L_\phi(\sigma_{Katz\text{-}m\kappa})$
p_1	Linear-with-fluence response independent of beam type	L_ϕ

Xu et al. [2025] developed a dose-response model labeled as mP. The mP model is based on fluence and multilevel probabilistic concepts and may be written as

$$R_{TE}(D;\mathbf{B}) = 100[1 - e^{-\lambda\sigma_{mp}}], \tag{A4}$$

$$\sigma_{mp} = p_1[1 - e^{-p_2 L^{p_3}}], \tag{A5}$$

where λ is the average number of ion traversals to a spherical target with radius r_t (μm) given by

$$\lambda = 6.24\pi r_t^2 \frac{D}{L}. \tag{A6}$$

The fixed target radii for each endpoint are calculated under the assumption of spherical cell nuclei. The values are taken as $r_t = 2.76$ μm for Harderian gland tumorigenesis [Chang et al. 2016], 3.09 μm for chromosome aberrations in blood lymphocytes [George et al. 2003, 2007, 2013; Hada et al. 2014], and 7.18 μm for chromosome aberrations in skin fibroblasts [Hada et al. 2014]. It is known that fibroblasts grown as adherent monolayers can have highly elliptical nuclei [Poignant et al. 2022]. The assumption of spherical geometry in this case may negatively impact model accuracy and uncertainty. The performance metrics used to assign ensemble member weights provide an objective means of adjudicating such issues.

A microdosimetric dose-response model was developed by Slaba et al. [2025] and may be written as

$$R_{TE}(D;\mathbf{B}) = p_1 d_0(D;\mathbf{B},p_r) + p_2 d_1(D;\mathbf{B},p_r) + p_3 d_n(D;\mathbf{B},p_r), \tag{A7}$$

$$R_{TE}(D;\mathbf{B}) = p_1[d_0(D;\mathbf{B},p_r) + d_1(D;\mathbf{B},p_r)] + p_3 d_n(D;\mathbf{B},p_r), \tag{A8}$$

$$R_{TE}(D;\mathbf{B}) = p_1 d_0(D;\mathbf{B},p_r) + p_2[d_1(D;\mathbf{B},p_r) + d_n(D;\mathbf{B},p_r)], \tag{A9}$$

where $p_i > 0$ are adjustable parameters. The target radius, p_r, is also treated as an adjustable parameter and allowed to vary between 1 μm and 10 μm. The term d_0 is the average dose received by spherical targets that were not directly traversed by an ion track but received energy deposition from delta-rays of nearby tracks. The terms d_1 and d_n are the doses delivered to spherical targets traversed by ion tracks exactly once and more than once, respectively. The

microdosimetric dose-response models defined in equations (A7) – (A9) will be labeled μD, $\mu D_{(01)}$, and $\mu D_{(1n)}$, respectively.

Constant nuclear radii are also considered for the microdosimetric models, giving rise to μD_r, $\mu D_{(01)r}$, and $\mu D_{(1n)r}$. As mentioned previously, the constant nuclear radii are 2.76 μm, 3.09 μm, and 7.18 μm for Harderian gland tumorigenesis, blood lymphocyte chromosome aberrations, and skin fibroblast chromosome aberrations experimental datasets, respectively.

In summary, there are five linear dose models, five linear quadratic dose models, four linear fluence models, six microdosimetric models, and one multilevel probabilistic model, yielding a total of 21 TE dose-response models for consideration within the ensemble.

NTE models

The NTE model from Chang et al. [2016] will be labeled Step_{LET} and may be written as

$$R_{NTE}(D;\mathbf{B}) = \begin{cases} p_1 L e^{-p_2 L}, D > 0 \\ 0 \quad\quad , D = 0 \end{cases}. \tag{A10}$$

A simplified form of the Chang model will be labeled Step and is given as

$$R_{NTE}(D;\mathbf{B}) = \begin{cases} p_1, D > 0 \\ 0, D = 0 \end{cases}. \tag{A11}$$

A dose-dependent NTE model developed by Shuryak et al. [2017a, 2022] will be labeled Asymptotic and written as

$$R_{NTE}(D;\mathbf{B}) = p_1(1 - e^{-p_2 D}). \tag{A12}$$

Xu et al. [2025] proposed an NTE model based on multi-level probabilistic concepts labeled as mP and may be written as

$$R_{NTE}(D;\mathbf{B}) = 100[1 - (1 - p_1)^{1-\lambda\mu}], \tag{A13}$$

with λ given by equation (A6), and the target radii for each experimental endpoint is fixed as discussed earlier in this section. The expression for μ is

$$\mu = \begin{cases} p_2 L^{p_3}, L \le L_0 \\ p_2 L_0^{p_3}, L > L_0 \end{cases}, \tag{A14}$$

where L_0 = 193 keV/μm. Further generalization of the mP NTE model allows L_0 to be treated as an adjustable parameter, yielding the mP_{gen} model.

In summary, there are five NTE models included within the ensemble, along with the case of no NTE correction.

CK models

The CK models considered were drawn from Chang et al. [2016] and may be written as

$$R_{CK}(D;\mathbf{B}) = e^{-p_1 D}, \tag{A15}$$

$$R_{CK}(D;\mathbf{B}) = e^{-(p_1 + p_2 L e^{-p_3 L})D}. \tag{A16}$$

These CK models will be labeled Exp and Exp_{LET}, respectively. There are two CK models included within the ensemble, along with the case of no CK correction.

Appendix B

In this Appendix, details of the RITCARD simulations used to calculate RBE_{max} values shown in Figure 23 are provided. RITCARD simulations were performed over a broad range of doses, particles, spherical cell nucleus sizes, and aberration types. The simulated dose-response results from RITCARD were then analyzed to facilitate RBE_{max} calculations. Three different nuclei were considered, using human B-lymphocyte GM12878 Hi-C data and spherical geometries with radii, r_s = 3, 4 and 6 μm. DNA damage repair was modeled for a time period of 48 hours post-irradiation. For all radii, the doses: 0.1, 0.2, 0.4, 0.8, 1.2 Gy were simulated for ions listed in Table B1.

Table B1. List of ions used in RITCARD simulations to enable global RBE_{max} calculations.

E (MeV/n)	*A*	*Z*	LET (keV/um)	*E* (MeV/n)	*A*	*Z*	LET (keV/um)
1059.6	1	1	0.22	164.6	12	6	18.51
318.6	1	1	0.34	135.5	14	7	28.84
155.8	1	1	0.53	106.3	16	8	44.92
1654.4	4	2	0.83	106.7	20	10	69.98
354.7	4	2	1.30	119.2	27	13	109.01
169.3	4	2	2.02	114.7	32	16	169.82
307.7	7	3	3.14	100.1	39	19	264.54
151.6	7	3	4.90	103.1	52	24	412.09
184.3	9	4	7.63	103.0	64	30	641.94
185.1	11	5	11.88	56.4	64	30	1000.00

The doses considered for Cs-137 (reference radiation) were 0.01, 0.05, 0.1, 0.2, 0.3, 0.4, 0.5, 0.6, 0.7, 0.8, 0.9, 1, 1.2 Gy. Additionally, the doses 1.6 and 2.4 Gy were modeled for r_s = 4 μm, and 1.6, 2.4 and 3.2 Gy for r_s = 6 μm to improve parameter estimates derived from dose response fitting. A total of 10^4 nucleus irradiations were calculated for each datapoint, with the exceptions of 0.01 and 0.05 Gy (10^5 nucleus irradiations), and doses beyond 1.6 Gy (5000 nucleus irradiations).

Two endpoints were considered: (1) true total exchanges, calculated as the sum of simple and complex exchanges and (2) true stable exchanges, calculated as the sum of simple and complex exchanges in cells carrying non-lethal aberrations only. The fits utilized a linear quadratic model, $y = \alpha D + \beta D^2$ (true total exchanges), or a linear quadratic model with a cell killing factor, $y = (\alpha D + \beta D^2)e^{-kD}$ (true stable exchanges), where y is the yield obtained for a given endpoint.

Appendix C

Uncertainty propagation in NSCR is achieved by sampling adjustable parameters contained within the radiation hazard rate (λ) and tissue dose equivalent (H_T) from prescribed distributions representing either a range of plausible values or relative uncertainty. For each set of sampled parameters, REIC or REID is evaluated, and the process is repeated a large number of times yielding a distribution from which the mean and confidence levels can be extracted. In this Appendix, probability distributions assigned to parameters within the uncertainty propagation procedure are described.

The radiation hazard rates for solid cancer tissue sites (T) and leukemia (L) from Section 5 can be written as

$$\lambda_i^{(T)} = C_T U_{\text{stat}} U_{\text{DS02}} \left[\tilde{\nu}_T \, \text{ERR}_T \, \lambda_{0,i}^{(T)} U_{\text{NS}} + (1 - \tilde{\nu}_T) \text{EAR}_T \right] \frac{\tilde{H}_T}{\tilde{\delta}} , \tag{C1}$$

$$\lambda_m^{(T)} = C_T U_{\text{stat}} U_{\text{DS02}} \left[\tilde{\nu}_T \, \text{ERR}_T \, \lambda_{0,m}^{(T)} U_{\text{NS}} + (1 - \tilde{\nu}_T) \text{EAR}_T \frac{\lambda_{0,m}^{(T)}}{\lambda_{0,i}^{(T)}} \right] \frac{\tilde{H}_T}{\tilde{\delta}} , \tag{C2}$$

$$\lambda_m^{(L)} = C_L U_{\text{stat}} U_{\text{DS02}} \left[\tilde{\nu}_L \, \text{ERR}_L \, \lambda_{0,m}^{(L)} U_{\text{NS}} + (1 - \tilde{\nu}_L) \text{EAR}_L \right] \tilde{H}_L , \tag{C3}$$

$$\lambda_i^{(L)} = C_L U_{\text{stat}} U_{\text{DS02}} \left[\tilde{\nu}_L \, \text{ERR}_L \, \lambda_{0,i}^{(L)} U_{\text{NS}} + (1 - \tilde{\nu}_L) \text{EAR}_L \frac{\lambda_{0,i}^{(L)}}{\lambda_{0,m}^{(L)}} \right] \tilde{H}_L , \tag{C4}$$

where functional dependencies have been removed for simplicity. The symbol $\tilde{\delta}$ denotes a sampled DDREF value, and $\tilde{\nu}_T$ denotes a set of sampled transfer weights. U_{stat}, U_{DS02}, and U_{NS} are sampled relative uncertainties. U_{stat} and U_{DS02} represent uncertainties attributable to site-specific solid cancer incidence (mortality in the case of leukemia) statistical errors and dosimetry errors, respectively, as discussed in the NSCR2012 report and elsewhere [Simonsen and Slaba 2020, 2021]. U_{NS} represents uncertainty associated with baseline never smoker cancer incidence and mortality rates and is only included if the never smoker population is considered.

The dose equivalent for each tissue is calculated as

$$\tilde{H}_T = U_{\text{phys}} \frac{10^{-8}}{6.24\rho} \sum_j \int_0^\infty \phi_j^{(T)}(E) \, \tilde{Q} \, L \, dE , \tag{C5}$$

where U_{phys} is a sampled relative uncertainty attributable to combined environment, physics, and transport models used to calculate tissue fluences. The symbol $\tilde{Q}$ represents a QF evaluated using parameters sampled from prescribed uncertainty distributions. Details of the adjustable parameters within the NSCR2012 and NSCR2025 QF can be found in Sections 5.7.2.3 and5.7.3.4, respectively.

Probability distributions assigned to adjustable parameters and relative uncertainties in equations (C1) – (C5) are defined in Table C1 for NSCR2020. Updated definitions used in NSCR2025 are provided in Table C2.

Table C1. Probability distributions used in NSCR2020.

NSCR Component	Quantity	Distribution
Excess risk	U_{stat}	Gaussian with a mean of 1.0 and tissue specific standard deviations, σ_T, ranging from 0.2 to 1.0[(1)]
	U_{DS02}	Log-N(0.9,1.3)
	U_{NS}	N(1,0.15)
	ν_T	Bernoulli distribution about preferred weights
Radiation quality	Σ_0/α_γ	Log-N(0.9,1.4) for solid cancer and Log-N(1.0,1.6) for leukemia
	κ	Log-N(0.95,1.4)
	m	Discrete distribution for values [2.0,2.5,3.0,3.5,4.0] with weights [0.2,0.2,0.35,0.2,0.05]
	s_{sparse}	N(1,0.15)
Dose-rate	DDREF	Student's t-distribution with 5 degrees of freedom and transformed argument
Physics	U_{phys}	N(1.05,1/3) for Z ≤ 2 and N(1,0.25) for Z > 2

(1) $\sigma_T = 0.2$ for bladder, breast, leukemia, liver, ovaries, prostate, stomach, and uterus; $\sigma_T = 0.3$ for brain and colon; $\sigma_T = 0.4$ for remainder and thyroid, $\sigma_T = 0.5$ for oral cavity, $\sigma_T = 0.6$ for lung, $\sigma_T = 1$ for esophagus.

Table C2. Probability distributions used in NSCR2025. Components in bold text have been updated from the NSCR2020 definitions in Table C1.

NSCR Component	Quantity	Distribution	
Excess risk	U_{stat}	Gaussian with a mean of 1.0 and tissue specific standard deviations, σ_T, ranging from 0.2 to 1.0[(1)]	
	U_{DS02}	Log-N(0.9,1.3)	
	U_{NS}	N(1,0.15)	
	ν_T	Bernoulli distribution about preferred weights	
Radiation quality	$\Sigma_{0\gamma}$	Log-N(-0.131,0.643) for solid cancer Log-N(-0.645,1.286) for leukemia	Rank correlation coefficients: $\rho(\Sigma_{0\gamma},k) = 0.491$; $\rho(\Sigma_{0\gamma},\mu) = -0.123$; $\rho(k,\mu) = -0.856$
	k	Log-N(-0.008,0.354)	
	μ	N(1,0.127)	
	s_{sparse}	N(1,0.15)	
Dose-rate	DDREF	Student's t-distribution with 5 degrees of freedom and transformed argument	
Physics	U_{phys}	N(1,0.2)	

(1) $\sigma_T = 0.2$ for bladder, breast, leukemia, liver, ovaries, prostate, stomach, and uterus; $\sigma_T = 0.3$ for brain and colon; $\sigma_T = 0.4$ for remainder and thyroid, $\sigma_T = 0.5$ for oral cavity, $\sigma_T = 0.6$ for lung, $\sigma_T = 1$ for esophagus.